SURFACE CHARACTERIZATION AND OPTIMIZATION OF WIRE ELECTRIC DISCHARGE MACHINING PROCESS OF P91 STEEL

By

SUJAY BHATTACHARYA

ENGG01201304027

BHABHA ATOMIC RESEARCH CENTRE, MUMBAI

A thesis submitted to the

Board of Studies in Engineering Sciences

In partial fulfillment of requirements

for the Degree of

DOCTOR OF PHILOSOPHY

of

HOMI BHABHA NATIONAL INSTITUTE

August 2020

Homi Bhabha National Institute

Recommendations of the Viva Voce Committee

As members of the Viva Voce Committee, we certify that we have read the dissertation prepared by **Sujay Bhattacharya** entitled **"Surface Characterization and Optimization of Wire Electric Discharge Machining Process of P91 Steel"** and recommend that it may be accepted as fulfilling the thesis requirement for the award of Degree of Doctor of Philosophy.

Chairman - Dr. S. Banerjee	Srikumar Banerjee
Guide - Dr. Vivekanand Kain	
Co-guide - Dr. G. K. Dey	Gautam Kumar Dey
Examiner - Dr. Dhiraj K. Mahajan	Mahajan
Member - Dr.(Smt.) S. B. Roy	
Member - Dr. N. K. Maheswari	Naresh Kr. Mahesh

Final approval and acceptance of this thesis is contingent upon the candidate's submission of the final copies of the thesis to HBNI.

We hereby certify that we have read this thesis prepared under our direction and recommend that it may be accepted as fulfilling the thesis requirement.

Date:
Place: Mumbai

Gautam Kumar Dey
(Prof. G. K. Dey)
Co-guide

(Prof. Vivekanand Kain)
Guide

STATEMENT BY AUTHOR

This dissertation has been submitted in partial fulfillment of requirements for an advanced degree at Homi Bhabha National Institute (HBNI) and is deposited in the Library to be made available to borrowers under rules of the HBNI.

Brief quotations from this dissertation are allowable without special permission, provided that accurate acknowledgement of source is made. Requests for permission for extended quotation from or reproduction of this manuscript in whole or in part may be granted by the Competent Authority of HBNI when in his or her judgment the proposed use of the material is in the interests of scholarship. In all other instances, however, permission must be obtained from the author.

S. Bhatt

(Sujay Bhattacharya)

DECLARATION

I, hereby declare that the investigation presented in the thesis has been carried out by me. The work is original and has not been submitted earlier as a whole or in part for a degree / diploma at this or any other Institution / University.

(Sujay Bhattacharya)

List of Publications arising from the thesis

Journal publications:

1. Sujay Bhattacharya, Abhishek Mishra, N. Keshkar, Santosh. Kumar, Vivekanand Kain, and G. K. Dey, "Wire Electric Discharge Machining of P91 Steel: Microstructure and Thermal Modeling Studies", Metallurgical and Materials Transactions A, 50 (2019): 5336-5355.

2. Sujay Bhattacharya, N. Tiwari, A. Mishra, S. Mitra, G. K. Dey, and S. Ghorui, "Underwater Electrical Discharges: Temperature, Density and Basic Instability Features with Different Anode Materials", Plasma Chemistry and Plasma Processing, 39 (2019):1019–1048.

3. Sujay Bhattacharya, Geogy J. Abraham, Abhishek Mishra, Vivekanand Kain, and G. K. Dey, "Corrosion behavior of wire electrical discharge machined surfaces of P91 steel", Journal of Materials Engineering and Performance, 27 (2018): 4561-4570.

Conference publications:

1. Sujay Bhattacharya, Abhishek Mishra, Tarvinder Singh, Srijit Bandyopadhyay, Santhosh Kumar, G. K. Dey, and V. Kain, "Simulation of Residual Stress using Thermo-mechanical Analysis on Wire EDM cut surface", 1st International Conference on Manufacturing, Materials Science & Engineering, ICMMSE-2019, 16–17 Aug, 2019, Hyderabad, published in Materials Today Proceedings 19, Part 2, (2019): 462-467.

2. Sujay Bhattacharya, Abhishek Mishra, G. K. Dey, and Vivekanand. Kain, "Numerical study of heat transfer effect of Wire EDM on P91, SS304, Al 1050 using COMSOL Multiphysics", COMSOL Conference 2019, 28-29 Nov, 2019, Bangalore, organised by COMSOL Multiphysics Pvt. Ltd.

S. Bhatt

(Sujay Bhattacharya)

DEDICATIONS

To My Father who inspired me all along

and

My Mother who taught me endurance in life

ACKNOWLEDGEMENTS

A decade long dream and hard work has been translated into research thesis. This motivational research work has nurtured me technically and helped to developed me socially through various interactions. Therefore, I would like to express my deep gratitude for all the people who have helped me in fulfillment of this research. I thank my research guide Dr. Vivekanand Kain for continuous guidance and give suggestions to improve the technical content and presentation of the thesis without which this research would not have come out well. My deepest gratitude goes to my co-guide Dr. G. K. Dey. He gave, in fact, day to day technical guidance during the thesis work and has been a guiding light for proper planning of my research work. His continuous encouragement for undertaking new thinking and study has helped me to carry out this developmental research work. He always pacified my mental turbulence and motivated me when I faced technical and other difficulties while carrying out this research work. I would like to thank Dr. S. Ghorui and Smt. Nirupama Tiwari for supporting me in the experiments related to plasma physics which has utmost significance in this work. Their guidance helped me to delve a new insight of the process involved in this research. I am also thankful for Dr. Geogy Abraham for expert advice in corrosion involved in the present research. Also, she helped me to understand the basics involved. I am thankful to Dr. Santosh Kumar who helped me to understand complex metallurgical aspects of the research area in simple and lucid way.

I would like to express my gratitude for Shri Nachiket Keskar for helping me in obtaining SEM images, without which it would not have been possible to investigate the machined surface at atomic level. Next I would like to thank Shri Abhishek Mishra, for helping me in planning and organizing all experiments and numerical analysis involved in this work. I am also thankful to Sri Tarvinder Singh and Shri Srijit Bandyopadhyay for helping me in residual stress related works involved in this thesis. I would like to thank Shri Anirudhha Ghosh, Shri Vishesh Shrivsatava, Shri Vinayak Viswanathan and Pushpendra Hazari for their valuable technical support.

Lastly, I would like to thank my family, specially my wife and daughters who always encouraged me. They have taught me to do hard work and stay positive in all situations. I would like to dedicate my thesis to my mother whose divine blessings has helped me to evolve positively even in difficult circumstances.

CONTENTS

LIST OF FIGURES

LIST OF TABLES

Chapter 7

Conclusion

This chapter presents the summary of the research done in this thesis along with conclusions of the work.

7.1 Plasma behavior of underwater spark under different electrodes

- The temperature of EDM plasma has been found to depend upon the composition of the work piece material. It is possible that the eroded material also becomes a part of plasma during implosion of plasma and these ablated materials significantly influences the thermodynamic and transport properties of plasma. The temperatures of the electric discharge zone for I SS304 and P91 are found to be of the order of 5500K and 7100K respectively. The highest temperature of plasma among the materials studied in this work was found for Zircaloy i.e. around 14372K. The temperature for copper reaches around 9048 K.
- The dynamic behavior of spark was studied using fast photographic camera. It revealed that plasma of EDM with water as dielectric has pressure driven flow. Strong anode jet through J×B pumping, sausage type instability, generation of pressure wave shock fronts, formation of multiple radial arc roots were observed and their significance in performance has been established. Physical observation of shocks and variation in its intensity with change in anode materials are possibly addressed for the first time. However, the information inferred in this study is

qualitative but may serve as good first-hand information for theoretical modelling and experimental understanding of wire EDM plasma. The observation of J×B pumping in EDM discharge is a very important phenomenon as it affects the amount of energy of the spark that interacts with the workpiece. This observation is also not possibly included in any of the previous literatures.

7.2 Characteristics and microstructure of Recast layer and Wire EDM machined surface of P91.

- The study showed recast layer is formed in WEDM of P91 and the layer has micro crack distributed in all directions. A mathematical relation was established to study the significance of process parameters on the thickness of the recast layer, the surface finish, the number density and the orientation of the cracks was found to depend on the machining conditions. The average length of micro crack in P91 varies from 2.2μm to 11.8μm under the experimental conditions used in this study.
- A detailed investigation of recast layer was carried out. It is concluded through the TEM image of the recast layer that this layers has the presence of re-casted grains. High resolution TEM also revealed that the layer has regions where no lattice could be seen and also regions where small crystals were observed. These regions had nano crystalline as well as amorphous structure. This could be possibly due to intense heating and rapid cooling experienced by the material after spark is off. Electron diffraction pattern from these regions also confirmed the presence of amorphous and nano crystalline regions. The numerical model also successfully explained the microstructure observed under the SEM. Residual stress and nano hardness of wire EDM machined surface of P91

7.3 Optimization of process parameters for P91 and general industrial materials

The study also concluded with the establishment of optimum process parameters for obtaining the desired surface characteristics like surface roughness, length of micro cracks, and orientation of micro cracks during machining of P91 and general industrial materials using wire EDM have been obtained. Medium energy condition (refer to chapter 5) are best suitable for wire EDM machining of P91.

7.4 Room temperature and high temperature behavior of wire EDM machined surface of P91

The corrosion study of machined surface of P91 showed that the P91 steel wire electrical discharge machined surfaces have better passivation than diamond polished surface in different pH buffer solution and in sulphuric acid environment. (pH-0 to pH-9.2). However, these surfaces behave similar to weldment of P91 steel qualitatively and quantitatively in sulphuric acid environment. The craters formed on the WEDM machined surface at as initiation sites of pitting corrosion. Therefore, the wire EDM machined surface has poor pitting resistance than diamond polished surfaces. The wire EDM machined surface has better chromium content along the carbides as compared to diamond polished surface. Hence the IGC resistance of P91 steel wire EDM machined surface is better than diamond polished surface.

Chapter 8

Future work

This chapter presents an extension to this thesis in the form the future work. The author wanted to explore more in the field of optimization of Wire EDM process. However, these due to diverse scope of research in this field a confined approach with identified aim was inevitable. Therefore, these works can be presented as future scope for research in wire EDM.

8.1 Suggestions for future Work

Some of the possible extensions of the present study are as follows

8.2 Non Fourier heat conduction modelling of Wire EDM plasma

The present study uses Fourier heat conduction to model the heat conduction involved in Wire EDM process. The heat transfer in wire EDM involved very high flux and very minuscule time of application of flux of the order of microseconds. Such high heat flux applied within such time interval can be explained with Fourier heat conduction model with some assumptions. A new approach of Non Fourier heat conduction can be used to study the heat transfer involved in the Wire EDM process. Non Fourier heat conduction are generally used to study the heat transfer phenomena involved in biological tissue where high heat fluxes are applied over concentrated areas for application like LASER therapy etc. The spark –workpiece interaction in EDM process has similar behavior, a very small area of application of flux form very small time interval. Therefore, a detailed look into wire EDM process through aspects of Non Fourier heat conduction can be studied.

8.3 Behaviour of wire EDM plasma using different dielectrics

In the present work characteristics of water plasma was studied. The behavior of plasma depend upon the composition of the dielectric and performance of the machining process also depend on the type of dielectric used. Therefore, an extensive study of plasma of different dielectrics could be done. This would help in selection of best dielectric for optimized performance of the Wire EDM process for different materials.

8.4 Modelling of convection at plasma and liquid interface in Wire EDM process

In the present study the only conduction mode of heat transfer form plasma to work piece has been studied. The plasma –liquid interface in the dielectric medium accounts for cooling of plasma during Wire EDM process. Therefore, a detailed investigation of plasma liquid interface under different dielectric and electrodes can be studied to assess the efficiency of WEDM process.

Surface Characterization and Optimization of Wire Electric Discharge Machining process of P91 steel (Summary)

Electrical discharge machining (EDM) is known as spark machining and widely used as a metal machining process. Material is removed from the work piece by a series of rapidly recurring current discharges between two electrodes, separated by dielectric liquid, due to pulsing voltage applied between tool and work-piece-electrode and this forms Plasma in the narrow channel causing intense heating which melts the work-piece material. The melted metal portion subsequently gets ejected out due to the implosion of plasma channel in voltage pulse off cycle and flushed out as debris. High machining accuracy can be obtained in EDM. In this thesis we have carried out study of the surface characterization and optimization of Wire EDM process of P91 steel. The study carried out is described in six chapters.

Chapter-1 dealt with basic physical process of plasma generation in spark channel in WEDM. It outlined the experimental investigation that are carried out for type and characteristics of plasma produced in various work piece materials, estimation of the spark plasma temperature in WEDM process, numerical modelling of transient heat transfer in the work-piece on application of the heat in 'voltage pulse on time' and study the effect of temperature transient on the microstructure of the cut surface. It also outlined the optimization of process parameters using response surface methodology carried out in P91 steel. The corrosion characteristics of cut surface of P91 steel with various energies were studied.

Chapter -2 covered the review of literatures published in EDM and WEDM in general. It gave following areas of research (a) Physics of EDM process (b) Improving machine performance in terms of material removal rate, tool wear and surface characteristics (c) study of heat transfer in WEDM using numerical modelling.

Chapter-3 covered the details of experimental work carried out on P91 steel and other industrial materials. Experiment was conducted using standard WEDM machine at various cutting energies which encompasses the variation of peak current, voltage and spark on/off time and combination of all these parameters and cut surface microstructural data was collected using Scanning Electron Microscopy and Transmission Electron Microscopy for in depth study of recast layer characteristics of cut surface.

Chapter-4 covered the experimental setup and theoretical investigation that were carried out for type and characteristics of plasma produced in various work piece materials and estimation of the spark plasma temperature in WEDM process by optical spectroscopic technique using 'line Pair method'. WEDM plasma temperature was estimated experimentally for P91, Zircalloy-4, SS304, Copper and Aluminum work-piece. It gave new finding of electromagnetic pumping prevalent during the spark occurring in spark on time.

Chapter-5 covered the detail study of transient heat transfer that takes place during one cycle of spark on-time. The heat source in the form of Gaussian pulse was applied with all necessary boundary and initial condition in finite element model to estimate the temperature profile with time along the depth for different cutting energy condition. The temperature so obtained was used to correlate the surface microstructural feature obtained in the study. Recast layer features like thickness, surface roughness, micro-cracks, crater sizes and residual stress were correlated with Numerical model estimation.

Chapter-6 covered the corrosion behavior of the P91 cut surface in pH-4, neutral pH 9 buffer solution, in $0.5\mathrm{M}H_2SO_4$ and H_2SO_4 combined with added NaCl buffer solution and the results were compared with diamond polished surface. Corrosion characteristics with respect to corrosion potential and corrosion current were estimated in different cutting energy condition. Inter granular corrosion was also studied for the cut surface.

Chapter-7 outlined the conclusion of the study and future work on WEDM.

Chapter 1

Introduction

1.1 Motivation and Significance

Electrical discharge machining (EDM) is used for alloys or those materials that are very difficult to machine with traditional techniques. This method mostly works with materials that are electrically conductive. Search for methods for machining ceramics has been also made. This technique can cut difficult contours in hardened steel without making it soft by heat treatment. This method works well with metals and alloys and can be put in the non-traditional or non-conventional category along with other processes such as electrochemical machining, cutting or water jet cutting as compared to the conventional group of machining processes like turning, grinding, drilling etc.

1.2 Research trend in the field of EDM

Machining of advanced materials viz. super alloys, ceramics, and composites, requiring high precision and surface quality at minimum machining cost is being pursued today. To meet these challenges, non-conventional machining process are used. The type of energy used for machining differentiates non-conventional process from conventional processes. The different types of non-conventional machining processes are Ultrasonic Machining (USM) [1], Water Jet Machining (WJM) [2], Abrasive Jet Machining (AJM) [3], Electric Discharge Machining (EDM), Electron Beam Machining (EBM) [4], Laser Beam Machining (LBM) [5], Chemical Machining (CM) [6] and Photochemical Machining (PCM) [7]. The EDM is a thermal material removal process. It is used now extensively to machine various advanced materials with high accuracy. Various EDM processes have evolved based on applications. Die-sinking EDM, Rotating pin electrode (RPE), Wire electrical discharge machining (WEDM), Micro-EDM, Dry EDM, Rotary disk electrode electrical discharge machining (RDE-EDM) are some of the variants [8]. There are a number of process parameters associated with WEDM process such as peak current, pulse-on time, pulse-off time, wire electrode material, wire speed, wire tension, flushing pressure, work material properties etc. which can be used as input to assess the outcome responses such as material removal rate, surface roughness, dimensional accuracy, recast layer etc. Several researchers have attempted to improve the performance characteristics of WEDM through use of Taguchi method, Response surface optimization and grey relational analysis apart from using artificial neural network. Ho et al. [9] have classified the wide range of published works relating to the WEDM process into three major areas, namely optimizing the process variables (process parameter design & process modeling), monitoring and control the process (fuzzy control system, wire inaccuracy adaptive control system, wire breakage, wire lag, wire vibration & self-tuning adaptive control system), and WEDM developments (hybrid machining process, WEDM applications). P.C. Pandey [10] presented a review of the area of research in EDM process. The major challenges in this field are to understand the behavior of the plasma channel both at macroscopic and microscopic levels and improve the Material removal rate (MRR). Some of the research areas in EDM are shown in Figure 1.1.

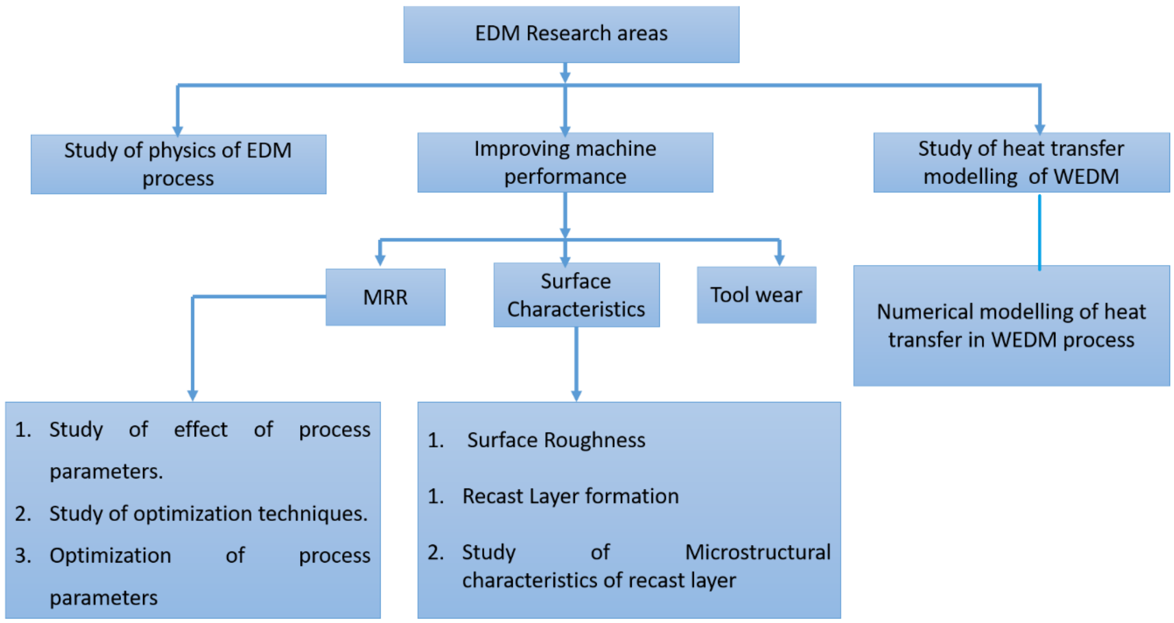

Figure 1.1 Research trends EDM [3]

P. T. Eubank and M.R Patel [11] proposed a variable mass cylindrical plasma model for EDM. The model consists of three differential equations, one each from fluid dynamics, energy balance and the radiation equation, combined with a plasma equation of state. A thermo physical property subroutine was used to allow realistic estimation of plasma enthalpy, mass density, and particle fractions by inclusion of the heats of dissociation and ionization for a plasma created from deionized water. Numerical solution of the model provides plasma radius, temperature, pressure, and mass as a function of pulse time for fixed current, electrode gap, and power fraction remaining in the plasma. Moderately high temperatures (> 5000 K) and pressures (> 4 bar) persist [11] in the sparks even after long pulse times (100to -500, µs) [11]. The plasma, once created by dielectric breaks down, radiates energy to the electrode surface and using them to melt and facilitate the ejection of liquid metal by the mechanism of superheating. It is estimated that 18%oftotalenergygoes to melting of cathode, 8%totheanode, and the remainder to enlarging the mass and the size of the plasma at the expense of the surrounding liquid [11]. The model evaluates the spark radius as function of effective discharge time with exponent coefficient [4]. The exponent coefficient of 3/4 was found for the plasma radius by Robinson [12] by exploding wires under water. They used a comprehensive plasma model including heat transfer and thermo physical properties including dissociation and ionization.

1.3 Gap areas in EDM research

A review of the literature [1-15] revealed that most of the research work has been directed towards optimization of WEDM operation and modeling of the process and directed to a particular material. A comparison of the effect of WEDM process for different materials is yet to be studied exhaustively. Most of the researchers concentrated their study on Material removal rate (MRR) [13] and tried to use adaptive control either using Artificial neural networking (ANN) [14] or Response surface methodology (RSM) [15]. The effect of discharge current, pulse duration, work piece material property (thermal conductivity, specific heat capacity and melting point) has not been studied extensively in relation to surface morphology on different materials.

1.4 Scope of the present work

There are a lot of research works done in EDM but no research work for P91 steel material was reported as per the knowledge of the author of the thesis. P91 steel is a martensitic steel and it is extensively used in high temperature applications. In this thesis, the EDM cutting of P91steel will be examined in detail. The scope of the present work contains the following main aspects.

1. Detailed examination of the generation of the plasma and its behavior with different anode materials during the cutting process using advanced experimental methods.
2. The creation of debris would be investigated by high speed photography giving a perspective which has not been focused so far in other research papers in much detail.
3. Investigation of effect of process parameters on the surface microstructure of the machined surface. This also includes study of nature of phases present, the grain size, grain morphology, cracks, recast layer characteristics, extent of heat affected zone.
4. Study of corrosion behavior of wire EDM machined surface of P91 steel and correlating the residual stresses present in the machined surface with process parameters and microstructure of the machined surface.
5. Optimization of wire EDM process for machining of P91 steel using RSM technique and preparation of a generalized table of optimized process parameters for general industrial materials.

1.5 References

[1] T. B. Thoe, D. K. Aspinwall, and M. L. H. Wise "Review on ultrasonic machining", International Journal of Machine Tools and Manufacture, 38 (1998): 239-255.

[2] W. Andreas Momber and Radovan Kovacevic "Principles of abrasive water jet machining", Springer Science & Business Media, 2012.

[3] Ruslan Melentiey and Fengzhou Fang "Recent advances and challenges of abrasive jet machining", CIRP Journal of Manufacturing Science and Technology, 22 (2018): 1-20.

[4] Okada Akira “Electron beam machining”, CIRP Encyclopedia of Production Engineering (2014): 446-452.

[5] Avanish Kumar Dubey and Vinod Yadava “Laser beam machining—a review”, International Journal of Machine Tools and Manufacture, 48 (2008): 609-628.

[6] Hashmi, Saleem: Comprehensive Materials Processing, Elsevier, 2014, eBook ISBN: 9780080965338.

[7] Hassan, EI-Hofy : Advanced Machining Processes, McGraw-Hill, 2005.

[8] Shih Hung Rung, and Kuen Ming Shu “A study of electrical discharge grinding using a rotary disk electrode”, International Journal of Advanced Manufacturing Technology, 38 (2008): 59-67.

[9] K.H. Ho, S.T. Newman “State of the art electrical discharge machining (EDM)”, International Journal of Machine Tools & Manufacture,43 (2003): 1287–1300

[10] Anand Pandey, Shankar Singh, “Current research trends in variants of Electrical Discharge Machining: A review”, International Journal of Engineering Science and Technology, 2(6), (2010): 2172-2191

[11] Mukund R. Patel, M.R. Barrufet et. al, “Theoretical models of the electrical discharge machining process. III. The variable mass, cylindrical plasma model”, J. Appl. Phys., 73, 7900 (1993)

[12] W. James Robinson, “Measurements of Plasma Energy Density and Conductivity from 3 to 120 kbar”, Journal of Applied Physics, 38 (1967): 210-216.

[13] Ravindranadh Bobbili, V. Madhu, and A. K. Gogia "Modelling and analysis of material removal rate and surface roughness in wire-cut EDM of armour materials", Engineering Science and Technology, an International Journal, 18, (2015): 664-668.

[14] Gopal Indurkhya, K. Rajurkar "Artificial Neural Network approach in modelling of EDM process", In Proceedings of the 1992 Artificial Neural Networks in Engineering, ANNIE'92, ASME, 1992: 845-850.

[15] Rajneesh Raghav, Subhash Singh, R. S. Mulik and Kaushik pal "Study of Machining Performance in EDM Through Response Surface Methodology", In Advances in Industrial and Production Engineering, Springer, Singapore, 2019: 207-219,

Chapter 2

Literature Survey

2.1 Introduction

The idea of spark machining was initiated as early as in 1920 in USSR. B.R Lazarenko and N.I Lzarenko in USSR originally developed [1] the technology of Electrical Discharge Machining (EDM). Since then, the process of EDM was being developed continuously in various applications [1]. The shop floor and tool room applications of WEDM took place rapidly in late 1980s. In this chapter research papers related to EDM plasma channel formation, its growth, the mechanism of erosion of the electrodes, mode of heat transfers from plasma to the workpiece, the effect of voltage and current variation on the material removal rate of the work piece and residual thermal stress on the cut surface are reviewed and discussed. The research papers can be broadly classified into five different categories, i.e. (i) papers related to plasma formation, (ii) growth and (iii) mode of heat transfer in plasma channel and (iv) study of microstructure of machined surface (v) tool wear rate (TWR)

2.2 Working principle and key features of EDM process

EDM works on the principle of erosion of material by electric discharge. The work piece and tool are made electrodes. The electrodes are separated from each other and gap between the electrodes is filled with a dielectric [2]. The gap between the electrodes is decided by the dielectric strength of the dielectric medium present between the electrodes. Pulsed voltage is applied to the electrodes which leads to breakdown of the dielectric. As soon as dielectric breaks down an electric discharge is generated. Continues flushing of dielectric is provided to the electrodes. The material of the work piece melts and is eroded by flushing of the dielectric. It is necessary to regain the dielectric strength of the liquid between the electrodes for next spark to occur. Therefore, the spark is kept on for specific time which is called spark on time (ton), after which spark gets off which is known as spark off time (toff) [3]. Other important key parameters of EDM process are pressure of flushing of dielectric, tension of wire (in case of wire EDM), peak current (IP) i.e. maximum current imparted to the electrodes) , voltage applied between the electrodes (V) [2] .

2.3 Material removal mechanism

Critical explanation of the mechanism of material removal during EDM was given by Van Dijik. In the work done by Van Dijik [2, 3 4] a thermal model along with a computational simulation are used to explain the phenomena occurring during discharge machining. However, in this work many assumptions were made and at that time when this model was formulated experimental data was not sufficient. In the late eighties and early nineties better models were developed to explain the phenomena occurring during EDM in terms of heat transfer theories. An investigation carried out at Texas ANM University gave the most advanced explanation for the process taking it as a thermal process [5-7]. Essentially three sets of papers developed, the first set addressing the material removal on the cathode presenting a thermal model [5], the second set addressing erosion opening on the anode side [6] and the third set described the plasma channel that is formed during the passage of the discharge current through the dielectric liquid [8]. Validation of these models was carried out by AGIE Corporation, a leading EDM manufacturer using experimental data also [5]. Material removal from the two electrodes because of melting or vaporization processes in conjunction with pressure dynamics established in the spark gap while the quality of the plasma channel had been used to model the process as a thermal process. The models developed so far were inadequate to explain all aspects of this process. These models assumed many factors which need not be applicable like discharge in gases, underwater spark and implosion of vapour bubbles of hot plasma collapse. Many new theories like electro mechanical theory, thermo mechanical theory a thermo electric theory had been proposed in recent literature to explain this process better [9, 10] . The model from the work of Singh and Ghosh [9] which considers the presence of an electrical force on the surface of the electrode that will be able to mechanically remove material and create the creators, is more appealing because of the fact that material near the surface has reduced mechanical properties due to an increase in temperature, making this possible. This set of workers were able to explain the process better than by thermal model for processes specially for small discharge energies which are typically adopted in micro EDM and in finishing operations. When mathematical modeling of the EDM process was done, problems were faced. The hydrodynamic, the thermodynamic behavior and the gap pollution of the working fluid are difficult to model. It appears that the material removal mechanism in EDM is not well understood and there is a need to validate testing models. It is difficult to create a theoretical model to explain all the technical results. The earlier efforts where governed by market demand for application oriented models and failed to give a unified EDM model. In electrical discharge, the removal of materials is based upon the erosion effect of electric sparks occurring between two electrodes. Several theories have been put forward in order to explain the phenomenon of complex nature occurring during the erosive spark process [10]. Some of these are the following:

1. Electro-mechanical theory

2. Thermo-mechanical theory

3. Thermo-electric theory

2.3.1 Electromechanical theory

In this it is postulated [10] that the removal of particles takes place as a result of concentrated electric field. This theory proposes that the forces of cohesion in the lattice of the material is exceeded by the force separating the material particles as a result of the electric field. The model proposed by Singh and Ghosh [9] postulates that removal of material around electrode is due to an electric force on the surface of the electrode that mechanically removes material from electrode creating craters. This is aided by the fact that the mechanical properties of the material are reduced due to temperature increase caused by the passage of the current.

2.3.2 Thermo-mechanical theory

In this theory [10] it is postulated that the material removal during EDM process occurs as a result of melting of the material under the influence of flame jets. The various electrical effects of the discharge lead to the formation of the flame jets. Like the previous set of models, this theory is also not able to explain all the experimental observations.

2.3.3 Thermoelectric theory

The models under this theory [10] assume the metal removal occurring during EDM takes place under the combined influence of electric field and the extremely high temperature of the process. The creation of a high temperature plasma channel due to the sparks generated in the electrode gap as a result of the discharge current, leads to this effect. Though this theory appears to be more comprehensive, it cannot interpret all the experimental observations. It is the based on thermo-electric mechanism and is able to explain the process best at the moment.

2.4 Process mechanisms

The concept of EDM process has been shown in Figure 2.1. A basic understanding of the different phenomena during process can help the machinist in selecting the best process parameters for a given surface and also troubleshooting. The physics behind the different phenomena occurring during the process can be understood step by step as follows:

In the gap between the electrode and the work-piece which is of tens of microns and is filled with a dielectric liquid like hydrocarbon oil or deionized water, pulsed arc discharges occur. In this case the dielectric medium in between works as a capacitor and has importance in avoiding electrolysis during the passage of spark.

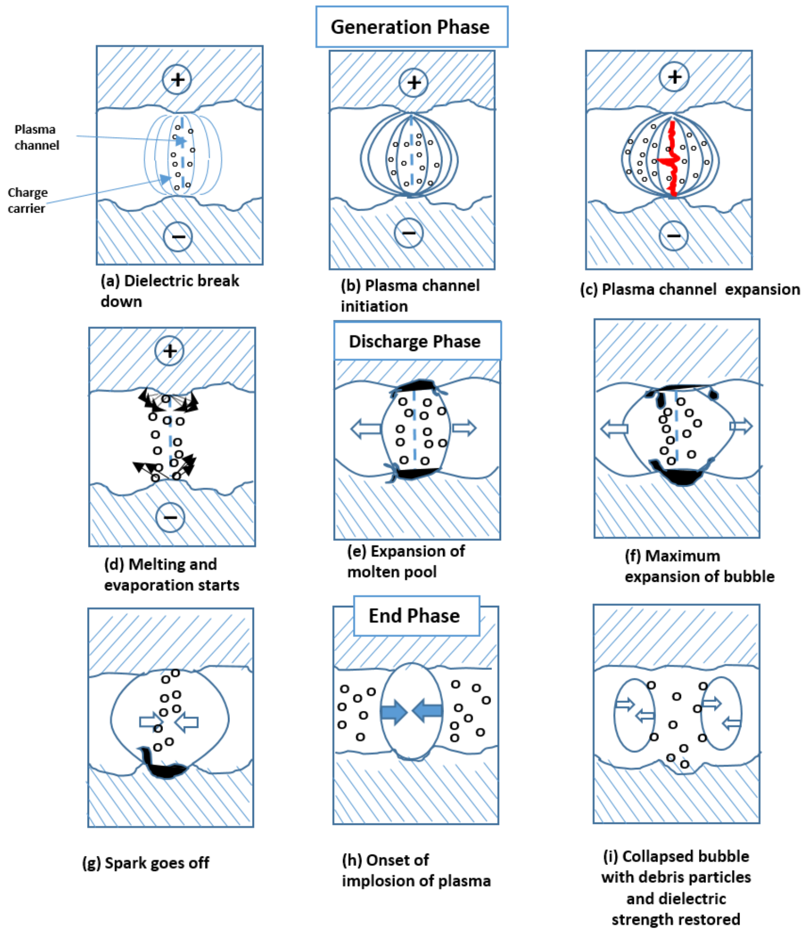

Figure 2.1 Schematic diagrams showing the different phases of the EDM process and the different phenomena occurring during machining [11].

In the gap between the electrode and the work-piece which is of tens of microns and is filled with a dielectric liquid like hydrocarbon oil or deionized water, pulsed arc discharges occur. In this case the dielectric medium in between works as a capacitor and has importance in avoiding electrolysis during the passage of spark.

The electric potential generated in the small gap of 10 to 100 microns due to the application of high voltage is able to exceed the electric breakdown strength of the medium in the small gap shown in Figure 2.1. It sets initiation of spark by breakdown of dielectric strength of dielectric used as shown in Figure 2.1(a)-(c). After that expansion of plasma channel starts and charge is carried by free ions and electrons [11]. As soon as the temperature of the plasma channel reaches to melting point of the materials, the work piece material starts melting and evaporating (Figure 2.1 (d) –(f) . At the end of spark on time the spark goes off. This phase leads to implosion of plasma bubble and the molten material gets eroded from the workpiece. Further the debris gets flushed by the incoming dielectric and dielectric strength is restored (Figure 2.1(g)-(i).In order to avoid short circuiting of the electrodes, a gap is needed especially when vibration of the formation tools and deposition of metal debris occurs due to inadequate flushing. Between the electrodes a channel of plasma is generated which further develops with duration of the discharge. Intense localized heating occurs in the narrow channel and the temperature exceeding 9000 to 13000 K is developed. Since the rate of removal of material is small, there is a need for the discharges to occur at very high frequencies (103-106Hz) [6].

The discharge occurs at a single location for every discharge till it is moved to a new location. Because of these occurrences small crater is generated on the work-piece surface as well as on the tool electrode. Due to the flow of the dielectric the material which comes out of either of the electrodes solidifies and is flushed away. In case of the wire EDM, the wire is moved continuously and therefore the location of the spark on the wire keeps changing. This ensures that the material is not removed repeatedly from one spot. The material removal from the electrode is controlled by applying suitable polarity

The temperature of the plasma generated by the spark drops rapidly after end of the discharge. End of the discharge leads to recombination of ions and electrons and the dielectric breakdown strength is restored. In order to get the next stable spark on, it is essential for the next pulse discharge to occur at a spot sufficiently far from the previous discharge location. This is achieved by controlling the mechanism of wire movement through Servo control by CNC. It is important to control the time interval between pulse discharges so that the dielectric breakdown strength of the liquid is restored. If this is not insured, it will occur at the same location leading to non-uniform erosion of the work-piece and the tool.

2.5 EDM plasma

In EDM process when current is passed, electrons are accelerated due to the presence of the electric field [12]. Ionization of the neutral species takes place because of collision with accelerated electrons. Sudden accumulation of ions creates an avalanche of electrons and this movement effects the electric field. Spark is created by this avalanche [12]. In this process, the discharge current density is of the order of 10^8 to 10^9 A/m^2 and the duration is of the order of hundreds of microseconds [12]. The high current density leads to uncontrollable discharge and location of discharge needs to be preciously controlled for achieving better machining. Electrons are emitted from cathode spot when discharge occurs. The collision of electrons leads to creation of secondary electrons, electrons emitted from field emission and thermal electrons [13]. The variation in electric field and the temperature of the plasma leads to variation in emission of electrons. The current density of the plasma increases due to the presence of such avalanche of electrons [13].

The discharge in EDM process lasts for few microseconds [4] and the size of the region affected by the plasma is also in micrometer, exact analysis of the EDM plasma formation is very difficult. Eubank is one of the scientist who analyzed the physics of the complex process of plasma formation by thermal modeling with different type of heat sources for example source cathode heating model circular expanding heat source [5, 6]. This group of scientists also examined the expansion of the plasma channel to see its effect on the work-piece surface. The energy of the discharge is distributed between the anode, the cathode and the plasma channel [12]. The amount of energy during the formation of a certain volume of crater during machining was estimated by comparing with the volume of material eroded and the volume of crater in the theoretical model. Magneto hydrodynamic analysis of EDM characteristics of the plasma has shown that sizable amount of energy is distributed to the electrodes and the amount of energy which gets transferred by convection and radiation models of heat transfer is negligible [14]. The generation of the spark is marked by the point at which voltage imparted goes above the dielectric strength of the air in the gap between the electrodes and the spark goes off at the end of the spark off-time. An arc between two copper plates separated in air was considered by them. At high temperature the air contains ions. This work [14] assumes that at high temperature the air contained ions and molecules - N, NO, O, N_2, O_2, copper ions and electrons. An estimate was made of the velocity of electrons, electromagnetic field, temperature and pressure. However, the model made many simplistic assumptions as compared to the actual situation prevailing during the EDM process. The few simplistic assumptions made were that the process occurred in air whereas in reality it occurs in a liquid. Similarly, material eroded in the electrode due to spark is not considered and the plasma was considered in a steady state and thermal equilibrium condition. Despite these shortcomings, the model gives an insight to the formation of plasma channel during EDM. Though EDM is a combination of several processes, except for short discharge it can be considered as a thermal process with a small error due to the thermal effect [1, 9]. Most of the researchers adopted the solution of thermal problem in order to model an EDM discharge and they considered it as a heat transmission problem where the heat input is representing the spark [5-7]. Solution of the thermal problem yields the temperature distribution inside the work piece, from which the shape of the generated craters can also be estimated. Several parameters like electrode material, the type of dielectric, on-time and current and voltage during the discharge govern the characteristics of EDM discharges such as the percent of energy that is transferred to the work piece by conduction, the size and shape of the discharge channel and the mechanism of material ejection [15-16]. The possible relations between the parameters are difficult to establish due to the difficulty in measuring the parameters in an experiment. Spectroscopy techniques [17-18] revealed that the temperature distribution inside the plasma channel is not uniform and the temperature distribution is Gaussian. The energy distribution in EDM is a function of the duration of discharge. The extent of erosion of anode and cathode is related to the spark on time. If the duration of discharge is altered, the rate of material removal will change even though the anode and cathode materials are same [5-6].

2.6 Pulse characteristics used in EDM process

Rapid developments in the field of EDM took place due to availability of powerful generators, better mechanical concepts, new wire tool electrodes, improved machining intelligence, better flushing etc. [19]. As compared to the initial speeds possible, wire EDM speeds have gone up to twenty times over the years leading to a decrease in machining cost by at least 30% over the years [19]. Parallel improvements in surface finish by as much as a factor of 15 and increase in discharge current by a factor of 10 have taken place [19].

2.6.1 Pulse generator

In early days, the EDM machines used pulsed generators of relaxation time based on capacitor discharges. Wire Electric discharge machining (WEDM) process specifically used this type of equipment till recent years because of the need of the high surface finish and throughput. In case of WEDM tool wear is not a major concern. The results from literature [12, 19, and 20] shows various conditions of discharge durations and peak current based on requirements. The straight capacitance which comes due to the wire and tool holders plays a vital role in deciding the minimum discharge energy per pulse. The stray capacitance only and not the extra capacitance is used in final finishing when minimum discharge energy is required [12]. If one uses lower peak current and longer discharge duration, the tool wear is less and surface roughness is better. This however, leads to lower energy efficiency and lower material removal rate because of the lower heat flux. A major fraction of the energy distributed to the workpiece in the forms of various modes of heat transfer [5]. A lower discharge frequency per unit time results because of longer discharge durations, therefore this pulse condition is suitable for finishing [12]. In the case of shorter discharge duration and higher peak current, the melted and evaporated regions in the work-piece are small and the rate of removal of material power pulse is small.

Shorter discharge duration and higher peak current provided better surface finish due to smaller discharge carters as compared to lower peak current and longer discharge duration, the material removal is considerably larger. In this case larger heat flux also results in higher energy efficiency. Because of shorter duration of the discharge the rate of repetition of discharge per unit time is higher which also results in higher material removal rate [12]. In this situation, the tool electrode wear rate is high. Because of this reason short discharge duration and high peak current are used in WEDM, in comparison to sinking EDM. This results in an insignificant tool electrode wear.

Relaxation type pulse generator

The relaxation type generators as shown in Figure 2.2 [12] have been replaced by transistors type generators in recent years with the development of large current high response power transistors. The transistorized circuit is shown in Figure 2.3 [12].

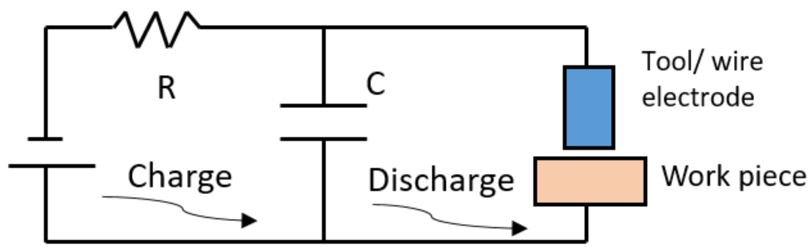

Figure 2.2 Schematic diagram of relaxation type pulse generator [12].

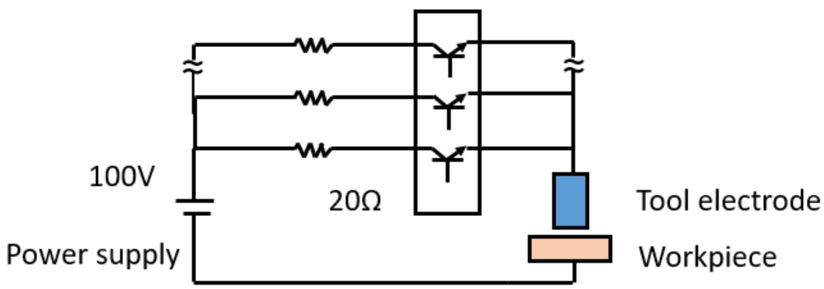

Figure 2.3 Schematic diagram showing the transistor type pulse generator [12].

The relaxation type pulsed generators, however, are still used in finishing and micromachining because of the difficulty of obtaining pulses of significantly short duration with constant pulse energy in transistor gate circuit. In case of the transistor circuit, it takes at least several tens of nano seconds for the discharge current to come down to zero after detecting the occurrence of discharge [12]. Because the electric circuit for detecting the occurrence of discharge takes certain amount of time to switch-off the power transistor which has its own delay time. Therefore, constant discharge durations, shorter than several tens of nano seconds is difficult to obtain using transistor type pulse generator. In Figure 2.4 [12], a series of resistances and transistors are connected in parallel in between the current source and the point of discharge gap. Occurrence of discharge takes place with the switching-on of any one transistor leading to a discharge current of ~4 A, at discharge voltage of 20 V [12]. The discharge voltage is almost constant at 20 V, irrespective of the discharge current because a higher degree of ionization is brought by a larger current. This results in greater diameter of the arc column causing increase in electrical conductivity of the plasma channel. The number of transistors switched on proportionally increased the discharge current. The current waveforms are shown in Figure 2.4 [12].

With switching the transistors with open voltage of 100V between the electrode and the work piece, the discharge does not occur immediately. It occurs after the ignition delay time t_d. The delay in discharge is needed over and above the statistical formative time lags for debris particles to from bridges between the electrodes. [12]

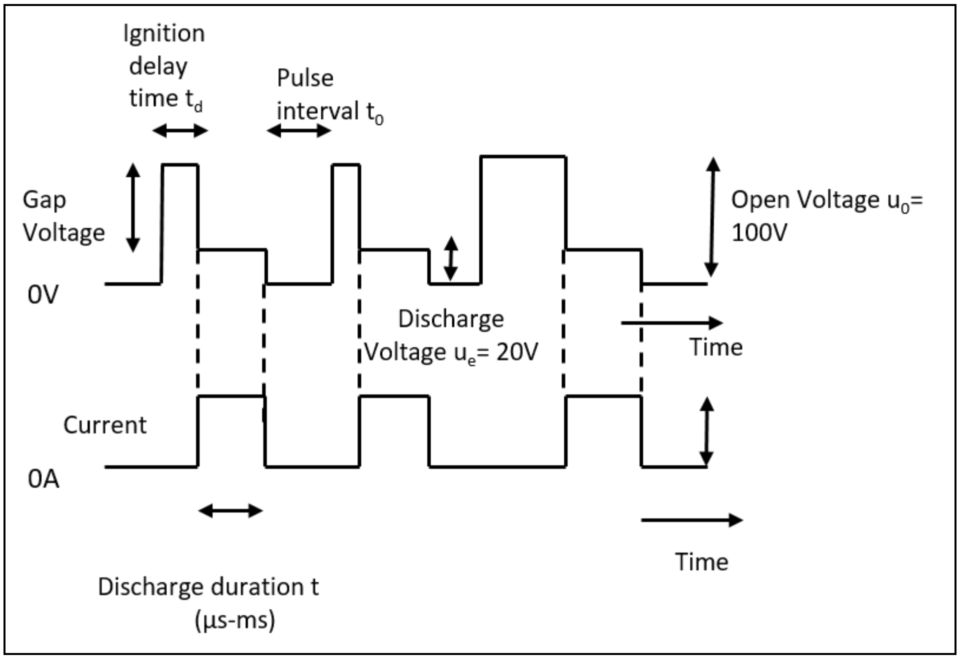

Figure 2.4 Variations of current and voltage shown in the form of waveforms during EDM [12].

A discharge current i_e is impressed through the gap after the dielectric breakdown. The power supply using the gate control circuit supplies the current continuously for discharge duration, t_e after the onset of discharge. This results in a uniform discharge crater size and with the onset of more discharge cycles, more debris are formed and thus ignition delay time varies, but the size of discharge crater is independent of the ignition delay time [12]. When the initial discharge cycle is complete, the transistors are again switched on and voltage is applied between the electrodes for next discharge.

2.6.2 Servo Mechanism for tool/wire control

The gap control which is achieved by servo mechanism of the tool electrode feed is not constant unlike in commercial machining methods [21]. In order to get the desired spark by keeping proper gap width, servo feed control is used. A higher gap voltage results from a larger gap width which causes ignition delays. The tool feed speed increases to maintain constant gap whenever the average voltage gap is higher than the servo reference voltage as pre-set by the operator. When the servo reference voltage is higher than the average gap voltage, the feed speed decrease or the electrode is retracted. This results in ignition delays of smaller magnitude. The humps of discharge crater and debris particles which short circuits, can be avoided by this process. Also, when tool electrode shapes are complicated a quick change in the working surface will not result in hazardous machining [21]. In some cases, in place of the average gap voltage the average ignition delay time is used to control and monitor the gap width, which is the case for smaller gap width resulting in a smaller ignition delay.

2.6.3 Different types of pulses used in the EDM process

Current pulses have a significant effect on material removal rate and surface roughness of EDM machining process. Performance measures such as MRR, tool wear, and surface finish for the same energy depend on the shape of the current pulses. The following four different electrical pulses may be distinguished, depending upon the situation in the gap which separates both the electrodes [22].

a) Open voltage or open circuit
b) Real sparks or effective discharges
c) Short circuit
d) Arcs

On the basis of time evolution of discharge current or discharge voltage, the above terms are defined. The effect of these may differ quite significantly in terms of tool wear and material removal. When the distance between the electrodes is quite large there is no material removal or electrode wear. On the other hand, when the tool and the work-piece come in contact, a short circuiting takes place and again there is no material removal. In between these two extremes there exists the electrode distance range which can be considered for actual discharges either in the form of arc or spark [23]. The characteristic voltage drop across the gap during a pulse occur in both the cases i.e. arc and spark. The difference between these two is very difficult to establish. The damage to the tool and the work-piece is severe during occurrence of an arc, because it occurs at the same spot. This happens because during arching the plasma channel during the previous pulse is not fully de-ionized, therefore the current during the following pulse prefers to flow along the same current path [24]. To initiate a new spark breakdown, the formation of the gaseous channel is considered to be necessary. Therefore, there is a need for distinguishing with respect to the effective discharges or real sparks during EDM. The general belief is that sparks really contribute to material removal [23-25].

2.6.4 Tool wear and rectangular and nonrectangular current pulses

As compared to the performance of the relaxation type generator, the rectangular pulse generator has resulted into improved material removal rates and reduced electrode wear [26]. However, the issue of electrode wear still persists and is considerably significant particularly, during finishing operations. During finishing it is not important to have MRR though it may be preferable. During finishing, accuracy is the key factor. In order to reduce tool wear, non-rectangular current pulses, comb current and other types of current pulses have been applied successfully besides the selection of proper parameters. The new state of the art electrical generators have been created to produce both the rectangular and non-rectangular current pulses, making it possible to observe their effects on machining performance. Some of the investigators have proposed reduction in tool wear by using slope current pulses [26]. The pulse on-time which for a given average current considerably influences the tool wear and the material removal was not considered completely in EDM studies [27]. Often, an attempt is made to find a region in which the non-rectangular pulses have a clear advantage over rectangular pulses [27]. Before S.T. Jilanai and P.C. Pandey [27] researchers have not given precise difference between the effect of rectangular pulses and non-rectangular pulses due to machine limitations. So those efforts are valid only for specific ranges.

The heat density on the electrode surfaces decreases by the same degree when the instantaneous discharge energy is constant. Therefore, at the beginning of a discharge with a small diameter of the discharge channel, maximum heat density exists. As the channel diameter increases the heat admitting surface expands and the proportion of energy dissipated by radiation, convection, and conduction rises markedly [12, 26]. If these physical mechanisms are true, the supplied discharge energy is not optimally utilized with the rectangular current pulse, because at the beginning of the discharge, the current density is so high that the material to be removed is heated far beyond the required melting temperature. The current density varying during a discharge must be regarded as the criterion for the electrode erosion because it is argued that at the beginning of the discharge; only the anode is thermally affected. In this phase the electrons in the plasma channel are accelerated towards the anode and transfer their energy of motion to the anode by impact. At that time the plasma channel rapidly expands but its diameter is still small [28]. The energy imposed on the anode decreases after a few microseconds because of the decrease in energy density on the anode, along with further expansion of the plasma channel. Thermal modeling of the process also shows that the input power and tool wear are related by thermal conductivity of the tool and pulse on-time. Therefore, an adaptation of the supplied power input will result in a reduction of the tool.

Another factor that influences tool wear is the pulse interval time. It is known that with the diminishing of the pulse interval to the limit at which the discharges deteriorate into stationary arcs leads to the generation of socket discharges by favoring deposition of graphite protective film [26]. This increases the resistance to electrical erosion of the copper tool electrode [29]. Inversely, an increase of pause interval determines both an increase of tool wear and the diminishing of graphite film deposition. Thus, the adequate conditions for the deposition of the graphite film and the diminishing of current at the beginning of discharge, causes the decrease of tool wear.

2.7 Dielectric fluid

The EDM setup consists of a power supply whose one lead is connected to the work-piece immersed in a tank having dielectric liquid. The tank is connected to a pump, dielectric reservoir, and a filter system. The pump provides pressure for flushing the work area and moving the oil while the filter system removes and traps the debris in the oil [30, 31]. The oil reservoir restores the surplus oil and provides a container for draining the oil between the operations [12, 16]. The main functions of the dielectric fluid are:

- To flush the eroded particles produced during machining, from the discharge gap and remove the particles from the oil to pass through a filter system.
- To provide insulation in the gap between the electrode and the work-piece.

- To cool the section that was heated by the discharge machining.

The two most commonly used fluids are petroleum based hydrocarbon mineral oils and de-ionized water [16]. The oils should have a high density and a high viscosity. These oils have the proper effects of concentrating the discharge channel and discharge energy but they might have a difficulty in flushing the discharge products.

For most die sinking EDM operations kerosene is the common die electric used with certain additives that prevent gas bubbles [32, 33]. Silicon fluids and mixture of these fluids with petroleum oils have excellent results. However, deionized water is used in WEDM most.

High removal rates, less tool wear and better surface finish have been obtained in the machining of titanium alloys. Other dielectric fluids with a varying degree of success include polar compounds such as aqueous solutions of ethylene glycol, water in emulsions and distilled water. The main things of dielectric that the EDM user should be concerned with are:

2.7.1 Flash point

This is the temperature at which the vapors of the fluid will ignite. This explanation is a little simplistic as conditions for testing are more involved but for the sake of discussion and safety's sake, the higher this number, the better [34]. Unless one is doing extremely small, low power cavity work or drilling the tiniest of holes, be especially concerned with anything on a spec sheet or MSDS rated lower than 180 degrees Fahrenheit.

2.7.2 Dielectric strength

This is the ability of the fluid to maintain high resistivity before spark discharge and in turn the ability to recover rapidly with a minimum amount of off-time. An oil with a high dielectric strength will offer a finer degree of control throughout the range of frequencies used, especially those used when machining with high duty cycles or poor flushing conditions. This will provide for better cutting efficiency coupled with a reduced potential arcing [33].

2.7.3 Viscosity

The lower the viscosity of the fluid the better is the accuracy and finishes that can be obtained. In mirror finishing or close tolerance operations, spark gaps can be as small as 0.005 or less [34]. With such tight, physical restrictions such as this, it is much easier to flush small spark gaps with lighter and thinner oil. Good finishing EDM oils are on the thin side. In the EDM operations requiring moderate finishes like in the forging dies, high MRR, high current values, heavier oils can be used. Viscosity in such conditions can be high because of larger spark gaps and this will also prevent the excess loss of fluid through vaporization.

2.7.4 Specific gravity

Often confused with viscosity, this is the “weight” of a substance measured by a hydrometer [33]. The “lighter” the oil or lower its specific gravity, faster the heavier particles (chips) settle down. This reduces the gap contamination and possibilities of secondary discharge and/or arcing.

2.7.5 Color

In order to facilitate viewing of the submerged part it is always better to start with a liquid that is as clear as possible. It is natural for all dielectric oils to eventually darken with use, but it seems only. In the starting condition the oil should be clear [33-34]. If it is not clear in the starting condition, then it means it carries undesirable or dangerous contaminants.

2.7.6 Odor

The oils that have a strong odor give an indication for the presence of sulfur which is undesirable in the EDM hence should be avoided as the dielectric properties will not be suitable [34].

2.8 Preventive Maintenance

In order to extend the life of the oil there is a need to carry out certain maintenance steps like regular filtration. Though very desirable, water contamination cannot be eliminated completely when the electrode will heat up, condensation will occur on the electrode surface. Because of their porous structure, graphite electrodes will contribute more to the condensation than the metallic electrodes as more moisture absorption from the air will take place. It is important, therefore, to store the graphite electrodes in dry areas. It is also possible to dry the graphite electrode before use by putting it in an oven for some time.

All oils darken in shades from amber to brown with use and age, because these products will break down when exposed to high heat. The color of the oil is an indication of its condition and necessitates replacement. Obviously, sustained high amperage machining will break down the oil more rapidly. Due to tars, resins and hydrocarbon generation by sustained high temperature machining as a result of breakdown of the oil, staining of the oil occurs. This does not necessarily indicate that the oil has deteriorated because this discoloration will not go with filtration.

2.9 Different Applications of EDM

2.9.1 Sinking EDM

In sinking EDM the shape of the machined piece is either created by replication of a properly shaped tool electrode or by 3D movement of a simple electrode as in a milling machine or a combination of the above motions. The most commonly used electrode materials are copper or graphite. The process of cutting occurs in the dielectric fluid. The function of the numerical control is to monitor the voltage and current and in other words the gap conditions, the pulse generator and the different axes [12]. The presence of graphite and metallic particles contained in the fluid can help electrical transfer of this nature in two ways: ionization in the dielectric oil/water is added by the particles which are in case of EDM, electrical conductors and can carry the charge directly; the electrical breakdown of the fluid is catalyzed by the particles [12, 35]. At the point where the distance between the electrode and work piece is least, the electrical field is strongest. Filtration is carried out to remove debris particles and decomposition products from the dielectric liquids.

Figure 2.5 gives the schematic view of WEDM process. Using this process with wire electrode of 0.02-0.33mm in diameter complicated shapes can be cut [35, 36]. Various materials are used as wire electrode such as plain brass, or coated wires like brass or zinc coated steel wires. Where thin wires are to be used normally tungsten or molybdenum are used as wire material. All types of ruled surfaces can be cut by this process because the wire orientation can be changed by controlling the horizontal position of the upper wire guide relative to the lower guide. Because of the fact that discharge currents of very short duration and high peak value are used, the current is supplied through the upper lower feeding brushes to ensure a quick rise in the discharge current avoiding wire breakage by joule heating. In order to reduce vibration and deflection, tension is applied to the wire, which also ensures cutting accuracy. In order to keep high open voltage and avoid electrolysis de-mineralized water is most commonly used as dielectric liquid for WEDM. This dielectric liquid has many advantages over hydrocarbon as a dielectric liquid. The important one being lack of fire hazard. Hydrocarbon dielectrics are normally used in sinking EDM because tool electrode wear is lower as compared to de-ionized water and surface roughness is better.

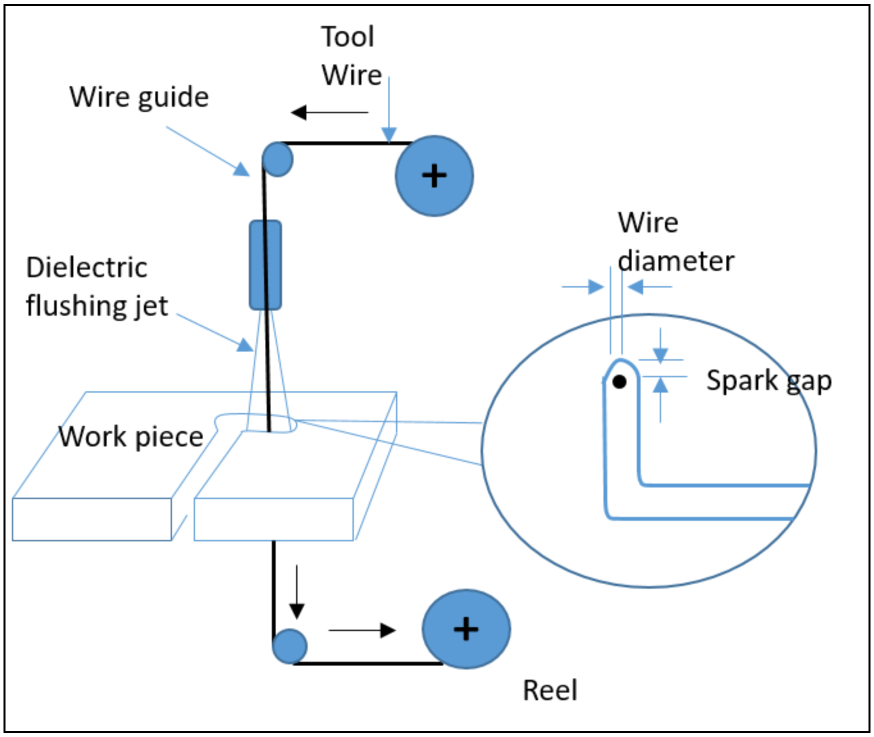

Figure 2.5 Schematic diagram showing the wire EDM set-up [36].

2.9.2 Micro EDM

Like conventional macro EDM, micro EDM is an erosion process where the material is removed by electrical discharges generated at the gap between two electrically conductive electrodes. This is used for making micro holes, channels and 3D micro cavities in electrically conductive materials including super alloys and stainless steels. This technique can also be used for making irregular cross-sections. The electrode prepared by the Wire electric discharge grinding (WEDG) determines the size and the shape of the micro hole made by micro EDM [37]. Uniform wear method with Computer aided design (CAD) and

Computer aided manufacturing (CAM) and machining of micro hole with high aspect ratio and noncircular blind micro hole are some of the recent activities of interest in this area [37].

2.9.3 EDM Drilling

Once relegated to a last resort method of drilling holes, fast hole EDM drilling is now used for production work. Drilling speeds have been achieved of up to 2 inches per minute [38, 39]. Holes can be drilled in any electrically conductive material, whether hard or soft, including carbide. Fast hole EDM drilling is used for putting holes in turbine blades, fuel injectors, cutting tool coolant holes, hardened punch ejector holes, plastic mold vent holes, wire-EDM starter holes, and other operations [40]. The term fast hole EDM drilling is used because conventional ram EDM can also be used for drilling. However, ram EDM hole drilling is much slower than machines specifically designed for EDM drilling. Fast hole EDM drilling uses the same principles as ram EDM. A spark jumps across a gap and erodes the work-piece material. A servo-drive maintains a gap between the electrode and the work-piece. If the electrode touches the work-piece, a short occurs. In such situations, the servo-drive retracts the electrode. At that point the servomotor retraces its path and resumes the EDM process. Literature survey shows most of the work in EDM investigates the influence of process parameters on the surface integrity of the EDM drilling process [23].

2.9.4 Wire EDM

In case of wire EDM, a continuously moving conductive wire works as tool electrode. This is an advanced electrical discharge machining process. In this process, metal removal takes place by complex erosion effect of electric sparks generated by a pulsating direct current power supply between two closely spaced electrodes in dielectric liquid [19,23]. Because of the high energy density, material is eroded from both the wire and work-piece by local melting and vaporizing. Since the new wire keeps feeding to the machining area, the erosion of the wire does not affect the process and material is continuously removed from the work-piece. The programmed trajectory of wire electrode movement leads to the cutting of the work-piece cut in the desired shape [21]. This process is extensively used in cutting hard materials for dies and molds. Advancements have taken place in the avoidance of wire breakage, development of monitoring and control system, database, machining of advanced materials. Besides this comparison of different wire performance and thermal as well as vibration modeling has also been done [41]. Figure 2.6 shows wire EDM

Figure 2.6 Photograph of a wire EDM machine [image courtesy CDM, BARC].

2.9.5 Abrasive Electro Discharge Grinding (AEDG)

The processes of cutting and grinding in the hybrid process known as AEDG. In this process of mechanical abrasion of a metal bonded diamond wheel is combined with the electro-erosion of EDM. The removal of the materials generated by abrasion is done by combined action of rapid, repetitive spark discharges between work-piece and rotating tool, separated by a flowing dielectric fluid and by a mechanical action of irregularly shaped abrasive particles on the periphery of the wheel [42].The recent advances made in AEDG process are a) monitoring and control, b) new power generator, c) 2-axis NC wheel dressing unit, d) environmental performance of different dielectric fluids [43, 44]. Strategy for optimizing neural network modeling, the study of self-addressing characteristics and sequence of operations and using neural networks for controls in AEDG form some of the recent areas of research in this method. The nature of the interaction of the energy generated during EDM with the work-piece depends on several properties of the material like thermal conductivity, electrical conductivity and the mechanical properties [29, 45]. The work piece is not just cut, the thermal effects of the process bring several changes in the material being cut on the surface and in the subsurface region. The extent of these effects depends not only on the properties of the material but also on the machining parameters [46]. The machining parameters decide the extent of energy generated. There have been studies dealing with the nature of the discharge created during the EDM process. These studies are complex because besides other factors the time period of the event is very small of the order of microseconds. The nature of the discharge occurring during the EDM process has been examined in some studies. During the period in which the pulse is on, the anode remains at ground potential and the cathode is at negative potential. Because of this the electrons move towards the anode and the ions in the plasma move towards the cathode. The electrons move faster and hit the anode, which is exposed to high temperature and undergoes local melting. Once the voltage jumps to the on period, the breakdown of the dielectric happens and a plasma channel is created between the electrodes with extremely high energy density [12]. Sudden generation of plasma leads to creation of very high dynamic pressure and generation of shock wave in the vicinity of the discharge gap driven by high inertia of the liquid dielectric [15]. There is melting of both the electrodes. However, the melting of the anode is faster because the electrons travel much faster. The part of the cathode in contact with the plasma is much smaller as compared to the anode because the cathode acts as almost like point source of electrons. The plasma channel undergoes a sudden collapse once the discharge stops. The sudden collapse of the plasma channel [47] leads to a burst of molten material on the electrode and the dielectric fluid. Part of the molten material thus solidifies on the electrode and part of it is carried away by the dielectric in the form of debris. The numerous EDM discharges create craters on the material being machined. The overlapping craters represent the EDM machined surface. The process of spark erosion is understood in a limited way and the development of EDM technology has been mostly by a trial and error approach. In order to have a systematic development of the process there is a need for better complete understanding which will involve understanding the complex interplay of hydrodynamics, electromagnetic, electrodynamics and thermodynamics at various temperature ranges and time scales. There is also a need for understanding the role of the different process parameters on the process. Earlier many researchers have studied the temperatures developed in the EDM plasma. There are many assumptions made in these studies. Besides actual measurement, high speed photography also has revealed some details of the process. The physical explanation of the material removal during electric discharge machining is presented by Van Dijck. [3]. Van Dijck presented a thermal model together with a computational simulation to explain the phenomena between the electrodes during electric discharge machining. However, this model suffers lack of explanation completely due to shortage of experimental data. Heat transfer models of EDM were developed in the late eighties and early nineties, including an investigation at Texas A&M University with the support of AGIE, now Agiecharmilles. It resulted in three papers: the first presenting a thermal model of material removal on the cathode by D.D. Di Bitonto [5], second paper on anode erosion model and third cathode erosion model. It was supported by the experimental data.

These models give the most authoritative support for the claim that EDM is a thermal process. It proposed that removing of material from the two electrodes takes place because of melting or vaporization, along with pressure dynamics established in the spark-gap by the collapsing of the plasma channel. However, for small discharge energies the models are inadequate to explain the experimental data. Model from Singh and Ghosh [9] indicates the removal of material mechanically from the electrode takes place due to the presence of an electrical force on the surface of the electrode and create the craters. Additionally, the material on the surface has altered mechanical properties due to an increased temperature caused by the passage of electric current.

2.10 Characteristics of EDM machined surface

The nature of the recast layer has very strong relationship with the type of dielectric [48]. The nature of the recasts layer differs in the case of kerosene and water and other dielectric medium. The formation of the recast layer occurs because of the re-solidification of the molten material which did not sweep away from the component surface during EDM process. The surface created is hard, brittle and has poor fatigue resistance due to the presence of cracks [49]. The characteristics of the recast layer depend on the EDM parameters. The region below the recast layer does not undergo melting. However, this region experiences high temperatures and may have some solid state phase transformations. These solid state transformations create changes in the properties of the material [49]. The recast layer thickness is lower in wire EDM [50]. This is primarily because of the differences in the di-electric fields, discharge control systems and electrode materials. The generation of high temperature not only leads to melting but does cause solid state phase transformations like martensitic transformation. These generate significant amount of stress on the surface which leads to crack formation [49, 51]. Even if the cracks do not form, the presence of residual stress on the surface is a matter of concern.

2.11 Modeling

There have been many modelling efforts to understand the different aspects of the process. The heat input has been modelled with different types of heat sources. The heat flux has also been modelled differently [13]. Gaussian flux model, thermo-hydraulic modelling with interaction between the different effects taking place. Thermal modelling essentially involves considering the spark as a heat source from which heat is transferred to the adjoining regions. With this the temperature distribution inside the work piece and a theoretical estimate of the craters can be made. The actual process is much more complex with a host of things happening together like formation of the discharge channel and the material ejection. All these processes cannot be handled by one model. The thermal modelling has been attempted by a very large number of researchers. Some others researchers have also have considered electrical forces generated during the discharge involved along with the thermal model.

2.12 Modelling and optimization of EDM process

Tariq Jilani and P.C. Pandey [53] presented metal removal in EDM as a thermal erosion process where the heat transfer is predominantly through conduction. In this paper, a two-dimensional heat transfer model, assuming the plasma channel to be a disc heat source, has been employed to study the effects of EDM input parameters, such as pulse duration, pulse energy and material properties, on metal removal and crater shape. Wataru Natsu, S. Ojima et al. [20] determined the EDM plasma by spectroscopic technique. They used line pair method and Ablel's inversion.

The authors P.C. Pandey and, S.T. Jilani [52] presented that the majority of models predict metal removal rates many times higher than that actually occur and normally do not account for the variable rate of energy supply to the plasma channel as the pulse progresses, and ignore the presence of a re-solidified layer. They presented an analysis of metal removal in the EDM process by accounting for the growth of the plasma channel during the pulse-on period. A method for computing the thickness of the re-solidified layer is also proposed.

Lhiaubet [54] studied the removal of electrode material by electric discharges in a dielectric liquid with a short inter electrode gap (about 50µm) and short discharge durations (20-2000 µs). They used voltage drop obtained by comparison of experimental results concerning mass loss at the electrodes and the molten volume computed after a linearized heat conduction model since it is therefore virtually impossible to measure the anodic and cathodic voltage drops of such discharges.

K. Gajjar [55] has presented a thermal model in COMSOL for single discharge EDM process. As the exact behavior of plasma at micro level is not known the paper simplifies the boundary conditions to model the geometry using single discharge. Multiple discharge process involves the flushing cycle also, in which the debris is flushed off by the dielectric so that the material removed may not stick back to the work piece.

Klocke et al. [56] investigated the properties of recast layer since they are very crucial for the mechanical behavior of the component as a whole. They investigated the surface layer in TEM and by EDS to identify the structural constitution of the microstructure. They also investigated influence of local defects and transformations on the work piece functionality. They found from Transmission electron microscopy (TEM) that white layer is mainly of amorphous microstructure and at boundary to parent material crystalline structures spread into the amorphous regions.

Kozak et al. [57] presented the results of experimental and theoretical investigations of the influence of discharge frequency and discharge energy on the material removal rate of WEDM of for Polycrystalline diamond blank. They reported that the machining feed rate was approximately directly proportional to the discharge frequency and increases as the capacitance C is increased.

Prohaszka et al. [58] evaluated the influence of the various wire electrode materials using magnesium, tin and Zn on the performance during WEDM. The operational parameters were kept constant during the whole series of experiments i.e. spark discharge time of 60 µs and total pulse cycle time is kept at 100 μs. They concluded that the coating with low work function material increase cutting efficiency of wire. They found that wires with small work function and high melting point performs better.

M. Kunida [29] has studied the bubbles and debris particles generated by single pulse discharge. They reported that the gap width between the electrodes is of much significance. During the spark discharge the plasma is generated and consists of ionized gas. The material removal rate in each discharge is small so to improve the material removal rate, the frequency of discharge per unit time should be increased. They also established that after spark ends the rapid cooling of the plasma and machined surface takes place. This results into recombination of ions and electrons and dielectric strength of the dielectric is regained. For better material removal rate the next spark shall occur adjacent to the last spark. The capacitance of the dielectric liquid gets reduced due to dielectric breakdown during ionization and shall regain the dielectric strength. Hence sufficient spark off time should be provided for next discharge cycle. [59]

Zingerman et al. [60] reported the size of the arc column increases with passage of time. It is roughly equal to the size of the crater observed on the machined surface. The size of the discharge bubble is much larger than the electrode gap. The plasma bubble rapidly expands due to evaporation of electrode materials, dielectric liquid and dissociation molecules and ionization of atoms.

Rebelo et al. [61] have analyzed the influence of pulse energy on surface integrity in EDM process, they revealed the surface integrity by using optical and scanning electron microscopy and found that the dimension of crater size increases with increase in pulse energy. X-ray diffraction was used for determining a white layer which consists of a new phase of cementite and microprobe analysis was used for confirmation. It was observed that heat affected area changes with change in discharge energy by using X-ray diffraction.

Shivam Kumar Singh and S. C. Jayswal [62] suggested that thermo physical properties (thermal and electrical conductivity, heat to vaporize from room temperate, boiling temperature, thermal expansion and melting temperature) of the work piece and tool electrode considerably affects the process performance like MRR, TWR and surface integrity of workpiece material.

Yan and Liao [63] employed proportion of abnormal sparks (abnormal ratio) and the sparking frequency to monitor and evaluate the gap condition of the WEDM process on-line. The relationships are investigated between these two sensing parameters and wire breaking phenomenon, MRR, and surface roughness of the machined part under various machining conditions. Based on the results, an Adaptive control optimization (ACO) system is developed. They developed Fuzzy rules based on operator experience, expert knowledge and a multivariable and three-region fuzzy controller.

Gokler and Ozanozgu [64] carried out an experimental study to select the combination of cutting parameters of WEDM process to get the surface roughness of the order of 1-3μm on material with thickness 30, 60 and 80 mm, and on 2379 and 2738 steel materials.

Spedding and Wang [65] attempted to model the cutting speed, surface roughness and surface waviness in wire EDM process through response-surface methodology and artificial neural networks (ANNs). They proposed a response surface model based on a central composite rotatable experimental design, and a 4-16-3 size back-propagation neural network for desired surface accuracy. They claimed EDM process, experiments showing that both of the models are able to predict the process performance, such as cutting speed, surface roughness, and surface waviness within a reasonable large range of input factor levels.

Y.S. Liao J.T. Huang [66], Y.H. Chen studied the method for obtaining good surface roughness, by modifying the traditional circuit using low power for ignition for machining. With the assistance of Taguchi quality design, ANOVA and F-test, machining voltage, current-limiting resistance, type of pulse-generating circuit and capacitance are identified as the significant parameters affecting the surface roughness in finishing process.

Tosun et al. [67] studied experimentally the variation of workpiece surface roughness with varying pulse duration, open circuit voltage, wire speed and dielectric fluid pressure in WEDM. They found that the increasing pulse duration, open circuit voltage and wire speed, increase the surface roughness whereas the increasing dielectric fluid pressure decreases the surface roughness. In this study, the analysis of variance (ANOVA) and F-test were performed to see statistically significant process parameters and the percent contribution of these parameters on R_a.

Newton et al. [68] conducted study on the effect of process parameters on the formation and characteristics of recast layer in wire-EDM of Inconel 718 alloy. They found that average recast layer thickness increased primarily with energy per spark, peak discharge current, and current pulse duration. Over the range of parameters tested, the recast layer was observed to be between 5 and 9μm min average thickness, although highly variable in nature. They found that recast material possess in-plane tensile residual stresses

Tomura and Kunieda [69] investigated the mechanism of electromagnetic force occurring in WEDM. They developed a two-dimensional finite element method (FEM) program to analyze the electromagnetic field taking into account electromagnetic induction. The electromagnetic force on the wire was estimated from the surface integral of the vector product between the current density and magnetic flux density over the cross section of the wire. Electromagnetic force generated by DC component alone was calculated. In this study, they developed an unsteady electromagnetic field analysis program based on solution of poison equation in FEM. Trapeziodal current profile (waveform) was assumed in their calculation. They have shown that calculated wire movement agreed with the measured wire movement. They indicated that electromagnetic force should be considered for the better accuracy in WEDM.

Portillo et al. [70] employed ANN to detect the degradation of the wire electric discharge machining (WEDM) process in a range of steel workpiece thicknesses (50-100 mm. The ANN model is based on three ELMAN model. The claimed that this approach gives advantages of one unique neural structure in order to avoid having a battery of heuristic rules per workpiece height, and also to taking advantage of the learning capacity of ANN.

Poro´s and Zaborski [71] studied the efficiency of wire electrical discharge machining of hard-to-machine materials experimentally. They conducted extensive study on the variation of WEDM cutting efficiency on different materials e.g. Titanium alloy Ti6Al4V and cemented carbide (B40). By applying different wire electrodes diameter with uncoated brass wire, zinc oxide coated brass and zinc coated brass wire. They used uncoated brass wire, 0.25 mm diameter, zinc oxide coated brass wire with brass CuZn (80:20)/(50:50) wires for study

[71]. Different process parameters like spark T_{on} and gap voltage. They developed a semi empirical model considering the work piece electrical and thermal conductivity, specific heat capacity and melting point. They concluded that the higher value of thermal conductivity, specific heat capacity and melting point of the machined material causes the decrease of efficiency of WEDM process.

Ramakrishnan and Karunamoorthy [72] performed a series of experiments under different cutting conditions of pulse on time, delay time, wire feed speed, and gap current. The material removal rate and surface roughness were predicted using artificial neural network models, and optimized by assigning different weight factor using multi response signal-to-noise (MRSN) ratio in addition to the Taguchi's method.

Ramakrishnan and Karuna Moorthy [73] carried out optimization of WEDM operations using Taguchi's robust design methodology with multiple performance characteristics. Multi response signal to noise (MRSN) ratio was applied to measure the performance characteristics deviating from the actual value. Analysis of variance (ANOVA) is employed to identify the level of importance of the machining parameters on the multiple performance characteristics considered

Cabanes et al. [74] developed acquisition system to capture discharge current and discharge voltage in order to obtain an extensive experimental database based on stable and unstable tests. They developed early detection methodology for instability in WEDM and to avoid unstable machining and wire breakage. In order to quantify the trend for instability they considered cause of poor flushing, variation of sparking frequency, discharge energy, ignition delay time, and peak current.

2.13 Optimization of EDM process parameters

Mahapatra and Patnaik [75] identified significant machining parameters affecting the machining performance as discharge current, pulse duration, pulse frequency, wire speed, wire tension, and dielectric flow using Taguchi Method also developed non-linear regression equations to establish the relationship between discharge current, pulse duration, pulse frequency, wire speed, wire tension & dielectric flow rate with the material removal rate, surface finish and the cutting width (kerf).

Han et al. [76] investigated the influence of the machining parameters like pulse duration, discharge current, sustained pulse time, pulse interval time, polarity effect, material and dielectric on surface roughness in the finish cut of WEDM. They have shown surface roughness can be improved by decreasing both pulse duration and discharge current and the removal rate is higher for a short pulse duration combined with a high peak current.

Anish Kumar [77] attempted modelling the response variable i.e. surface roughness in WEDM process using response surface methodology of pure titanium (grade-2). The experimental plan is based on Box-Behnken design. Six parameters i.e. pulse on time, pulse off time, peak current, spark gap voltage, wire feed and wire tension has been varied to investigate their effect on surface roughness. The surface roughness has been optimized using multi-response optimization through desirability. ANOVA has been applied to identify the significance of developed model. The test results confirm the validity and adequacy of the developed RSM model. Finally, they presented the optimum parametric setting for the optimization of process.

J.T. Huang, Y.S. Liao [78] attempted to unveil the influence of the machining parameter (pulse-on time, pulse-off time, table feed-rate, flushing pressure, distance between wire periphery and workpiece surface, and machining history) on the machining performance of WEDM in finish cutting operations. The gap width, the surface roughness and the recast layer depth of the machined workpiece surface are measured and evaluated. Based on the Taguchi quality design method and numerical analysis, it is found that the pulse-on time and the distance between the wire periphery and the workpiece surface are two significant factors affecting the machining performance. They established mathematical models relating machining parameters and performance by regression, and non-linear programming using the Feasible-direction algorithm for obtaining the optimal machining parameters.

A. Erden [79] investigated the EDM process both theoretically and experimentally to determine the effects of electrode materials on the machining performance. Author modelled a single and isolated spark physically and mathematically and its three phases viz., breakdown, discharge and erosion are investigated. Re-solidified electrode materials as suspended particles in the dielectric liquid are found to be the most significant factor in the breakdown phase. Mathematical expressions relating the time lags to particle concentration are evaluated and which can be used to determine the effects of particle concentration on the machining performance. The author [12] studied the polarity effect both theoretically and experimentally. Author concluded that optimum machining conditions can only be obtained by proper selection of the tool material, workpiece material and discharge medium since they affect the initiation and development of the discharge and erosion of electrode materials.

Based on the literature survey a number of gaps have been observed in WEDM process. They also studied the influence of the discharge current on machining surfaces, by applying thermo-analysis on material removal in the finish cut of WEDM using the finite element method. They found that high peak current with short pulse duration gives gasifying ejecting morphology whereas low peak current with long pulse duration gives melting morphology of cut surface [12, 29].

2.14 References

[1] K. H. Ho, S. T. Newman, S. Rahimifard, and R. D. Allen, "State of the art in wire electrical discharge machining (WEDM)", International Journal of Machine Tools and Manufacture, 44 (2004): 1247-1259.

[2] F. S. Van Dijck, and W. L. Dutre, "Heat conduction model for the calculation of the volume of molten metal in electric discharges", Journal of Physics D: Applied Physics , 7 (1974): 899.

[3] F. V Dijck, and R. Snoeys, "Metal removal and surface layer in electro-discharge machining", International conference on production engineering, Tokyo, pp. 46-50. 1974.

[4] F. Van Dijck, "Physico-mathematical analysis of the electro discharge machining process PhD Dissertation Catholic University of Leuven", (1973).

[5] D. Daryl DiBitonto, Philip T. Eubank, Mukund R. Patel, and Maria A. Barrufet, "Theoretical models of the electrical discharge machining process. I. A simple cathode erosion model", Journal of applied physics, 66 (1989): 4095-4103.

[6] Mukund R Patel, Maria A. Barrufet, Philip T. Eubank, and Daryl D. DiBitonto, "Theoretical models of the electrical discharge machining process. II. The anode erosion model", Journal of applied physics, 66 (1989): 4104-4111.

[7] Philip T Eubank , Mukund R. Patel, Maria A. Barrufet, and Bedri Bozkurt, "Theoretical models of the electrical discharge machining process. III. The variable mass, cylindrical plasma model", Journal of applied physics, 73 (1993): 7900-7909.

[8] Xia Heng, Masanori Kunieda, and Nobuhiko Nishiwaki, "Removal amount difference between anode and cathode in EDM process", IJEM 1 (1996): 45-52.

[9] Ajit Singh, and Amitabha Ghosh, "A thermo-electric model of material removal during electric discharge machining", International Journal of Machine Tools and Manufacture, 39 (1999): 669-682.

[10] T. Ponnarasan, J. Chandradass, "Performance analysis and process optimization of EDM parameters on Inconel 600 with copper electrode", International Journal of Innovative Research in Technology, 2 (2015): 112-115, ISSN: 2349-6002.

[11] M Bernd Schumacher, "After 60 years of EDM the discharge process remains still disputed", Journal of Materials Processing Technology 149, no. 1-3 (2004): 376-381.

[12] M. Kunieda, Bert Lauwers, Kamlakar P. Rajurkar, and B. M. Schumacher, "Advancing EDM through fundamental insight into the process", CIRP annals, 54 (2005): 64-87.

[13] T.H. Lee "T-F theory of electron emission in high-current arcs", Journal of Applied Physics, 30 (1959): 166-171.

[14] Shinya Hayakawa, “Numerical analysis of arc plasma temperature in EDM process based on magneto-hydrodynamics”, Trans. JSME (B), 62 (1996): 263.

[15] A Kojima, “Observation of arc plasma expansion and delayed growth of discharge crater in EDM”, Proceedings of the 16th International Symposium on Electro machining, 2007, pp. 1-4.

[16] Y. S Liao, and Y. P. Yu, “Study of specific discharge energy in WEDM and its application”, International Journal of Machine Tools and Manufacture, 44 (2004): 1373-1380.

[17] B. Izquierdo, J. A. Sanchez, S. Plaza, I. Pombo, and N. Ortega, “A numerical model of the EDM process considering the effect of multiple discharges”, International Journal of Machine Tools and Manufacture, 49 (2009): 220-229.

[18] A. Descoeudres, Ch Hollenstein, G. Wälder, and R. Perez, “Time-resolved imaging and spatially-resolved spectroscopy of electrical discharge machining plasma”, Journal of physics D: Applied physics, 38 (2005): 4066.

[19] C.P.S Prakash, “A study on the machining characteristics in wire EDM process”, PHD dissertation, Dr. M.G.R Educational and research Institute, Chennai (2008).

[20] Natsu Wataru, Satoyuki Ojima, Teruki Kobayashi, and Masanori Kunieda, “Temperature distribution measurement in EDM arc plasma using spectroscopy”, JSME International Journal Series C Mechanical Systems, Machine Elements and Manufacturing, 47 (2004): 384-390.

[21] Altpeter Friedhelm, and Roberto Perez, “Relevant topics in wire electrical discharge machining control”, Journal of Materials Processing Technology, 149 (2004): 147-151.

[22] R. Snoey., D. Dauw, and M. Jennes, “Survey of EDM adaptive control and detection systems”, CIRP Annals 31 (1982): 483-489.

[23] Koc. Muammer, Tugrul Ozel, “Modern manufacturing processes” John Wiley & Sons inc. USA (2019), ch.16-page no. 377-402, 2019.

[24] R. A. Mahdavinejad, and A. Mahdavinejad, “ED machining of WC–Co”, Journal of materials processing technology, 162 (2005): 637-643.

[25] S.H. Yeo, E. Aligiri P. C. Tan, and H. Zarepour, “An adaptive speed control system for micro electro discharge machining”, In AIP Conference Proceedings, vol. 1181, no. 1, pp. 61-72. AIP, 2009.

[26] C. J Feeney, and J. R. Crookall, “The Effectiveness of Non-Rectangular Current-Pulse Forms in Electro-Discharge Machining”, Proceedings of the Nineteenth International Machine Tool Design and Research Conference, pp. 551-557. Palgrave, London, 1979.

[27] S. Jilani. Tariq, and P. C. Pandey, “An analysis of surface erosion in electrical discharge machining”, Wear, 84 (1983): 275-284.

[28] H. E. De Bruyn, “Slope Control: a great improvement in spark erosion”, Annals of CIRP 16 (1967): 183-191.

[29] Masanori Kunieda, “Electrical Discharge Machining Processes”, Handbook of Manufacturing Engineering and Technology, Springer-Verlag London 2013, page1-26.

[30] Kuldeep Singh, Ajay Kumar Agarwal Gianender, and Rinki Yadav Ajit, “Effect of Dielectric fluids used on EDM Performance: A Review”, International Journal of Emerging Technologies in Engineering Research (IJETER) 2017, Volume 5, Issue 10, ISSN: 2454-6410, EverScience Publications.

[31] M.L. Jeswani, “Electrical discharge machining in distilled water”, Wear, 72 (1981): 81-88.

[32] T. Masuzawa, “Machining characteristics of EDM using water as a dielectric fluid”, Proceedings of the Twenty-second International Machine Tool Design and Research Conference, pp. 441-447. Palgrave, London, 1982.

[33] G. Kibria, B. R. Sarkar, B. B. Pradhan, and B. Bhattacharyya, “Comparative study of different dielectrics for micro-EDM performance during micro-hole machining of Ti-6Al-4V alloy”, The International Journal of Advanced Manufacturing Technology, 48 (2010): 557-570.

[34] D. Kumar, K. Kumar, H. S. Payal and K. K. S Mer, “A State-of-the-art Review on Dielectric fluid in Electric Discharge Machining: Uses and Its Effects”, International Research Journal of Engineering and Technology (IRJET) (2017), Vol. 04, Issue 07, e-ISSN: 2395 -0056.

[35] B. J Ranganath, K. G. Sudhakar, and A. S. Srikantappa, “Wire failure analysis in wire-EDM process”, In International Conference on Mechanical Engineering. 2003.

[36] Brijesh Kumar Singh, Ganesh Singh Yadav, and Anurag Yadav, “Study on electric discharge machining and scope for new era”, International Research Journal of Engineering and Technology, 3 (2016): 2214-2219.

[37] Chen Shun-Tong, and Hong-Ye Yang, “Study of micro-electro discharge machining (micro-EDM) with on-machine measurement-assisted techniques”, Measurement Science and Technology, 22 (6): 065702. IOP Publishing Ltd, 2011.

[38] T. Masuzawa, J. Tsukamoto, and M. Fujino, “Drilling of deep micro-holes by EDM”, CIRP Annals, 38 (1989): 195-198.

[39] M. P Jahan, M. Rahman, and Y. S.Wong, “A review on the conventional and micro electro-discharge machining of tungsten carbide”, International Journal of Machine Tools and Manufacture, 51 (2011): 837–858.

[40] H. Tong, Y. Li, L. Zhang, and B. Li, “Mechanism design and process control of micro EDM for drilling spray holes of diesel injector nozzles”, Precision Engineering, 37 (2013): 213–221.

[41] A. Puri. B, and B. Bhattacharyya, “Modelling and analysis of the wire-tool vibration in wire-cut EDM”, Journal of materials processing technology, 141 (2003): 295-301.

[42] Jerzy Kozak, Maria Zybura-Skrabalak and Grzegorz Skrabalak “Development of advanced abrasive electrical discharge grinding (AEDG) system for machining difficult-to-cut materials”, Procedia CIRP, 42 (2016): 872-877.

[43] J. H Zhang, X. Ai, K. W. Lee and P. K. Wong, "Study on electro discharge diamond wheel grinding (EDGM) of ceramic materials", Material and Manufacturing Process, 11 (1996): 763-774.

[44] P. Koshy, V. K. Jain, and G. K. Lal, "Mechanism of material removal in electrical discharge diamond grinding", International Journal of Machine Tools and Manufacture, 36 (1996): 1173-1185.

[45] Philip Koshy, V. K. Jain, and G. K. Lal, "Grinding of cemented carbide with electrical spark assistance", Journal of Materials Processing Technology, 72 (1997): 61-68.

[46] Chang-Ho Kim, "Influence of the Electrical Conductivity of Dielectric Fluid on WEDM Machinability", Dept. of Mechanical Engineering, Dong-Eui University, Gaya-2 Dong, Pusanjin-Gu, Pusan (2004): 614-714.

[47] Frans Van Dijck, "Physico-mathematical analysis of the Electro Discharge Machining process", Dissertation KU Leuven, the Netherlands (1973).

[48] Li. Chaojiang, Xi Xu, Yong Li, Hao Tong, Songlin Ding, Quancun Kong, Lei Zhao, and Jun Ding, "Effects of dielectric fluids on surface integrity for the recast layer in high speed EDM drilling of nickel alloy", Journal of Alloys and Compounds, 783 (2019): 95-102.

[49] P. Govindan, and Suhas S. Joshi, "Analysis of micro-cracks on machined surfaces in dry electrical discharge machining", Journal of Manufacturing Processes, 14 (2012): 277-288.

[50] R. E Williams, and K. P. Rajurkar, “Study of wire electrical discharge machined surface characteristics”, Journal of Materials Processing Technology, 28 (1991): 127-138.

[51] Bulent Ekmekci, Oktay Elkoca, A. Erman Tekkaya, and Abdulkadir Erden, “Residual stress state and hardness depth in electric discharge machining: de-ionized water as dielectric liquid”, Machine science and technology, 9 (2005): 39-61.

[52] P.C. Pandey, S.T. Jilani, “Plasma channel growth and the resolidified layer in edm”, Precision Engineering, 8 (1986) :104-110.

[53] S. T. Jilani, and P. C. Pandey, “Analysis and modelling of EDM parameters”, Precision Engineering, 4 (1982): 215-221.

[54] C. Lhiaubet, and R. M. Meyer, “Method of indirect determination of the anodic and cathodic voltage drops in short high-current electric discharges in a dielectric liquid”, Journal of Applied Physics, 52 (1981): 3929-3934.

[55] K. Gajjar, U. Maradia, and K. Wegener, “Thermal Model for Single Discharge EDM Process Using Comsol Multiphysics”, In Proceedings of COMSOL Conf. 2012.

[56] F. Klocke, L. Hensgen, A. Klink, L. Ehle, and A. Schwedt, “Structure and composition of the white layer in the wire-EDM process”, Procedia CIRP 42 (2016): 673-678.

[57] J. Kozak, K. P. Rajurkar, and S. Z. Wang, “Material removal in WEDM of PCD blanks”, Journal of engineering for industry, 116 (1994): 363-369.

[58] J. Prohaszka, A. G. Mamalis, and N. M. Vaxevanidis, “The effect of electrode material on machinability in wire electro-discharge machining”, Journal of materials processing technology, 69 (1997): 233-237.

[59] Abdülkadir Erden, and Bilgin Kaftanoglu, “Heat transfer modelling of electric discharge machining”, In Proceedings of the Twenty-First International Machine Tool Design and Research Conference, pp. 351-358. Palgrave, London, 1981.

[60] A.S Zingerman, “Effect of Thermal Conductivity upon the Electrical Erosion of Metals”, Soviet Physics-Technical Physics, 1 (1956): 1945-1958.

[61] J. C. Rebelo, A. Morao Dias, D. Kremer, and J. L. Lebrun, “Influence of EDM pulse energy on the surface integrity of martensitic steels”, Journal of Materials Processing Technology, 84 (1998): 90-96.

[62] Shivam Kumar Singh, and S. C. Jayswal, “Electric Discharge Machining: A Review”, International Journal of Engineering Technology Science and Research, (2018) Volume 5, Issue 5.

[63] M. T Yan., and Y. S. Liao, “Adaptive control of the WEDM process using the fuzzy control strategy”, Journal of manufacturing systems, 17 (1998): 263-274.

[64] Mustafa Ilhan Gokler, and Alp Mithat Ozanozgu, “Experimental investigation of effects of cutting parameters on surface roughness in the WEDM process”, International journal of Machine tools and manufacture, 40 (2000): 1831-1848.

[65] A Trevor Spedding, and Z. Q. Wang, “Parametric optimization and surface characterization of wire electrical discharge machining process”, Precision Engineering, 20 (1997): 5-15.

[66] Y.S Liao, J. T. Huang, and Y. H. Chen, “A study to achieve a fine surface finish in Wire-EDM”, Journal of Materials Processing Technology, 149 (2004): 165-171.

[67] N. Tosun, C. Cogun, and A. Inan, “The effect of cutting parameters on workpiece surface roughness in wire EDM”, Machining Science and Technology, 7 (2003): 209-219.

[68] Thomas R. Newton, Shreyes N. Melkote, Thomas R. Watkins, Rosa M. Trejo, and Laura Reister, “Investigation of the effect of process parameters on the formation and characteristics of recast layer in wire-EDM of Inconel 718”, Materials Science and Engineering: A, 513 (2009): 208-215.

[69] Tomura Shunsuke, and Masanori Kunieda, “Analysis of electromagnetic force in wire-EDM”, Precision engineering, 33 (2009): 255-262.

[70] E. Portillo, Marga Marcos, Itziar Cabanes, Asier Zubizarreta, and José Antonio Sánchez, “ANN for Interpolating Instability Trends in WEDM”, IFAC Proceedings, 41 (2008): 2230-2235.

[71] Poroś Dariusz, and Stanisław Zaborski, “Semi-empirical model of efficiency of wire electrical discharge machining of hard-to-machine materials”, Journal of materials processing technology, 209 (2009): 1247-1253.

[72] R. Ramakrishnan., and L. Karunamoorthy, “Multi response optimization of wire EDM operations using robust design of experiments”, The International Journal of Advanced Manufacturing Technology, 29 (2006): 105-112.

[73] R. Ramakrishnan R, and L. Karunamoorthy”,Modeling and multi-response optimization of Inconel 718 on machining of CNC WEDM process”, Journal of materials processing technology, 207 (2008): 343-349.

[74] I. Cabanes , E. Portillo, M. Marcos, and J. A. Sánchez, "An industrial application for on-line detection of instability and wire breakage in wire EDM", Journal of materials processing technology, 195 (2008): 101-109.

[75] S. Mahapatra , and Amar Patnaik, "Optimization of wire electrical discharge machining (WEDM) process parameters using Taguchi method", The International Journal of Advanced Manufacturing Technology, 34 (2007): 911-925.

[76] Han Fuzhu, Jun Jiang, and Dingwen Yu, "Influence of machining parameters on surface roughness in finish cut of WEDM", The International Journal of Advanced Manufacturing Technology, 34 (2007): 538-546.

[77] Anish Kumar, Vinod Kumar, and Jatinder Kumar, "Prediction of surface roughness in wire electric discharge machining (WEDM) process based on response surface methodology", International journal of engineering and technology, 2 (2012): 708-719.

[78] J.T Huang, Y. S. Liao, and W. J. Hsue, "Determination of finish-cutting operation number and machining-parameters setting in wire electrical discharge machining", Journal of Materials Processing Technology, 87 (1999): 69-81.

[79] Abdulkadir Erden, "Effect of materials on the mechanism of electric discharge machining (E. D. M.)", ASME, Transactions, Journal of Engineering Materials and Technology, 105 (1983): 132-138.

Chapter 3

Experimental Methodology

3.1 Introduction

P91 steel plates in normalized (1080 ^{o}C, 30 min) and tempered (770 ^{o}C and 30 min) condition were used in this study. P91 is 9Cr1Mo ferritic martensitic steel. The microstructure of P91 is tempered martensitic with precipitates of vanadium / niobium nitrides and carbides, as it is produced by normalizing in the temperature range of 1040-1080 ºC and followed by tempering in the range of 750-780°C [1]. During tempering the carbides precipitates, which improves the strength of P91 [2]. The elemental composition of P91 is presented in table 3-1. The physical and mechanical properties of P91 relevant to this study have been listed in table 3-2. Rolled P91 plates of dimension 130mm×120mm×40 mm were used in the study. A schematic of machining process is shown in Figure 3.1. The samples were machined using WEDM and microstructure of the machined surface was analysed. The processing parameters were optimized to improve the response. Again the samples were cut using optimized control parameters and analysed to verify the improvement in the surface. It also acts as the cooling medium after the implosion of the plasma channel and helps in erosion of molten material. The effect of medium on the surface layer has been investigated by researchers [3]. In this case, the surface layer had all the characteristics of a typical recast surface.

Table 3-1 Elemental composition on P91

Element	Fe	Al	C	Cr	Mn	Mo	Ni	Nb	N	P	Si	S	V
Weight (%)	88.58	0.04	0.08-0.12	8.0-9.5	0.3-0.60	0.85-1.05	0.4	0.06-0.1	0.03-0.07	0.02	0.20-0.5	0.01	0.18

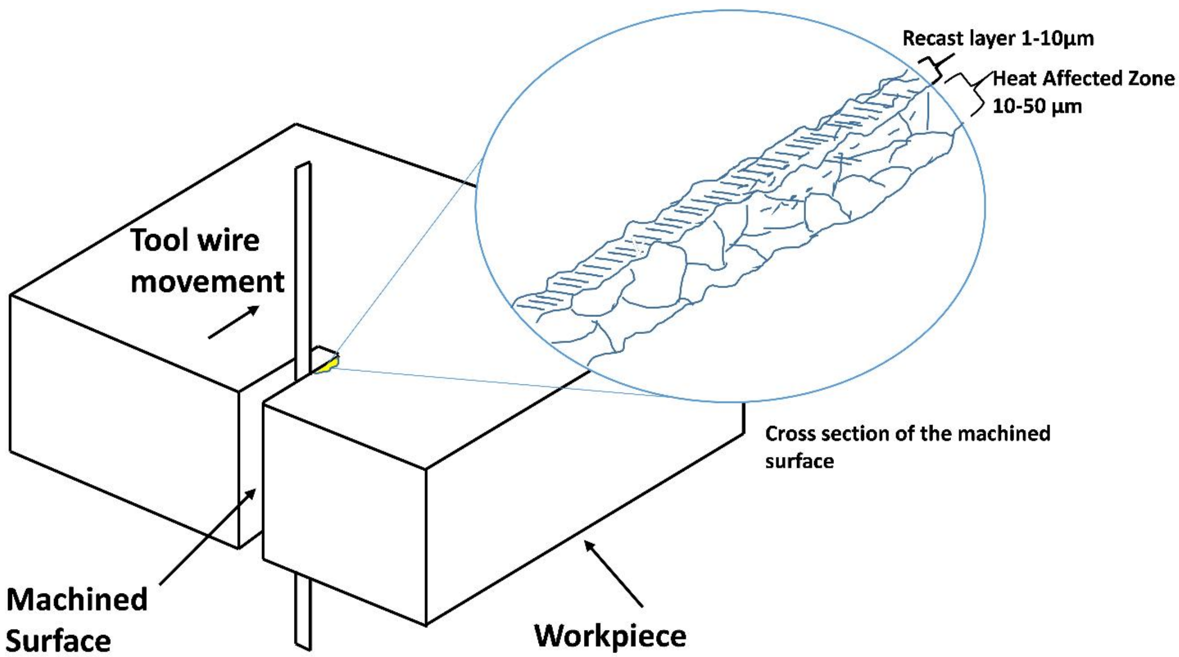

Figure 3.1 Schematic diagram showing the interaction of the wire and the workpiece and generation of the machined surface during WEDM process.

Table 3-2 Physical and mechanical properties of P91

Properties	**Value**
Density	7850kg/m^3
Tensile Strength, Ultimate	750 MPa
Tensile Strength, Yield	550 MPa
Modulus of Elasticity	210GPa
Bulk Modulus	160GPa
Poisson ratio	0.29
Shear modulus	80.0GPa
CTE, Linear	12.0µm/m-^{o}C
Specific heat capacity	0.470 J/Kg-^{o}C
Thermal Conductivity	55.0 W/m-K

3.2 Design of Experiment

The experiments were designed to study the influence of the individual process parameter and the combination of process parameters on the surface integrity. For second order regression analysis in Response Surface Modelling the size of experiments becomes large and analysis becomes very complicated when variables involved are more than three levels. Such extensive study will require a large number of experiments, which are time consuming and uneconomical for industry. Therefore, a systematic combination of parameters was used to screen the significant parameters and optimize the response of the experiment using those parameters. The range of process parameters were selected on the basis of capability of machine. Central composite design was used for designing the experiment since central composite design is the most commonly used in response surface designed experiment. It is a factorial or fractional factorial design with center points, augmented with a group of axial points (also called star points) that allow estimation of curvature. This gives a well-designed experiment plan to reduce the size of experiments. Central composite rotatable design of second order was used for establishing the relation of response surface using smallest number of experiments without losing accuracy. In this experiment eight design points were taken at the origin and two points for each variable at a distance of α from origin, where $\alpha = (2k)^{1/4}$ and k is the no of parameters in the study. A total 32 samples were cut during the experiment.

Based on previous literatures on optimization of WEDM, discharge current (I_g), gap voltage (V_g), pulse on time (T_{on}), Pulse off time (T_{off}), were chosen as variables to study their effect on the morphology of the machined surface [4] and this was used to generate the ANOVA table and the response surface. ANOVA analysis was performed by considering 95% confidence interval to assess the significance of the process parameters which affect the surface roughness response of the machined surface. To study the effect of process parameters a polynomial response for surface roughness was fitted in the equation 3.1.

$$y = \beta_0 + \sum_{i=1}^{k} \beta_i \times x_i + \sum_{i=1}^{k} \beta_{ii} \times x_i^2 + \sum_{i=1}^{k} \beta_i \times x_i \times x_j + \in \qquad (3.1)$$

Where x_i, x_j, x_k are input or independent process parameters. $ß_0$, $ß_i$, $ß_{ii}$, $ß_{ij}$ are unknown coefficients of parameters called regression coefficients. Response surface is obtained by plotting the response *y*. The optimum value of the process variables was obtained by solving the regression equations and by analysing the response surface plots.

3.3 Machining of P91 samples

The experimental work was carried out using CNC ULTRACUT WEDM (Electronic Machine Tools Ltd). It consists of CNC WEDM machine tool, a pulse generator to provide pulsating DC voltage, wire drive mechanism for circulation of tool wire, supply tank for de-ionized water (dielectric) at room temperature and dielectric flushing system. The operator can vary the control parameters to optimise the machining process. Zinc coated brass wire of diameter 250µm was employed for machining. The wire traverses through the work piece from two guides placed above and below the work piece and equipped with flushing jet to remove debris.

The main processing parameters of WEDM machining are discharge current (I_g), gap voltage (V_g), pulse on time (T_{on}), Pulse off time (T_{off}), wire feed rate (WF), Wire Tension (WT), Flushing pressure (FP), and Wire Diameter. The process parameters can be divided into two categories namely Electrical parameters and Non electrical parameters. Electrical parameters contain discharge current (I_g), gap voltage (V_g), pulse on time (T_{on}), Pulse off time (T_{off}) and non-electrical parameters contain wire feed rate (WF), Wire Tension (WT), Flushing pressure (FP), Wire Diameter etc. This paper focuses on the surface integrity of machined surface in terms of various features of recast layer. Recast layer is formed by solidification of un-eroded molten material on substrate, volume of which depends mostly on the energy of spark. Therefore, in this paper electrical process parameters like peak current (IP) in ampere, voltage (V) in volts , spark on time (T_{on}) in µs, spark off time (T_{off}) in µs, were selected for parametric optimization of WEDM of P91. The reponse parameters are surface roughness (SR), length of micro crack (L_c) and number density of micro crack (N_{da}). The value of process parameters for machining are presented in table 3-3. The medium used in this study was deionized water, which has good dielectric strength of 65-70 MV/m for generation of spark between the electrodes. It also acts as the cooling medium after the implosion of the plasma channel and helps in erosion of molten material.

Table 3-3 Cutting parameters

Sl No.	Process parameters				Response parameter		
	IP(A)	V(V)	T_{on}(µs)	T_{off}(µs)	SR, R_a(µm)	L_c(µm)	N_{da} (%)
1	70	20	120	30	1.653	2.2	70
2	130	20	120	30	3.15	11.6	65
3	70	80	120	30	1.568	8.7	47
4	130	80	120	30	2.865	10.6	72
5	70	20	130	30	1.89	3.6	44.5
6	130	20	130	30	2.78	7.6	68
7	70	80	130	30	1.32	9.8	55
8	130	80	130	30	1.91	3.5	78
9	70	20	120	60	3.45	2.2	63.5
10	130	20	120	60	3.87	9.3	68
11	70	80	120	60	1.784	8.7	62

12	130	80	120	60	2.428	4.4	53.6
13	70	20	130	60	2.535	2.3	40
14	130	20	130	60	1.896	6.8	65
15	70	80	130	60	1.783	5.8	67
16	130	80	130	60	1.113	2.8	73.8
17	100	50	125	45	2.35	5.8	61
18	100	50	125	45	1.698	3.1	58
19	100	50	125	45	1.438	2.9	65
20	100	50	125	45	1.832	3.8	69
21	70	50	125	45	1.311	6.9	57
22	130	50	125	45	3.165	8.7	73
23	100	50	125	45	1.7356	8.3	48
24	100	50	125	45	1.7735	6.4	53
25	100	50	115	45	1.9832	10.4	59
26	100	50	135	45	1.5324	11.8	62
27	100	50	125	45	2.786	8.8	47
28	100	50	125	75	2.35	9.3	63
29	100	50	125	45	2.89	4.9	41
30	100	50	125	45	2.8	7.9	52

3.4 Optical spectroscopy of underwater plasma

A dedicated setup was fabricated resembling principle EDM process. It consists of a dielectric tank, a linear stage for movement of tool, a rotational stage for adjusting probe of optical spectroscope, a micrometer scale to adjust the gap between the electrodes as shown in Figure 3.2.The schematic of the plasma spectroscopy experiment is shown in Figure 3.3.

Figure 3.2 Photograph showing the experimental setup.

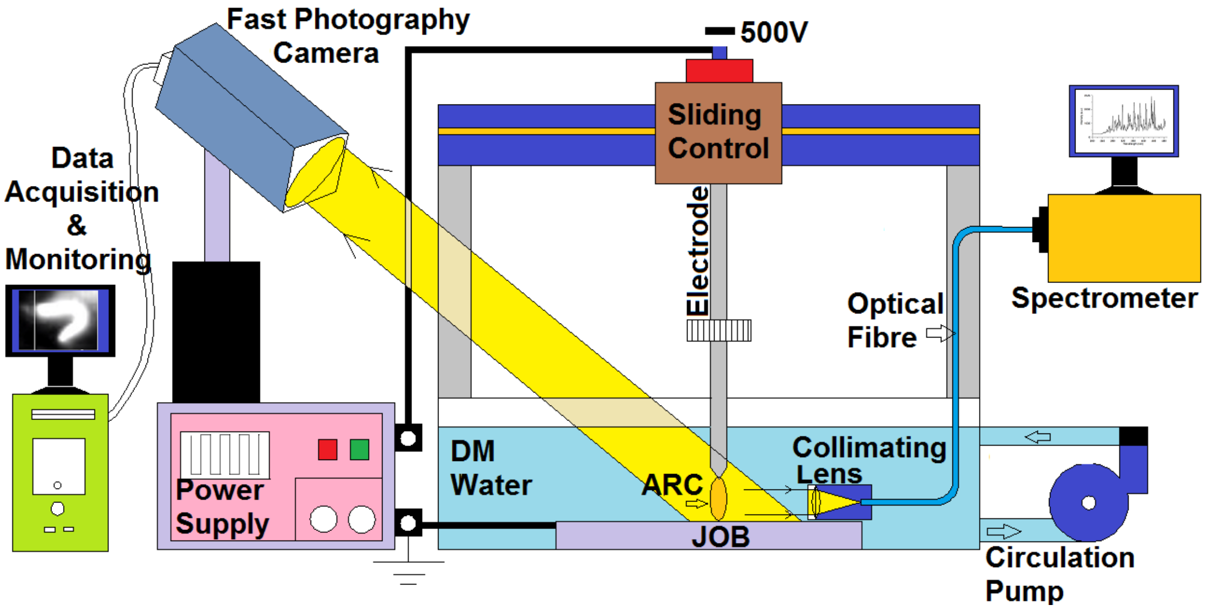

Figure 3.3 Schematic diagram showing experimental setup for spectroscopy.

It consists of two electrodes. One vertical rod type made of tungsten with conical tip (tip angle 30°) working as cathode and the other rectangular block (100mm x 52mm x 6mm) working as anode. It also consists of a pulsed power supply for imparting pulsed voltage to the electrodes (waveform shown in Figure 3.4), a small recirculation pump for flushing the dielectric (pumping rate 51 lpm), fiber optic based spectral data acquisition system with collimating lens at the fibre tip, fast photographic camera equipped with necessary data acquisition, control and monitoring system. The cathode is screwed to a linear movable platform which was further powered with a servomotor to control the travelling speed. The anode is fixed on the bottom of the tank with metallic screw. The tungsten electrode is connected to one terminal of power supply of 10 kHz generating a pulsed voltage of maximum magnitude 500V and maximum current 2A. The anode is connected to the other terminal of power supply through metallic screws. The gap between the cathode tip and the anode surface, adjusted through an attached micrometre screw, is maintained within 40-50μm and both the electrodes are fully immersed in de-mineralised water (used as dielectric). This water is continuously circulated using a centrifugal pump to replenish the dielectric strength of the dielectric at the gap between the electrodes. When voltage between the terminals increased beyond the dielectric breakdown voltage of the demineralized water, arc formed between the cathode tip and the job. This generated arc is used for melting and eroding the workpiece material. The point of connection between the arc and the job is called arc root. Thermally constricted arc at the anode arc root results in extremely high current density (in excess of 10^6 A/m^2). Resulting highly localized intense ohmic heating at the arc root causes fast melting of the anode material at the root location. Under the influence of extremely high temperature of the arc, the molten material soon vaporises, dissociates into atoms, gets ionized and becomes part of the arc plasma so generated. Four different materials namely SS304, copper, zircaloy, ferritic martensitic steel (P91) were used in the experiment as anode to investigate the behaviour of the generated arc for different anode material. The intense light emitted from the electric discharge carried the signature of ionic and molecular species present in the plasma. Therefore, this characteristic signature of the species indirectly gives information about the temperature of the plasma. The light generated in the plasma is collected using an optical fibre, mounted with a collimating lens at its tip as shown. The other end of the fibre is connected to a triple grating spectrograph (Shamrock SR-303i) with Czerny-Turner arrangement and 303mm focal length. The triple grating turrets are fitted with gratings: 300 lines/mm, 1200 lines/mm and 2400 lines/mm. In this study the spectra were recorded with grating of 1200l/mm. Obtained wavelength resolution was around 0.1 nm.

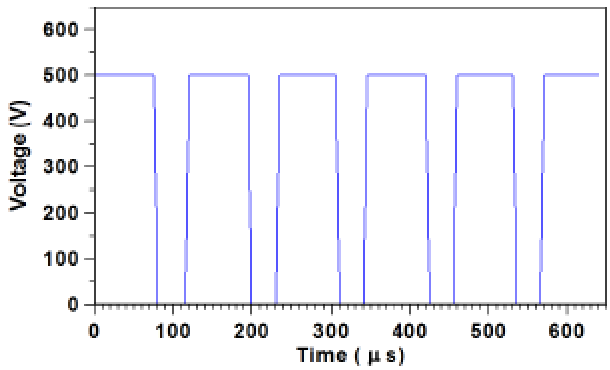

Figure 3.4 The voltage waveform from the power supply.

The generation and evolution of the plasma was recorded using a fast photography camera (PCO1200hs) with a frame rate of 2500 frames per second or higher. The camera has a maximum resolution (horizontal × vertical) of 1280×1024 (pixels), pixel size of 12 µm x 12 µm, minimum exposure time of 1 µs. In the present study the pulse on time of the power supply was 80 µs and pulse off time was 35µs (Figure 3.4).

The inter-frame time for the fast camera was around 234µs in most of the cases. Depending on chosen frame size, the actual inter frame time was automatically set by the camera. It is evident from the inter-frame time that it was not possible to capture more than one image per discharge event in the present setup.

3.5 Surface roughness measurement

Surface roughness of the machined surface of each sample was measured using stylus type profilometer. The profilometer has cut-off length of 500µm. It measures all three types of surface finish parameters namely R_a, R_z, and R_{rms}. Average surface roughness was expressed as R_a in µm, which is commonly used in manufacturing industry. The stylus of the profilometer took 5 readings from random points along a line and calculates an average of the absolute slope of the profile within the sampling length. Such 5 readings were made on different random lines of the machined surface of each sample and the average of the five was selected as the surface roughness of the sample.

3.6 Nano Hardness measurement

The machined surface has recast layer of the order of 2-8 µm relevant to this study. So an investigation of the hardness profile of the machined surface was necessary to understand the physical characteristics of the recast layer. Since the size of the recast layer was very small it was very difficult to resolve the difference in hardness of the recast layer and the bulk material by normal Hardness test. Therefore, hardness profile on the cross section of the machined surface was obtained by measuring nano hardness from recast layer to the bulk material. Samples were polished and nano indentation was made on the cross-section of the machined surface using Berkovich diamond indenter (UNHT, CSM). Standard procedure for nano indentation was followed. a) The indenter was lowered to touch the cross section of machined surface b) Load of 5 mN was applied and indenter was moved up c) Unloaded up to 90% then subsequently d) upholding and total unloading. Similar reading were taken in 5 different positions on the machined surface and an average of the five readings were selected as the average hardness of the recast layer.

3.7 Scanning Electron Microscopy (SEM) of WEDM machined surface of P91

The microstructure of the machined surface was observed under SEM. In this study SEM images were taken by using Carl zeiss cross beam, Auriga and TEM images were taken by using TEM JEOL 3010. The SEM examination was done at 5kV voltage with maximum magnification of 30KX.The uneroded molten materials gets redeposited as recast layer. The thickness of the recast layers varies with the energy of the spark. Therefore, to revel the microstructural features of the machined surface the samples were cut into smaller pieces of dimension (25×5×10 mm) and mirror polished in sequential grades of SiC paper followed by diamond paste polishing. The polished samples were then etched with Villella's reagent (95 ml of ethyl alcohol, 5 ml of hydrochloric acid, and 1 g of picric acid).SEM images for two section were extracted. The plan view of the machined surface showed the size of craters and micro cracks and the cross sectional view shows the thickness of the recast layer and cracks present in the recast layer.

3.8 Transmission Electron Microscopy (TEM) of WEDM machined Surface of P91

The SEM images of the machined surface revealed that the recast layer has very fine or featureless surface. Therefore, for deeper insight the recast layer region was investigated under TEM. The sample of TEM was prepared by Focussed ion Beam Technique (FIB). In this method a beam of gallium ions are bombarded on the selected region. The accuracy of the region selected for taking out the sample for TEM can be of the order of 1µm. In this study a section of recast layer with length 10 micron and thickness 1 micron was selected for TEM investigation. The sample of TEM was cut from the SEM sample by FIB and then welded to a copper base holder. The sample was then examined in TEM to reveal the in depth features of the recast layer.

3.9 Measurement of experimental responses

The experimental responses were measured in terms of parameters like surface roughness of the machined surface, recast layer thickness, nano-hardness and microstructure of recast layer, density, average length and orientation of micro cracks.

The polished samples were etched with Villella's reagent (95 ml of ethyl alcohol, 5 ml of hydrochloric acid, and 1 g of picric acid) to reveal the microstructure of the machined surface to study the characteristics of the recast layer. The micro cracks seen in recast layer were classified into two categories. In this study all micro cracks which are inclined 0° -30° and 150-180° with respect to the cutting line are termed as lateral crack and those inclined between 30° -150° w.r.t cutting line is termed as axial micro cracks. Average length of micro cracks (L_c), number density of micro cracks (N_d) and orientation of micro-cracks (%N_d, as ratio between axial and lateral cracks) were determined for different energies for the given area of machined surface using the equations 3.2 and 3.3 shown below

$$L_c = \frac{\sum_{j=1}^{5} L_{cj}}{\sum_{j=1}^{5} N_{cj}} \tag{3.2}$$

$$\% N_d(A \text{ or } L) = \frac{N_{d(A \text{ or } L)}}{N_{d-total}} \times 100 \tag{3.3}$$

Where, L_{cj} is the length of micro crack, N_{cj} is the number density of micro cracks in each Scanning electron micrographs and A_j is the area of each micrograph [5 6]. The typical procedure for calculation of the above mentioned parameters are presented in Figure 3.5. Surface roughness (SR) measurements of the walls of the square channels cut were made using a stylus type profilometer. The profilometer has cut-off length of 500μm. The micrographs of the machined surface were observed and length, number and orientation of micro cracks on machined surface were measured.

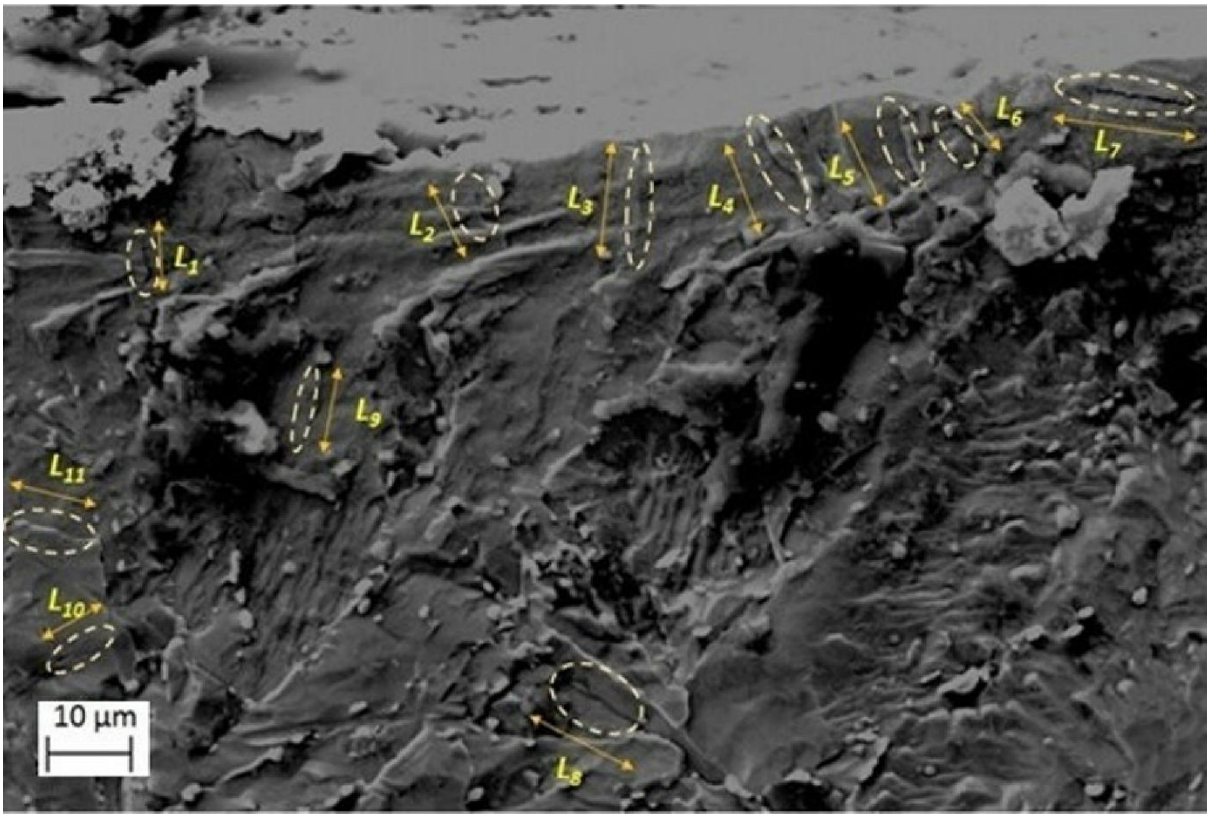

Figure 3.5 SEM image of machined surface used for response parameter calculation.

3.10 Corrosion Samples preparation

The cracks and craters in the machined surface of WEDM samples were tested for passivation. The cracks and craters can be a site of initiation of corrosion, which can further lead to failure of the component. In the corrosion experiment the WEDM machined P91 steel plates were normalized (1080ºC, 30min) and tempered (770ºC and 30min). To compare the corrosion behaviour of WEDM machined surface of P91 with diamond polished surface two samples in coupon size of 30×15×5 mm were prepared for electrochemical experiments. The coupons were cleaned with acetone and lacquer coating was done on the edges and all the other sides except the area of exposure for electrochemical measurements. The coupons were placed under potentiodynamic Polarization test carried out in solutions with different pH. The solutions used were 0.5M H_2SO_4, Borate buffer solution (pH-9.2), 0.5M H_2SO_4 + 0.25M NaCl, 0.1M NaH_2PO_4 + 0.1M NaOH (pH-7) and 0.06M NaH_2PO_4 + 0.025M KH_2PO_4 (pH-4). The tests were carried out in a conventional three-electrode cell using a Platinum (Pt) electrode as the auxiliary (counter) electrode and a saturated calomel electrode (SCE) as the reference electrode. The samples after electrochemical experiments were characterised using an SEM. Argon gas purging was done for 30-45 minutes before the potentiodynamic polarization measurement and this purging continued during the experiment. The potentiodynamic polarization measurements were carried out using a Biologic VSP-300 potentiostat at room temperature (26 ± 1°C). First the open circuit potential was measured for the sample for 20-30 minutes. After that cathodic cleaning was done at -1.0 V A vs E_{ref} for 1 minute to remove any contamination or oxide layer from the sample surface and then again open circuit potential was measured. Linear sweep voltammetry technique was used. A sweep rate of 20mV/min was employed. Double-loop electrochemical potentiodynamic reactivation (DL-EPR) studies were carried out at -50 mV below the open circuit potential (OCP) to +500 m V_{SCE} and reverse scan till OCP in deaerated 0.003M H_2SO_4 solution at a scan rate of 100 mV/min. The samples after electrochemical experiments were characterised using an SEM.

3.11 Residual stress measurement

The recast layer in WEDM machined surface has residual stresses which could be fatal for the service life of the component. Residual stress on the machined surface was measured by standard GIXRD technique used for metals [6]. The thickness of the recast layer in WEDM machined surface was of the order of 2-10 μm, therefore grazing incidence angle XRD was used for determining residual stress. The cross section of the machined surface was prepared by polishing the samples and the space lattice distortion was measured and compared with powder diffraction file of same material. The distortion of space lattice gives an indication of strain and hence residual stresses.

3.12 References

[1] Swadesh Dixit, Vikas Chaudhari, and D. M. Kulkarni, "Effect of tempering time on mechanical and fracture behavior of SA 387 Gr. 11 pressure vessel steel", Journal of Materials Processing Technology, 276 (2020): 116419.

[2] C. Pandey, and M. M. Mahapatra, "Effect of heat treatment on microstructure and hot impact toughness of various zones of P91 welded pipes", Journal of Materials Engineering and Performance, 25 (2016): 2195-2210.

[3] G. Kibria, B. R. Sarkar, B. B. Pradhan, and B. Bhattacharyya, "Comparative study of different dielectrics for micro-EDM performance during microhole machining of Ti-6Al-4V alloy", The International Journal of Advanced Manufacturing Technology, 48 (2010): 557-570.

[4] Vikaram Singh, and S. K. Pradhan, “Optimization of WEDM parameters using Taguchi technique and response surface methodology in machining of AISI D2 steel”, Procedia Engineering 97 (2014): 1597-1608.

[5] P. Govindan., and Suhas S. Joshi, “Analysis of micro-cracks on machined surfaces in dry electrical discharge machining”, Journal of Manufacturing Processes, 14 (2012): 277-288.

[6] R. Thomas Newton, Shreyes N. Melkote, Thomas R. Watkins, Rosa M. Trejo, and Laura Reister, “Investigation of the effect of process parameters on the formation and characteristics of recast layer in wire-EDM of Inconel 718”, Materials Science and Engineering: A 513 (2009): 208-215.

Chapter 4

Estimation of temperature of WEDM plasma using spectroscopy

4.1 Introduction

Underwater wire electrical discharge machining (EDM) is gaining rapid momentum in recent years due to its unique ability to cut and shape wide range of solid materials where conventional techniques give poor performance. It involves high temperature plasma [1]. While both the electrodes start melting as they are exposed to the high heat flux, the anode melts faster as it receives the fast electrons during pulse on-time [2]. The complete EDM process involves hydrodynamics, electromagnetics, electrodynamics, thermodynamics and different transport processes. Dielectric strength and viscosity of the liquid, electrical and thermal conductivity of the liquid dielectric as well as electrodes, and dependence of these properties on pressure and temperature are important parameters determining the overall nature of the discharge. Set physical parameters like discharge gap voltage, discharge current, pulse on-time, pulse interval, gap distance etc. also play very important roles. It is almost impossible to maintain uniform values of all these parameters in every applied pulse due to inherent nature of the process itself. Time and space averaged behavior may be of only practical relevance. A simple and comprehensive theory of the phenomenon is naturally absent. Nevertheless, a number of efforts have been made to achieve an analytical model giving good match with the experimental erosion rate.

Breakdown of liquid dielectric has been studied earlier in various fields like exploding wires [3], laser produced plasma [4] and condensed matter [5]. Plasma studied in this work is similar to them in parameters but different in kinetics and evolution as they depend on specific electrode configurations, dielectric and operating conditions used. Density and temperature achieved in these plasmas give them a special status of non-ideal plasmas and lead to interesting behavior, much of which are not explored enough. While numbers of theoretical and numerical studies exist on the EDM plasma, experimental studies on the basic discharge phenomenon inside the dielectric, which lies at the heart of the process, are highly limited. Tiny size of the plasma, short duration, weak luminous intensity, problem of placing intrusive electrostatic probe inside liquid dielectric, poor reproducibility due to continuously evolving electrode surface profiles and dielectric contamination from eroded electrode materials are some of the difficulties of the experimental study.

Available theoretical and numerical material removal models for EDM machines assume extremely high temperature (owing to intense current density in the constricted plasma channel) as the primary cause for erosion [2-5]. Electro-thermal semi-infinite cylinder model with a circular heat input [6], two-dimensional heat flow model with medium bounded by adiabatic cylindrical surface in the radial direction [7], semi-infinite cylinder model with disc heat source[8], point heat source conduction model for cathode erosion [9] and anode erosion [10], point heat source model for cathode and circular disc heat source model for anode [2], variable mass, semi-infinite cylinder model with circular heat input [11], expanding circular heat source model with time varying heat flux [12], lossy dielectric media model using particle physics approach [13], multi-scale model with Gaussian heat flux [14], thermo-hydraulic coupling model with consideration of phase transition [15] are some of the available theoretical models in this regard. Other theoretical calculations like estimation of net emission coefficient of EDM arcs [16] also have been reported. However, when compared with corresponding experimental results, sometimes the theoretical material removal rate (MRR) is found to be more than 8.5 times the experimental one [17]. While some of the later developments were able to predict MRR in reasonable agreement with experimental one for certain longer pulses and high current, they are found to overestimate the temperature distribution and give values for MRR off by a factor as high as 46 for shorter pulses [17]. Nevertheless, all these studies have significant contributions in reaching the present level of understanding.

For any accurate model, one needs to identify the details of the basic physical processes involved. Analysis of the fast photographic images of the EDM arcs can give the characteristic features of the dynamic evolution of the discharge and direct indication of the fundamental processes involved. Analysis of wavelength distribution in the spark and respective intensities may give information about participating species, their densities, average temperature of the discharge zone, signature of the physical processes and regime of operation. While a good volume of work is available on modelling, experimental studies to understand the dominant mechanisms are only few and behaviour of the developed plasma is still poorly understood.

Albinski et al. [18] studied the temperature of an EDM plasma. Fe-I lines (411.854 nm and 413.29 nm) were captured and temperature was determined using ratio of two line intensities.

Descoeudres et.al did time-resolved imaging and spatially-resolved spectroscopy of EDM plasma in 2005 [19]. The same results were republished by them again in 2008 [20]. The estimation of temperature was based on the line intensity ratio measurements using three copper lines 510.55 nm, 515.32 nm and 521.82 nm. Ramkumar et.al. [21] did similar optical spectroscopic study of EDM plasma using line pair method and the Stark broadening, for plasma temperature and electron density respectively. Temporally and spatially resolved electron density in the filament of a pulsed spark discharge in water was investigated by Niu et.al. [22] using broadening of H_α line.

It may be emphasized here that the ratio of two line intensities method (RTLIM), used in most of the above studies, give accurate temperature if and only if the energy levels associated with the chosen lines maintain LTE (Local Thermodynamic Equilibrium) distribution. Unfortunately, most of the EDM plasmas do not maintain LTE. Rather, they maintain PLTE (Partial Local Thermodynamic Equilibrium), under which few of the energy levels are not populated as per Boltzmann distribution. If any of the chosen lines in the RTLIM arise out of transition involving levels not maintaining LTE, the temperature estimated is bound to be erroneous. This important aspect is not explicitly addressed in any of the above studies. The Boltzmann plot technique used in the present study is unique in the sense that it first checks the whole emission range with specific anode material to identify the region where large numbers of emission lines are available over a short wavelength range. This ensures nearly similar general absorption features for all the chosen lines. Next, it checks whether the chosen lines follow LTE distribution or not. This is done by simply checking the linearity maintained by the lines in the Boltzmann plot. Any emission line, originating from levels not maintaining LTE does not follow linearity in the plot. Since instead of only two lines (as used in RTLIM), a number of lines are considered in the determination of temperature and LTE is ensured, the calculated temperature is expected to be reliable and reasonably accurate. Observed high linearity in the Boltzman plots, offered by the used lines for every anode material, is presented in the experimental analysis part.

Basic limitation of the previous time and space resolved studies of EDM discharge [19, 20] is that they could not capture the occurrence of variety of important dynamics and their dynamic evolution, happening over larger spatial scales and longer time scales. Quality of the recorded images was poor and no distinct structure could be identified. All the captured images looked highly identical due to extremely small time difference between consecutive images. Estimated temperatures from the captured spectra at different spatial locations also exhibited no significant variation. Nearly similar features were observed for electron density as well. In such scenario, the present experiment was planned to explore the full set of the associated dynamics in EDM discharges and understand their time evolution. Adopted experimental plan selected large enough spatial scale to capture the dynamics occurring over extended region. Highest possible frame rate, compatible with the chosen spatial scale was set to capture the images using fast camera. It may be noted that the afforded highest frame rate, detailed in the experimental part, was not enough to capture more than one image per pulse. To overcome this limitation, the study employed a key idea similar to 'ensemble average' concept in statistical mechanics. Somewhat complete information about all possible dynamics in EDM arc discharge may be obtained if large numbers of images are captured in sequence. Different images will correspond to different time instants after initiation of the pulsed discharges. The instants of grabbing the image will span over the full pulse length in the limit when number of captured images is very large. This is the principle followed in this study. For practical presentation purpose, only selected images, representative of specific dynamics for a given anode material are presented in this article. Interesting discharge dynamics, its time evolution, and interaction with the electrodes, apparently not explored earlier, have been obtained from the fast-photography results. Unique material dependent behaviour has been revealed through emission spectroscopic analysis. Electron density is extracted from broadening of corresponding H_α line. Plasma temperature is determined using Boltzmann Plot method. Here it may be remarked that supporting observed material (anode) dependent behaviour (temperature, density, arc dynamics) through computational fluid dynamic (CFD) simulation including shocks and electromagnetic body forces arising out of current carrying nature of the generated plasma requires availability of thermodynamic and transport properties of the underwater plasma loaded with evaporated anode material at elevated pressures and different temperatures. Calculation of required thermodynamic and transport properties like density, specific heat, reactive thermal conductivity, translational thermal conductivity, electrical conductivity, viscosity, diffusion coefficients etc. as a function of temperature as well as pressure involves extensive modelling efforts and remains beyond the scope of the present study. Nevertheless, the experimental findings obtained from the study may serve as data for fundamental understanding and benchmarking of the future simulation results.

4.2 Results

As the EDM discharge event starts, it breaks the H-OH bond of the dielectric (water). Presence of extremely high temperature of the arc further breaks the OH radicals into H and O atoms. Observed atomic lines of H and O in the EDM spectra, irrespective of anode material used, supports this fact. Complete breakdown happens very fast (<50 ns) and a substantial plasma volume forms near the electrode gap in the form of a cylindrical channel of diameter of few hundred micrometers. To understand the behaviour, the discharge phenomenon may be modelled using the following gross overall reaction kinetics:

$$H_2O \rightarrow H + OH \tag{4.1}$$

$$H \rightarrow H^+ + e \tag{4.2}$$

$$OH \rightarrow O + H \tag{4.3}$$

$$O \rightarrow O^+ + e \tag{4.4}$$

$$O + O \rightarrow O_2 \tag{4.5}$$

$$H + H \rightarrow H_2 \tag{4.6}$$

$$M \rightarrow M^+ + e \tag{4.7}$$

During discharge, the plasma developed is expected to include all the species mentioned above. 'M' corresponds to metal, 'M^{+}' is its first ion and 'e' is the electron. Because of low ionization energy of metallic atoms and presence of high temperature it is possible that higher ionized state of metal atoms may also exist. Depending on the anode and cathode material a number of metallic atoms and ions may be present. If an alloy is used as anode material, number of different types of metallic species may be even more. However, the dominant lines in the emission spectra are usually contributed by the metallic constituents from the anode material. It may be pointed out that although tungsten is used as cathode in all the studies, possibly due to its high melting point or much weaker line intensity compared to the other lines present, its lines are rarely seen.

Among different anode materials used in the study, SS304 plates includes Cr (18.2%), Ni (8.1%), Mn (8.1%), C (0.55%), Si (0.35%) and S (0.001%) apart from Fe. Used P91 is an alloy of Fe with Cr (9%) and Mo(1%) for high temperature strength, improved oxidation resistance and creep resistance. It also includes very small quantities of Ni and Mn to increase hardenabilty. Elemental composition of zircaloy includes Zr (98.23%), Sn (1.5%), Fe (0.12%), Ni (0.05%) and Cr (0.1%).

General notion about material removal in EDM discharges includes two phase: vaporizing stage and splashing stage at the end of discharge. Material removal capacity in the later stage is found to be much greater than that in the vaporizing stage. While large hydrostatic pressure difference is suspected to be the primary driving force for debris removal, the fundamental mechanisms like possibilities of electromagnetic pumping are not discussed in literature to the best of the author's knowledge. Needless to mention that associated shearing flow has significant potential to influence the crater morphologies and deposition of material in the surrounding area. However, it is estimated that only a small fraction (<10%) of the molten material is removed in the process and rest of the material undergoes re-solidification [15]. Accurate numerical simulation of the process demands details of the arc dynamics and associated attributes of thermo-hydraulic coupling during the EDM discharge process. The primary objective of the fast photographic study in this work is to explore the domain and extract direct evidences of possible dynamics.

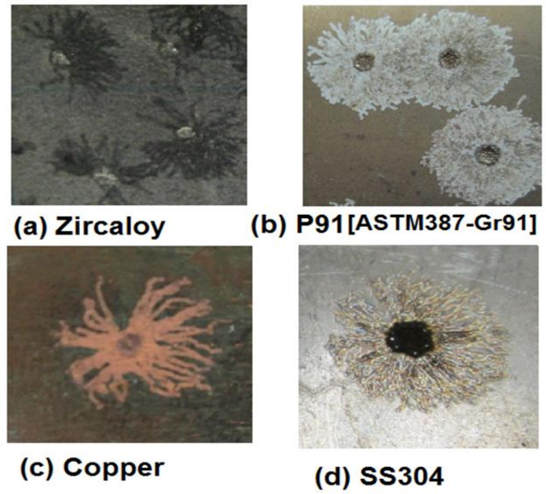

Figure 4.1 Photographs showing arc spots and traces of the arc paths driven by instability in different materials.

Figure 4.1(a-d) presents the physical image of the surfaces of different anode blocks made of different materials, each subjected to series of EDM discharges of similar time span. Apart from the expected central crater exactly below the cathode, the interesting observations are the traces of the arc paths surrounding it. It is observed that the nature and distribution of the arc paths have significant dependence on the anode material. While for zircaloy, the azimuthal distribution of arc parth is observed to be fairly asymetric, the same for P91 and SS304 are highly symmetric. For copper the distribution is found to be inbetween. The behaviour is extremely important as it indicates to be a fundamental phenomenon involved in the process and has signficant impact on thermal distribution, process quality and process efficiency. A rigorous fast photographic study of the phenomenon, presented in this study was motivated by this.

The primary problem in capturing an arc image is its extreme brightness. This often leads to saturation and does not reveal the underlying details of the internal structure of an arc linked to fundamental processes. Fortunately, it was surprisingly easy to manage this problem using the fast photography camera, PCO1200hs. The camera has the facility to cut down the intensity in a manner that it gradually exposes the higher intensity internal structures developed inside the plasma avoiding the problem of saturation and glare [23]. In its extreme stage, only the highest intensity zones remain visible, which is nothing but the arc path, well resolved in space. Using this facility, the camera can brilliantly capture any non-uniformity in the media similar to visualization using techniques like shadowgraphy, schlieren photography etc.

Highly nonlinear dependence of associated plasma transport properties on temperature, existence of steep temperature gradient, pulsed nature of the discharge and continuously evolving electrode microstructures make the arc dynamics continuously evolving in time. It is therefore difficult to reproduce the same plasma structure with identical operating parameters. However, our study reveals that the typical features of the average behavior under similar operating conditions are reasonably reproducible. It may be pointed out that the recorded spectral intensity comes from the whole tiny plasma volume rather than any particular location. It also must be noted that the discharge gap within which the plasma forms is only few tens of μm. Due to spatial and temporal uncertainties in the discharge caused by short-lived pulses and very nature of the arc, it was not practical to focus at any particular location of the evolved arc. The revised Boltzmann Plot technique, used in determination of central axis temperature, is suitable for spatially unstable arc discharges and pulsating arcs.

Whenever there is a curvature in the current path caused by a kink [Figure 4.2], magnetic field lines are more concentrated towards the center of the curvature. This makes the magnetic field inside curvature (B_{in}) greater than that (B_{out}) outside. Corresponding magnetic pressures may be expressed as:

$$P_{Bin} = \frac{B_{in}^2}{2\mu_0} \tag{4.8}$$

$$P_{Bout} = \frac{B_{out}^2}{2\mu_0} \tag{4.9}$$

μ_0 is the permeability of the medium. Naturally, P_{Bout} is less than P_{Bin}, which leads to development of magnetic pressure gradient in radially out ward direction as shown in Figure 4.2. Higher the degree of curvature, greater is the driving force. This is how "kink induced magnetic pressure driven flow" arises in the present case. It is very obvious, that this phenomenon may happen with any magnitude of current whenever there is a curvature in the current path in the medium.

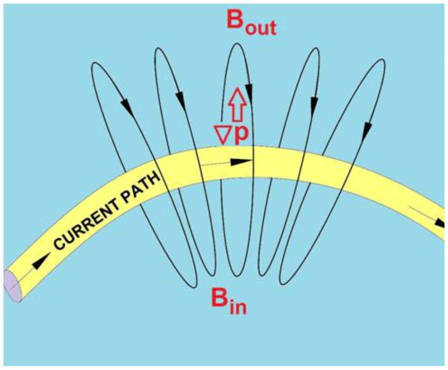

Figure 4.2 Schematic diagram showing kink induced magnetic pressure driven flow.

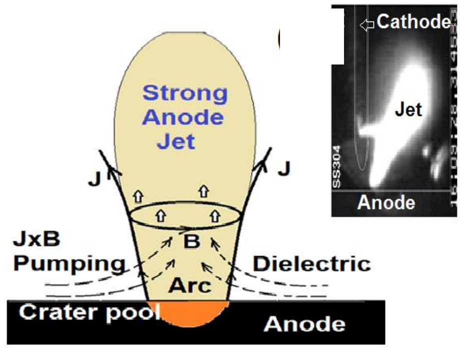

Figure 4.3 Depiction of mechanism of JXB pumping for removal of anode material [24] and image captured by fast camera (inset) as a combined effect of JXB pumping and kink.

Through numerous observations in the fast photographic study, one phenomenon is found common with all anode materials: flow in the form of an expanding jet [Figure 4.3] and images in [Figure 4.3-Figure 4.8]. This is a very significant phenomenon and not considered in any of the earlier theoretical or experimental studies in this context.

Nevertheless, this particular phenomenon is actually well discussed in thermal plasma literature [24] and termed as 'J×B' pumping. When associated current lines in a conducting medium arrange in a vertically diverging configurations Figure 4.3, the magnetic field at the top is less compared to the same at the bottom (inversely proportional to the radius of the column). Similarly, the current density (J) is also less at the top compared to the same at the bottom (due to larger area of cross-section at the top). As a result, net JxB body force at the top (F_{Btop}) is less compared to the same at the bottom ($F_{Bbottom}$). Therefore, net pressure (P_{top}) in the upper region is the sum of plasma pressure (nk_BT) and contribution due to F_{Btop}. The same (P_{bottom}) in the bottom region is the sum of plasma pressure (nk_BT) and contribution due to $F_{Bbottom}$. Obviously P_{top} is less than P_{bottom}. In such a situation, a gradient in pressure develops in the vertically upward direction:

$$\nabla p \quad \infty \quad (P_{top} - P_{bottom}) \tag{4.10}$$

This is the root cause of formation of an expanding plasma jet propagating in the upward direction. Since, associated flow is driven by gradient in pressure and not absolute pressure, even a slightest gradient in the pressure may induce such flow. It may also be noted that the phenomenon may happen with any nonzero current, provided the current configurations is able to produce a pressure difference.

Notably, the captured images of the jet are always found to be slightly inclined with respect to vertical [Figure 4.3]. This is expected if we consider the curvature of the arc path and register the effect of kink induced magnetic pressure driven force acting in radially outward direction [Figure 4.2].

As far as removal of material from the anode piece is concerned, this has potential to play a very dominant role. It has immense importance in theoretical modelling as well as experimental understanding of the material removal mechanisms involved. In our opinion, this is a phenomenon of high impact, missed by the community for long time.

For different anode materials, emission spectra from the discharge were different due to ionic and atomic contribution to the plasma specific to that anode material. However, since water is used as dielectric in all the cases, H_α emission line, contributed by dielectric water was observed in all. Most of the necessary spectroscopic data like transition energy levels, degeneracy, transition probability, and wavelength have been taken from NIST database [25], except for Zr-II lines. Other than wavelength information, no other spectroscopic data is available in NIST data base for Zr-II. Necessary data have been obtained from Ref. [26].

4.3 Fast photographic study

4.3.1 Discharge with P91

Snapshots of the discharge kinetics observed with P91 as anode are presented in Figure 4.4. Three important features, namely, kink instability [27], sausage instability [27] and J×B pumping [24] are clearly observed. The kink in Figure 4.4 (a) and Figure 4.4 (e) embodies higher magnetic field in the concave side compared to the same in the convex side. Resulting difference in magnetic pressure ($B^2/2\mu_0$) causes a strong mass flow across the arc in radially outward direction as observed (here μ_0 is Permittivity of free space). Once the flow detaches from the arc, typical movement of the plasma bubble is captured in Figure 4.4 (f). Figure 4.4(b) and Figure 4.4 (c) present observed mass flow related to J×B pumping effect, discussed above. Material from the arc root region flows like an intense expanding jet in the vertically upward direction. On its way, it interacts with the kink induced magnetic pressure driven force and finally chooses a resultant path slightly inclined with the vertical. The interaction zone and the point of deflections are identifiable.

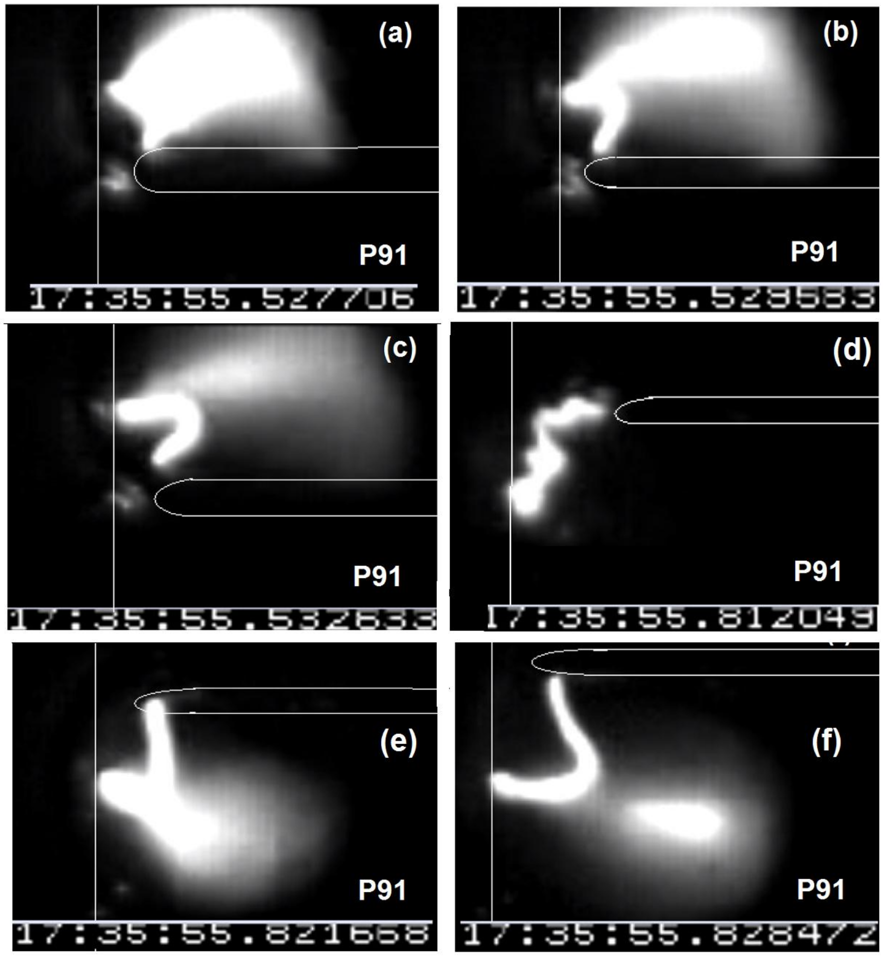

Figure 4.4 Observed evolution of arcs in underwater EDM discharges with P91 as anode material (The cathode is not visible. Approximate location of the cathode (finger shaped) and anode (vertical line) are sketched (a-f).

Due to intensive cooling by the dielectric, the plasma channel becomes thin and current density becomes extremely high. Associated pinching effect leads to interesting sausage type instabilities in the arc as observed in Figure 4.4(d). It may be emphasized that this transient phenomenon is observed in the zone of dielectric media (water), where temperature is much lower compared to the same in the main arcing zone. The thin filamentary arc transiently passes through such colder zone making it further thinner through thermal pinching. While there exists lots of ambiguities about diameter of EDM arc channel [28], present observation indicates that it is thin enough to make self-pinching force greater than the force exerted by plasma pressure, a requirement for sausage type instability to occur. The fast photographic images are the direct proofs that such phenomena happen. An estimate of the maximum possible radius of the plasma channel compatible with the flowing current as following:

The magnetic field produced by a plasma column of radius R (carrying current I) at its edges may be written as:

$$B_R = \frac{\mu_0}{4\pi} \cdot \frac{2I}{R} \tag{4.11}$$

For initiation of sausage type instability, the magnetic pressure must be comparable with the plasma pressure. If this happens for a maximum arc channel radius of say R_{max}, one obtains:

$$\frac{B_{R\max}^2}{2\mu_0} = nk_B T \tag{4.12}$$

Where, n, k_B and T are respectively number density, Boltzmann constant and temperature.

This gives:

$$R_{\max} = \sqrt{\frac{\mu_0}{4\pi} \cdot \frac{1}{2\pi n k_B T}} . I \tag{4.13}$$

For P91, estimated number density and plasma temperature [see table 4-1] give R_{max} around 1.5 μm for an arc current of 2A. This is an important outcome of the study, giving a direct estimate of arc channel radius in EDM discharge with water as dielectric.

Table 4-1 Details of the Hα lines for discharges with different anode material and derived quantities

Sl. No.	Anode material	Position of H_α line (nm)	Wavelength shift (nm) from 656.28 nm	$\Delta\lambda_O$ (nm)	$\Delta\lambda_S$ (nm)	Electron density ($x10^{24}/m^3$)	Temperature (K)	Coupling parameter (Γ)
1	P91	658.5	2.22	1.2	1.15	0.297	8159	0.22
2	Zr	658.2	1.92	1.4	1.35	0.376	14525	0.13
3	SS304	656.45	0.15	0.35	0.30	0.041	6151	0.15
4	Cu	661.0	4.72	1.95	1.90	0.621	10534	0.22

4.3.2 Discharge with SS304

Discharge kinetics with SS304 as anode is presented in Figure 4.5(a) to Figure 4.5(f).

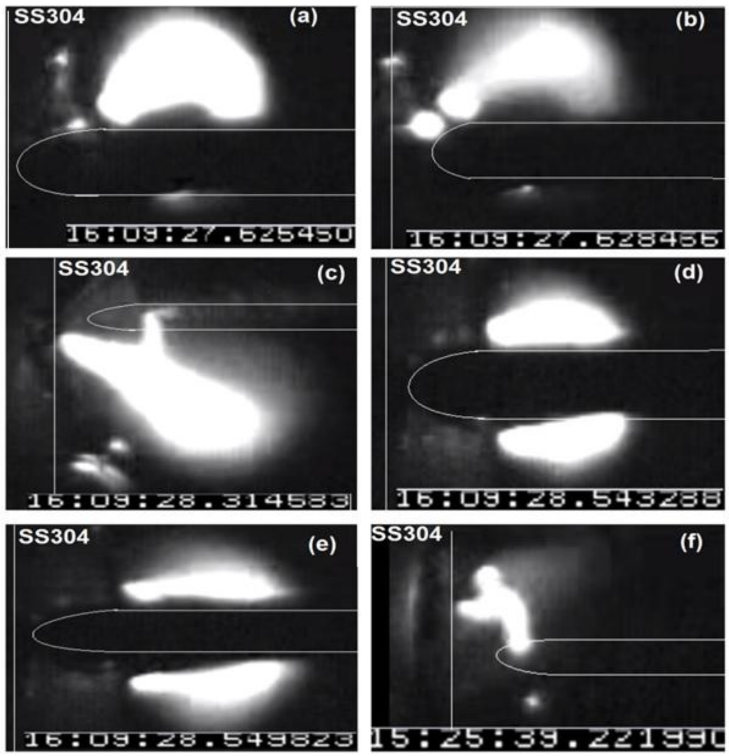

Figure 4.5 (a-f) Evolution of arcs in underwater EDM discharges with SS304 as anode material. Approximate location of the cathode (finger shaped) and anode (vertical line) are sketched.

Together with J×B pumping and kink effect, existence of multiple simultaneous arc connections over the anode are the special features in this. In Figure 4.5 (a) it is observed that the kink induced high magnetic pressure shifts the connection of the arc over the cathode upward along its length. The discharge is no more between the tip of the cathode and the point over the anode, exactly below the tip. It has been observed that although in different magnitude, depending on cases, the magnetic pressure has potential to shift the connections both at cathode and anode end. In fact the movement of the anode arc root leaves traces over the anode piece. In Figure 4.5 (b) two simultaneous arc spots are observed. Removal of material from the other spot through J×B pumping and anode jet formation is clearly observed. In Figure 4.5 (c) the shape of the anode jet under combined influence of kink effect and J×B pumping is clearly observed. Off the tip connection of the arc over the cathode is noted. The arc always tries to maintain its minimum voltage configuration, achieved at its minimum length. On the other hand, the kink induced pressure force and J×B pumping force tries to deform it from its minimum voltage configuration. The competition among these forces is visible in Figure 4.5 (c). In Figure 4.5 (d), two simultaneous arc spots over the anode and their different off the tip connections on the cathode are seen. It appears that the kink induced pressure keeps on shifting the cathode connection upward till total voltage drop across the length of the arc becomes no more sustainable by the power supply and the arc goes off. Figure 4.5 (d) and Figure 4.5(e) captures such events just before extinction. In Figure 4.5 (f) an interesting event is captured where there are two connections over the anode and only one connection on the cathode. Possibly two individual arcs, existing earlier with separate connections over the cathode have been merged together at the cathode end during evolution driven by the instabilities. It may be pointed out that most of the time the discharge event starts at the location over the anode, nearest to the cathode tip. Developed instability might have driven the arc to the other locations later. Due to limitation in the frame rate, the fast camera was unable to capture all events and recorded only those physical states during evolution as received by the camera at the instant of the snaps taken, marked on each frame.

4.3.3 Discharge with Copper

Typical features observed in the EDM discharges with copper as anode are presented in Figure 4.6 (a) - Figure 4.6 (d).

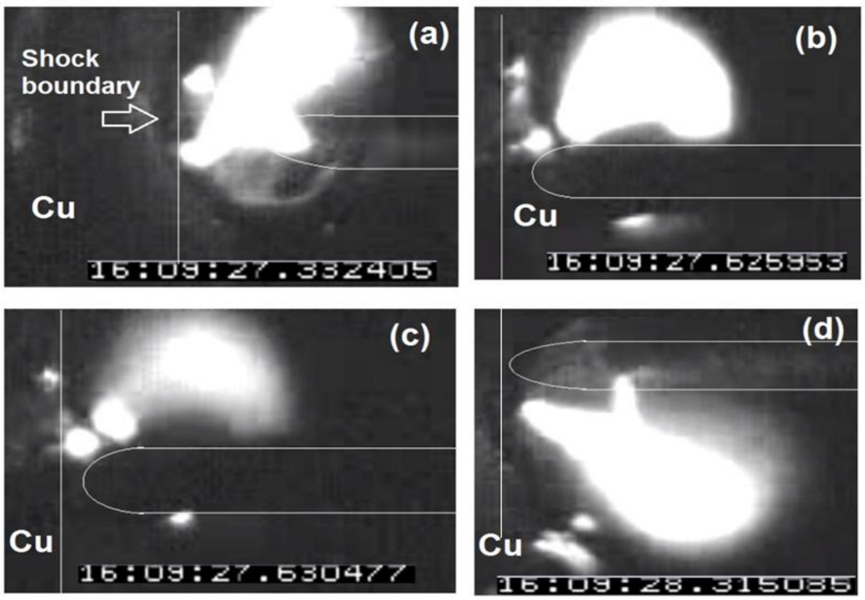

Figure 4.6(a-d) Evolution of arcs in underwater EDM discharges with copper as anode material. Approximate location of the cathode (finger shaped) and anode (vertical line) are sketched.

Figure 4.6 (a) shows clearly visible shock boundaries as well as prominent anode jet under combined influence of J×B pumping and kink induced magnetic pressure. Movement of the arc connection over the cathode driven by magnetic pressure is captured in Figure 4.6 (b). Dual arc spots over the anode and movement of debris in the form of plasma blob, detached from the anode jet are seen in Figure 4.6 (c). Formation of anode jet in similar fashion as in Figure 4.6 (c) with off the tip arc connection over the cathode is observed in Figure 4.6 (d). It may be pointed out that unlike earlier two cases, observation of very prominent shock boundaries indicates occurrence of much higher temperature in this case compared to the earlier cases. Spectroscopic study presented in the next section also supports this fact well. Typical propagation of the shock fronts, captured with vivid details at different stages of the arc discharge, are presented in Figure 4.7 (a)-(d). Bubbles, acting as scattering centers are encircled in Figure 4.7 (b), (c) and (d). Applying built in digital intensity reduction facility in the camera, only shock fronts and very high intensity arc zones are visible in Figure 4.7 (a) and bubbles (low intensity scattering centers) are invisible.

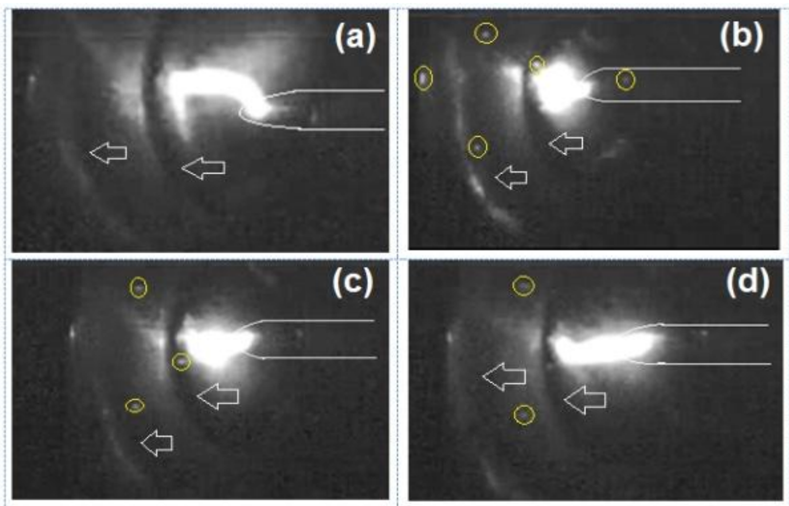

Figure 4.7 Details of the observed shock fronts captured in different discharge events. Bubbles, acting as scattering centers are encircled in (b), (c) and (d). Applying built in digital intensity reduction facility in the camera, only shock fronts and very high intensity arc zones are visible in (a) and bubbles (low intensity scattering centers) are visible. [Possible locations of the cathode are sketched].

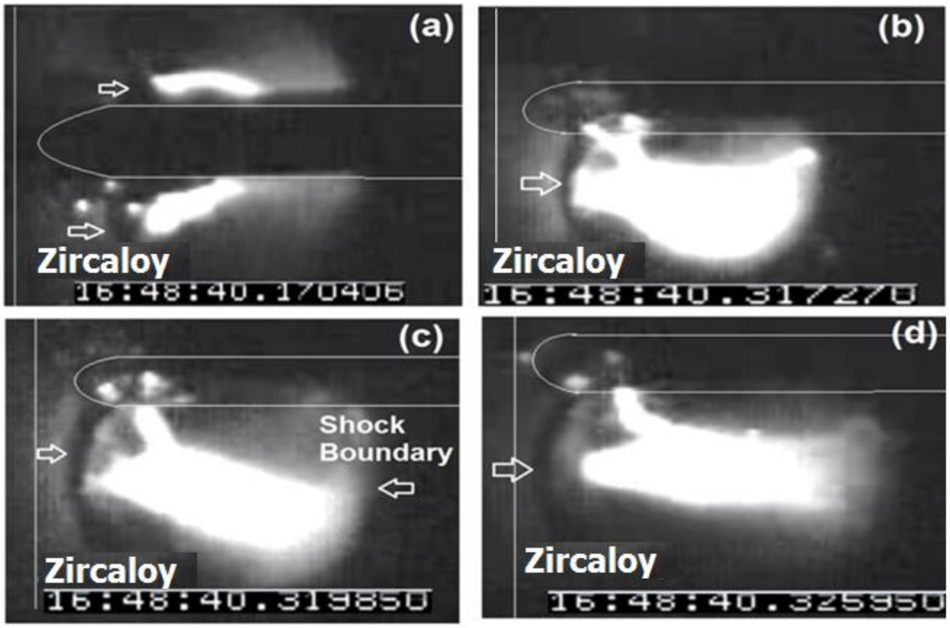

Figure 4.8(a-d) Evolution of arcs in underwater EDM discharges with zircaloy as anode material. Arrows indicate prominent shock boundaries. Approximate location of the cathode (finger shaped) and anode (vertical line) are sketched.

4.3.4 Discharge with zircaloy

EDM discharge with zircaloy as anode material exhibits features substantially different from the earlier three. In all frames highly prominent shock boundaries, indicative of occurrence of high temperature, have been observed. The fact is also supported by the spectroscopic measurements, presented in the later part of this study. Existence of two simultaneous arcs is observed in Figure 4.8(a). Emerging strong anode jet via J×B pumping and interesting multiple simultaneous connections of arc over the cathode are seen in Figure 4.8(b). Strong anode jets under combined influence of kink induced magnetic pressure and J×B pumping are seen in Figure 4.8(c) and Figure 4.8(d) as well.

4.4 Emission spectroscopic study

For EDM spectra with different anode materials, a wide spectral range is scanned initially using low resolution grating (300 lines/mm) for gross identification of location of the peaks and then focused in the region of interest using high resolution grating (1200 lines/mm or 2400 lines/mm) to obtain accurate details. Parts of the spectra, used in determination of temperature for discharge with different anode material, are presented in Figure 4.9. It has been observed that none of these spectra shows presence of H_β line while presence of H_α line is observed in every spectrum. Relatively low temperature (~eV) and high density, observed as characteristic feature of EDM arc discharges are identified as the primary reason for strong Stark broadening of the $H\alpha$ line (656.285nm) and vanishing of the H_β line (486.127nm).

After a thorough scrutiny of the recorded lines over a wide range of wavelengths and study of their appearance in the overall spectra, relevant regions of the respective spectra have been chosen for determination of axial temperature. The following aspects have been kept in consideration while choosing the lines in each case: (i) the lines must be well resolved, (ii) the lines must have appreciable intensities (iii) number of suitable lines in the chosen range must be four or greater (iv) The wavelength range within which the lines occur, must be short so that effect of absorption if any remains nearly identical for all the wavelengths considered (v) the energy levels corresponding to the considered lines should not involve ground state. The last requirement follows from Partial Local Thermodynamic Equilibrium (PLTE), discussed in the later part of this section. As presented in Figure 4.9, the considered wavelength range is 40 nm or less in all the cases. Numbers of lines available for Boltzmann plot are 7, 5, 7 and 7 for Zr, Cu, P91 and SS304 respectively. Exhibited high linearity in the Boltzmann plots [Figure 4.10 (a-f)] ensures PLTE.

Although Fe is the major constituent of both P91 and SS304, content of Cr in SS304 is 19% while that in P91 is only 9%. SS304 does not include Mo while P91 includes 1% Mo. Although both have Fe lines, influence of Cr and Mo makes the overall emission spectra from P91 and SS304 slightly different as may be clearly noticed from the spectra presented in Figure 4.9. In this study, the same Fe lines of 407.36 nm and 407.174nm have been used in the Boltzmann plots of both P91 and SS304. However, other five lines have been chosen different based on the criteria mentioned.

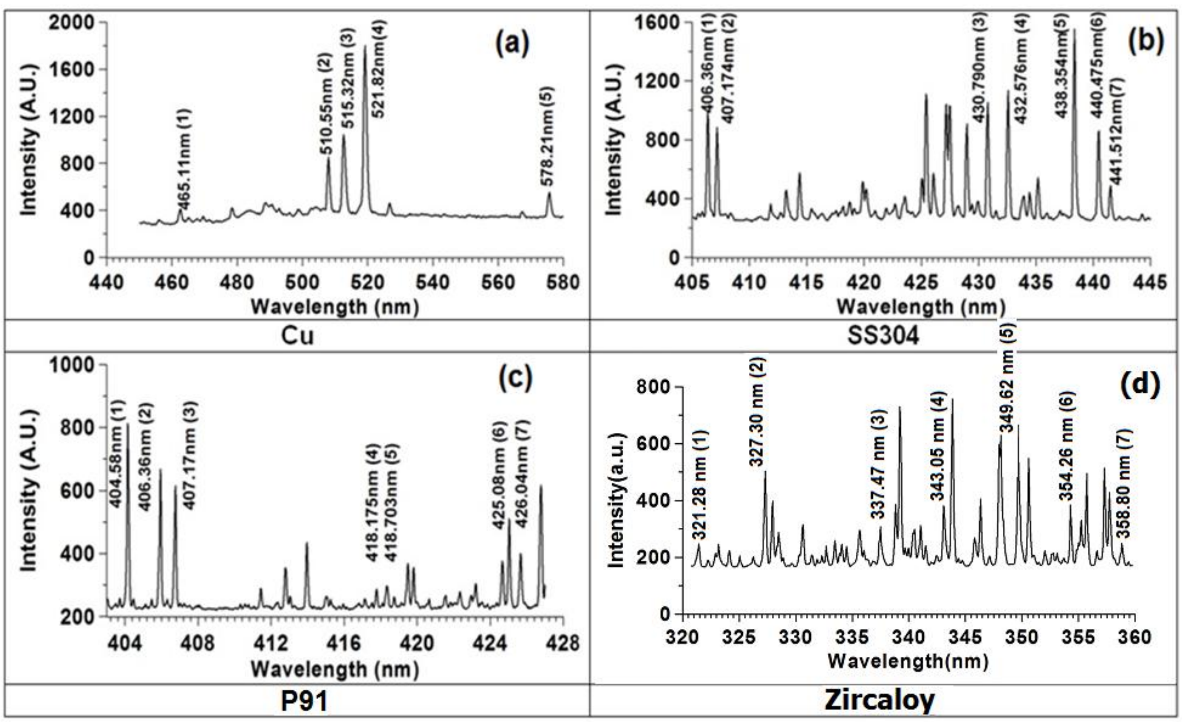

Figure 4.9 Spectra recorded during EDM discharge with different anode materials: (a) Cu (b) SS304 (c) P91 (d) Zircaloy.

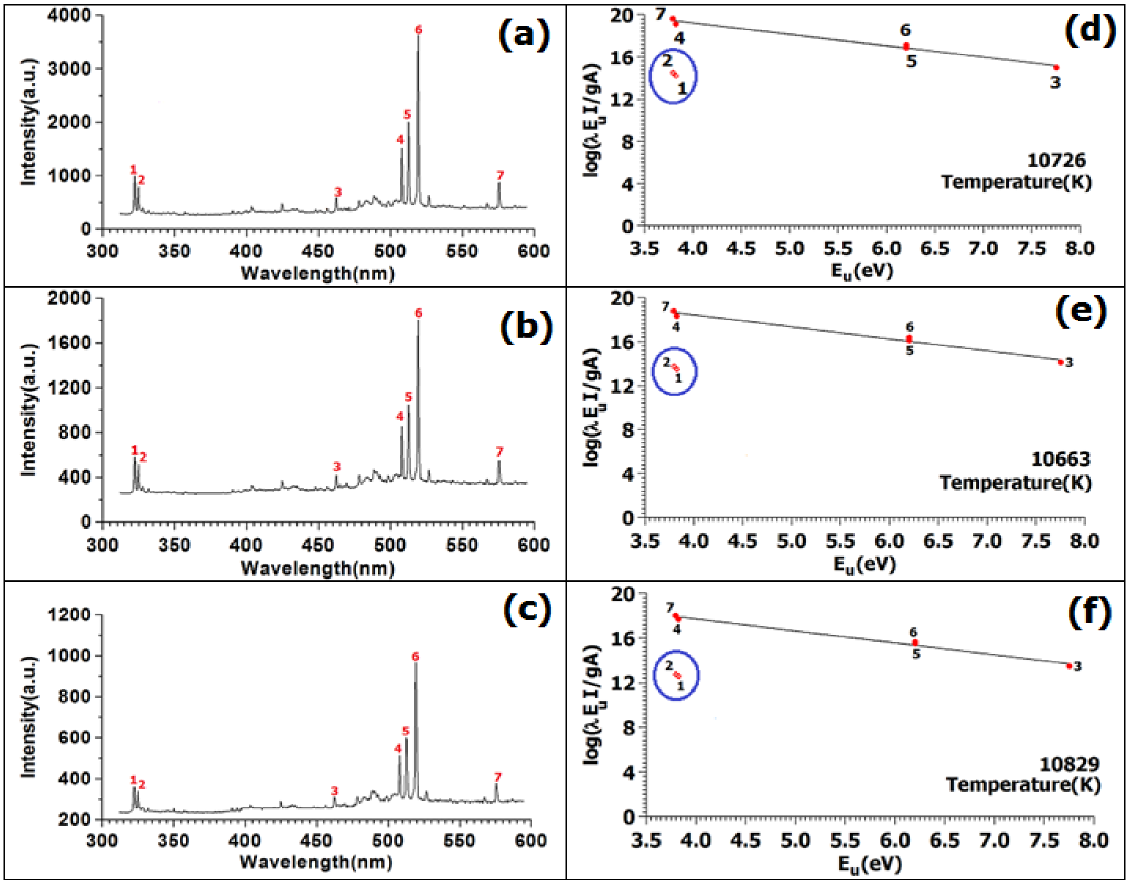

Figure 4.10 (a)-(c):Copper emission lines recorded from EDM discharge at three different instances [Table-4.1]; (d) –(f) Corresponding Boltzmann plots indicating deviation from LTE for the line 1 and 2 (324.75 nm and 327.4 nm, circled) involving ground state.

When a system is in thermal equilibrium, various energy levels are populated according to Boltzmann distribution. Under such condition, the intensity (I_{ui}) of radiation of wavelength (λ_{ui}) due to transition from level 'u' to 'i' follows the relation [29]

$$ln\left(\frac{I_{ui}\lambda_{ui}}{g_u A_{ui}}\right) = -\frac{E_u}{k_B T} + C \qquad (4.14)$$

Where, k_B is the Boltzmann constant, A_{ui} is the 'transition probability' for the specific transition. E_u and g_u are the excitation energy and statistical weight factors of the upper level 'u'. It is obvious from equation (4.14) that at a given temperature 'T', a plot of $\ln\left(I_{ui}\lambda_{ui}/g_u A_{ui}\right)$ along vertical axis and E_u along horizontal axis for different λ_{ui} will result in a straight line, and the excitation temperature 'T' can be determined from the slope of the straight line. The method of extracting temperature is known as Boltzmann plot technique.

While it is common in the literature to use equation (4.14) in determination of plasma temperature, the formula cannot give correct axial temperature for inhomogeneous axi-symmetric plasmas without performing the Abel inversion, in the case of spatially integrated line intensity measurements. The complexity in determination of temperature in welding arcs due to sharp temperature gradient, temporally unstable nature of the arc and absorption of radiation in the colder layer has been discussed by Uhrlandt [30]. In the present study, we have used a formula suitable for finding the central axis temperatures in inhomogeneous, axisymmetric, optically thin, LTE plasmas having strong gradient Gaussian temperature profile [31]. Specialty of this method is that it avoids the necessity of Abel inversion. Due to its integral features, it is well suited for rapid monitoring of spatially unstable arc discharges and pulsating arcs [31]. Experimentally, the error found in the determination of the central axis temperature of a high current arc in argon using this method and the Abel inversion technique did not exceed 1.5% [31]. The method can give better axial temperature in the case of LTE violation compared to Abel inversion as inaccuracies in the measurements at the edges of the plasma column (where non-LTE prevails) propagate to the central axis temperature in the later case. Limitation of this method is that it gives only the value of axial temperature and cannot find the radial profile.

The formula used in the present study differs from the usual expression (4.14) only in the logarithmic part and may be expressed as [31]:

$$ln\left(\frac{I_{ui}E_u\lambda_{ui}}{g_uA_{ui}}\right) = -\frac{E_u}{k_BT} + C \qquad (4.15)$$

Axial temperature is determined from the slope of the linear plot similar to (4.14).

Experimentally, the collection optics focused the region of shortest distance between the cathode tip and the planer anode (few tens of micrometers). Once a pulse is applied, the arc initiates in this region in the form of a thin cylindrical plasma column of high gradient. Although, subsequent dynamics takes the arc to other spatial locations, light is collected primarily in this configuration. Steep radial gradient of the plasma column is further assisted by surrounding coolant dielectric (water). Applied method records total spatially integrated radiation line intensities over the plasma diameter and determines only the temperature at the central axis of the plasma column.

The used method relies on optically thin assumption of the chosen lines. It may be noted that the absorption of electromagnetic radiation by water in the gas phase occurs mainly in three regions: microwave (rotational transitions), infrared (vibrational transitions) and vacuum ultraviolet (electronic transitions) regions. Absorption of the chosen lines by water is negligible in the region of spectrum considered in the study (table 4-2). Spectroscopic measurements in short metal arcs through careful analysis of line profiles using Fabry-Perot interferometer revealed absence of self-absorption of atomic lines in the wavelength range considered [32,33].

It is noted from Figure 4.10that the intensities of the three Cu-I spectra [Figure 4.10 (a), (b) and (c)], recorded under three different instances with similar operating conditions, vary appreciably due to spatially unstable nature of the arc. However, the method, based on relative line intensities, gives nearly similar axial temperature each time. Good reproducibility of the observed behavior is noted from this.

Often it has been observed in laboratory plasmas that complete local thermal equilibrium (CLTE) does not hold good [29]. Sometimes, there exist few levels, which are not populated as per Boltzmann distribution due to lack of enough collisions. Apart from these levels, rest of the energy levels follow Boltzmann distribution and the system exhibits partial local thermal equilibrium (PLTE) [29].

PLTE in so-called thermal plasma is a subject of research over many decades [34-38]. Validity conditions for Complete Local Thermodynamic Equilibrium (CLTE) and PLTE of homogeneous, time-independent, and optically thin copper plasmas have been derived [35]. It has been observed that for Cu I, electron densities of $n_e > (5 \times 10^{22} - 5 \times l0^{23})\ m^{-3}$ are required for CLTE and a density $n_e > (5 \times 10^{21} - 5 \times 10^{22})\ m^{-3}$ is necessary for PLTE for electron temperatures ~ 1 eV [36]. When the electron density n_e is sufficiently large, radiative processes may be neglected compared to the collisional processes and CLTE is maintained. However, as the electron density decreases, deviations from equilibrium start in the ground state and progress to the higher excitation states [37, 47]. In arcs, depending on discharge condition, appreciable deviations from LTE have been observed in spite of high temperatures (above 20000 K) and high electron densities (up to $2 \times 10^{23}\ m^{-3}$) [38]. The electric field, providing energy for the discharge, strongly affects the free electrons of high mobility and quickly establishes a common kinetic temperature among them through collisional processes. However, if the collision rates between electrons and heavy particles are not high enough, the situation may lead to deviations from the Boltzmann distribution. The ground state is separated from all excited states by a relatively large energy gap. Since the inelastic cross section for collisions with electrons is significantly lower for the ground state than for the excited states, a deviation in the Boltzmann distribution between the ground state and the excited states creeps in [38]. Nevertheless, the Boltzmann plot technique can still be used to determine temperature using the emission lines not involving ground states, as the method employs ratio of line intensities in which the under population factor of the excited states, if any, mostly cancels out [38].

Typical spectra observed in different EDM discharge systems are presented in Figure 4.9 (a), (b), (c). Considered emission lines and associated energy levels are mentioned in table 4-3. As presented in the later part of this section, the excitation temperature is estimated to be around 1 eV and the measured electron density is around 6.2 x 1023 m-3 (for copper, see table 4-1). According to previous studies [34, 37], the system is expected to be close to CLTE. For verification, we focus on the Cu I emission spectra recorded from the EDM plasma at three different instances with identical operating conditions [Figure 4.10 (a),(b),(c)]. We note from table 4-3, that the emission lines at 324.75 nm (line-1) and 327.4 nm (line-2) associate transitions involving ground states. Rests of the considered lines do not associate ground state (table 4-3). Figure 4.10 (d),(e) and (f) represent the Boltzmann plots corresponding to spectra of Figure 4.10.(a), (b) and (c) respectively. If the system is in CLTE, a perfectly linear plot is expected for all the lines. Interestingly, it is observed in all the plots that line-1 and line-2 consistently stays off the straight line followed by other emission lines [Figure 4.10 (d), (e) and (f)]. This supports existence of PLTE in the system.

Table 4-2 Spectroscopic parameters for the emission lines used in temperature determination using Boltzmann plot technique

Line No	λ(nm)	E_k(cm^{-1}) (upper)	g	A ($10^{-8}s^{-1}$)	Ref.	Line No	λ(nm)	E_k(cm^{-1}) (upper)	g	A ($10^{-8}s^{-1}$)	Ref.
Cu (Cu-I lines)					[25]	Zircaloy (Zr-II lines)					[26]
1	465.11	62403	8	.380		1.	321.28	36869	6	0.28	
2	510.55	30784	4	.020		2.	327.3	31866	10	1.2	
3	515.32	49935	4	.600		3.	337.47	37682	4	1.2	
4	521.82	49942	6	.750		4.	343.05	32899	8	0.5	
5	578.21	30535	2	.0165		5.	349.62	28909	8	1.2	
						6.	354.26	42410	12	1.2	
						7.	358.79	30435	4	0.13	
SS304 (Fe-I lines)					[25]	P91 (Fe-I lines)					[25]
1	406.36	37163	7	.69		1	404.58	36686	9	.75	
2	407.17	37521	5	.80		2	406.36	37163	7	.69	
3	430.79	35768	10	.34		3	407.17	37521	5	.80	
4	432.57	36079	7	.52		4	418.17	46745	7	.23	
5	438.35	34782	11	.50		5	418.70	43633	5	.21	
6	440.47	35257	9	.28		6	425.08	36079	7	.10	
7	441.51	35612	7	.12		7	426.04	42816	11	.39	

Table 4-3 Different emission lines and associated energy levels

Cu I				SS304 (Fe-I)			
Sl.	Wavelength (nm)	Upper level energy (eV)	Lower level energy (eV)	Sl.	Wavelength (nm)	Upper level energy (eV)	Lower level energy (eV)
	324.75	3.82	0		4063.6	4.61	1.56
	327.40	3.79	0		4071.74	4.66	1.60
	465.11	7.75	5.08		4307.9	4.44	1.56
	510.55	3.82	1.39		4325.76	4.48	1.61
	515.32	6.20	3.79		4383.54	4.32	1.49
	521.82	6.20	3.82		4404.75	4.37	1.56
	578.21	3.79	1.64		4415.12	4.42	1.61
Zr II				P91 (Fe-I)			
Sl.	Wavelength (nm)	Upper level energy (eV)	Lower level energy (eV)	Sl.	Wavelength (nm)	Upper level energy (eV)	Lower level energy (eV)
1	321.28	4.58	0.71	1	404.58	4.55	1.48
2	327.3	3.95	0.16	2	406.36	4.61	1.56
3	337.47	4.67	1.00	3	407.17	4.65	1.68
4	343.05	4.08	0.46	4	418.17	5.80	2.83
5.	349.62	3.58	0.04	5	418.70	5.41	2.45
6.	354.26	5.26	1.76	6.	425.08	5.38	2.47
7.	358.79	3.77	0.32	7.	426.04	5.31	2.40

As observed from table 4-2 and table 4-3, the temperature is estimated in each discharge system excluding the lines having transition involving ground states. To avoid error in the intensity estimation, we have excluded the lines, which are not well resolved and the lines having very low intensities. Typical Boltzmann plots obtained for different anode materials are presented in Figure 4.11 (a-d). Observed good linearity in the plots ensures PLTE among the levels considered. Average axial temperature is determined from independent measurements using the same set of emission lines. Typical scatters in the measured axial temperatures are indicated by the associated error bars in Figure 4.12. Different transition lines considered in the study for different anode materials and relevant spectroscopic parameters are listed in table 4-2. Figure 4.12 presents the axial temperatures of the plasma estimated in discharges with different anodes. Application of Boltzmann Plot method to the spectra received from discharge with SS304 anode gives an average axial temperature of 6151K. Similarly, obtained average axial temperatures with P91 and Cu anodes are respectively 8159K and 10534 K. However, for zircaloy observed emission was found to be radically different. Unlike the previous three cases where emission lines were primarily from atomic transitions (Fe-I or Cu-I), most of the intense emission lines from discharge with zircaloy anode are found to be from singly ionized Zr (Zr-II). Since first ionization potential (I_P) of Cu, Fe and Zr are close to each other ($I_{P(Cu)}$=7.7 eV, $I_{P(Fe)}$= 7.9eV, $I_{P(Zr)}$ = 6.6 eV), this itself is indicative of existence of higher temperature in the discharge with zircaloy as anode. Slightly lower ionization potential of Zr might have contributed as well to this effect. Estimated average axial temperature from Boltzmann plot using Zr-II lines is found to be 14525K. It is noted that under similar operating conditions, estimated temperature of the discharge zone with zircaloy as anode is substantially higher compared that for others. The observation is supported by other evidences like pronounced shock boundaries in Figure 4.8 and presence of ionic lines of Zr Figure 4.9(d). The error bars in Figure 4.12give observed scatter in the respective data due to uncertainties in the measurement. Under a given operating condition with a specific anode, temperatures determined from independent measurements were found to be close to each other (refer Figure 4.12).

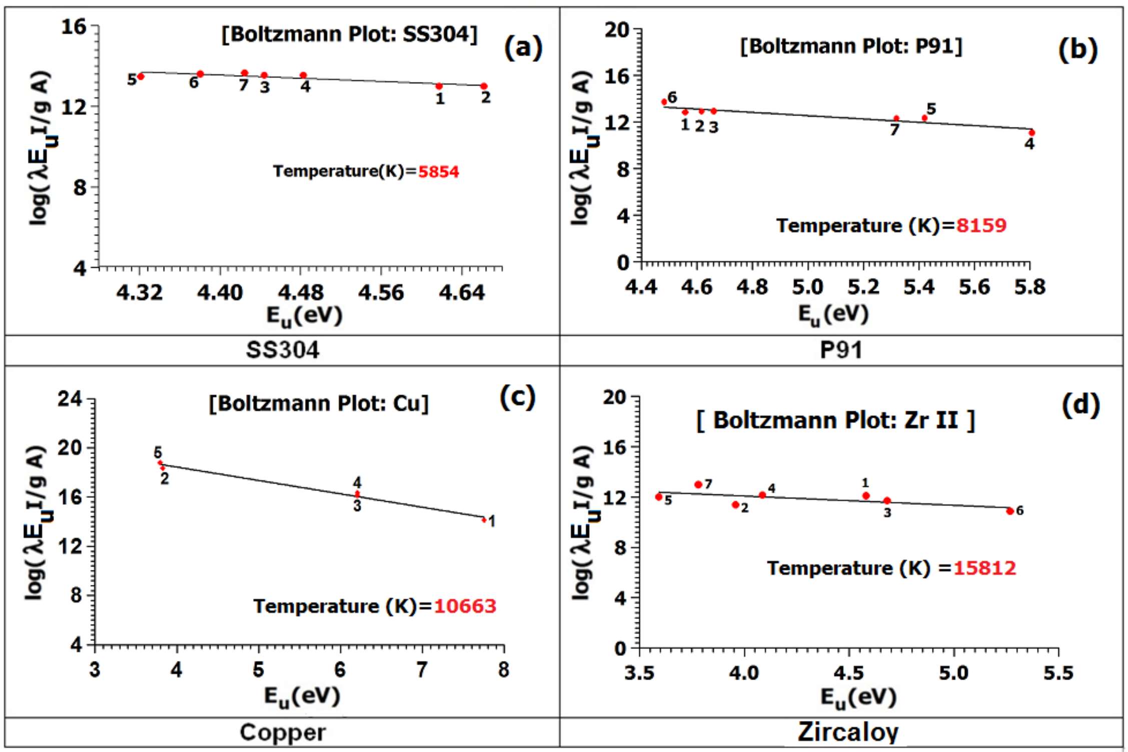

Figure 4.11 Typical Boltzmann plot obtained for discharges with anode material (a) SS304 (b) P91 (c) copper and (d) Zircaloy [Number attached to data point indicates respective line number in Table 4-2].

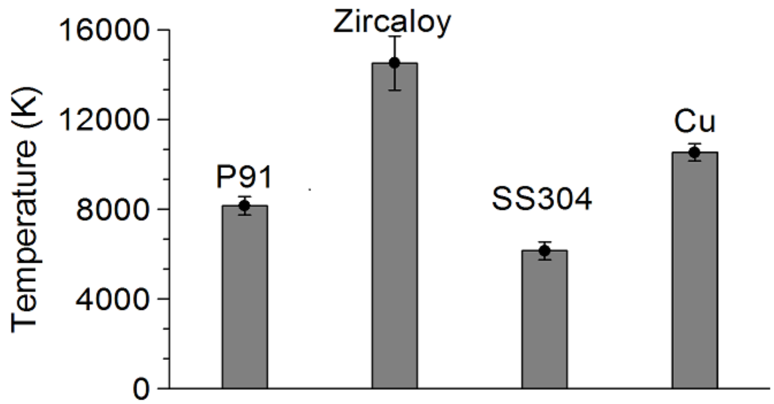

Figure 4.12 Temperatures as obtained from Boltzmann plot for discharges with different anode materials. [Bars indicates the typical scatter in the data, estimated over independent measurements].

It has been observed that under similar discharge parameters the temperature of the plasma depends significantly on the specific type of the anode material used. Constriction in the arc root region, determining the local current density and hence ohmic heating and intensity of ablation of the anode material, depends on the specific anode material used. On the other hand, density of ablated material in the plasma substantially influences its thermodynamic and transport properties including electrical conductivity and hence volumetric heat generation inside the plasma column. Notably, under similar discharge parameters, the spectra recorded at different instances with same anode material result in nearly similar axial temperatures within the error limits (See Figure 4.12, for example). Although interesting variations are observed, typical electron temperature observed in the study is low (~ eV). This is consistent with the reported observations in similar plasmas discussed in the introduction part. High density of the EDM plasma results in rapid loss of energy of the electrons through collision, leading to low electron temperature. However, due to high density of plasma, high frequency of collision among electron, neutral and charged species thermalize them and all the species are expected to have nearly the same temperature.

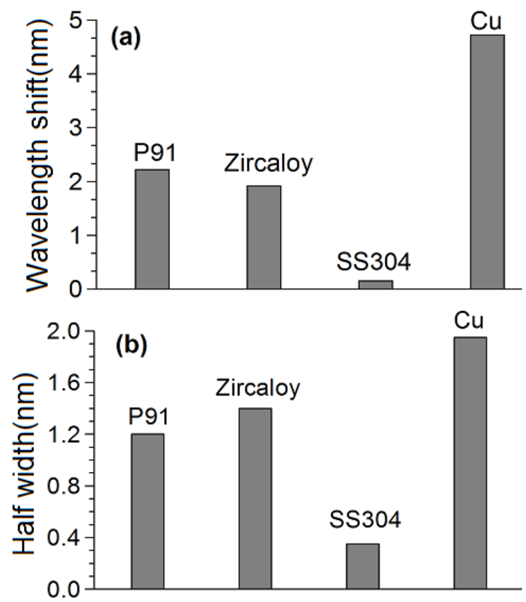

Figure 4.13 (a) Shift in wavelength and (b) Lorentzian half widths of Hα lines for discharge with different anode materials.

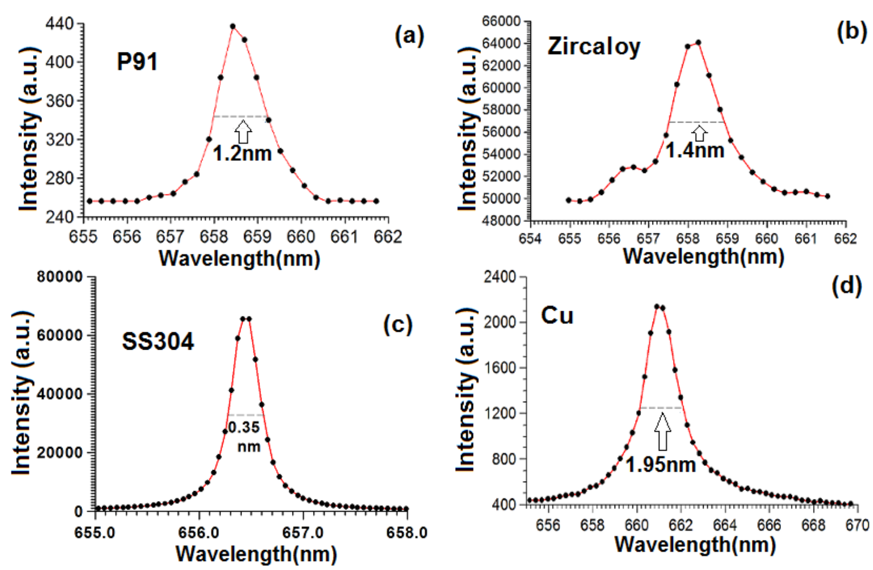

Figure 4.14 Recorded Hα line profiles: (a) P91 (b) Zircaloy (c) SS304 and (d) Copper.

Depending on density of electron and temperature, acceleration of the electrons by the ion field (AEIF) and contribution due to dipole ionic-electronic shift (DIES) results in a shift of the H_α peak with respect to theoretical position of the $H_\alpha$line (656.28 nm) as reported by [39] and [40]. Figure 4.13 (a) presents the measured shifts of H_α line for EDM discharges with different anode materials. Measured full width at half maxima (FWHM) of the Lorentzian profile of the H_α line for different anode material are presented in Figure 4.13 (b). Recorded H_α line profiles for different anode materials are presented in Figure 4.14. Numbers of theoretical and experimental studies on stark broadening and shift of the H_α line, mainly dealing with estimation of electron density and origin of the shift, are available in literature. Recently, advanced calculations including the effects of ion dynamics in the estimation of electron densities have been reported. Half width ($\Delta\lambda$) of the Lorenzian profile of the H_α lines is related to the number (N_e) of electrons per m^3 as [40, 41]

$$\Delta\lambda_{H_\alpha}(nm) = 0.549 \times \left(\frac{N_e}{10^{23}}\right)^{0.67965} \tag{4.16}$$

It is observed that the obtained line profiles are predominantly Lorentzian in shape. Broadening of a spectral line primarily occurs from several factors: natural broadening caused by finite lifetime of excited states, Doppler broadening due to the movement of the emitting atoms, instrumental broadening due to diffraction effect of slit and Stark broadening due to presence of randomly oriented electric fields around the emitting atoms. Doppler broadening results in a Gaussian shape and rest of the broadening mechanisms result in Lorentzian shape of the line profile. While predominant Lorentzian shape of the lines indicates negligible Doppler broadening in the present case, its contribution to the total width at a given temperature T can be approximated for an emitted line of central wavelength λ_o as [29]:

$$\Delta\lambda_D = \sqrt{\frac{8k_B T ln2}{mc^2}}\lambda_0 \tag{4.17}$$

k_B is the Boltzmann constant, m is the mass of emitting atom, c is speed of light. Doppler contribution in the width of $H_\alpha$line (λ_o =656.28 nm), estimated from the above formula, comes to be less than 0.04 nm for temperature less than 8000K. It will be further less at lower temperatures. On the other hand, typical value of natural broadening is very less and is of the order of 0.01 pm [29, 47]. It is several orders of magnitude lower than the broadening observed in the present study (Figure 4.14 (a-d)).

An upper limit of the instrumental broadening is obtained in the study from the Lorentzian fit of the recorded line shape (Figure 4.15) of a monochromatic light (632.8 nm line of He-Ne laser) [42]. As observed, instrumental broadening in the present setup is around 0.05 nm.

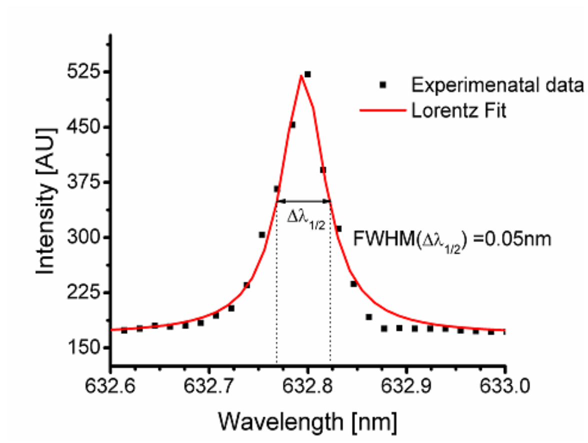

Figure 4.15 Estimation of instrumental broadening: line shape recorded by the spectrograph for monochromatic 632.8 nm line of He-Ne laser giving full width at half maximum (FWHM) ~0.05 nm.

Since the observed line profiles in Figure 4.14 exhibit predominantly Lorentzian shapes, the lines are primarily broadened due to Stark effect and instrumental broadening (since both have Lorentian shapes). Broadening contribution from Stark effect ($\Delta\lambda_S$) is obtained from observed total broadening ($\Delta\lambda_O$) and instrumental broadening ($\Delta\lambda_I$) as [43].The estimated electron densities for different anode materials are presented in table 4-2.

$$\Delta\lambda_s = \triangle\lambda_o - \triangle\lambda_I \tag{4.18}$$

In ideal plasma Coulomb collisions are negligible. In all other cases, where the effects of inter-particle interactions govern the plasma behavior, the plasma is considered as non-ideal. At low temperature and low densities, the particles (mixture of electrons, atoms and ions) in partially ionized plasma usually possess mean free path much greater than the average inter particle distance and the plasma behaves mostly in the ideal regime. As density increases, average inter-particle distance decreases and the particles start interacting strongly with each other via Coulomb field. When the average energy of inter-particle interaction becomes comparable with the thermal energy, the plasma is considered as truly non-ideal. In the present case, the sudden outburst of discharge produces considerably high pressure. Clearly visible shock boundaries are indicative of that. From the measured electron temperature T_e and number density n_e, non-ideality of the generated plasma can be estimated through the plasma coupling parameter Γ, defined as ratio of electrostatic Coulomb energy to the thermal energy [44]:

$$\Gamma = \frac{e^2}{4\pi\varepsilon a k_B T} \tag{4.19}$$

Where, e is the electronic charge, k_B is the Boltzmann constant and 'a' is the average inter-particle distance. 'a' can be estimated from the density (n) using the equation:

$$a = [\frac{3}{4\pi n}]^{1} \quad (4.20)$$

If Γ much less than 1, the plasma is considered ideal. If Γ is comparable to 1, the plasma is weakly non-ideal and if Γ is much greater than 1, the plasma is said to be strongly coupled. As calculated in table 4-1, the coupling parameter for different anode material is close to 1 in all the cases. Hence, the cold and dense plasma produced by EDM discharge is always weekly non-ideal plasma.

Another important effect is that the extreme density caused by the pressure exerted by the dielectric lowers the ionization energy and hence wipes out the upper energy levels in the hydrogen atoms [43]. This leads to two effects: (i) vanishing of the radiation lines involving higher lying states like H_β (486.127nm) and H_γ (434.046nm) etc and (ii) increase in the continuum radiation. Absence of H_β and H_γ in the recorded spectra supports the fact very well.

In a system containing hydrogen, if n_{max} is the quantum number of the highest energy level of the hydrogen atom for the detected transitions, then a rough estimate of the electron density in the system (n_e in cm^{-3}) may be obtained from Inglis-Teller equation as [45]:

$$\log(n_e) = 23.26 - 7.5\log(n_{max}) \quad (4.21)$$

In our case, H_α line of the Balmer series corresponding to transition from level 3 to level 2 is detected but H_β line of the same series corresponding to transition from level 4 to level 2 is not seen. Hence one can assume n_{max} within 3 and 4 in the present case, giving value of n_e~$10^{24}/m^3$. It may be noted that the value so obtained is of the same order of magnitude as obtained from the analysis of Stark broadening of H_α line.

Apart from stark broadening and shift of the line location, several other important information about the system are also obtained from the $H_\alpha$line. A scrutiny of the recorded H_α profile shape in Figure 4.14 reveals that it is not perfectly symmetric like a Lorentzian profile. Observed slight asymmetry owes its origin to the interactions between other ions present in the weakly coupled non-ideal plasma and the H_α emitting hydrogen atom.

Another important observation is that the recorded H_α profiles with most of the anode material reveal existence of tiny bumps and dips near their base. Resonant interaction between Stark splitting and the ion acoustic turbulence induced oscillating electric field may explain the observed structures [46].

4.5 Summary and conclusion

EDM process is a state of the art technology to cut and shape wide range of materials of technological interest. While it is a matured technology, developed mainly through trial-and-error approaches, understanding full potential of the technology requires a thorough scientific understanding of the processes. Hydrodynamic, electromagnetic, electro-dynamic, thermodynamic and different transport processes play vital roles in shaping the discharges involved. The present study aims at understanding the complex nonlinear processes through fast photography and emission spectroscopic signatures in discharges with different anode materials. Using a specially designed experimental rig, signature of the species in the generated plasma has been extracted using a fiber optic based spectrograph system. Presence of H_α line, but absence of H_β line in the emission spectra is an interesting observation [47]. High density, caused by the pressure exerted by the dielectric, lowers the ionization energy and hence wipes out the upper energy levels in the hydrogen atoms and vanishes the radiations like H_β involving higher lying states. For an EDM discharge with a given anode material, the emission lines, characteristic to the anode material, have been used in determining the plasma temperature using Boltzmann plot method. Width of the Stark Broadened Lorentzian profile of H_α line has been used in determining the density of electrons in the plasma. From the obtained plasma quantities, plasma coupling parameter has been estimated and it has been established that the generated plasma falls in the regime of weekly non-ideal plasma.

Temperature of EDM plasma has been found to significantly depend on the specific type of anode material used [47]. Possibly, ablated material becomes part of the plasma and substantially influences its thermodynamic and transport properties, which in turn results in their distinctive behavior observed. The temperatures of the discharge zone for iron based substances like SS304 and PL91 are found to be around 5500K and 7100K respectively. The same for copper reaches around 9048 K and that for zircaloy touches 14372K [47]. This in turn influences the dynamical behavior and evolution of the arc for each type of anode.

Dynamic evolution of the arcs has been studied using fast photographic camera. Formation of strong anode jet through J×B pumping, kink induced magnetic pressure driven flow, sausage type instability, generation of distinct shock fronts, formation of simultaneous multiple arc roots over anode as well as cathode and drift of arc roots on electrode surfaces are some of the important features observed. Physical observation of shocks and variation in its intensity with change in anode materials are possibly addressed for the first time. The information is qualitative but may serve as good first-hand information for theoretical modelling and experimental understanding. Direct observation of simultaneous multiple arc attachments over cathode as well as anode is another aspect not discussed previously in this context. All available studies are based on single electrode attachment points. The direct observation of multiple attachments may assist in more realistic modelling and better interpretation of experimental results. Observation of J×B pumping in EDM discharge is a very important phenomenon not included in any of the previous experimental or theoretical studies [47]. Kink induced magnetic pressure driven flow, directly identified through fast photography has potential to contribute significantly in relevant mass transport processes in CFD models of EDM discharge. Physical observation of plasma blob detachment process in underwater arcs may help in understanding the overall transport process. Direct observation of "sausage type instability" gives information about possible current paths, its diameter and distortion. Any distortion in the current path may induce body forces through electromagnetic interaction which must be taken into account for interpretation of results and modelling of the system. It is believed that obtained information may contribute significantly towards enhanced understanding of EDM discharges.

4.6 References

[1] Mehdi Hourmand, Ahmed AD Sarhan, and Mohd Sayuti, "Micro-electrode fabrication processes for micro-EDM drilling and milling: a state-of-the-art review",

The International Journal of Advanced Manufacturing Technology, 91 (2017): 1023-1056.

[2] W. James Robinson, Mooyoung Ham, and Ammon N. Balaster, "Ultraviolet radiation from electrical discharges in water", Journal of Applied Physics, 44 (1973): 72-75.

[3] Peter Bårmann, Stefan Kröll, and Anders Sunesson, "Spectroscopic measurements of streamer filaments in electric breakdown in a dielectric liquid", Journal of Physics D: Applied Physics, 29 (1996): 1188.

[4] O Eric Forster, "Progress in the understanding of electrical breakdown in condensed matter", Journal of Physics D: Applied Physics, 23 (1990): 1506.

[5] R. Snoeys, "Investigations of EDM operations by means of thermo mathematical models", Annals of the CIRPI, 20 (1971): 35-36.

[6] F. S. Van Dijck, and W. L. Dutre, "Heat conduction model for the calculation of the volume of molten metal in electric discharges", Journal of Physics D: Applied Physics, 7 (1974): 899-910.

[7] V. James Beck, "Large time solutions for temperatures in a semi-infinite body with a disk heat source", International Journal of Heat and Mass Transfer, 24 (1981): 155-164.

[8] V. James Beck, "Transient temperatures in a semi-infinite cylinder heated by a disk heat source", International Journal of Heat and Mass Transfer, 24 (1981): 1631-1640.

[9] Daryl D. DiBitonto, Philip T. Eubank, Mukund R. Patel, and Maria A. Barrufet, "Theoretical models of the electrical discharge machining process. I. A simple cathode erosion model", Journal of applied physics, 66 (1989): 4095-4103.

[10] Mukund R. Patel, Maria A. Barrufet, Philip T. Eubank, and Daryl D. DiBitonto, "Theoretical models of the electrical discharge machining process. II. The anode erosion model", Journal of applied physics, 66 (1989): 4104-4111.

[11] Philip T. Eubank, Mukund R. Patel, Maria A. Barrufet, and Bedri Bozkurt, "Theoretical models of the electrical discharge machining process. III. The variable mass, cylindrical plasma model", Journal of applied physics, 73 (1993): 7900-7909.

[12] P.C. Tan, and S. H. Yeo, "Modelling of overlapping craters in micro-electrical discharge machining", Journal of Physics D: Applied Physics, 41 (2008): 205302.

[13] J. Christopher Lewis, "Development of a numerical simulation tool for modeling a DCarc discharge in a liquid dielectric media. Brigham Young University", 2010.

[14] Y. B. Guo, A. Klink, and F. Klocke, "Multiscale modeling of sinking-EDM with Gaussian heat flux via user subroutine", Procedia CIRP, 6 (2013): 438-443.

[15] Tang, Jiajing, and Xiaodong Yang, "A novel thermo-hydraulic coupling model to investigate the crater formation in electrical discharge machining", Journal of Physics D: Applied Physics, 50 (2017): 365301.

[16] V. R . Adineh, Oldrich Coufal, and Milada Bartlova, "Calculation of net emission coefficient of electrical discharge machining arc plasmas in mixtures of nitrogen with graphite, copper and tungsten", Journal of Physics D: Applied Physics, 48 (2015): 405202.

[17] S. H. Yeo, W. Kurnia, and P. C. Tan, "Electro-thermal modelling of anode and cathode in micro-EDM", Journal of Physics D: Applied Physics, 40 (2007): 2513.

[18] Albinski Kazimierz, Karol Musiol, Adam Miernikiewicz, Stefan Labuz, and Marek Malota, “The temperature of a plasma used in electrical discharge machining”, Plasma Sources Science and Technology, 5, no. 4 (1996): 736.

[19] A. Descoeudres, Ch .Hollenstein, R. Demellayer and G. Wälder, “Optical emission spectroscopy of electrical discharge machining plasma”, J. Phys. D: Appl. Phys., 37(2004):875–882

[20] A. Descoeudres, Ch Hollenstein, G. Wälder, R. Demellayer, and R. Perez, “Time-and spatially-resolved characterization of electrical discharge machining plasma”, Plasma Sources Science and Technology, 17 (2008): 024008.

[21] Janakrajan Ramkumar, Nick Glumac, Shiv G. Kapoor, and Richard E. DeVor, “Characterization of plasma in micro-EDM discharge using optical spectroscopy”, Journal of Manufacturing Processes, 11 (2009): 82-87.

[22] N.I.U. Zhiwen, W. E. N. Xiaoqiong, R. E. N. Chunsheng, and Qiu Yuliang, “Measurement of temporally and spatially resolved electron density in the filament of a pulsed spark discharge in water”, Plasma Science and Technology, 18 (2016): 821.

[23] N. Tiwari, S. Bhandari, and S. Ghorui, “Stability and structures in atmospheric pressure DC non-transferred arc plasma jets of argon, nitrogen, and air”, Physics of Plasmas, 25 (2018): 072103.

[24] E. Pfender, “Energy transport in thermal plasmas”, Pure and Applied Chemistry, 52, (1980): 1773-1800.

[25] https://physics.nist.gov/PhysRefData/ASD/lines_form.html . Accessed 12 Feb 2018

[26] G. Malcheva, , K. Blagoev, R. Mayo, M. Ortiz, H. L. Xu, Sune Svanberg, Pascal Quinet, and Emile Biémont, “Radiative lifetimes and transition probabilities of

astrophysical interest in Zr II", Monthly Notices of the Royal Astronomical Society, 367 (2006): 754-762.

[27] F. Francis Chen, "Introduction to plasma physics and controlled fusion", Vol. 1. New York: Plenum press, 1984.

[28] Hamid Reza Shahri, Ramezanali Mahdavinejad, Mehdi Ashjaee, and Amir Abdullah, "A comparative investigation on temperature distribution in electric discharge machining process through analytical, numerical and experimental methods", International Journal of Machine Tools and Manufacture, 114 (2017): 35-53.

[29] R, Hans Griem, "Plasma spectroscopy in inertial confinement fusion and soft x- ray laser research", Physics of Fluids B: Plasma Physics, 4 (1992): 2346-2361.

[30] D. Uhrlandt, "Diagnostics of metal inert gas and metal active gas welding processes", Journal of Physics D: Applied Physics, 49 (2016): 313001.

[31] A. Marotta, "Determination of axial thermal plasma temperatures without Abel inversion", Journal of Physics D: Applied Physics, 27 (1994): 268.

[32] N. Vogel, Kolacinski Z (1987) Spectroscopic measurements of radial temperature distributions in short electric arcs. J. Phvs. D: Appl. Phys 20: 545-547

[33] MattiAula "Optical emission from electric arc furnaces", PhD Thesis submitted to University of Oulu, Oulu, (2016) Finland

[34] V Zhovtyanskii, V. A., K. V. Nelep, and O. M. Novik, "Recombining-plasma spectroscopy in the LTE-PLTE transition region", Journal of Applied Spectroscopy, 49 (1988): 906-911.

[35] A. Anders, S. Anders, and E. Hantzsche, "Validity conditions for complete and partial local thermodynamic equilibrium of nonhydrogenic level systems and their

application to copper vapor arcs in vacuum", IEEE Transactions on Plasma Science, 17 (1989): 653-656.

[36] M. Numano, "Criteria for local thermodynamic equilibrium distributions of populations of excited atoms in a plasma", J. Quant. Spectrosc. Radiat. Transfer, 43 (1990): 311-317

[37] G. M. W. Kroesen, D. C. Schram, C. J. Timmermans, and J. C. M. de Haas, "The energy balance of a plasma in partial local thermodynamic equilibrium", IEEE Transactions on Plasma Science 18, no. 6 (1990): 985-991.

[38] Gerrit Kühn, and Manfred Kock, "A spatially resolved relaxation method for pLTE plasma diagnostics in free-burning arcs", Journal of Physics D: Applied Physics, 39, (2006): 2401.

[39] A. Escarguel, E. Oks, J. Richou, and D. Volodko, "Highly nonlinear, sign-varying shift of hydrogen spectral lines in dense plasmas", Physical Review E 62 (2000): 2667.

[40] E. Oks, "Reduction of spectral line shifts due to the acceleration of electrons by the ion field in plasmas", Journal of Physics B: Atomic, Molecular and Optical Physics, 35 (2002): 2251.

[41] A. Macro Gigosos, Manuel Á. González, and Valentín Cardeñoso, "Computer simulated Balmer-alpha,-beta and-gamma Stark line profiles for non-equilibrium plasmas diagnostics", Spectrochimica Acta Part B: Atomic Spectroscopy, 58 (2003): 1489-1504.

[42] Lin Yang, Xiaohua Tan, Xiang Wan, Lei Chen, Dazhi Jin, Muyang Qian, and Gongping Li, "Stark broadening for diagnostics of the electron density in non-

equilibrium plasma utilizing isotope hydrogen alpha lines", Journal of Applied Physics, 115 (2014): 163106.

[43] D. M. Devia, L. V. Rodriguez-Restrepo, and E. Restrepo Parra, "Methods employed in optical emission spectroscopy analysis: a review", Ingeniería y ciencia, 11 (2015): 239-267.

[44] V. E. Fortov, and I. T. Iakubov, "Physics of Non-Ideal Plasmas Hemisphere", New York (1990).

[45] R. Do. Inglisand, E. Teller, "Ionic Depression of Series Limits in One-Electron Spectra", The Astrophysical Journal 90 (1939): 439.

[46] Y. Vitel, M. El Bezzari, T. V. Gavrilova, M. Skowronek, L. G. D'yachkov, and Yu K. Kurilenkov, "On dense hydrogen and noble gases plasma spectra", Physica B: Condensed Matter, 228 (1996): 161-165.

[47] S. Bhattacharya, N. Tiwari, A. Mishra, S. Mitra, G. K. Dey, and S. Ghorui,, "Underwater Electrical Discharges: Temperature, Density and Basic Instability Features with Different Anode Materials", Plasma Chemistry and Plasma Processing, 39 (2019): 1019-1048.

Chapter 5

Characterization of wire EDM surface and optimization of process parameters

5.1 Introduction

Advanced machining processes like laser beam, electron beam and electric discharge machining (EDM) are used for fabricating components with intricate geometry in high strength steels [1-3]. The molten material is flushed out from the melting site in the form of debris due to the collapses of the plasma channel during the off cycle [4]. Rapid extraction of the heat by the cold work piece by conduction and quenching of heat by surrounding fluid leads to rapid cooling of a thin layer of material close to the cutting face. This rapid cooling leads to re-solidification and quenching of the molten material and it forms a thin layer on the machined surface, called recast layer [5]. The morphology of the machined surface and micro-structural characteristics of the recast layer depend on the WEDM process parameters and thermo-physical properties and physical metallurgy of the material. The recast layer may contain tensile residual stresses and cracks, which are detrimental for fatigue life of the manufactured parts [6]. It has been reported that the average recast layer thickness and its standard deviation increases with increase in spark energy [7]. Below the recast layer is a heat- affected zone (HAZ) which can be composed of several different layers, depending on chemical composition of the work piece [8]. Tang and Guo have optimized the machining parameters in machining of S-03 special stainless steels [9]. They have reported the optimized combinations of process parameters for surface roughness and material removal rate as objective parameters. The recast layer and surface roughness of the machined surface increased with increase in the spark energy and peak current [10-11]. Lee [12] has reported micro cracks and holes in recast layer. The physics of material removal by WEDM is complex and minimization of the recast layer and micro crack is a major problem in WEDM industry. Therefore, it requires optimization of process parameters for desirable surface integrity of the machined surface.

While substantial literature exists on different aspects of WEDM of different materials like Stainless Steel S-03, Aluminium, Inconel 718, tool steels and die steels, there are certain important aspects which have not been attempted in earlier studies [5]. These aspects are thermal modelling of the process in order to predict the nature of the surface finish and the subsurface microstructure. Both these aspects are of considerable practical significance in this machining process. The surface finish is a factor, importance of which cannot be underestimated in any cutting process. The microstructure of the material under the cut surface is also very important as this decides the mechanical properties of the cut surface. The present research work focuses on WDEM machining of P91 [13-15], no work has been done so far in WEDM machining of P91. In addition, it has also addressed the aspects of generating a deeper understanding of the surface finish and underlying microstructure through thermal modelling. An effort has been made to come up with a surface response approach in this study to select the parameters which lead to least surface roughness and smaller cracks of harmless orientation and thereby improving the quality of machined surface using optimization of process parameters of WEDM. ANOVA table is prepared to check the statistical significance of the main parameters followed by optimization of machined surface in terms of surface roughness and density of cracks in the recast layer by response surface methodology. The surface integrity of machined surface is elucidated after parametric optimization [16]. The formation of craters has been examined experimentally and verified by thermal modelling. The formation of the craters and its size have a direct impact on the surface roughness.

The fine features of the craters, thickness of the recast layer and the microstructural details have been extensively examined by using FEG SEM. The fine structure at the cut surface has been probed by HRTEM. Besides microstructural characterization, the surface properties like hardness have been measured by nano-indentation, residual stress by x-ray diffraction and surface finish by profilometer. The cause of cracks and micro-structural features observed have been presented and discussed in terms of process parameters and properties of the material. This chapter also gives a general guideline for selecting process parameters for WEDM machining of common industrial materials like SS304, Aluminium and Zircaloy by thermal modelling approach.

5.2 Heat transfer modelling

The thermal modelling gives time dependent temperature distribution with distance from cut surface and helps in better understanding of the temperature dependent metallurgical features at each thickness due to the cooling rates during quenching and consequential microstructural changes. The thermal modelling helps in ascertaining the size of the crater which in turn determines the surface roughness.

Numerical modelling is performed in general purpose finite element software ABAQUS. Model contains 3634 number of linear quadrilateral elements with 3760 number of nodes. Nonlinear behaviour of the material is simulated using elastic plastic material model. Apart from nonlinear behaviour material conductivity, latent heat, thermal expansion coefficients are also provided as an input. Temperature variation with different material phases and volumetric changes with temperature are incorporated with user subroutine. Melting temperature is also simulated in the model in such a way that, if material temperature reaches 1200 ^{0}C then the material loses all of its strength and both considered in the transient heat transfer analysis.

WEDM process involves heat transfer from spark generated in the gap between the tool wire and the workpiece. The amount of material removed depends on the energy of spark. In this study, average energy of the spark which interacts with the material is expressed by Eq.5.1 [17].

$$E_e = \int_0^t v(t).\,i(t).\,dt \cong V.I.t \tag{5.1}$$

Where, E_e = Discharge energy, V= Discharge voltage, I = Current, and t = pulse on time. In this study the temperature of the spark generated during WEDM process was measured by spectroscopic technique using Boltzmann Plot method and a high speed camera. During these measurements the highest temperature was estimated to be of the order of ~15000K for high energy configuration [18]. Fourier heat conduction equation was used to model the heat transfer process using Gaussian heat source as shown in Figure 5.1.

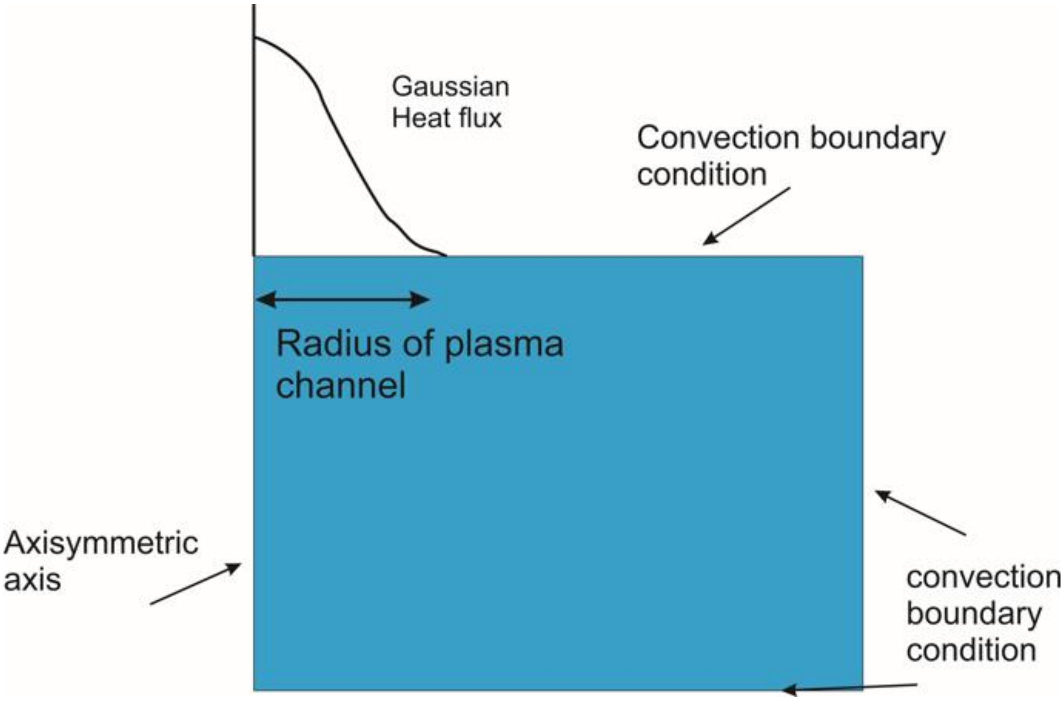

Figure 5.1 Schematic diagram of the geometry adopted for Numerical modeling.

Governing equations

$$\rho Cp \frac{\partial T}{\partial t} + \rho C\, u.\nabla T = \nabla.(k\nabla T) + Q \tag{5.2}$$

$$\rho Cp \frac{\partial T}{\partial t} + \rho C\, u.\nabla T = \nabla.(k\nabla T) + Q \tag{5.3}$$

Boundary conditions

$$k \frac{\partial T}{\partial r}(x, 0, t) = q \tag{5.4}$$

$$k\frac{\partial T}{\partial r} + h[T - T_{\infty}] = 0 \tag{5.5}$$

Since all boundaries of work piece are in contact with water

Initial conditions

$$T(r, z, 0) = T_{\infty} \tag{5.6}$$

Where ρ, Cp, q, T, t, Q, k, u, h are density, heat capacity, heat flux (pulsed), temperature, time, internal energy, thermal conductivity, velocity vector and heat transfer coefficient respectively.

T_{∞}= 295°K.

Three levels of energy were selected to study the effect of process parameters on the microstructure of the machined surface. The higher energy level corresponds to high level of average pulse current, voltage and spark on time, the lower energy level has low current, voltage and spark on time. The modelling parameters for the three energy conditions are presented in table 5-1. The radius and heat flux of plasma was estimated using equation (5.7) and equation (5.8) [19-22].

$$R_p = 2.04 \times 10^{-3} \times I_g{}^{0.43} \times T_{on}{}^{0.44} \tag{5.7}$$

$$q(r) = \frac{4.5 \times V \times I_g \times 0.08}{\pi Rp^2} \; e\left(-4.5\left(\frac{r}{Rp}\right)^2\right) \tag{5.8}$$

Where R_p is in meter and T_{on} is in seconds. In the present case plasma flushing efficency (PFE) has been estimated by equation used in refernce [19, 22]. The theoretical volume of material eroded is different from the actual volume of material eroded. Their ratio is known as Plasma flushing efficiency. In WEDM process the workpiece experiences thermal cycle because of application of a pulsed voltage. The thermal profile of the work-piece has been numerically modelled to understand the behavior of cooling cycle. The microstructure of the machined surface is dependent on the thermal cycle due to application of pulsed voltage.

5.2.1 Effect of Phase change

The phase change of P91 during cooling plays a vital role in the determination of residual stress on the "White' layer (re solidified layer). When the WEDM spark is "ON", the temperature of work piece reaches above melting point (1500 ^{o}C) for fraction of seconds in the area of heated zone and then cools down to room temperature rapidly during spark "OFF" time. The rapid heating and cooling changes the base metal microstructure at the heat affected zone. During heating the initial structure (Ferrite and tempered Martensite) begins to transform to austenite above AC_1 temperature. The AC_1 temperature for this steel is 819 ºC-850 ºC [23].

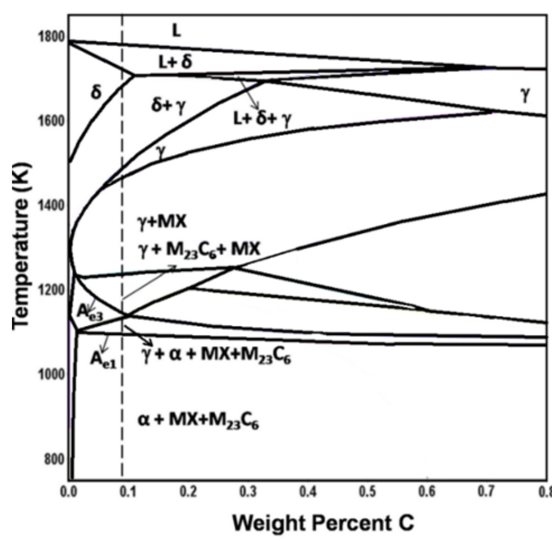

Figure 5.2 Phase diagram of P91 steel showing the domains of stability of the different phases [24].

Upon cooling Martensite starts forming along with metal carbides and nitrides. A thermal Martensite formation in P91 steels has been studied extensively, especially with respect to the Martensite start temperature Ms. The phase diagram of P91 is shown in Figure 5.2. The amount of Martensite formation depends only austenizing temperature and is independent of time when a steel is cooled below the M_s temperature. The quantity of martensite transformed from austenite depends on the temperature under-cooling below the M_s. In order to trace the formation of martensite during cooling cycle, the differential form of Koistinen-Marburger equation (5.9) [25,26] was used in the finite element model and which is expressed as

$$\Delta f_m = \{-0.011.\exp[0.011(\mathrm{T} - M_s)\}\Delta T \qquad (5.9)$$

Where Δf_m is the change of martensite fraction due to change in temperature ΔT during cooling cycle

During Austenite formation volume shrinkage takes place. Later when cooling takes place, Martensite starts forming due to diffusion less athermal transformation. The bigger hump in the dilatation-temperature curves which is observed during quenching, is due to the formation of a thermal Martensite below the M_s temperature (375^{o}C) [23]. Ms temperature generally decreases with increasing carbon and other alloy content and can be expressed by equation (5.10) [23]

$$M_S = 454 - 210[\mathrm{C}] + \frac{4.2}{[C]} - 27[Ni] - 7.8[Mn] - 9.5[Cr] + [Mo] + [V] + [W] + 1.5[Si] - 21[Cu] \qquad (5.10)$$

Where, M_s is in ^{0}C and element wt is in %. Martesitic finish temperature M_f is not definitive since martensitic transformation becomes increasingly difficult with amount of carbon in the remaining austenite becoming less and less. The volume fraction of Martensite can be estimated by using equation (5.9) and (5.10) However, when cooling slows down the formation of a thermal Martensite stops, and an isothermal transformation associated with volume expansion starts. The volume expansion varies with austempering -temperature and has large values at higher austempering temperatures. The corresponding dilation time curves clearly show a short incubation time, followed by a large expansion, when maintained at the corresponding austempering temperature lower than critical temperature. Schematic diagram of the volume change due to phase transformation is indicated in Figure 5.3 (dilatometry curve for both heating and cooling process of P91). The lower carbon content in the austenitic matrix will increase the martensitic transformation temperature and the rapid quenching process will have great impact on the martensitic morphology.

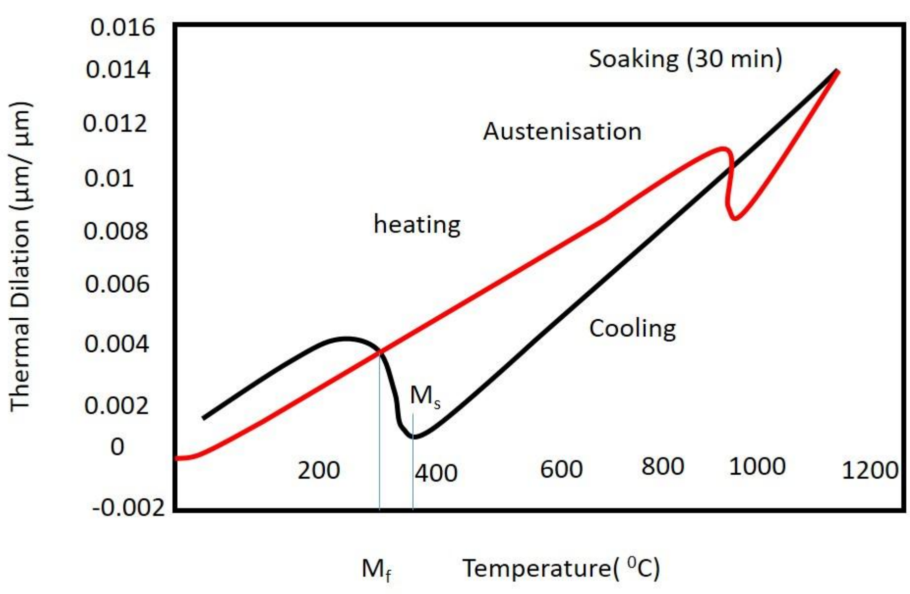

Figure 5.3 Dilatometric curve of ASTM387 gr 91(P91) steel showing the sequence and temperatures of different phase transformations.

Quenching process taking place in WEDM couples three major phenomenon.

a) Thermal gradients,

b) Phase transformation

c) Thermal dilation due to phase change.

For P91 steel martenisite starts forming at 360 ^{o}C and end at 200 ^{o}C [23]. In the simulation study material properties are considered as temperature and microstructure dependent. Thermal and mechanical and phase related properties e.g. density, latent heat during phase change, thermal expansion coefficient, Young's modulus and yield stress of material were applied as time dependent temperature field. Standard Fourier heat conduction model was considered. Phase related properties were taken from Reference [26] which were interpolated from experimental value and were applied to the program input as polynomial expression. In the above analysis the effect of residual stress due to volume change during martensitic transformation and yield stress dependent on temperature were added for calculating the total strain [25,26] which is given in equation (5.11).

$$\Delta\varepsilon = \Delta\varepsilon^{E} + \Delta\varepsilon^{Pl} + \Delta\varepsilon^{Th} + \Delta\varepsilon^{\Delta V} \tag{5.11}$$

Where the components are strain rate due to elastic, plastic, thermal loading and volumetric change. Transformation induced plasticity is not considered here. The volumetric change strain is maximum in the temperature of 360^{0}C -280 ^{0}C. $\Delta\varepsilon^{\Delta V}$ is evaluated from equation (5.12).

$$\Delta\varepsilon^{\Delta V} = \Delta f_{m.}\Delta\varepsilon^{\Delta V*} \tag{5.12}$$

The value $\Delta\varepsilon^{\Delta V*}$ is taken as $3.75x10^{-3}$ (though some authors used $7.5x10^{-3}$) [23] for the FEM analysis and $\Delta f_{m.}$ is estimated from Equation (5.9). The total strain $\Delta\varepsilon$ is accommodated in FEM by modifying the thermal expansion coefficient. The temperature dependent material properties of P91 is taken as shown in Figure 5.4. Properties during phase transformation of steel has been taken from reference which was taken for the analysis along with the coefficient of thermal expansion given in Figure 5.4 [26]. The formation of surface features like craters and cracks at HAZ is investigated using the heat transfer study. The other important feature which is part of the surface is cracks. The conditions that lead to the formation of cracks need to be ascertained.

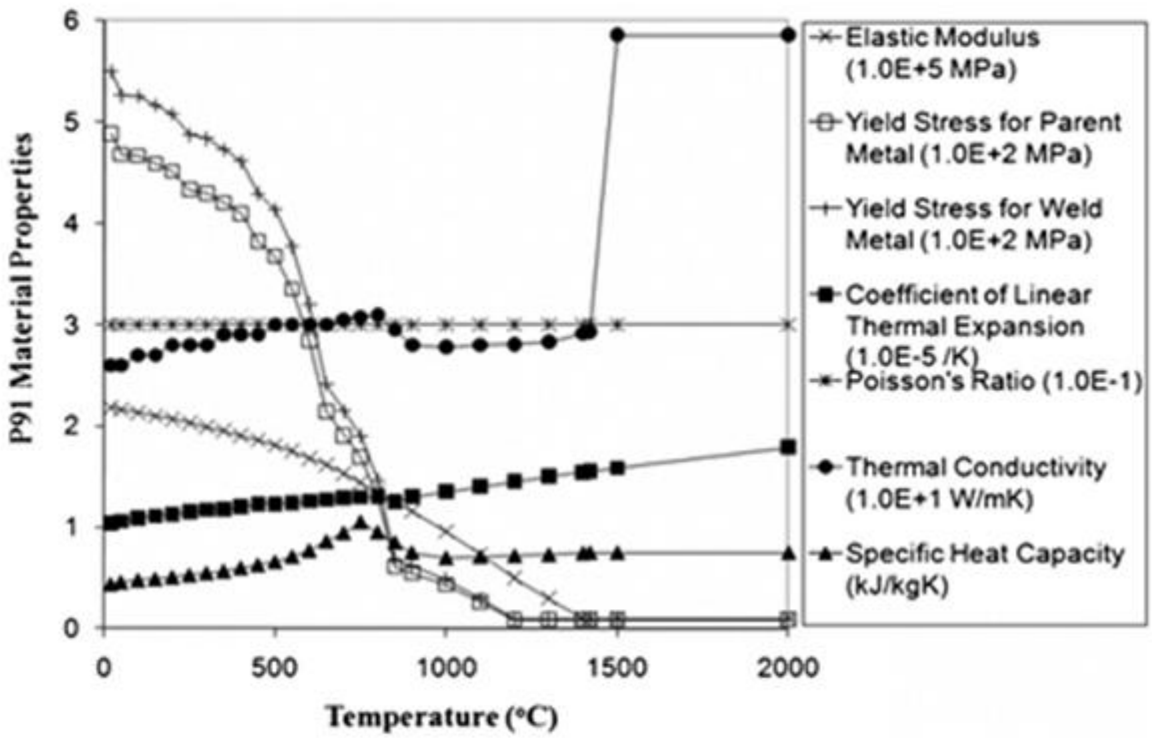

Figure 5.4 Physical properties of P91 as a function of temperature [26].

Table 5-1 Process parameters for heat transfer modelling

	High energy	Medium energy	Low energy
Gap Current (Ig), A	5	2	1.5
Gap Voltage (V)	80	60	20
Spark on time (T_{on}), µs	130	48	100
Effective Spark on time ($T_{on\ effective}$), µs (40% of T_{on})	52	48	40
Radius of plasma estimated (µm)	53	34	28
PFE	0.22	0.15	0.14
Crater Size (µm)	21.67	13.48	4.18

5.3 Results and Discussion

5.3.1 High energy condition

The radius of the plasma formed in this case is estimated to be of the order of 53µm. Equation (5.7). the heat transfer analysis for high energy condition was carried out for 5A discharge current and effective spark on time of 52 micro seconds. The numerically estimated size of the crater is of the order of 35 µm as shown in Figure 5.5 and table 5-1. The theoretical estimated size of the crater is of the order of 21 µm (after incorprating PFE). It is evident from Figure 5.5 the maximum temperature reaches upto 1800^0C after spark is off. The cooling rates obtained is also highest among the three energy conditions. The cooling rate at 1µm form the onset of spark off time is of the order of $4x10^8$ K/s as shown in Figure 5.6.

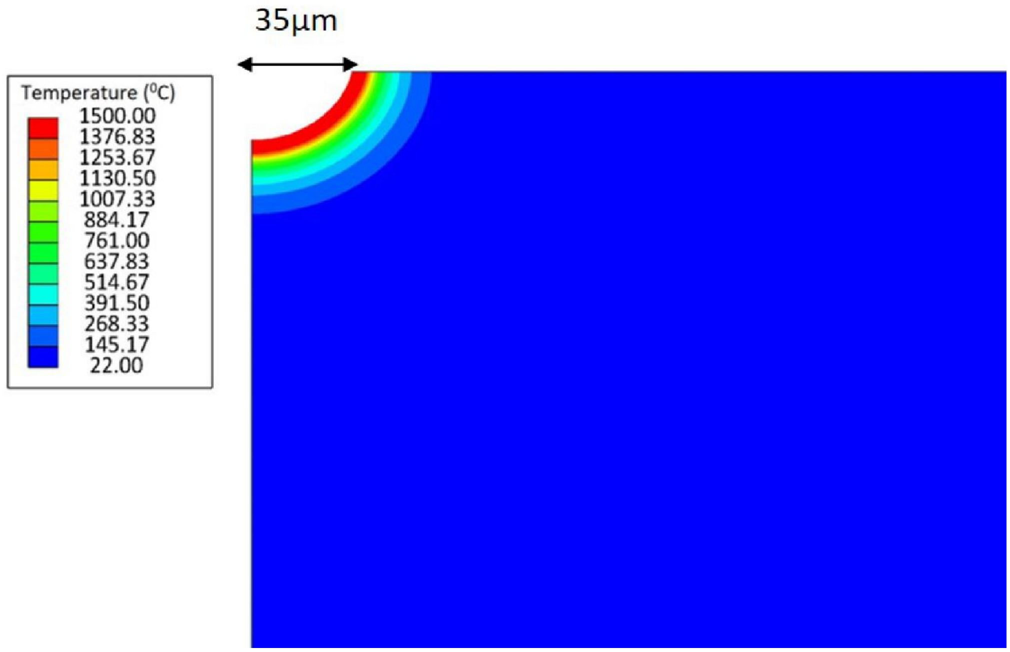

Figure 5.5 Temperature profile of machined surface at high energy.

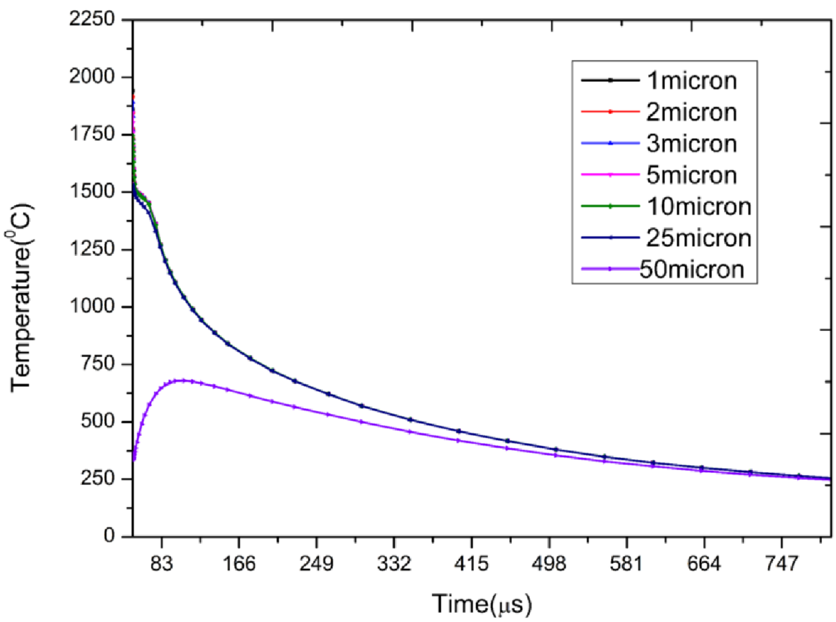

Figure 5.6 Temperature variation across the machined surface at high energy.

5.3.2 Low energy condition

The radius of the plasma formed in this case is estimated to be of the order of 28μm as estimated from equation (5.7). The heat transfer analysis for low energy condition was carried out for 1.5 A discharge current and effective spark on time of 40 micro seconds. Hence the theoretical size of crater (after incorprating PFE) is of the order of 4 μm. The numerical estimated size of the crater is of the order of 8 μm shown in Figure 5.7. It is evident from Figure 5.7 that the maximum temperature reaches up to 1400^{0}C after spark is off. As we move inward towards the bulk material the rate of cooling starts decreasing from $3x10^7$ K/s at 1 μm to $1x10^6$K/s at 10 μm as shown in Figure 5.8. It is also observed that after 25 micron from the cutting edge no significant temperature change takes place in work-piece.

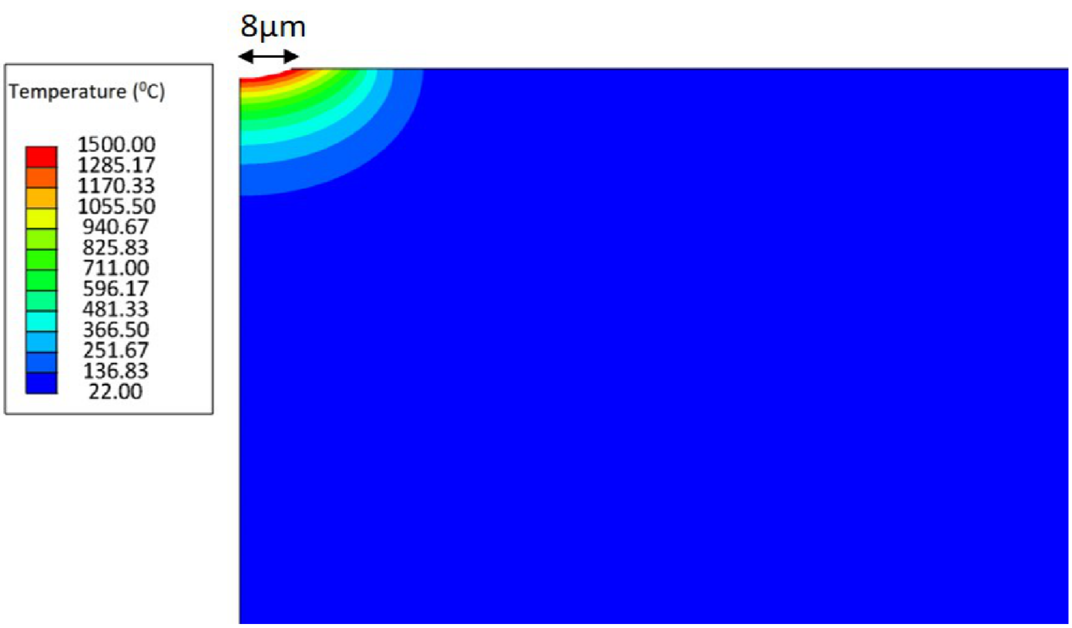

Figure 5.7 Temperature profile of machined surface at low energy (contour).

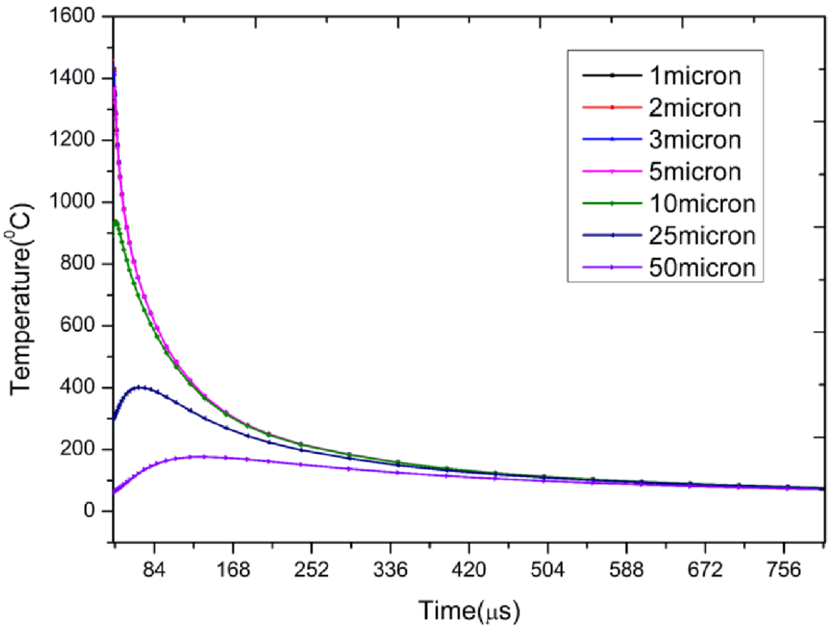

Figure 5.8 Temperature variation across machined surface at low energy.

5.3.3 Medium energy condition

The radius of the plasma formed in this case is estimated to be of the order of 34μm. The heat transfer analysis for medium energy condition was carried out for 2A discharge current and effective spark on time of 48 micro seconds. Though the process parameters show a little variation from those used for low energy conditions, the computation results show that the temperature profile from the cutting edge to the bulk differs considerably. Hence the theoretical size of crater (after incorprating PFE) is of the order of 13 μm. The numerical estimated size of the crater is of the order of 25 μm as shown in Figure 5.9. After the end of spark on time the cooling rate at 1μm is of the order of $2x10^8$K/s shown in Figure 5.10. The cooling rate was found to decrease on proceeding towards the bulk material.

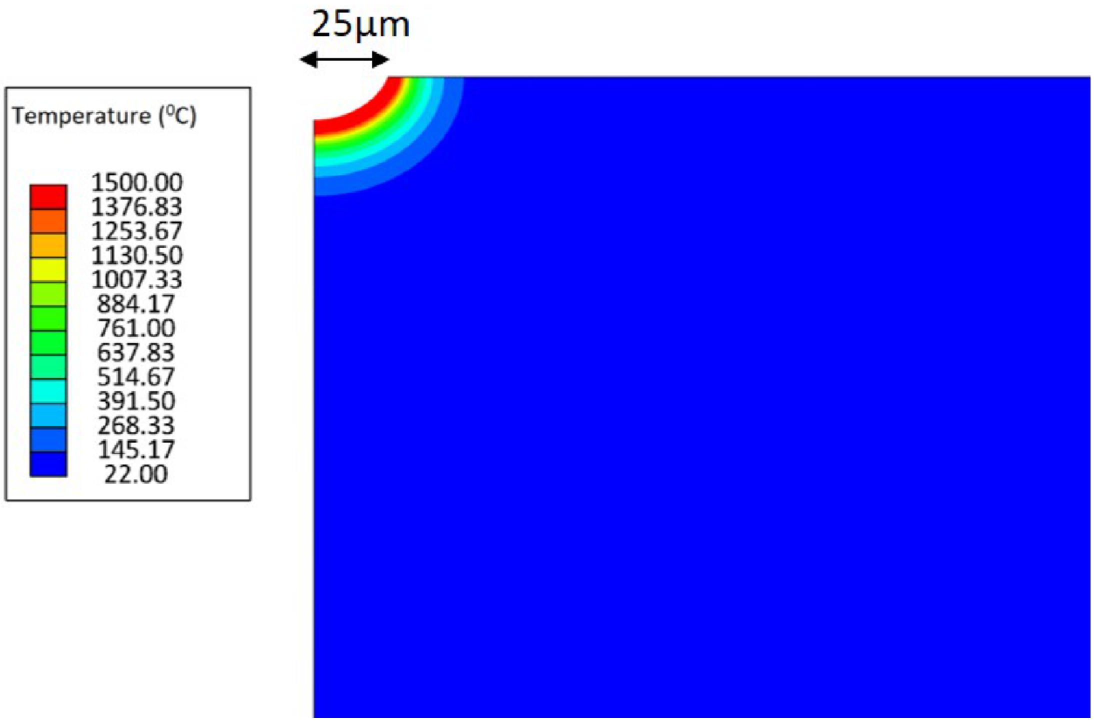

Figure 5.9 Thermal profile of machined surface at medium energy conditions (contour).

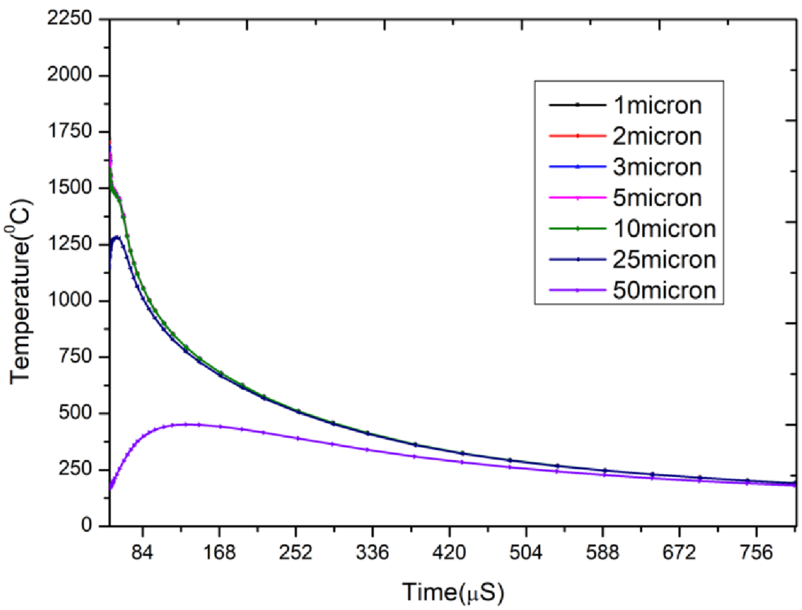

Figure 5.10 Temperature gradient across machined surface at medium energy condition.

5.4 Microstructure

The cut surface microstructure was analysed for changes involved in WEDM. Figure 5.11, Figure 5.12 shows sub grain structure, typical of a tempered ferritic martensitic steel. The sub-grain boundaries are decorated with carbide precipitates, which are reported in the literature as $M_{23}C_6$ type precipitates [13]. WEDM machining involves intense heat generation causing local melting and even evaporation of the material followed byrapid cooling. The machined surface gets heated by the micro pulsed spark and flow of heat takes places predominantly towards the bulk material due to which the material is continuously heated. The morphology of EDM machined surface is distinct due to complex heating, cooling and erosion mechanism. The SEM image of the machined surface revealed that the surface texture is composed of solidified material having several randomly distributed features like cracks, craters and precipitates.

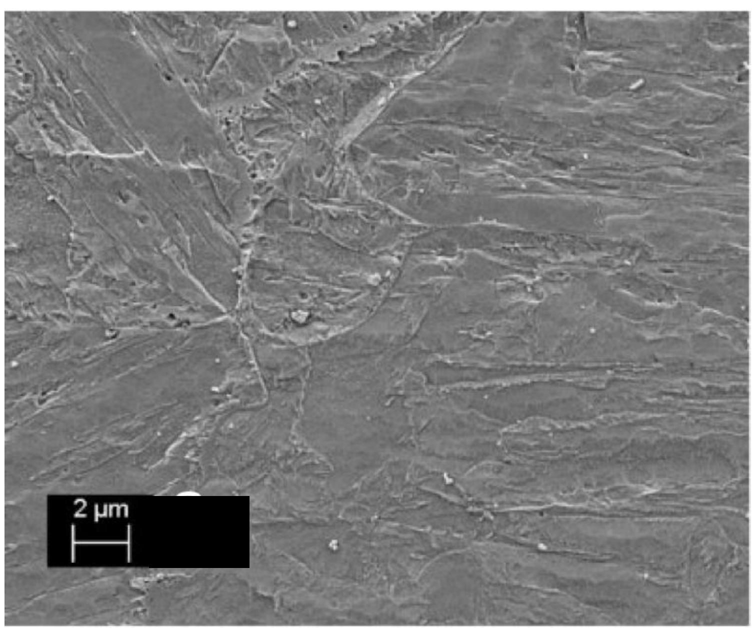

Figure 5.11 Base Microstructure of P91 steel as seen in the SEM.

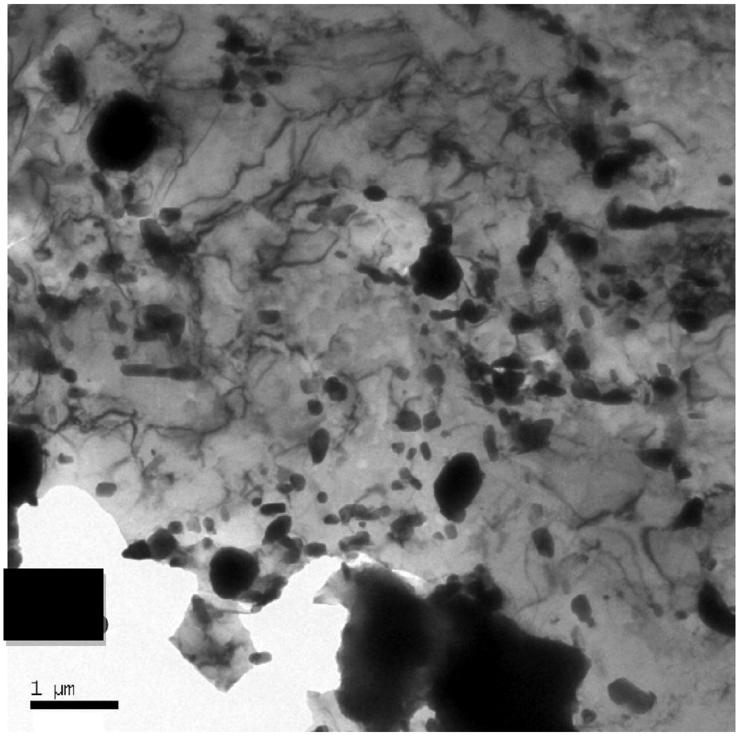

Figure 5.12 TEM of base microstructure P 91 steel showing the features of the tempered structure.

The microstructure of the machined surface depends on the thermal history of machining parameters. The heat evolved during WEDM process and inefficient flushing of the molten material leaves behind a layer of re-solidified molten material on the machined surface called recast layer or white layer. This layer contains micro holes and cracks which are fatal for fatigue life of the component [27]. Micro cracks are formed due to differential cooling of parent material and the re-solidified layer estimated by theoretical modelling.Improper flushing of the molten material leads to non-uniform temperature distribution causing thermal stresses on the machined surface. Orientation of micro cracks plays a significant role in the fatigue life of the machined component [6, 28]. Micro cracks are formed when stresses in the recast layer exceeds the ultimate tensile strength of the material [27]. To study the performance of the machined surface three zones were identified considering the microstructure and Nano hardness of machined surface. Outermost surface is recast layer, which has re-casted material and craters. The next layer is heat affected zone where material has been heated to high temperatures and then cooled, followed by the bulk material as third region. Besides the thickness of the recast layer and the heat affected zone; the roughness of machined surface is accounted by shape and size of crater formed and micro cracks present on the machined surface. The size and orientation of solidified stripe shaped features also varied with energy and with zones mentioned above. The elemental composition of the machines surface was more or less homogenous. In high energy conditions it has been observed from experimental results that the surface is irregular. High energy leads to melting of the work piece and material gets eroded due to high pressure shock during implosion of the plasma. As estimated by numerical modelling the cooling rate at the cut surface is highest under this condition and was found to drastically reduce on proceeding towards the bulk material. The effect of this high cooling rate and its variation on the microstructures was extensively examined by different tools and is described in this section.The plan view of SEM of machined surface in Figure 5.13 shows craters which are roughly circular in shape. The molten material is pulled in the gap between the electrodes. It can be seen in the Figure 5.13 and Figure 5.14 that there are large number of pores visible on the machined surface. Also some craters seem to penetrate inside the work piece.

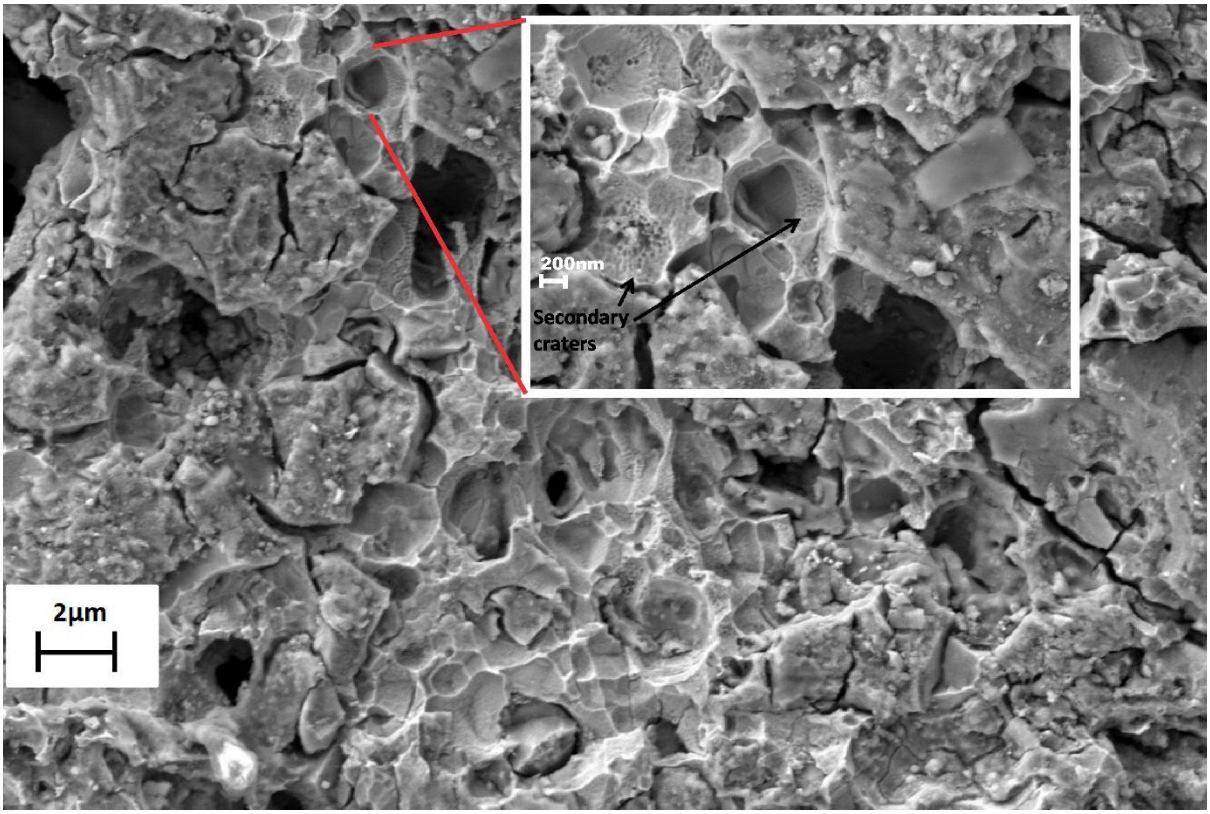

Figure 5.13 SEM image of machined surface at high energy with cracks in the machined surface and secondary craters- plan view.

High energy of the spark forms larger volume of molten pool which gets solidified during the off cycle of the spark. Some debris particles attached in the form of spherical globules can be observed form the image. Since the energy of the discharge is high, the recast layer formed in previous cycles gets heated by the subsequent spark and during spark off time some material gets eroded from the re-solidified material of the earlier recast layer, thereby forming small eroded craters. It is evident from Figure 5.13 that there are several cracks of size varying from 1-8 µm present on the machined surface. The walls of the crater has small circular features which resemble secondary craters. The width of the crack opening is of the order of 0.5-1µm. At high energy the temperature of molten pool volume is larger as compared to that of low energy and same flushing time leads to very high cooling rate of the order of 10^9 K/s. This causes high thermal stress and causes cracking in the re-solidified material.

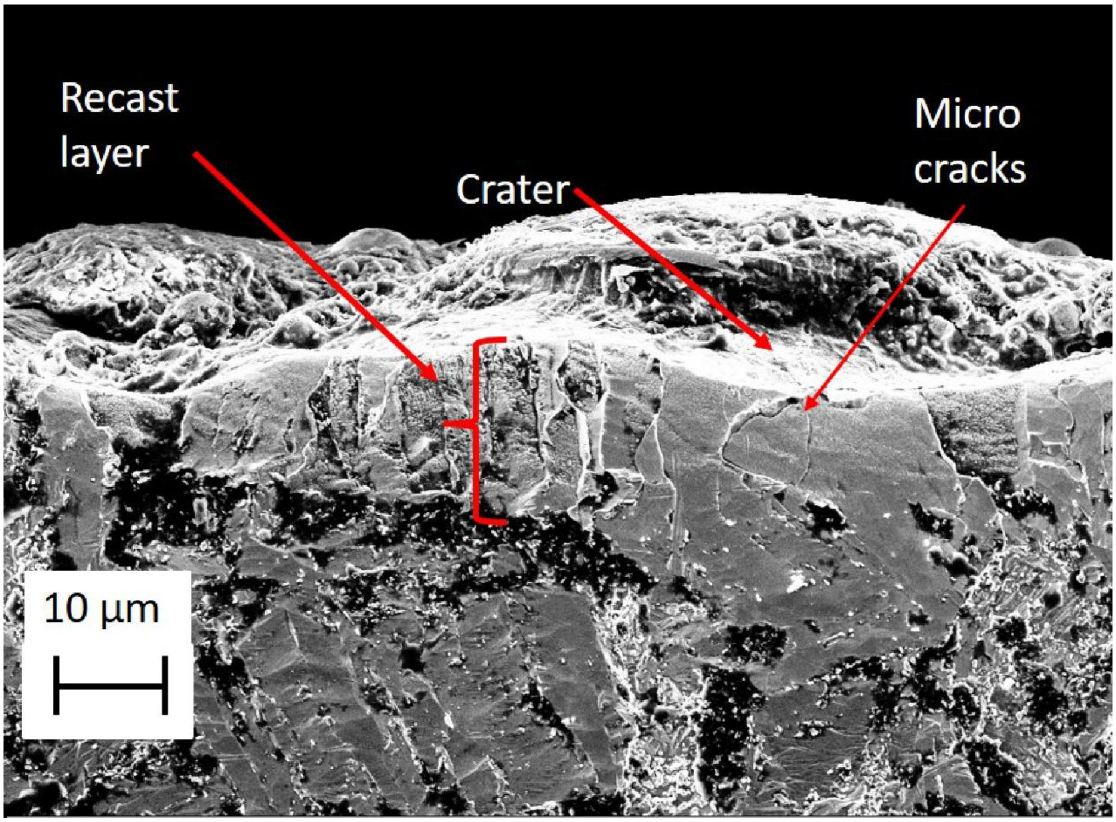

Figure 5.14 SEM image of machined surface with recast layer showing cracks- cross sectional view.

Cross sectional view of the machined surface is shown in Figure 5.14. The SEM images revealed that for specimen machined at high energy level, the recast layer thickness was largest among the three energy conditions. In the discharge cycle the material near the edge gets melted and eroded during the implosion of the plasma channel. The recast layer in this case essentially was featureless as seen in the SEM. However, in some parts of the recast layer very fine martensitic feature could be observed. It had cracks of length typically about

4-5 μm and debris incorporated in it. The boundary between the recast layer and the heat affected zone was found to be distinct. Each spark cycle results in partial heating of the previously solidified layer and continuously heats the substrate material. In heat affected zone the number density of precipitates is low. This can be attributed to rapid heating and fast cooling of material in HAZ. The thickness of the HAZ can be verified from the SEM of machined surface in different energy conditions and the extent of heat affected zone is of the order of 15-20 μm under higher energy level. The temperature of material has gone above the ferritic to austenite transformation temperature followed by rapid quenching leading to the dissolution of precipitates and transformation of austenite into martensite in this region. The martensite volume fraction in the HAZ is therefore much higher and the volume fraction of the precipitates is much lower in this region.

The nature of the martensite in some parts of the heat affected zone was very fine as could be seen in Figure 5.15. This was because of much higher cooling rate in that region. Higher spark energy often leads to instability of the plasma and pressure shock waves are generated during the implosion of the plasma channel. This pressure waves causes thermal spalling of the solidified material and SEM observations revealed a brittle rupture of recast layer shown in Figure 5.15, as spalled region in heat affected zone. The microstructure is also characterized by micro cracks. These cracks are oriented in different directions and number density of the micro cracks is high for high energy. The rapid heating and cooling during spark off cycle generates a brittle surface which develops thermal cracks in it. The molten material is subjected to differential cooling leading to formation of residual stress in the machined surface. Figure 5.16and Figure 5.17shows the extent of residual stress as a function of distance from the cutting edge. In high energy condition the residual stress reaches up to

700 MPa at 10μm away from the cutting edge. This value is unusually high. Other researchers have also found similar behavior in other materials [29]. In each level of process parameters, SEM images revealed that the grain size in the recast layer is different for different energy levels. It also revealed fine spherical precipitates arranged inside the grain and in the grain boundary. The patterns of deposited debris and material in the recast layer depend on the thermal nature of the process.

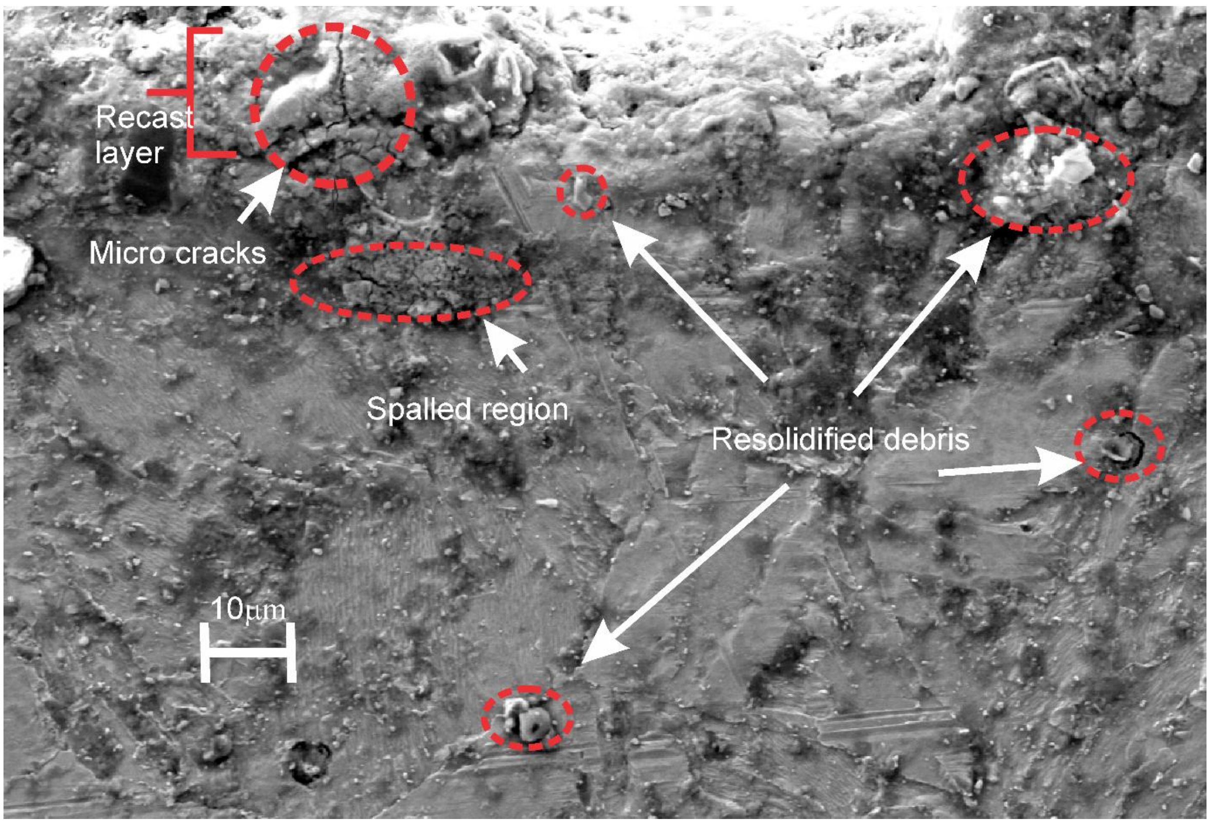

Figure 5.15 SEM image of machined surface at high energy condition- cross sectional. view.

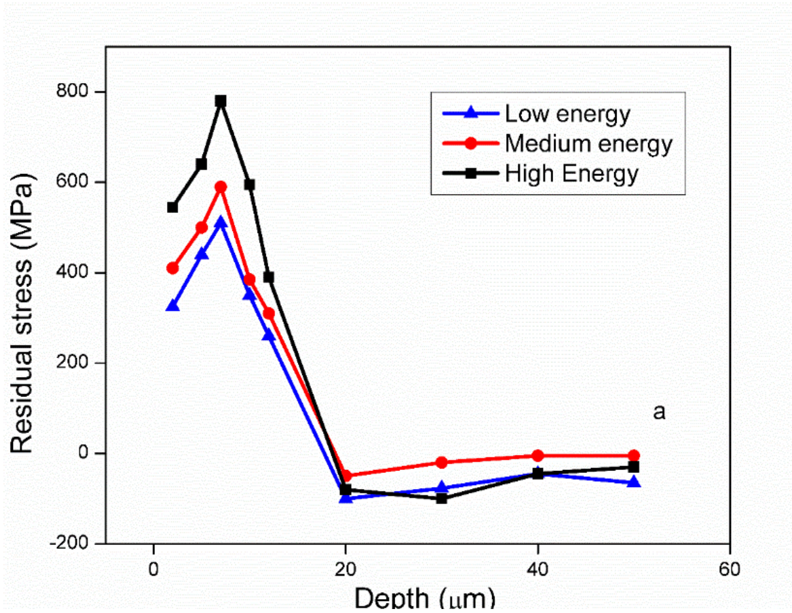

Figure 5.16 Residual stress of the machined surface at different peak currents (experimental).

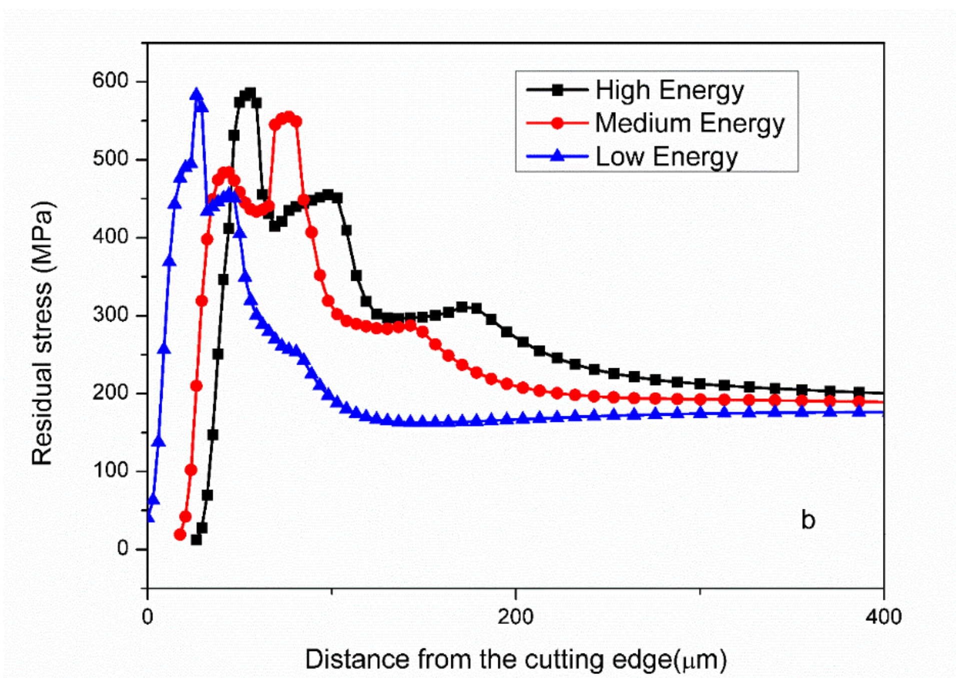

Figure 5.17 Residual stress of the machined surface at different peak current (numerical).

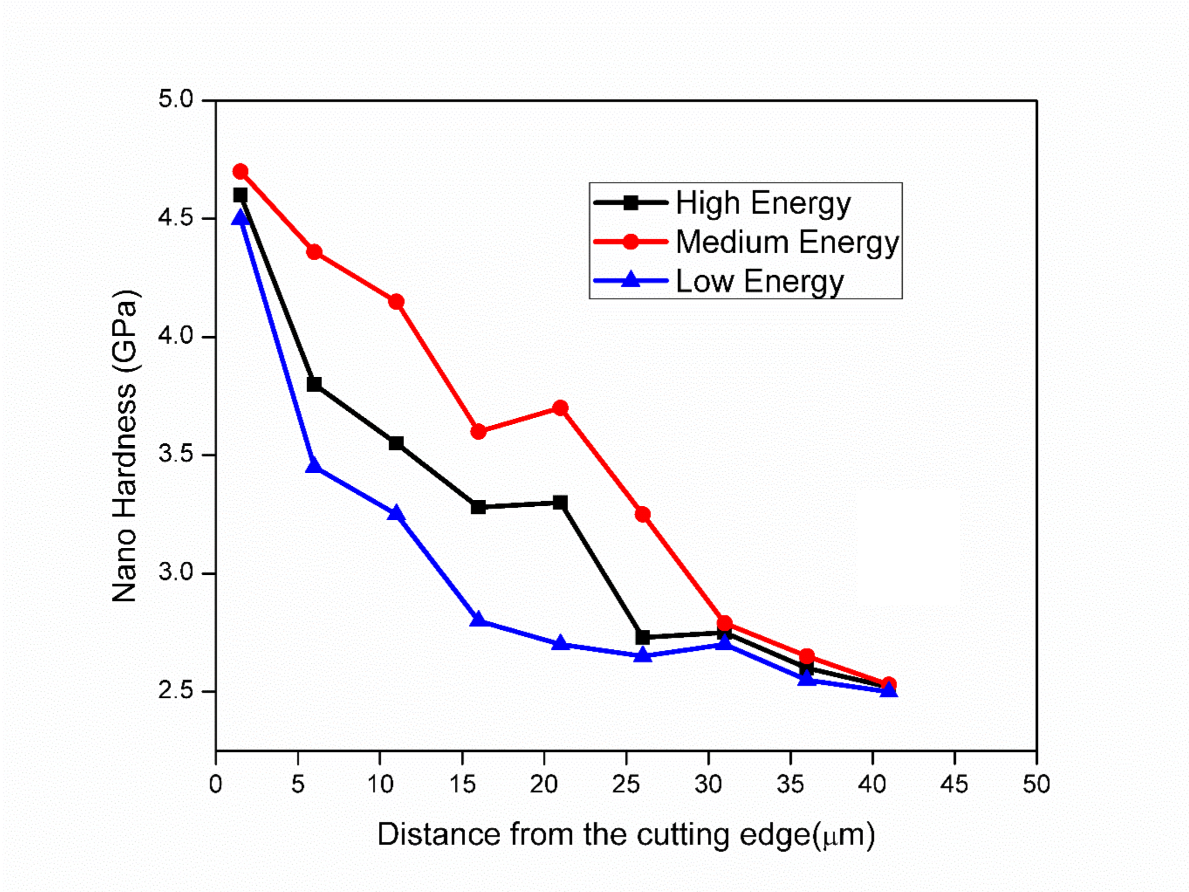

Figure 5.18 Nano Hardness of the cross section of machined surface.

Previous literatures on WEDM reported that the recast layer is hard and brittle [30, 31], thus it aids crack growth. The gradient of Nano hardness from recast layer to the bulk material as shown in Figure 5.18 indicated the recast layer has hardness of the order 1.5-2 times as that of the bulk material. The nano- hardness of the machined surface washigh since the recast layer is hard and the extent of hardened layer is higher for wide recast layer. Besides the aforementioned features, craters were also seen in the recast layer surface. The radius of the plasma channel generated during EDM has been studied in detail [18]. In that study fast photography of EDM spark had revealed the plasma channel. On comparison with the results of that work it could be seen that the radius of the crater was dictated by the radius of the plasma channel generated during WEDM.

The microstructure of the region below the crater had different characteristics. The recast layer in these regions was normally found to be thinner. The base microstructure was found to have a higher density of carbides. Lower thickness of the recast layer lead to a higher cooling rate leading to the creation of very fine martensitic structure. A FIB section of the sample also revealed the recast layer is porous in nature as shown in Figure 5.19. The TEM image of the recast layer showed the presence of re-casted grains. At the machined surface high resolution TEM image showed regions where no lattice could be seen and also regions where small crystals were observed. (Figure 5.19). These regions were mixture of both nano crystals and amorphous structure. Electron diffraction pattern from these regions confirm the facts that this region is a mixture of amorphous and nano crystalline phases as shown in Figure 5.19. Observation of the amorphous and nano crystalline regions is consistent with the fact that the machined surface experienced rapid melting due to intense heat generated in spark and rapid cooling which lead to melting and re-solidification of the un-flushed molten material at very high rates of the order of $3x10^8$K/s. At such high cooling rates in alloys amorphization of phase and nano-crystal formation takes place. Numerical modelling also indicates that in the specimens cut at lower energy too this region will be present because of rapid solidification occurring after rapid heating. However, the thickness of this region will be much smaller as estimated from the heat transfer modelling. The surface roughness measured in high energy condition by profilometer is of the order of 2-4 µm. High current value leads to bigger plasma channel as compared to that in case of low energy condition and hence larger melt pool size. In this case melt pool does not get efficiently eroded by flushing and implosion of plasma bubble at end of spark on time. This results into re-solidification of the uneroded melt pool forming the recast layer. Al details of surface roughness, length of micro crack, number density of micro crack and orientation of microcrack are mentioned in table 5-2.

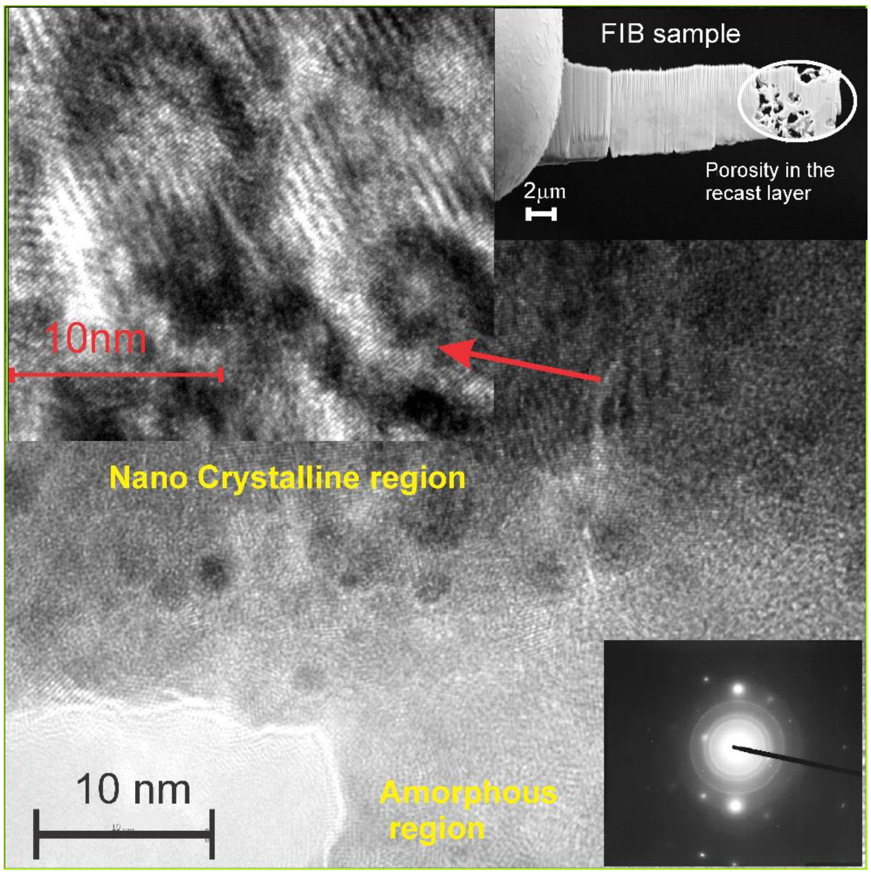

Figure 5.19 TEM sample of recast layer prepared by FIB technique, showing porosity in recast layer and High resolution TEM showing nano crystalline grains and diffraction pattern.

Among the three energy conditions analysed in this work, the thickness of the recast layer is minimum when machining is done under low energy conditions. The SEM image of the machined surface revealed that the density of micro cracks is also low and secondary craters are not apparent in the recast layer as shown in Figure 5.20. This can be attributed to poor reheating of the re-solidified material because of lower volume of the melt pool. The observed crater size is of the order of 4-10μm, which is very close to the size predicted by the numerical model. It can also be observed that under this machining condition the machined surface has very fine structure with no micro cracks as seen in Figure 5.20. The results of the heat transfer model shows, the maximum temperature reached is well above the melting point of the material and the microstructural features on the machined surface confirms local melting.

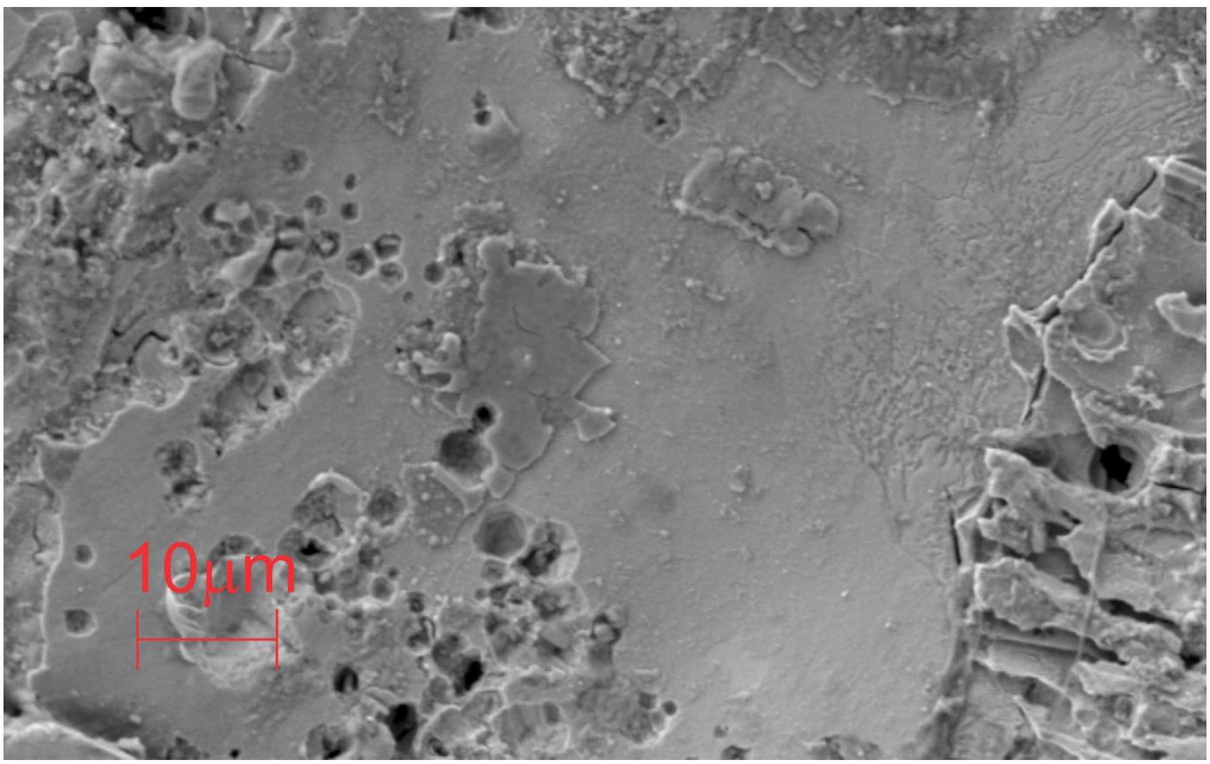

Figure 5.20 High resolution SEM image of machined surface at low energy condition - plan view.

Figure 5.21 shows the cross sectional view of the machined surface under low energy conditions. It can be noticed that the thickness of recast layer in this case is of the order of 1-2 µm. Figure 5.16 and Figure 5.17 shows the residual stress on machined surface under low energy condition. It can be observed that for case of low energy conditions the residual stresses are less as compared to that in case of high energy condition. This leads to small number of cracks in the recast layer. The estimated cooling rate from the modelling calculations is of the order of $\sim 2x10^8$K/s at 1µm from the cutting edge. The recast layers besides being thinner in this case, have coarser microstructure. It was observed that the number density of micro-cracks is significantly less in lower energy conditions. The size of craters in the recast layer is larger in this case, this may be attributed to better erosion of molten pool as the volume of molten pool is low in lower energy conditions. This leads to better surface finish but lower material removal rate. In low energy condition the thickness of the recast layer was less as most of the material gets eroded during the flushing cycle. But the subsurface flaws like the size of blow holes and size of craters were larger. It can be attributed to the better flushing of molten material during the flushing cycle leaving larger craters.

In high energy condition the craters are filled with the re-solidified material which remains unflushed during the flushing cycle. In low energy condition, the boundary between the recast layer and heat affected zone is very uneven. The width of the HAZ was found to be much smaller than the high energy conditions. In low energy condition the precipitates are arranged on the grain boundary. No thermally spalled features were observed in lower energy condition because of better stability of plasma channel. The small thickness of recast layer in this condition causes significant reduction in nano-hardness of the machined surface. The microstructure below the craters was found to be devoid of carbides because of low heat input and relatively lower rapid cooling. The different zones below the crater which is of much smaller size can be clearly seen in Figure 5.21. The surface roughness measured in Low energy condition by profilometer is of the order of 1-2 µm. Low current value leads to smaller plasma channel and hence smaller melt pool. Small melt pool gets efficiently eroded by flushing and implosion of plasma. This results into better surface finish of the machined surface but the material removal rate in this case is very poor.

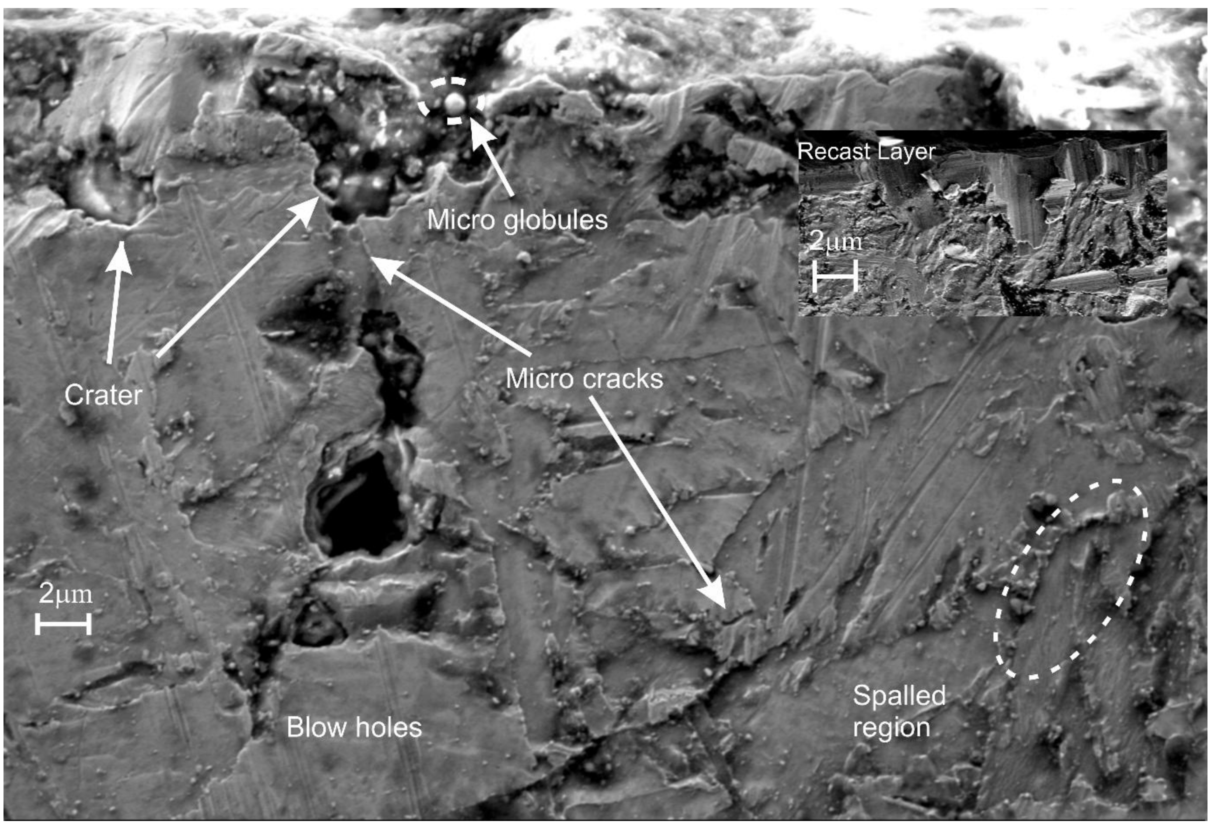

Figure 5.21 SEM image of machined surface at low energy condition- cross sectional view.

In medium energy conditions plan view of SEM image of the machined surface shown in Figure 5.22 revealed that there are some flat areas along with small pores present in the machined surface. In the medium energy level, the features are in between those of higher energy level and lower energy level in terms of number density of cracks, orientation of cracks and craters, debris and inclusions. An increasing trend in thickness of the recast layers can be seen in the medium energy level shown in Figure 5.23. It is observed that the number of craters was less as the craters were filled with re-solidified material. The Nano hardness of the machined surface was more on the edge in HAZ region.The crater size is small and the recast layer thickness is uniform. Presence of carbides in the base microstructure below the recast layer can be clearly seen.The surface roughness measured in medium energy condition by profilometer is of the order of 1.5-4 μm.

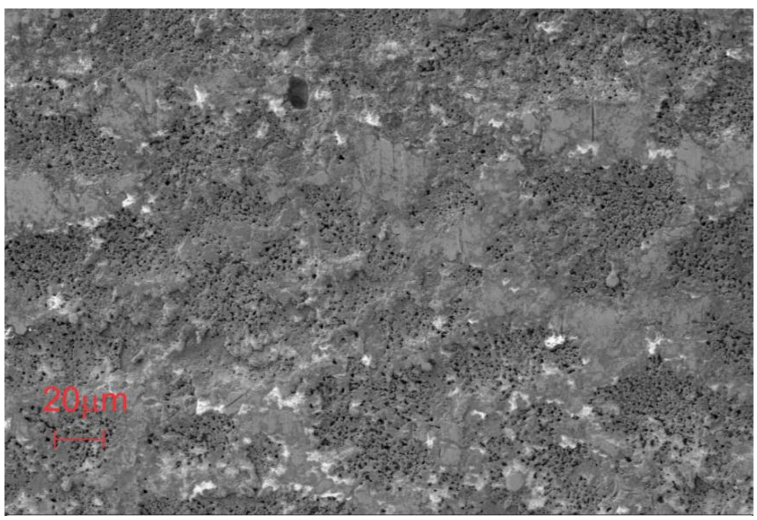

Figure 5.22 SEM image of machined surface at medium energy condition - plan view.

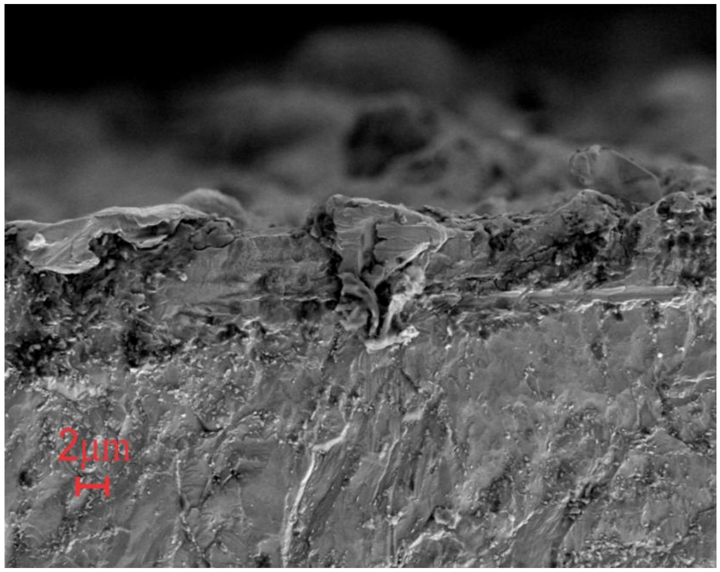

Figure 5.23 SEM image of machined surface at medium energy condition – cross sectional view.

5.5 Response surface analysis of machined surface of P91

5.5.1 Effect of process parameters on surface roughness.

The effect of process parameters on surface roughness of the machined surface has been examined by response surface methodology. The results show in preceding sub-sections that the most prominent factor is peak current which affects the surface roughness of the machined surface. During EDM cutting, some portion of molten material is redeposited on the parent material surface as the entire volume of molten metal does not gets ejected out. Due to this, it leaves behind a redeposited layer in the next cycle. As the tool wire moves during the cut process, the material gets heated and subsequently cooled forming recast layer. In the next cycle of spark on time, a part of molten metal gets redeposited adjacent to the previously solidified layer. Surface roughness is high when there is discontinuity in the machined surface in terms of multiple molten pool deposit. It is observed in Figure 5.14 that the machined surface has micro holes and debris particles. Blow holes are formed due to emission of gases during breakdown of dielectric which get trapped between the layers of molten pool which gets redeposited adjacent to the recast layer formed in previous spark on time. When the energy per spark is more, greater craters are formed due to inefficient cooling of the molten pool and some material gets eroded in the form of flakes by thermal spalling in addition to evaporation as shown in Figure 5.15.

Figure 5.24 shows that when peak current is increased from 70A to 130A, surface roughness increases.

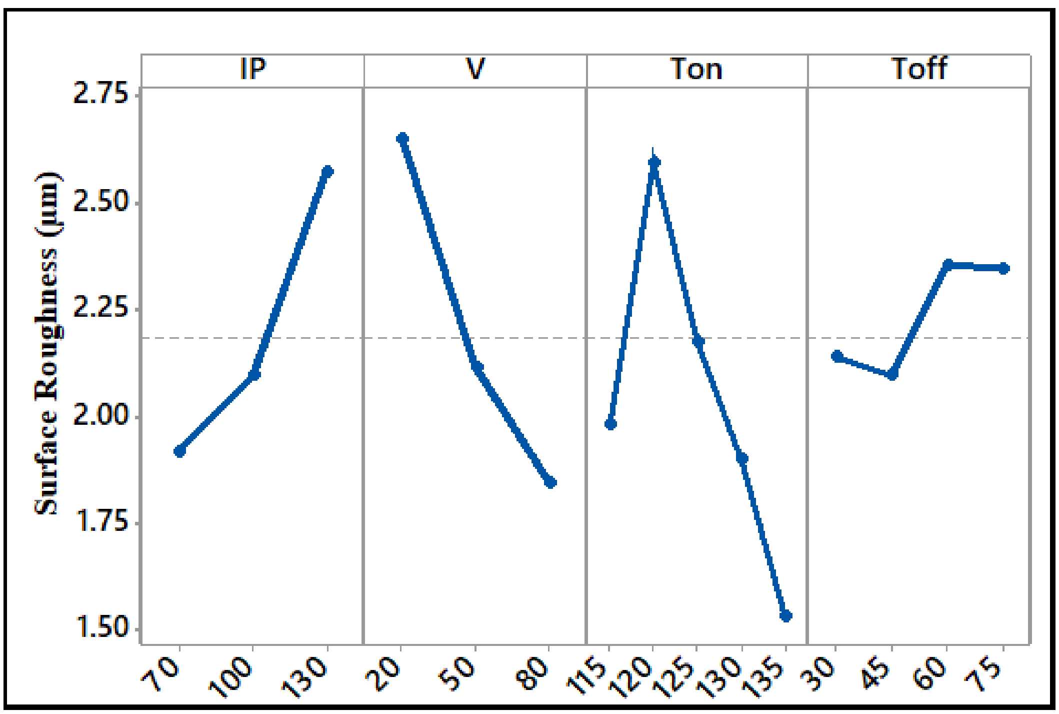

Figure 5.24 Effect of process parameter on surface roughness on WEDM machined surface of P91 steel.

The energy of discharge increases when peak current is increased keeping all other parameters constant. When voltage was kept on the lower side, the breakdown of dielectric was difficult and hence discharge was unstable leading to higher surface roughness [14]. Higher voltage requires smaller gap between the work piece and the tool electrode and reduces the fluctuation in discharge. Hence, re-deposition of recast layer will be smooth [15]. The lowest surface roughness was observed at T_{on}=135μs. The interaction time of the spark with the work piece increases with higher pulse on time and consequently the molten pool area increases. This also brings temperature stability in the molten pool area and recast layer gets detached from the machined surface resulting into better surface roughness as seen in SEM micrograph Figure 5.25 [32]. Effect of combination of process parameters on surface roughness is presented in Figure 5.26. While cutting with higher spark off time lesser number of discharges takes place and with lower current of cutting, the molten pool becomes smaller. It also provides sufficient time to flush out. This causes minimum surface roughness and this is evident at setting peak current to 70 A and pulse off time to 45μs. A regression equation of surface roughness in terms of process parameters and their contribution is estimated in equation (5.13).

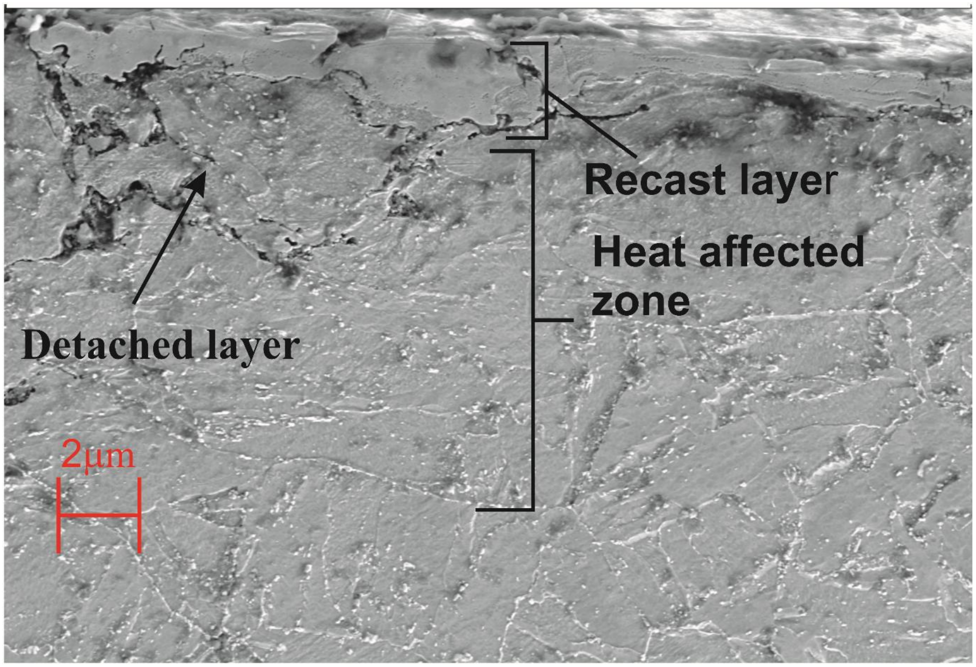

Figure 5.25 SEM image showing detached recast layer on the P91 base metal.

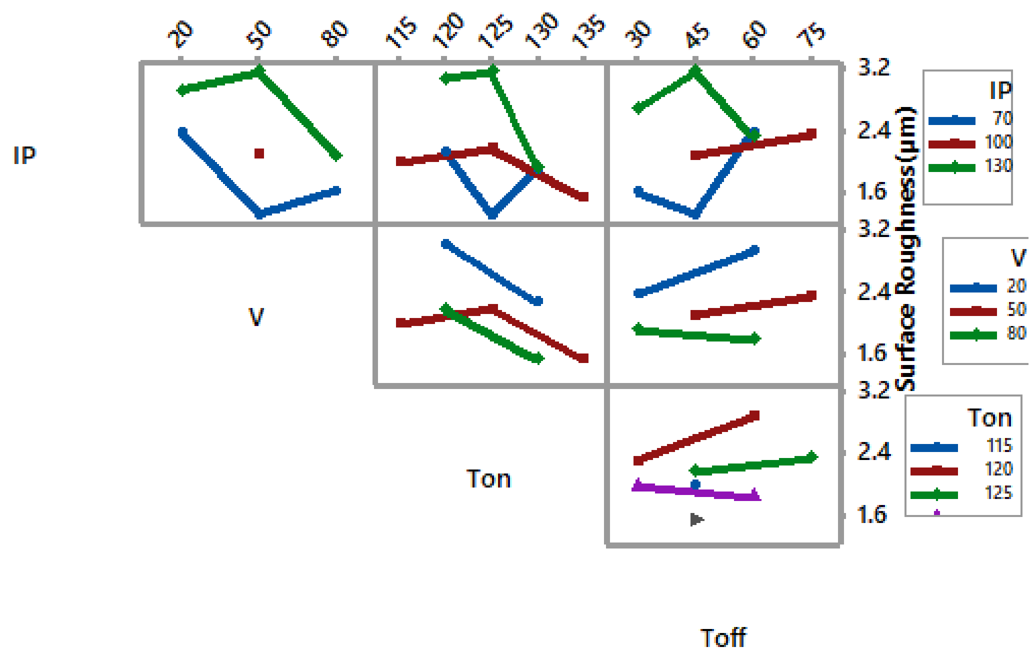

Figure 5.26 Two way interaction plot of process parameters on surface roughness for WEDM machined surface of P91 steel.

Regression equation

$$SR = -127.1 + 0.268\,IP - .0109\,V + 1.80T_{on} + 0.415T_{off} - 0.000177\,IP^2 + 0.000894V^2 - 0.00639\,{T_{on}}^2 - 0.000292{T_{off}}^2 - 0.000021\,IP.V - 0.001536\,IP.T_{on} - 0.000628\,IP.T_{off} + 0.000210\,V.T_{on} - 0.000393\,V.T_{off} - 0.00239T_{on}.T_{off} \quad (5.13)$$

5.5.2 Effect of process parameters on micro-cracks

SEM images shows many micro cracks are visible in the recast layer ranging from 1µm to13 µm [32]. The average length of micro cracks for each set of process parameters was estimated and response surface regression was analysed on the basis of results observed by analysis of variance (ANOVA). Peak current (IP), Pulse off time (T_{off}), linear combination of peak current and voltage (IP×V), peak current and pulse on time (IP×T_{on}) and square of pulse on time (T_{on}) are the significant process parameters which affects the average length of micro crack.

Regression equation

$$L_c = 531 + 0.841\,IP + 0.616\,V - 9.03\,T_{on} - 0.526T_{off} + 0.00060\,IP^2 - 0.00016\,V^2 + 0.0384\,{T_{on}}^2 + 0.00439{T_{off}}^2 - 0.002549\,IP.V - 0.00621\,IP.T_{on} - 0.000653\,IP.T_{off} - 0.00229\,V.T_{on} - 0.000903\,V.T_{off} + 0.00142T_{on}.T_{off} \quad (5.14)$$

Average length of micro crack is lowest for peak current 70A. This may be attributed to the low volume of molten material. The length of micro cracks increases with the increase in current. Higher peak current and pulse on time increases the energy per spark whereas lower pulse off time gives less time for efficient removal of debris and inefficient cooling time. Average length of micro crack is observed to increase linearly and then decreases with increase in discharge voltage. When discharge voltage is increased the effective electric field (E= V/d) required for breakdown of the dielectric used for generating spark gets lowered

[18]. This effectively increases the gap between the electrodes and thus delivers lesser amount of energy to the work piece. It is observed that on increasing pulse off time (T_{off}) average length of micro crack first decreases and then increases at T_{off}equal to70μs. The lowest value of average length of micro crack is observed at T_{off} equal to 60μs. High pulse off time gives more time for flushing and quenching of the re-solidified layer. It provides more time for restoration of dielectric strength of dielectric used and the fluctuations in the spread of spark is reduced, resulting into smaller micro cracks. [18]. Figure 5.27 and Figure 5.28 show the effect of individual and interaction of process parameters on the length of micro crack respectively. The product of peak current and T_{on} and IP had 31.87% contribution in variation of length of micro cracks. Lowest average length of micro crack is observed for IP (70A) and V (20V). Lower value of discharge energy produces lower length of micro cracks as explained earlier.

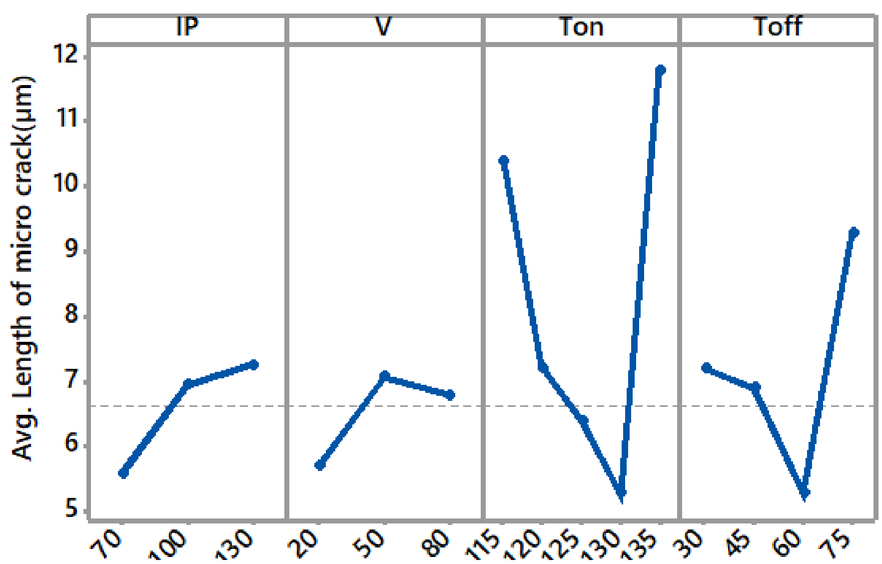

Figure 5.27 Effect of process parameters on average length of micro cracks for WEDM machined surface of P91 steel.

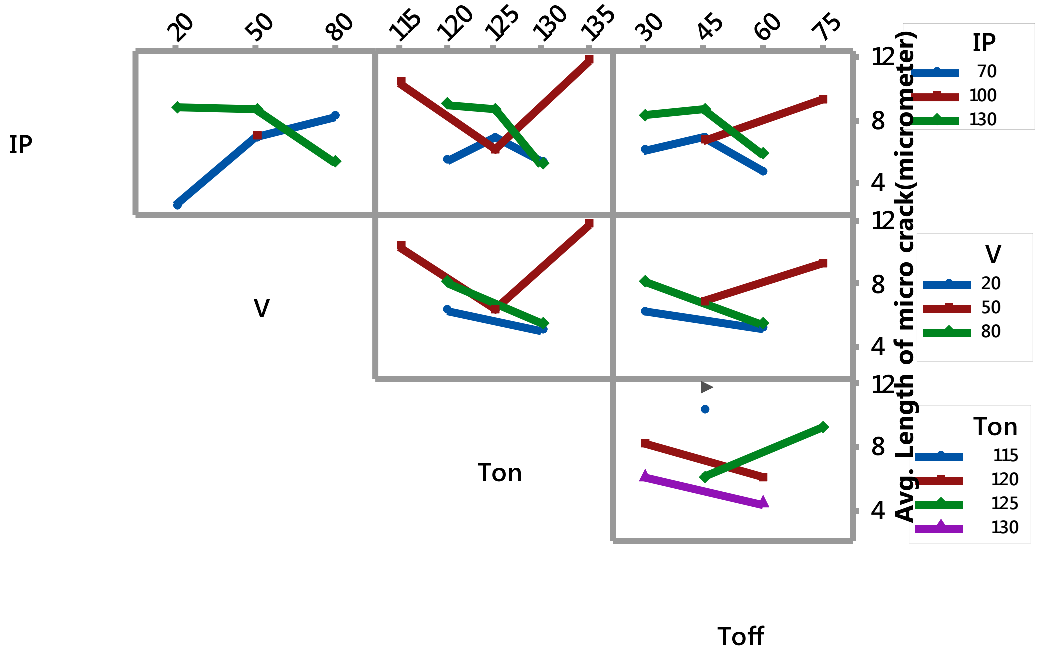

Figure 5.28 Interaction plot of process parameters for average length of micro cracks for WEDM machined surface of P91 steel.

5.5.3 Effect of process parameters on orientation of micro crack

Response surface analysis has been carried out for the prediction of process parameters in the orientation of micro-cracks preferably in the axial direction. It was observed from the 'ANOVA' table that effect of the process parameters considered has significant 'P" value (less than 0.05). Figure 5.29 shows that with less ($V \times T_{on}$), the % of axial cracks are less while increasing T_{on} the number of cracks increases. The fluctuation in the distribution of spark increases due to the probability of uneven distribution of spark energy. The probability of uneven distribution of discharge energy increases when discharge energy is higher. When voltage is higher the dielectric breaks down and spark occurs immediately and there is less time for even distribution of spark energy. The non-uniform distribution of energy causes cracks oriented in random directions. The thermal stresses lead to formation of micro cracks in the axial direction. It can be observed from the interaction plot shown in Figure 5.30, that the lowest percentage of axial cracks are present for product of discharge voltage and pulse on time ($V \times T_{on}$). Higher pulse on time increases the interaction time of the spark which facilitates fluctuation in the distribution of spark causing more cracks. Regression equation for number density of axial micro cracks in the machined surface is presented in equation below.

Regression equation

$$\begin{aligned} N_{da}(\%) = {} & 2680 - 6.52\,IP - 1.85\,V - 35.5T_{on} - 1.91T_{off} + .01867\,IP^2 - .02778\,V^2 \\ & + 0.1230{T_{on}}^2 + 0.01736{T_{off}}^2 - .00011\,IP.V + 0.0259\,IP.T_{on} \\ & - 0.00536\,IP.T_{off} + 0.0368\,V.T_{on} + 0.00214\,V.T_{off} + 0.0060T_{on}.T_{off} \end{aligned} \tag{5.15}$$

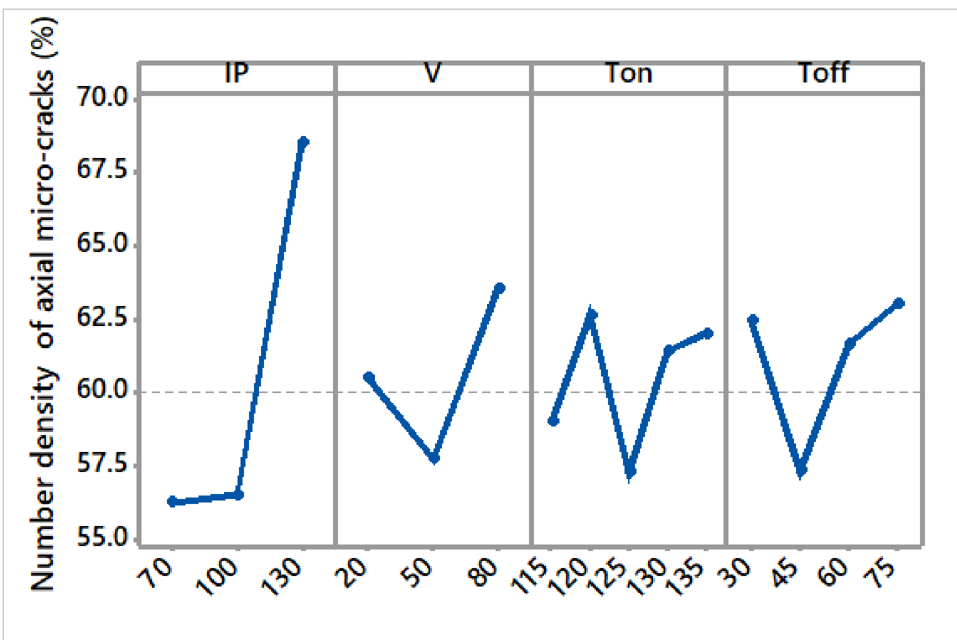

Figure 5.29 Effect of process parameters on number density of micro crack on WEDM machined surface of P91 steel.

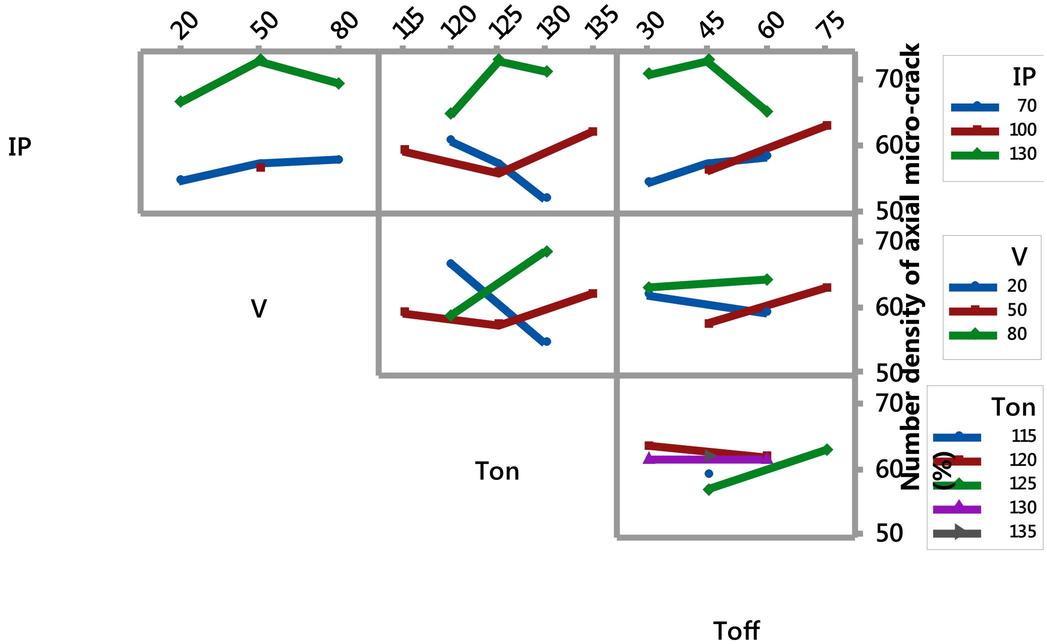

Figure 5.30 Two way interaction of process parameters on number density of micro crack on WEDM machined surface of P91 steel.

5.6 Optimization of Response parameters for P91

The response surface analysis discussed above shows that the level of process parameters significantly affects the surface integrity of the machined surface. Surface characteristics can be improved by optimizing the control parameters. Response optimization was carried out and optimum level of process parameter for best surface performance are presented in table 5-2. After optimization the length of micro cracks was minimised to 2.13 µm and number density of axial micro cracks was optimized from 70% (average) to 25.07%. Confirmation experiments with optimized process parameters was done to verify the computational result of the response surface optimization. The results shows good agreement with the predicted response as presented in Figure 5.31. The Average length of micro crack and the orientation of micro crack got reduced in the range of predicted results**.**

Table 5-2 Optimum process parameters for desired response

	Optimized response Parameter (RSM model)	Optimized Response parameter (confirmation experiment)
Parameters: IP: 70 A, Voltage: 55 V, T_{on}: 120 mSec, T_{off}: 30 mSec		
Surface roughness, R_a(µm)	0.852	0.813
Parameters: IP: 70 A, Voltage: 20 V, T_{on}: 123 mSec, T_{off}: 47 mSec		
Avg. Length of micro cracks (µm)	2.131	1.97
Parameters: IP: 91 A, Voltage: 20 V, T_{on}: 130 mSec, T_{off}: 45 mSec		
Number density of axial micro cracks (%)	25.07	26

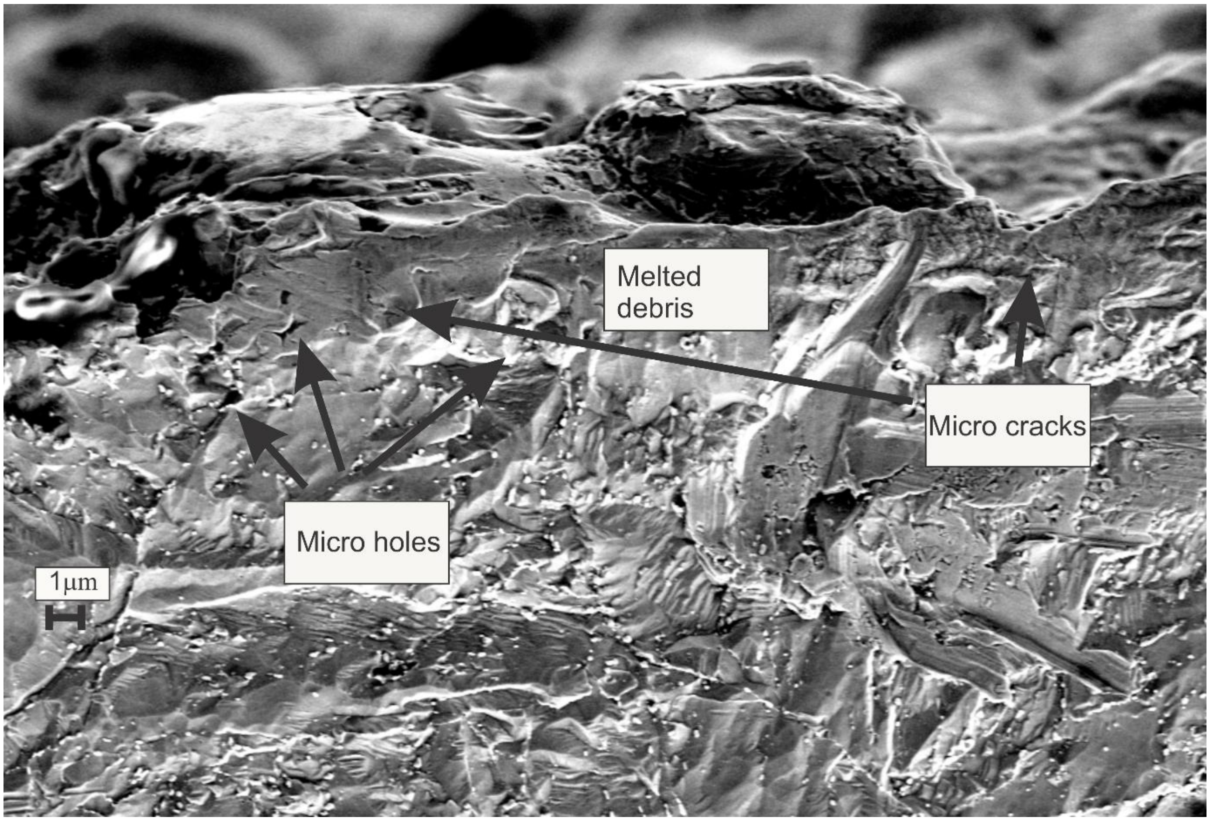

Figure 5.31 SEM image of machined surface using optimized process parameters for WEDM machined surface of P91 steel.

In manufacturing industry, the operator needs to select the process parameters to achieve desired surface characteristics. The response surface analysis study of WEDM gives best fit cutting parameters required for achieving desired surface roughness in P91. The contour plots of variation of different process parameters adjustments have been shown to achieve the optimized finish. Two process parameters have been fixed and variation of other two has been plotted. From the Contour plot in Figure 5.32, it can be observed that if the operator wants a surface roughness in the range 2.25-2.5 μm then he has to choose upon the values of spark off time somewhere around 50μs and voltage of the order of 55V with peak current value at 100A and spark on time at 125 μs.

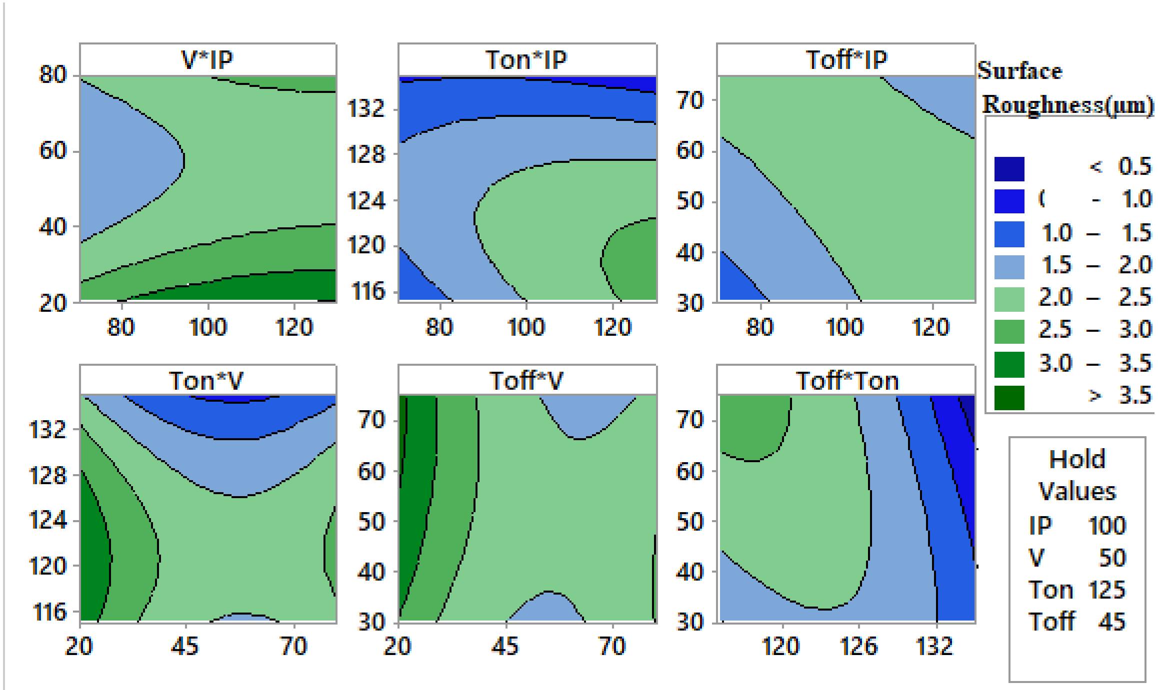

Figure 5.32 Contour plot for optimum process parameters for WEDM machined surface of P91 steel.

5.7 Optimized process parameters for WEDM of general industrial materials

This study gives an insight into extending the use of results obtained for WEDM machining of P91 for other materials used generally in manufacturing industry. The interesting microstructural observations and response surface optimization for WEDM machined surface of P91 inspired the researchers to do preliminary investigation through a similar approach in SS304, Aluminium, and Zircaloy. These materials were chosen for study because they are very frequently used in manufacturing industry. Samples of these three materials were machined at same energy and the machined surface was investigated using SEM to understand the effect of conductivity on the cut surface. The thickness of the recast layer, surface roughness, microstructure of the recast layer HAZ has been estimated experimentally. The size of crater in SS304 is of the order of 28 μm as shown in Figure 5.33. The corresponding modelling results of crater size is shown in Figure 5.34. The SEM image of the machined surface shows a large number density of porous blowholes which are caused due to emission of gases during electric discharge as shown in Figure 5.33. The SEM images of Zircaloy machined surface revealed that crater size is of the order of 39 μm as shown in Figure 5.35. The corresponding modelling results of crater size is shown in Figure 5.36, also the machined surface contains a large number of cracks oriented in different direction. This could be due to poor stability of spark. In aluminum the size of the crater is of the order of 19 μm and the surface has a repetitive pattern of spherical globules around the crater as shown in Figure 5.37. The corresponding modelling results of crater size is shown in Figure 5.38. Surface roughness of the machined samples under same energy condition was measured. This gives the idea of effect of thermal conductivity on the performance of machining. Table 5-3 shows the comparative result of surface roughness of the abovementioned materials measured experimentally. From the results it can be inferred that the size of crater and its morphology is also guided by the thermal conductivity and melting point of the material.The higher the thermal conductivity and lower the melting point the size of crater formed on the machined surface is larger. The comparative analysis of the machined surface of the abovementioned materials would help the operator to get an essence of effect of thermal conductivity of the machining performance and hence process parameters for machining can be selected wisely.

Table 5-3 Surface roughness of EDM machined surface of common industrial materials

Material	Melting point(°C)	Thermal conductivity (W/mK)	Surface roughness Ra(μm)
SS304	1450	16.2	3.33
Zircalloy	1850	21.5	3.43
Aluminium	660	210	4.28

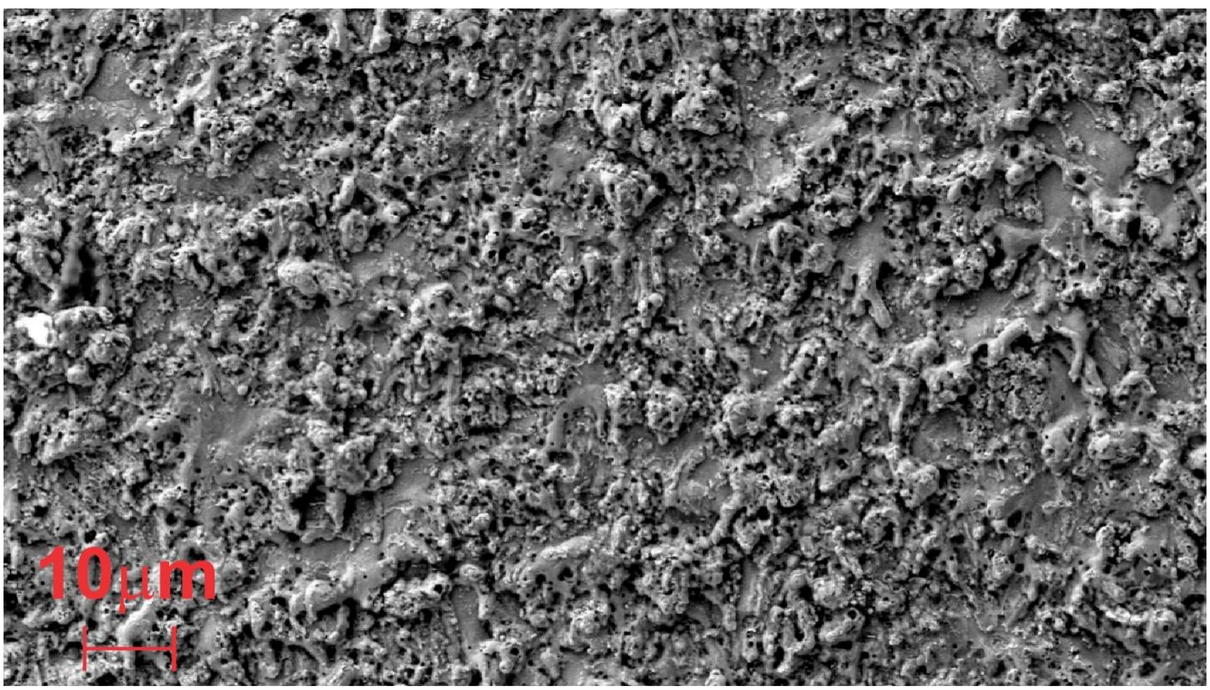

Figure 5.33 Machined Surface of SS304 at high energy condition (plan view).

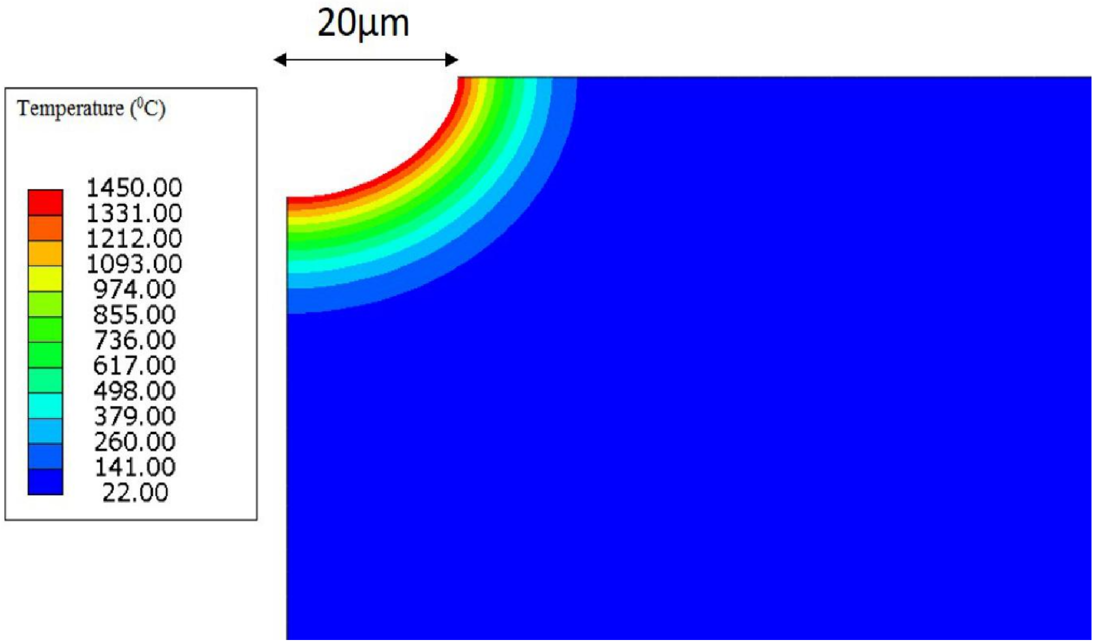

Figure 5.34 Thermal and Crater profile of SS304 under 5A estimated from numerical modelling.

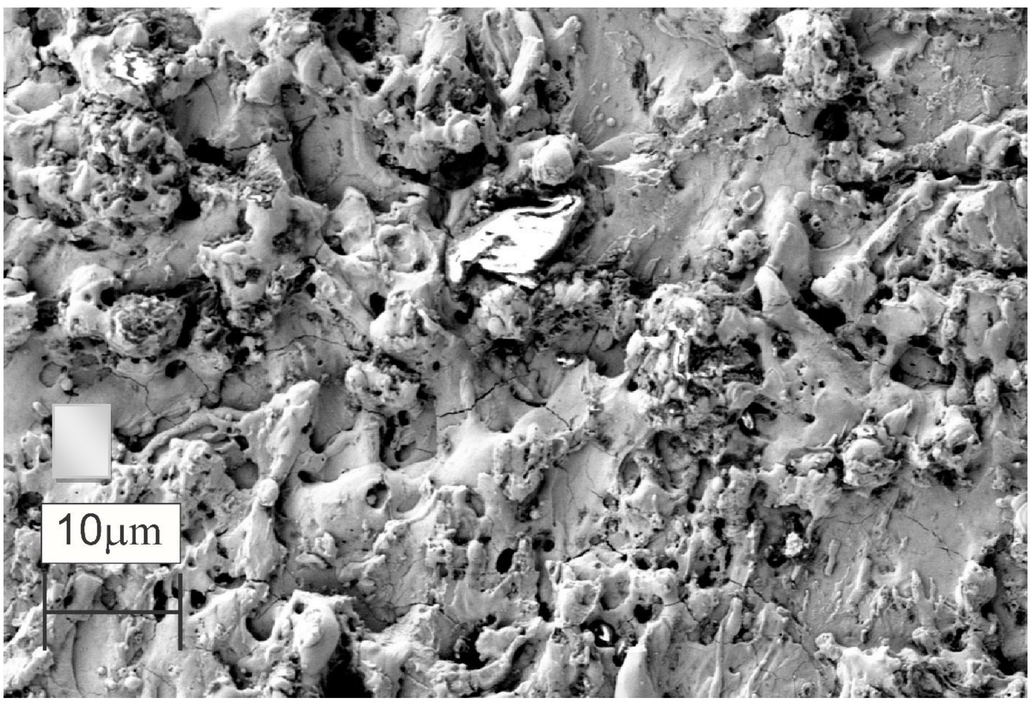

Figure 5.35 Machined Surface of Zircaloy at high energy condition (plan view).

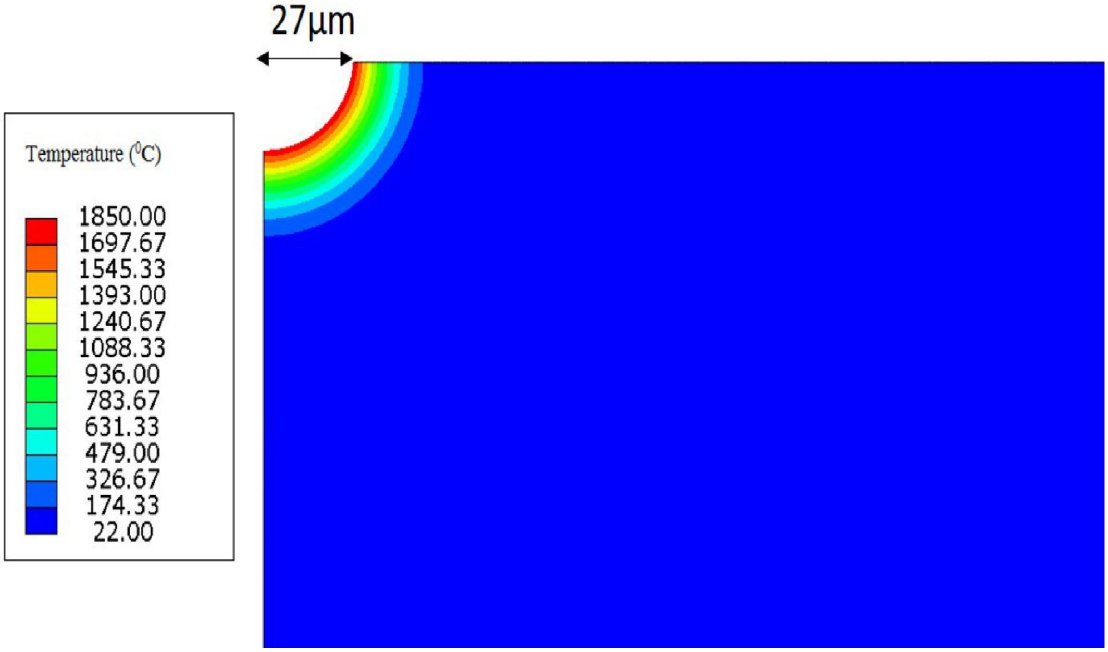

Figure 5.36 Thermal and Crater profile of Zircaloy under 5A estimated from numerical modelling.

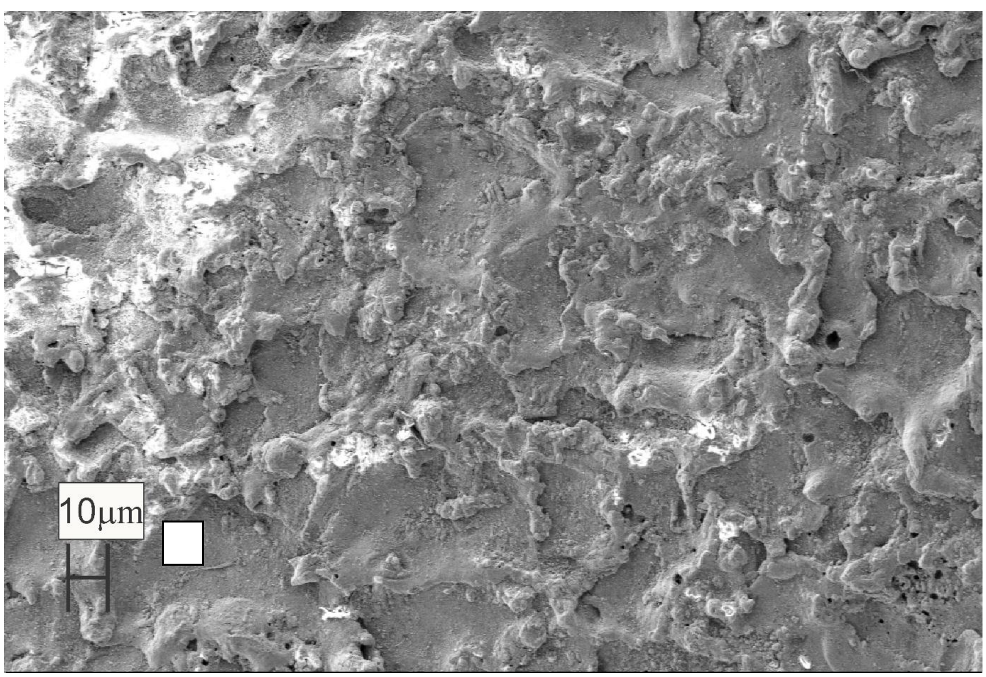

Figure 5.37 Machined Surface of Aluminum at high energy condition (plan view)

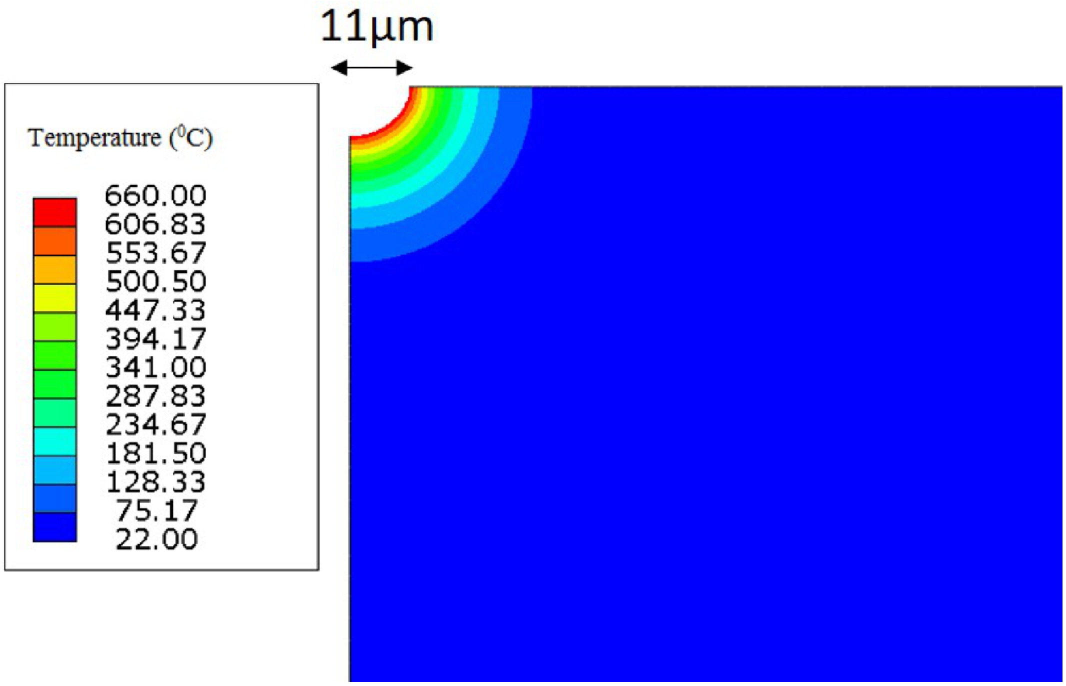

Figure 5.38 Thermal and Crater profile of Aluminium under 5A estimated from numerical modelling.

5.8 Conclusion

In the present research work, the effect of process parameters on the Wire Electric Discharge Machining of P91 has been investigated. Square channels of P91 were fabricated using WEDM technology [32]. To obtain the desired surface characteristics, a detailed study of the control parameters which have significant effect, on the response such as surface roughness, average length of micro cracks in the recast layer, orientation of the micro cracks in the recast layer is analyzed [32]. The results of the study can be concluded with the help of following points.

1. Recast layer is formed in WEDM of P91 and the layer has micro crack distributed in all directions. The thickness of the recast layer, the surface finish, the number density and the orientation of the cracks was found to depend on the machining conditions. The average length of micro crack varies from 2.2μm to 11.8μm under the experimental conditions explained earlier[32].
2. The surface finish was primarily governed by the presence of craters, their size and occurrence density, micro holes, craters, globules of un-expelled debris and spalled area. The formation of secondary craters could also be seen. Process parameters were optimized significantly reducing the formation of holes, voids and carters [32].
3. The heat generated and the cooling rates estimated were successfully used for explaining the underlying microstructure and the size of the craters of the machined surface [32].
4. The factors affecting the orientation of micro cracks was evaluated and the process parameters were optimized for orientation having minimal effect on fatigue life of the component [32].
5. Nano hardness of the machined surface was observed to decrease from the react layer to the parent material. The reduction of Nano hardness was more at higher peak current setting [32].
6. Desired surface characteristics could be achieved by optimizing the process parameters. In this study optimum process parameters for surface roughness, average length of micro crack and orientation of micro crack in the WEDM machined surface of P91 have been obtained [32].

7. The energy generation and heat transfer studies have given a new perspective for predicting the surface finish of the machined surface and for explaining the underlying microstructure. This approach could also be successfully tested for estimating the surface finish in other materials [32].

5.9 References

[1] Erdem Sireli, Nilufer Orhon, and Guldem Kartal Sireli, “Effects of wire-electro discharge machining process on surface integrity of WC-10Co alloy”, International Journal of Refractory Metals and Hard Materials, 64 (2017): 190-199.

[2] F.S. Van Dijck, and W. L. Dutre, “Heat conduction model for the calculation of the volume of molten metal in electric discharges”, Journal of Physics D: Applied Physics, 7 (1974): 899.

[3] P.V. Krakhmalev, Jacob Sukumaran, and Anders Gaard, “Effect of microstructure on edge wear mechanisms in WC–Co”, International Journal of Refractory Metals and Hard Materials, 25 (2007): 171-178.

[4] Han-Taw, Chen, and Lin Jae-Yuh, “Numerical analysis for hyperbolic heat conduction”, International Journal of Heat and Mass Transfer, 36 (1993): 2891-2898.

[5] R. Thomas Newton, et al, “Investigation of the effect of process parameters on the formation and characteristics of recast layer in wire-EDM of Inconel 718”, Materials Science and Engineering: A, 513 (2009): 208-215.

[6] Bulent Ekmekci, “Residual stresses and white layer in electric discharge machining (EDM)”, Applied Surface Science, 253 (2007): 9234-9240.

[7] Zhang Yanzhen, Liu Yonghong, Ji Renjie, and Cai Baoping, “Study of the recast layer of a surface machined by sinking electrical discharge machining using water-in-oil emulsion as dielectric”, Applied surface science, 257 (2011): 5989-5997.

[8] I. Maher, A. A. D. Sarhan, and H. Marashi, “Effect of Electrical Discharge Energy on White Layer Thickness of WEDM Process”, Comprehensive Materials Finishing, Elsevier (2016): 231-266.

[9] L. Tang, and Y. F. Guo, “Electrical discharge precision machining parameters optimization investigation on S-03 special stainless steel”, The international Journal of advanced manufacturing Technology, 70 (2014): 1369-1376.

[10] J. T Huang, Y. S. Liao, and W. J. Hsue, “Determination of finish-cutting operation number and machining-parameters setting in wire electrical discharge machining”, Journal of Materials Processing Technology, 87 (1999): 69-81.

[11] Ahmet Hasçalýk, and Ulaş Çaydaş, “Experimental study of wire electrical discharge machining of AISI D5 tool steel”, Journal of Materials Processing Technology, 148 (2004): 362-367.

[12] Hwa-Teng Lee, and Jiahn-Piring Yur, “Characteristic analysis of EDMed surfaces using the Taguchi approach”, Materials and Manufacturing Processes, 15 (2000): 781-806.

[13] C. Pandey, and M. M. Mahapatra, “Evolution of phases during tempering of P91 steel at 760ºC for varying tempering time and their effect on microstructure and

mechanical properties", Proceedings of the Institution of Mechanical Engineers, Part E: Journal of Process Mechanical Engineering, 231 (2017): 1141-1161.

[14] C. Pandey, and M. M. Mahapatra, "Effect of heat treatment on microstructure and hot impact toughness of various zones of P91 welded pipes", Journal of Materials Engineering and Performance, 25 (2016): 2195-2210.

[15] G. Kibria, B. R. Sarkar, B. B. Pradhan, and B. Bhattacharyya, "Comparative study of different dielectrics for micro-EDM performance during microhole machining of Ti-6Al-4V alloy", The International Journal of Advanced Manufacturing Technology, 48 (2010): 557-570.

[16] Vikram Singh, Vikram, and S. K. Pradhan, "Optimization of WEDM parameters using Taguchi technique and response surface methodology in machining of AISI D2 steel", Procedia Engineering, 97 (2014): 1597-1608.

[17] D. Daryl DiBitonto, Philip T. Eubank, Mukund R. Patel, and Maria A. Barrufet, "Theoretical models of the electrical discharge machining process. I. A simple cathode erosion model", Journal of applied physics, 66 (1989): 4095-4103.

[18] S. Bhattacharya, N. Tiwari, A. Mishra, S. Mitra, G. K. Dey, and S. Ghorui, "Underwater Electrical Discharges: Temperature, Density and Basic Instability Features with Different Anode Materials", Plasma Chemistry and Plasma Processing, 39 (2019): 1019-1048.

[19] Shantanu Shahane, and S. S. Pande, "Development of a thermo-physical model for multi-spark wire EDM process", Procedia Manufacturing, 5 (2016): 205-219.

[20] P. Govindan, and Suhas S. Joshi, “Analysis of micro-cracks on machined surfaces in dry electrical discharge machining”, Journal of Manufacturing Processes, 14 (2012): 277-288.

[21] S. Jithin, Upendra V. Bhandarkar, and Suhas S. Joshi, “Analytical simulation of random textures generated in electrical discharge texturing”, Journal of Manufacturing Science and Engineering, 139 (2017): 111002.

[22] Mohammadreza Shabgard, Reza Ahmadi, Mirsadegh Seyedzavvar, and Samad Nadimi Bavil Oliaei, “Mathematical and numerical modeling of the effect of input-parameters on the flushing efficiency of plasma channel in EDM process”, International Journal of Machine Tools and Manufacture, 65 (2013): 79-87.

[23] G. Vimalan, G. Ravichandran, and V. Muthupandi, “Phase transformation behaviour in P91 during post weld heat treatment: a gleeble study”, Transactions of the Indian Institute of Metals, 70 (2017): 875-885.

[24] S. Haribabu, C. Sudha, S. Raju, R. N. Hajra, R. Mythili, J. Jayaraj, S. Murugesan, and S. Saroja, “Effect of Al Addition on the Microstructure and Phase Stability of P91 Ferritic-Martensitic Steel”. Metallurgical and Materials Transactions A, 50 (2019): 1421–1436

[25] Dean Deng, and Hidekazu Murakawa, “Prediction of welding residual stress in multi-pass butt-welded modified 9Cr–1Mo steel pipe considering phase transformation effects”, Computational Materials Science, 37 (2006): 209-219.

[26] A. H. Yaghi, T. H. Hyde, A. A. Becker, and W. Sun, “Finite element simulation of welding and residual stresses in a P91 steel pipe incorporating solid-state phase

transformation and post-weld heat treatment", The Journal of Strain Analysis for Engineering Design, 43 (2008): 275-293.

[27] M. Kunieda, Bert Lauwers, Kamlakar P. Rajurkar, and B. M. Schumacher, "Advancing EDM through fundamental insight into the process", CIRP annals, 54 (2005): 64-87.

[28] Jin Wang, Y. B. Guo, Cheng Fu, and Zhixin Jia, "Surface integrity of alumina machined by electrochemical discharge assisted diamond wire sawing", Journal of Manufacturing Processes, 31 (2018): 96-102.

[29] J.F Liu, and Y. B. Guo, "Residual stress modeling in electric discharge machining (EDM) by incorporating massive random discharges", Procedia CIRP, 45 (2016): 299-302.

[30] S. Rajesha, C. S. Jawalkar, Radha Raman Mishra, A. K. Sharma, and Pradeep Kumar, "Study of recast layers and surface roughness on Al-7075 metal matrix composite during EDM machining", International Journal of Recent advances in Mechanical Engineering, 3 (2014): 53-62.

[31] Nadeem Faisal, Divya Zindani, and Kaushik Kumar, "Micro and Nano Machining—An Industrial Perspective", Micro and Nano Machining of Engineering Materials. Springer, Cham, (2019). 9-29.

[32] S. Bhattacharya, A. Mishra, N.Keshkar, S. Kumar, V.Kain, G.K.Dey, " Wire Electric-Discharge Machining (WEDM) of P91 Steel- Microstructure and Thermal Modelling Studies", Metallurgical transactions A, 50 (2019): 5336–5355.

Chapter 6

Corrosion study of wire EDM machined surface of P91 steel

6.1 Introduction

The P91 steel is widely used in the energy industry due to its excellent mechanical properties such as high creep strength, high thermal conductivity, low thermal expansion, good corrosion resistance and good mechanical properties after irradiation [1-3]. It is identified as a candidate material for structural components of Generation IV nuclear power plants and fusion reactors [3, 4]. The wire electrical discharge machining (WEDM) process is used for manufacturing of certain intricate structural components for nuclear reactors. WEDM is preferred in terms of its capability to produce high precision contours of complex geometry with tight tolerance as it is a non-contact type machining method [5-6]. Subsequently as the discharge phase ends an implosion of plasma channel takes place resulting in parts of the molten metal getting deposited on to the EDM surface as re-solidified layer (also known as recast layer). The recast layer in WEDM recast layer constitutes a dendritic structure [7] whereas at other times it also comprises of dendrites and columnar structures [8-9]. The dielectric medium also has some effect on the microstructural constituents of the recast layer [7, 10-11]. In the presence of water as medium it is observed that there is incorporation of oxides in recast layer and with oil medium there is increased carbon content. The top surface of the recast layer could be amorphous [8] or crystalline [12-13]. Klocke et al. [9] observed that upper portion of recast layer is amorphous and the lower half which is nearer to parent material is crystalline in tool steels. These recast layers are generally harder than the bulk alloy due to presence of carbides and oxides. In case of carbon free alloys, the recast layer hardness is comparable to the hardness of bulk alloy. The thickness of recast layer/recast layer is a function of spark energy and current. Due to high cooling rates in WEDM process thermal stresses get generated leading to cracks in the recast layer. Below the recast layer is a heat- affected zone (HAZ) which can be composed of different microstructural layers, depending on the alloy composition [7-12].

The WEDM surface containing recast layer has many inhomogeneties on the surface such as cracks and pores [8-10]. These surfaces are potential sites for initiation of localized corrosion if exposed to an aggressive environment. The EDM surface corrosion resistance has been studied for different alloy systems [5, 14-17]. In the available literature on corrosion resistance of EDM surfaces of alloys there are many contradictory observations. Yan et al. [14] in his studies on Al-Zn-Mg alloy machined by EDM showed better uniform corrosion resistance in 10%NaOH environment as compared to that of ground surface. The improved resistance was assigned to formation of an amorphous layer in the recast layer. Ntasi et al., [15] showed inferior corrosion resistance to pitting and crevice corrosion of EDM machined Cr-Co alloys and Ti alloy as an implant material. Uno et al. [16] showed that corrosion resistance for electron beam machined surfaces was better than that of EDM cut surfaces of low alloy steel. Selective dissolution of Co was observed in composites made of WC-Co after EDM machining [17]. There is no literature available on corrosion evaluation of P91 WEDM surfaces. The present chapter involves the electrochemical evaluation of P91 steel WEDM cut surfaces for its passivation in different pH buffer solution and sulphuric acid and localized corrosion resistance in sulphuric acid and sodium chloride environments. The intergranular corrosion behaviour of P91 steel was also studied.

Two P91 steel WEDM surfaces namely Face1 and Face 2 were used for comparison with diamond polished surface finished with 0.5 µm diamond paste. The WEDM process parameters varied for Face 1 and Face 2 in terms of peak current 70A and 130A, voltage 80V and 20V and spark off time of 30 µsec and 60 µsec respectively. A typical polarization curve has been shown in Figure 6.1.

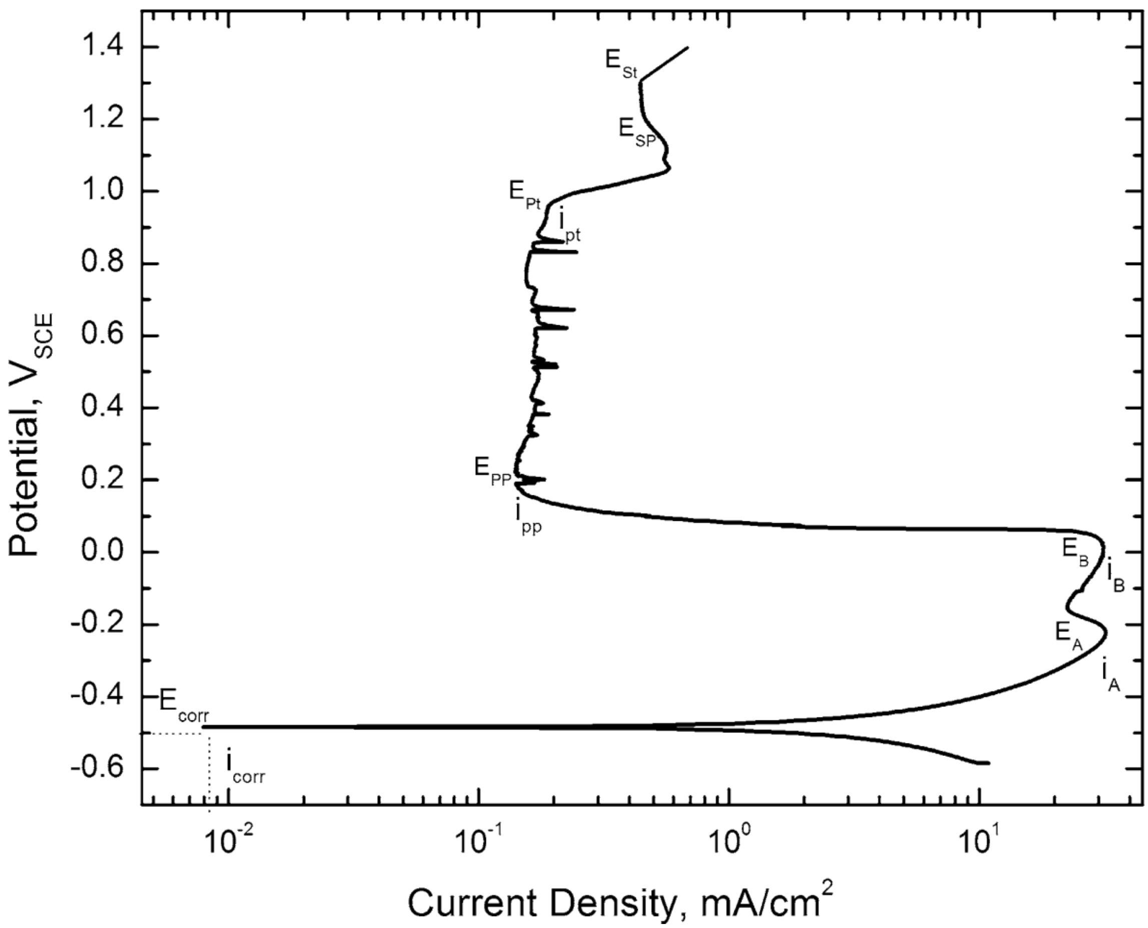

Figure 6.1 Representative polarization plot describing the electrochemical parameters that are evaluated in the present electrochemical investigation of P91steel.

6.2 Results & Discussion

6.2.1 Microstructural characterization

The cross-sectional microstructure for WEDM surface of P91 steel was observed under SEM wherein the outermost layer which is around 2-8 μm thick is a solidified layer due to implosion of the plasma channel which is termed as the recast layer (Figure 6.2). The thickness of recast layer is calculated by finding the area of the recast layer and dividing by length as the thickness of the recast layer is not uniform over the surface [7-12]. The recast layer is non-uniform and showed multiple layers of deposition. It has micro cracks and pores which extend till heat affected zone (HAZ) region (Figure 6.3). Figure 6.4 shows that it has dendritic structure with different phases present like the martensite needles, retained austenite and carbides. The recast layer also has a finer multi grain structure and is amorphous in nature as observed under TEM diffraction. The grain size calculated using the annular ring gap is 10^{-10} m. Subsequently the grain size increases in the HAZ to the order of tens of micrometer. In the diamond-polished surface which is the bulk structure of the WEDM surface depicted as parent metal in Figure 6.2, the microstructure is predominantly tempered martensite with carbides there could also be fine MX_2 carbides or nitrides within the ferrite [18-19].

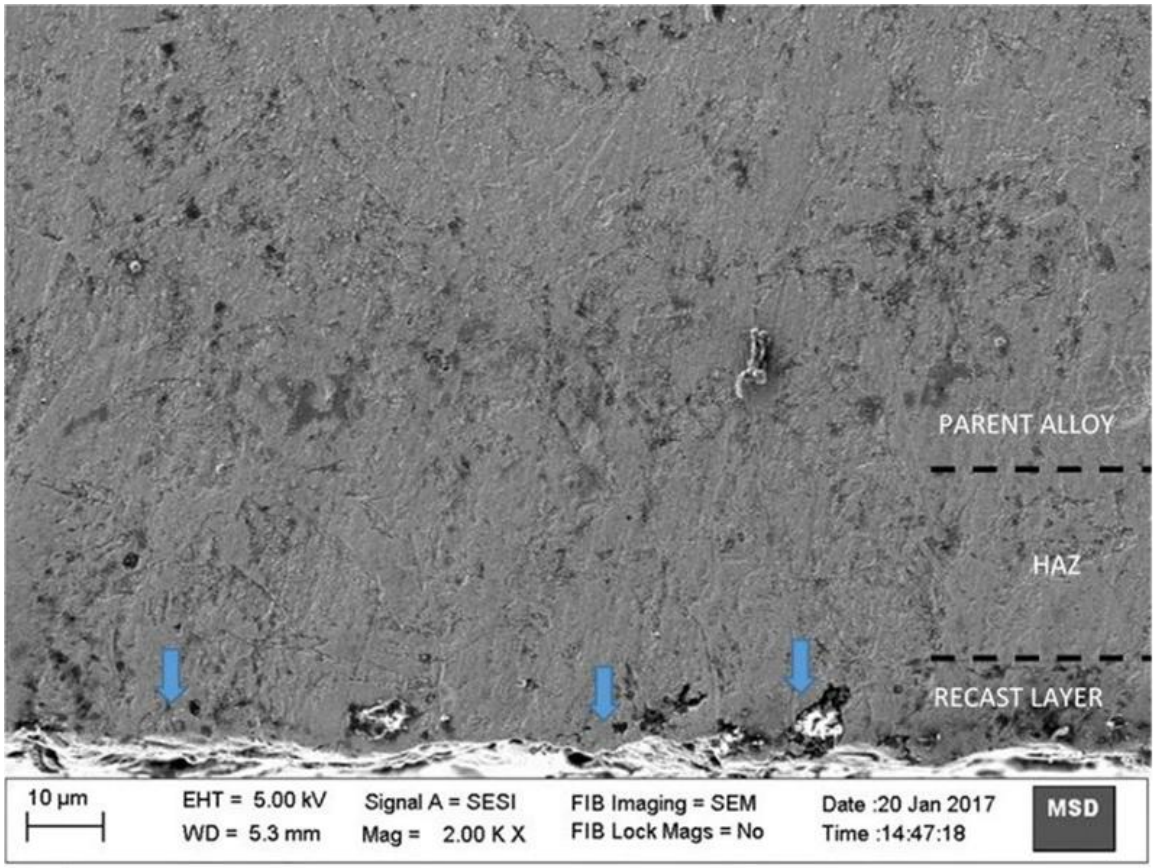

Figure 6.2 SEM of the cross section of the EDM surface P91 showing the three distinct microstructural layers and presence of pores (marked by arrows) in the recast layer.

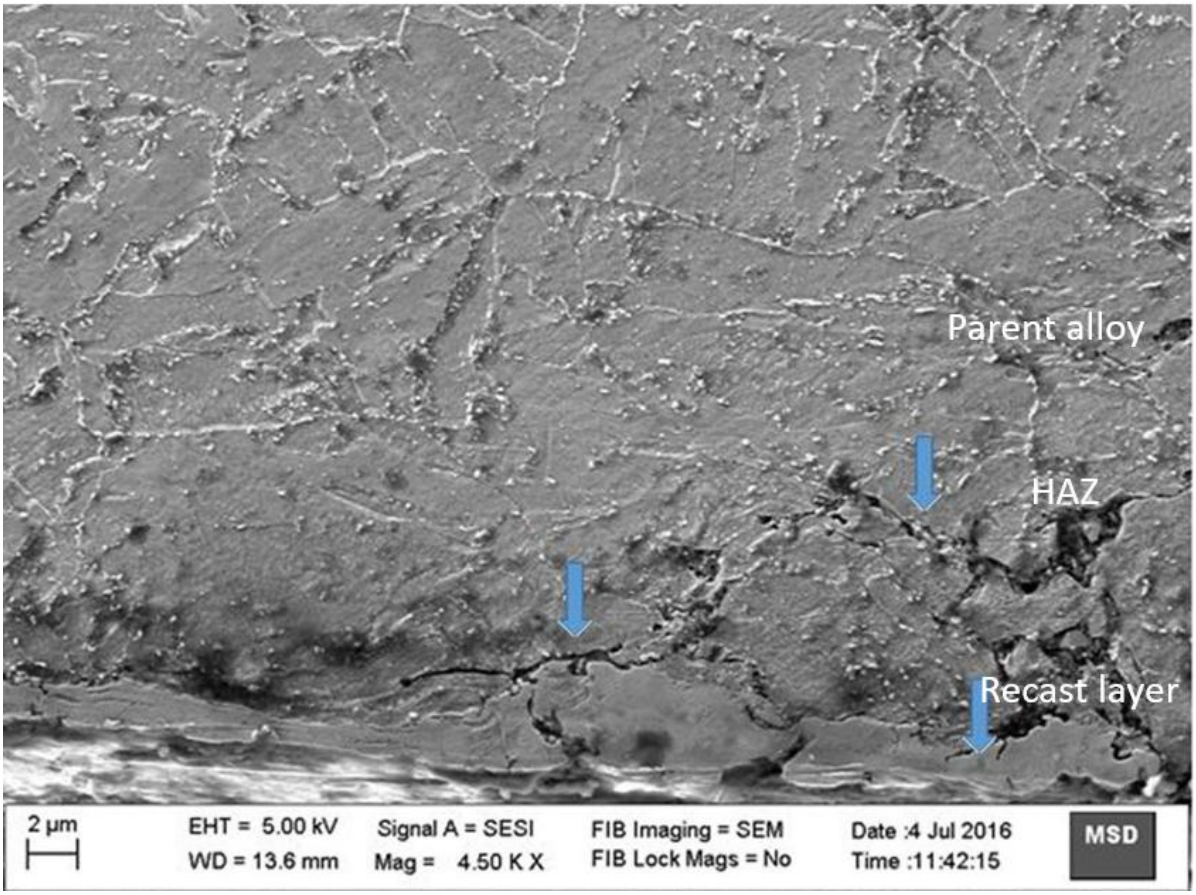

Figure 6.3 SEM of the cross section of the EDM surface P91 showing presence of cracks (marked by arrow) in the recast layer extending to the HAZ.

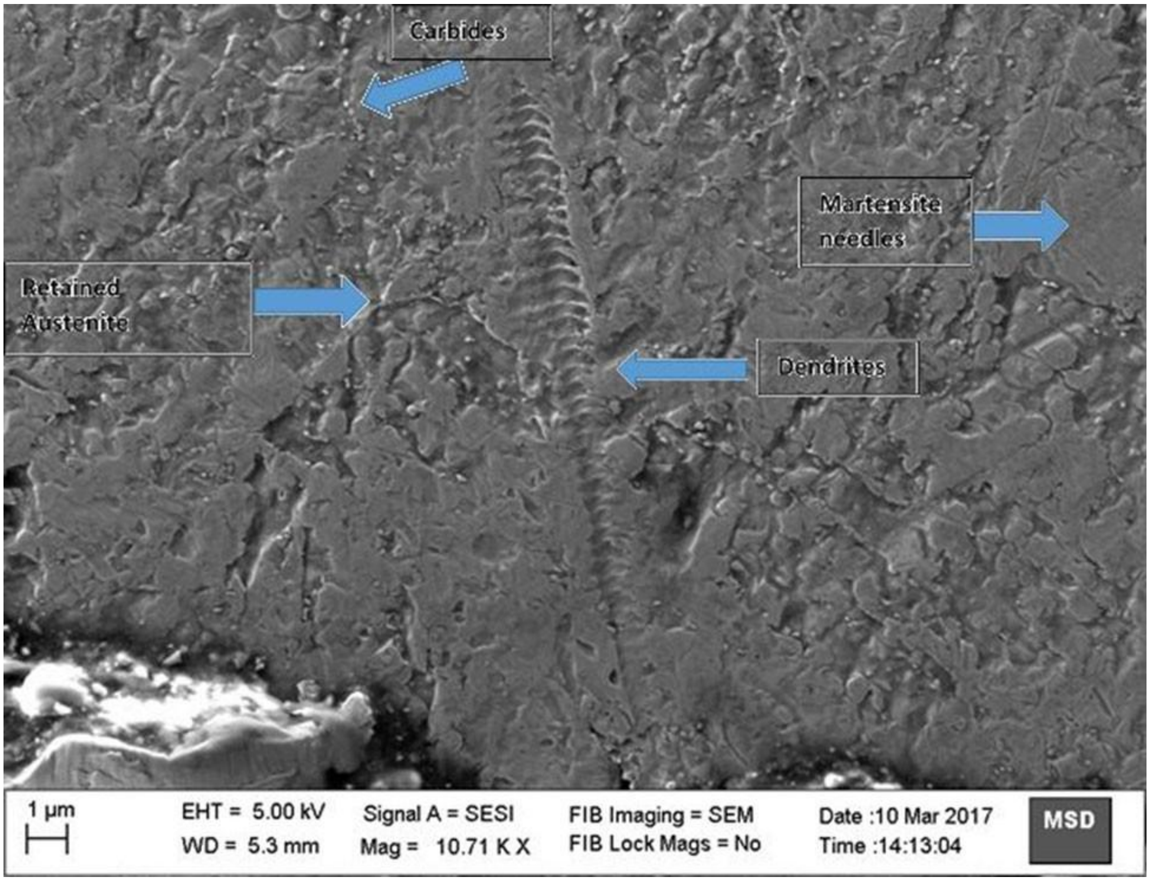

Figure 6.4 SEM of recast layer of EDM surface 1 of P91 steel showing dendrites, carbides along retained austenite boundaries and marten- site needles.

6.2.2 Electrochemical characterization

The electrochemical evaluation to understand the general passivation behavior was done in three buffer solutions of different pH (4, 7 & 9). The two WEDM surfaces and diamond polished surface of P91 steel were also exposed to sulphuric acid environment and after addition of chloride. The electrochemical measurements in buffer solutions and in sulphuric acid with varying surface conditions of P91 steel give an insight on passivation and the passive film stability. Potentiodynamic studies were also carried out with sulphuric acid in the presence of chloride to understand the pitting corrosion resistance. The DL-EPR studies were done for WEDM and diamond polished surfaces of P91 steel for evaluating the susceptibility to IGC.

6.2.3 In pH-4 solution

The exposure of the two WEDM and polished P91 steel surface was carried out in sodium diphosphate with potassium diphosphate (pH-4) buffer solution [20]. In Figure 6.5, the diamond polished surface of P91 steel showed better passivity in acidic pH as compared to WEDM surface. The E_{corr} potential is anodic for WEDM surface (-0.038V_{SCE}) as compared to that for diamond polished surface (-0.564 V_{SCE}). The Ecorr potential of diamond polished surface being more cathodic to WEDM surface indicates that the cathodic reactions reduced for the WEDM cut surfaces in the buffer solution (pH 4). The potentiodynamic plots show the presence of two passivity regimes in the given environment. The passivity at lower potentials is termed as primary passivity and at higher potential it's termed as secondary passivity. Similar behaviour has been found in sulphuric acid environment by Geogy et al. [19]. The primary passivity is attributed to the formation of chromium oxide layer and the secondary passivity to the iron oxide layer [21]. Due to the presence of two passive regions there are two transpassive dissolution regimes. Bojinov et al. [22] observed the two-stage transpassivity in the Fe-Cr alloys. The first transpassivity is due to initial dissolution of Cr^{+3} to Cr^{+4} but the dissolution rates are not high since Fe^{+3} ions present in the passive layer obstructs the further dissolution resulting in the second passivity observed. In case of transpassive dissolution at higher potentials, Cr^{+3} gets converted to Cr^{+6} resulting in increased current density. Though the primary passive film stability for WEDM surface is poor resulting in the first transpassive dissolution at 0.42 V_{SCE} (E_{pt}) while the primary passive film break down is observed for polished surface only after 0.88 V_{SCE} (E_{pt})(Figure 6.5). The WEDM surface already has some iron oxide (Fe_2O_3& Fe_3O_4) present and subsequently there is a mixed oxide of Fe_2O_3 and Cr_2O_3 that gets formed on the surface as observed in Raman plots (Figure 6.6). The Raman peak identification for iron oxide and chromium oxide is based on literature data [23, 24]. Since we have a P91 steel where the Cr content is 9 wt%, the passive film that gets formed will have lesser concentration of Cr_2O_3 and more of Fe_2O_3. It has been reported that a presence of chromium above 13 wt% in the alloy results in a Cr_2O_3 dominated passive film [25]. In case of breakdown of secondary passivity, it takes place almost at the same potential of 1.3 V_{SCE} on both the surfaces. The primary passivity is also governed by the oxide layer which is formed during the WEDM operations on the P91 surface due to its interaction with the dielectric medium and air. The passivity behaviour of the WEDM face 1 and face 2 seems to be almost the same. The corrosion rates in table 6-1are comparatively higher for P91 steel for both WEDM and diamond polished surfaces in the pH-4 solution compared to pH-7 and 9 solutions primarily because it is in acidic regime. Table 6-2 shows that the WEDM parameter variations have not brought about any formidable change in surface microstructure and composition which should result in significant effect on electrochemical response of the surfaces.

Table 6-1 Corrosion potential (E_{corr}), corrosion current density (i_{corr}) and corrosion rate (CR) in mils per year (mpy) of P91 steel in acidic, neutral and basic environment

P91 Surface condition	pH-4 solution			pH-7 solution			pH-9 solution		
	E_{Corr} V_{SCE}	i_{Corr} mA/cm^2	CR mpy	E_{Corr} V_{SCE}	i_{Corr} mA/cm^2	CR mpy	E_{Corr} V_{SCE}	i_{Corr}, mA/cm^2	CR Mpy
EDM Face-1	-0.038	3.23E-5	0.015	-0.133	8.45E-6	0.004	-0.200	5.27E-6	0.003
EDM Face-2	-0.054	1.45E-5	0.006	-0.163	3.69E-6	0.001	-0.174	4.45E-6	0.002
Diamond polished	-0.564	1.99E-5	0.009	-0.248	1.48E-6	0.006	-0.196	9.22E-7	0.0004

Table 6-2 Corrosion potential (E_{corr}), corrosion current density (i_{corr}) and corrosion rate (mpy) in H_2SO_4 and NaCl

P91 Surface condition	0.5M H_2SO_4			0.5M H_2SO_4 + 0.25M NaCl		
	E_{Corr} V_{SCE}	i_{Corr} mA/cm^2	CR mpy	E_{Corr} V_{SCE}	i_{Corr} mA/cm^2	CR mpy
EDM Face-1	-0.484	0.00793	3.62	-0.463	0.03004	13.69
EDM Face-2	-0.489	0.00303	1.38	-0.473	0.04401	20.06
Diamond polished	-0.501	0.00397	1.81	-0.496	0.00837	3.82

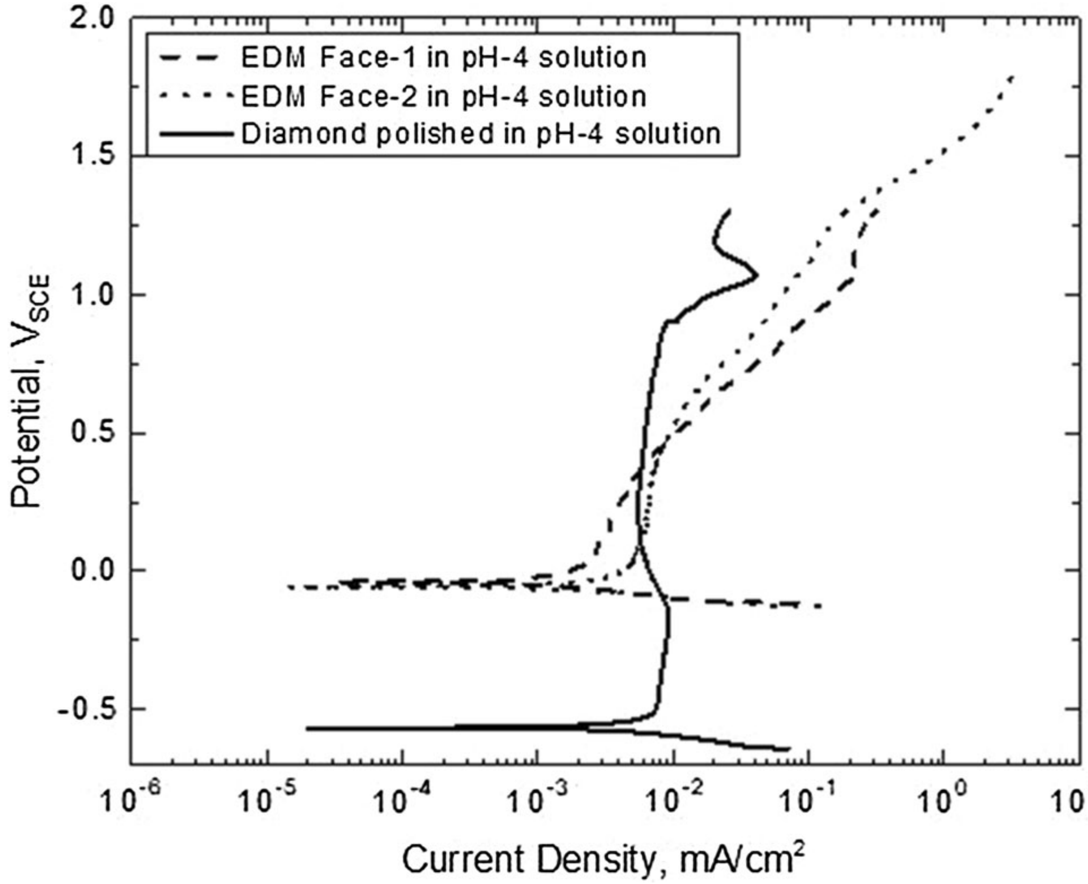

Figure 6.5 Potentiodynamic plot for EDM and diamond polished P91 steel in pH-4 buffer solution.

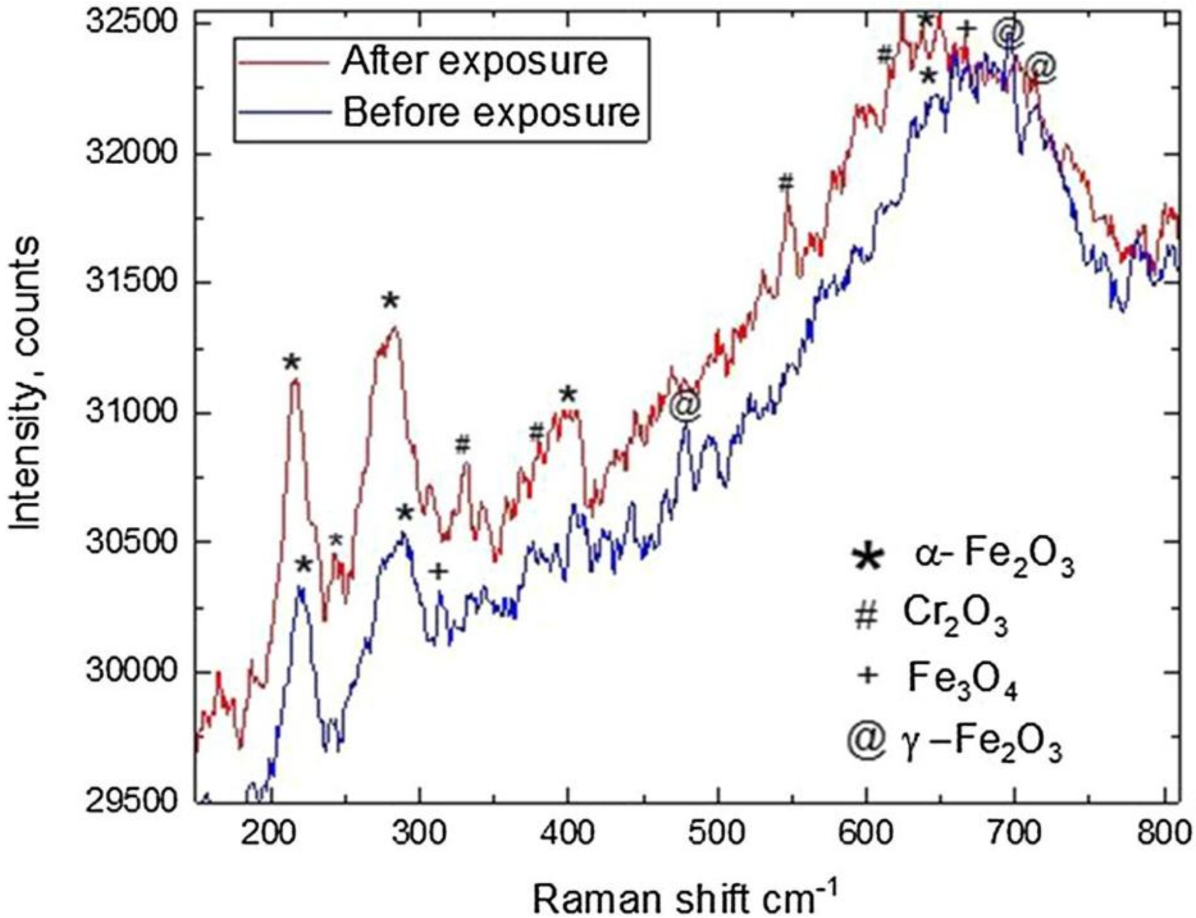

Figure 6.6 Raman plot for EDM P91 steel in pH-4 buffer solution (a) before exposure and (b) after exposure showing presence of iron and chromium oxide.

6.2.4 In pH-7 solution

The buffer solution, a mixture of sodium hydroxide and sodium diphosphate was used to evaluate the passivation behaviour in neutral pH [26]. In Figure 6.7, it is clearly observed that the E_{corr} potential is slightly anodic for WEDM surfaces. The increased corrosion potential as seen in table 6-1 is a result of the prior oxide film present on WEDM surfaces as compared to the diamond polished surface of P91. But the primary passive current densities (i_{pp}) are almost the same indicating that in neutral environment the passivation tendency of the WEDM and polished surfaces is nearly the same. The neutral pH environment is less aggressive to the P91 surface resulting in an instantaneous formation of passive film. The passivation current densities are one order of magnitude lower than in the pH-4 solution due to increased stability of the film that gets formed in this environment. The potentiodynamic plot also shows the presence of two passivity regions which is characteristic of Fe-Cr steels [19]. The primary passivity region for the WEDM surfaces is about 0.6 V_{SCE} which is 200 mV larger than the pH-4 passivity region indicating stability of film in the environment. The secondary transpassive potential (E_{st}) for P91 steel for the two different surfaces in this environment is 1.0 V_{SCE}. The corrosion rates tabulated in table 6-1 show that the corrosion rates are very low and the neutral solution results in lower corrosion current densities. The shift in E_{corr} potential to the anodic region indicates oxide formation as soon as the P91 steel surface is immersed.

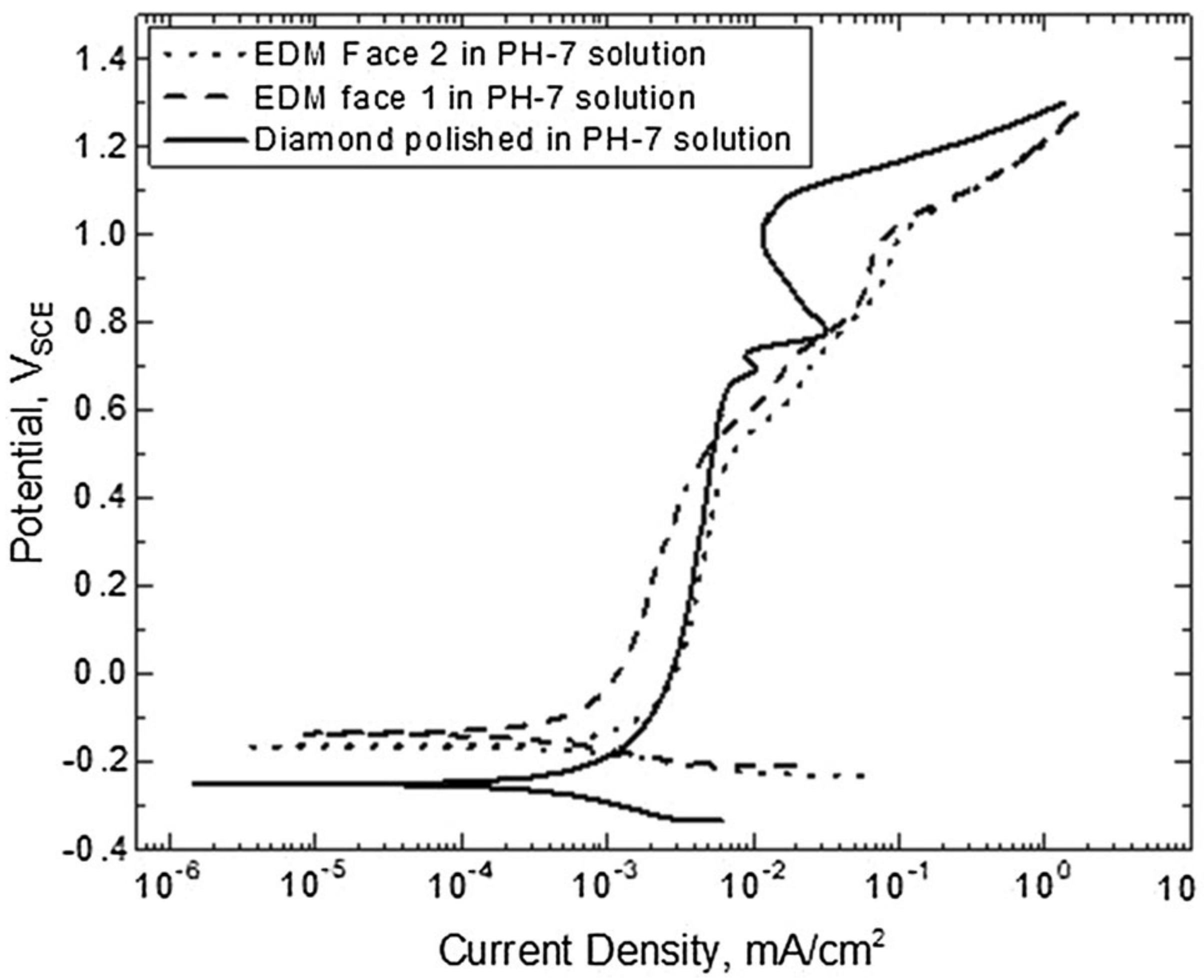

Figure 6.7 Potentiodynamic plot for EDM and diamond polished P91 steel in pH-7 buffer solution.

6.2.5 In pH-9 solution

In the alkaline borate buffer solution [26], the corrosion behaviour of the EDM and polished surface was almost similar. In Figure 6.8, E_{corr} potential and primary passive current density (i_{pp}) is almost the same for both the surfaces. The only difference is in terms of the secondary passivation (i_{sp}) where the passive film growth and stability is less for WEDM surfaces. The passivity in ferritic steels is due to formation of corrosion products of dissolved metal ions in the environment tested. The primary passivity is a result of the formation of chromium hydroxide while secondary passivity is due to iron oxide formation. Table 6-1 gives an insight into the corrosion rates of the surfaces of P91steel in the pH-9 solution which is very low and comparable to the corrosion rates in pH-7 solution. The lower rates of corrosion are linked to the less aggressive nature of the solution and the metal surface reactivity to alkaline solution. The diamond polished surface in the pH-9 solution has the least corrosion rates as the surface is instantly passivated in the given alkaline environment. The primary passive current density (i_{pp}) obtained for the surfaces of P91 steel is around 10^{-6} A/cm^2. The primary passivity is stable till 0.5 V_{SCE} after which there is a gradual increase in the current values as the potentials are increased. This increase is due to the constituent metal ions such as Fe and Cr dissolution in passive film. The secondary passivity is again a result of the Cr dissolution being curtailed by the Fe^{+3} ions that are forming at the primary transpassive potential (E_{pt}).

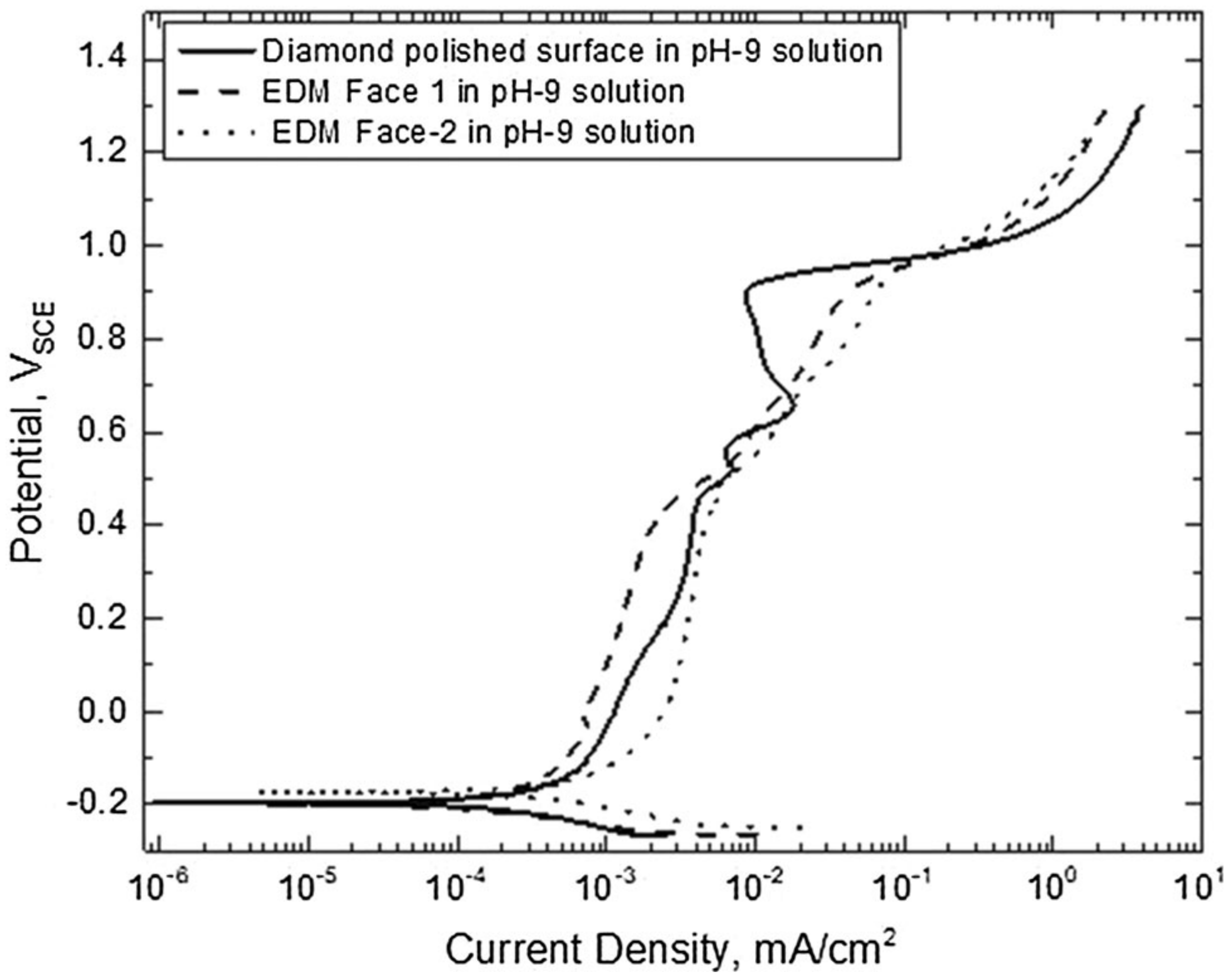

Figure 6.8 Potentiodynamic plot for EDM and diamond polished P91 steel in pH-9 buffer solution.

6.2.6 In H_2SO_4 solution

The polarisation behaviour of P91 steel in 0.5M H_2SO_4 solution shows a very different dissolution and passivation behaviour. There is presence of two anodic dissolution peaks denoted as E_A and E_B in Figure 6.9. The first anodic peak is the active dissolution of the elements that are present in the alloy simultaneously at rates nearly proportional to their bulk composition**.** There are various interpretations to this second anodic peak in literature such as attack along the chromium depleted region along grain boundaries due to sensitization, the oxidation of hydrogen absorbed during the open circuit corrosion, oxidation of nickel sulphide and dissolution of the copper layer deposited on surface. The peak observance cannot be pin pointed to one phenomenon. In the present case, though during the immersion of the P91 steel in the sulphuric acid environment at open circuit potential there was formation of a black layer which is the corrosion product of the dissolved elements reacting with the environment. Hence the i_{corr} values are very low as shown in table 6-2. These corrosion products would act as a catalyst for hydrogen ion reduction which would shift the open circuit potential to noble potentials and result in the increased anodic dissolution. The second peak could probably be due to dissolution of the different alloying elements such as Fe, Cr, Mo at distinct potentials. The pH of the solution used is zero. This makes the steel active during the initial scan subsequently there is formation of the chromium hydroxide which results in initial passivation at 0.15 V_{SCE} and the secondary passivation takes place as iron hydroxide also get formed on the surface at higher scanned potentials. The occurrence of primary passivity and secondary passivity in ferritic steels in sulphuric acid is well documented [21]. Generally, native oxide film that forms on Fe-Cr alloys have double layer. The inner layer being spinel oxide of Fe and Cr while the outer oxide layer is Cr_2O_3 layer [27]. The primary passive current density values for the WEDM surface P91 was one order of magnitude less than the diamond polished surface. The lowered primary passive current density is a result of presence of oxide film on the WEDM surfaces which would aid in the easy passivation of the remainder bare surface on the P91 steel. The potentio dynamic plot for P91 WEDM surface almost matches with the potentiodynamic response from P91 weld metal as observed in the studies carried out by Geogy et al. [19]. The passivation studies carried out by Geogy et al. [19] in 0.5 M H_2SO_4 solution for weldments of 9Cr-1Mo steel showed that the weld metal had the worst corrosion resistance in the medium. This establishes the fact that, the microstructure of the recast layer which is formed by the solidification of liquid metal droplets, behaves like a weld metal structure with poor passivity and lowered primary transpassive potentials (E_{pt}). Apart from the microstructure it's also the inhomogeneity that is present within the recast/recast layer such as pores and cracks that results in the lowered corrosion resistance of the WEDM surface. It's already established that in case of the low Cr steels that the passive film that gets formed in the acidic medium are loose corrosion deposits and are unstable [28]. The presence of oxides on the EDM surface makes the passivation currents to be reduced to one order of magnitude lower than the diamond polished surface when exposed to the sulphuric acid environment. The micrograph of the EDM surface as shown in Figure 6.10 indicates presence of the oxide layer (white regions in the micrograph) formed during the machining operations. There are also regions which are dark in colour where oxide formation has not taken place. The surface does not show uniform dissolution in sulphuric acid medium as observed in Figure 6.11. The surfaces which have selectively dissolved are regions which were having no oxide on it. These regions when dissolved shows that the microstructure of the underlying bulk P91 steel is similar to that is observed when P91 diamond polished surface is exposed in sulphuric acid environment.

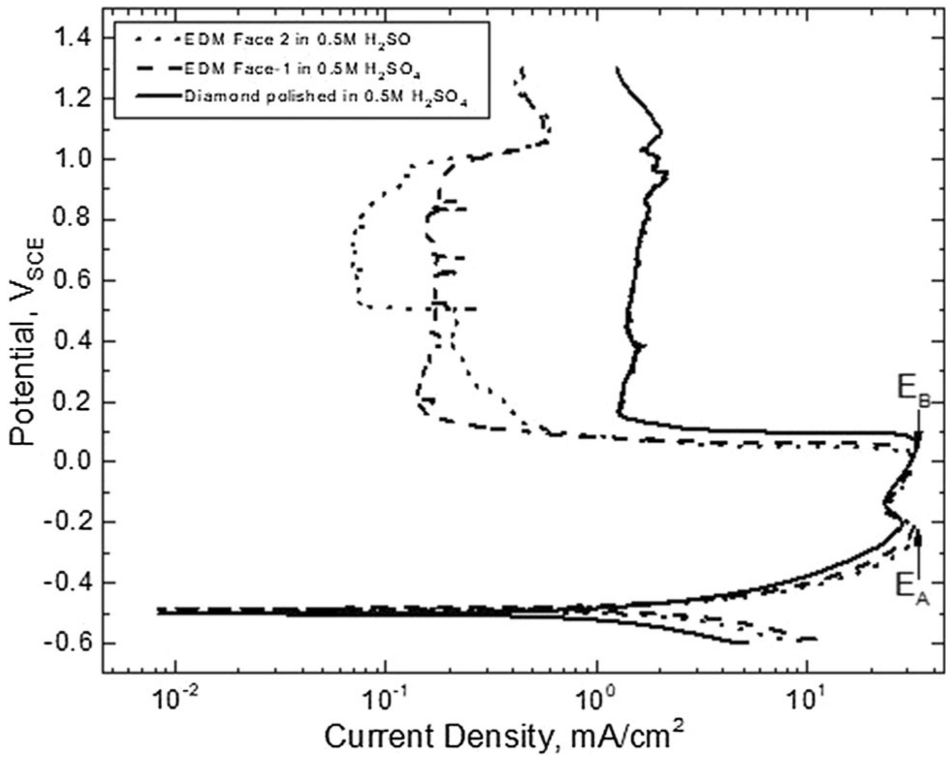

Figure 6.9 Potentiodynamic plot for EDM and diamond polished P91 steel in 0.5 M H_2SO_4 solution.

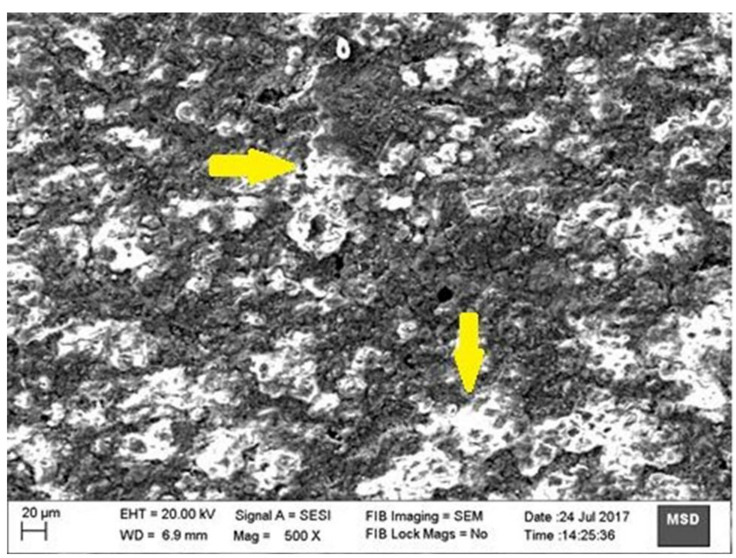

Figure 6.10 SEM of P91 EDM surface Face1 before polarization in 0.5 M H_2SO_4 solution showing some areas with oxides (marked with arrow) region.

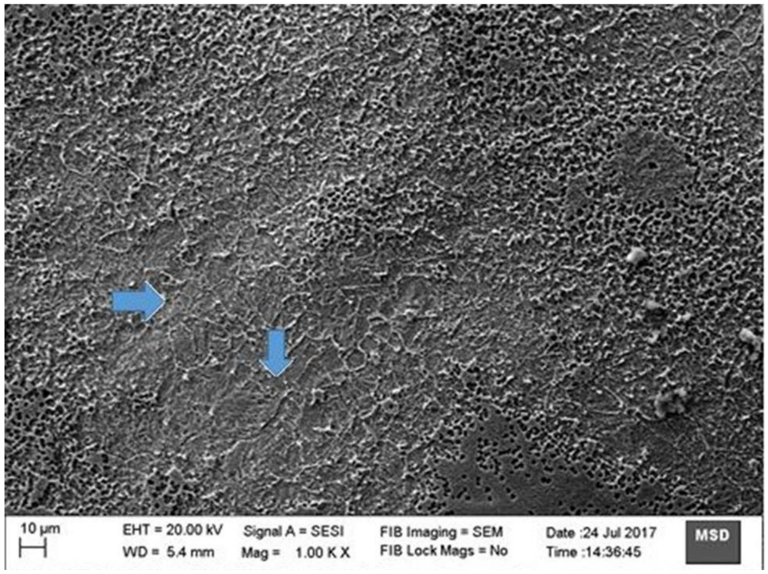

Figure 6.11 SEM of P91 EDM surface Face 1 after polarization in 0.5 M H_2SO_4 solution showing where base metal grain structure is revealed due to transpassive dissolution of recast layer (marked with arrow).

6.2.7 In H_2SO_4 + NaCl solution

The polarisation as shown in Figure 6.12 of P91 steel WEDM surfaces and diamond polished surfaces in 0.5M H_2SO_4 + 0.25M NaCl solution resulted in an increased anodic current density with no indication of passivity. This is a result of the unstable passive film formed on the P91 surfaces in this environment. The alloy doesn't show two anodic peaks as the dissolution is very high in such an aggressive solution. As compared to WEDM surface, the diamond polished surface showed lesser anodic current density for dissolution (Figure 6.12). In case of WEDM surface, as seen in Figure 6.10 the surface is having prior oxide formation on the surface. The oxide that gets formed on these surfaces imparts pseudo passivity after exposure to sulphuric acid-chloride environment. The passive layer that would get formed in the presence of sulphuric acid is inhibited by these oxides which act as sites for increased dissolution in the presence of chloride environment. This makes a condition of galvanic coupling on the surface resulting in an increased dissolution of the surface. The increased anodic current densities observed in potentiodynamic plot (Figure 6.12) indicates that pitting has been initiated as soon as surfaces were exposed to the environment. The dissolution kinetics is much faster in case of WEDM surface since it has oxidized surface which is porous and unstable (table 6.2). The resistance to pitting is very poor and it starts pitting as soon as the WEDM surface is exposed to the chloride environment. The current noises observed on the plots for WEDM and diamond polished surfaces shows that there is metastable pitting taking place on the surfaces. The diamond polished surfaces at the beginning itself shows several film breakdown and reformation activities which further leads to sustained pitting and growth. Figure 6.13 shows pitting of the diamond polished surface after potentiodynamic scanning up to a current density of 5 mA/cm^2 and holding it for 60 sec. The holding at this current density value resulted in shallow and deep pits getting formed on the surface. In case of WEDM surface, as seen in Figure 6.14, the potentiodynamic scanning and holding at 5 mA/cm^2 resulted in fine but densely populated pits getting formed on the surface which contributed to the increased anodic dissolution current density.

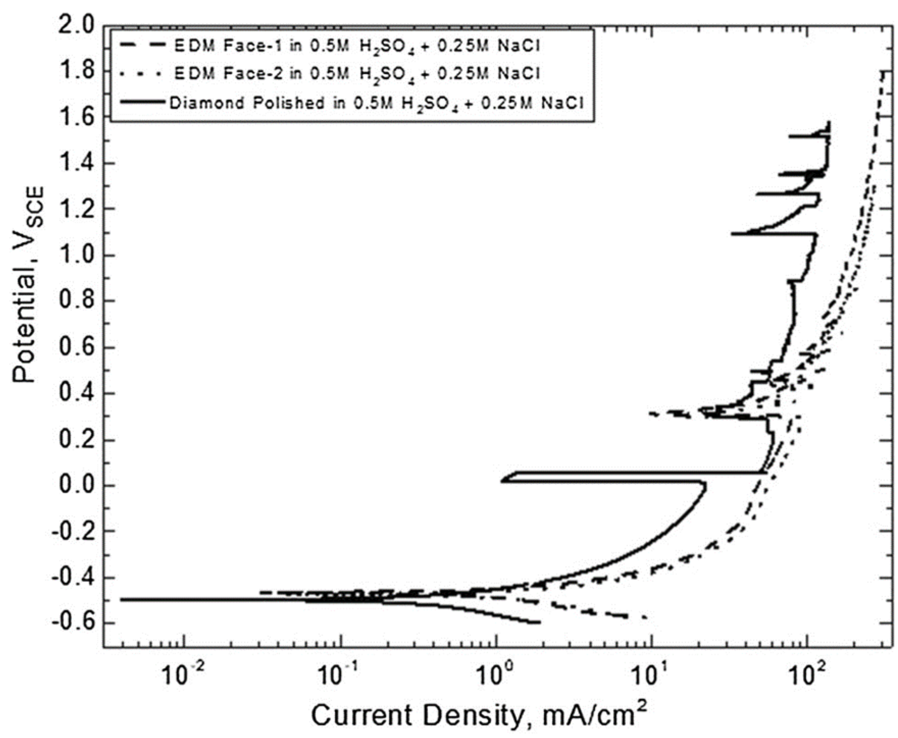

Figure 6.12 Potentiodynamic plot for EDM and diamond polished P91 steel in 0.5 M H_2SO_4 + 0.25 M NaCl solution.

6.3 Reactivation studies

The DL-EPR studies were carried out for diamond polished surface and two WEDM surfaces of P91steel. The experiments were conducted in a low concentration sulphuric acid environment. Though generally EPR studies are carried out using a depassivator such as KSCN which has not been used in the present experiments. This is primarily due to the excessive pitting and uniform corrosion of martensitic steels due to depassivators resulting in no clear intergranular corrosion effects [29-31]. EPR studies have already been reported on martensitic steels using sulphuric acid [30, 31]. It clearly showed a difference in the reactivation potential and currents [32]. In the present studies, we have a tempered martensitic structure for the diamond polished surface (Figure 6.3) while for the WEDM surface it is martensitic structure with carbides and retained austenite in the recast layer (Figure 6.4).Figure 6.15 shows an increased reactivation current density for diamond polished P91steel as compared to EDM cut surface. This is primarily due to the microstructural difference between the two surfaces. In case of diamond polished surface the microstructure is primarily tempered martensite with carbide. In case of the WEDM surfaces the microstructure is a mixed structure comprising of martensite, retained austenite and carbides. It is a weld structure due to the molten metal getting solidified on the surface as mentioned earlier. Also, the grain size has reduced considerably as shown by the TEM analysis of the recast layer. In such conditions the chromium depletion around the carbides is much less as the replenishment from the matrix is quite fast [33]. Hence the IGC susceptibility measured in terms of degree of sensitisation (DOS) is less for the WEDM surfaces compared to the diamond polished surface of P91steel. In case of the diamond polished (Figure 6.16) the IGC attack is more concentrated along the prior austenite grain boundaries and along the martensite lathes. In Figure 6.17 the attack on the WEDM surface is very different from that seen on the diamond polished surface. The attack seems to be uniform attack and not concentrated at the grain boundaries.

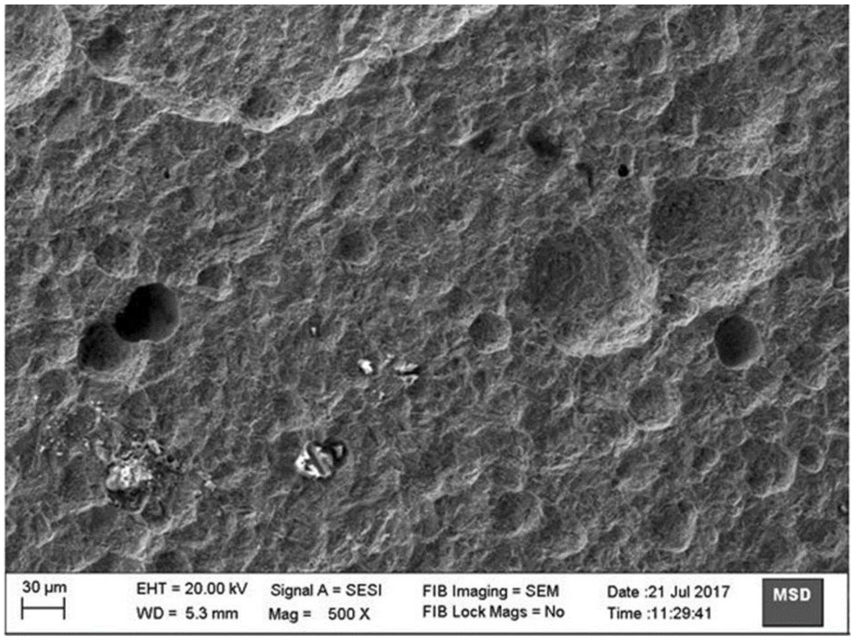

Figure 6.13 SEM of diamond polished P91 after polarization in 0.5 M H_2SO_4 + 0.25 M NaCl solution showing distinct pit formation.

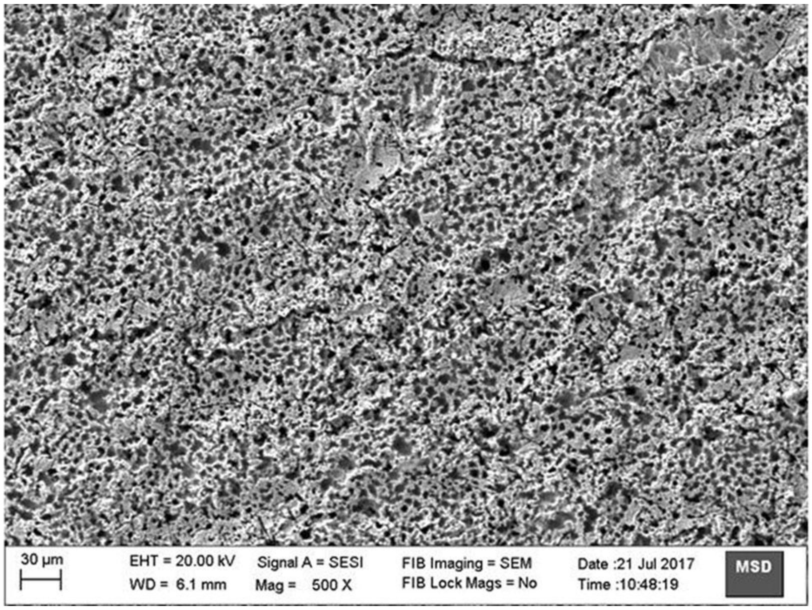

Figure 6.14 SEM of P91 EDM surface Face 1 after polarization in 0.5 M H_2SO_4 + 0.25 M NaCl solution showing distinct pit formation.

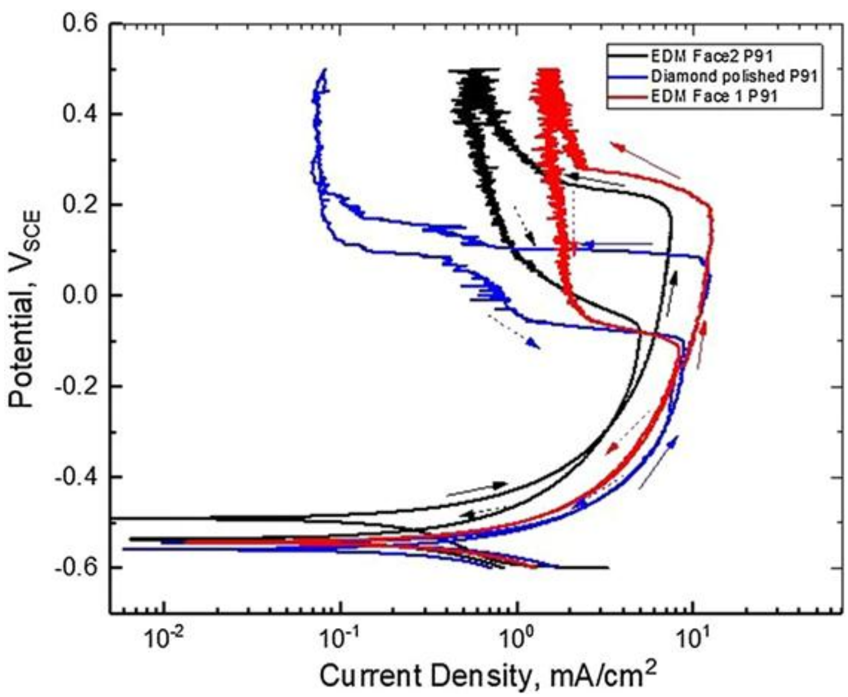

Figure 6.15 DL-EPR plots for P91 WEDM and diamond polished surface in 0.03 M H_2SO_4 solution.

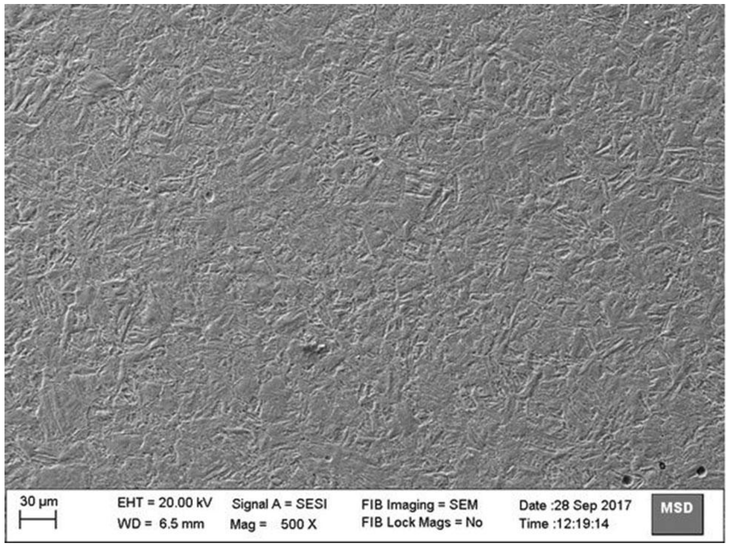

Figure 6.16 SEM pictures show the attack on the diamond polished P91 surface after DL-EPR studies at 0.03 M H_2SO_4 solution at room temperature.

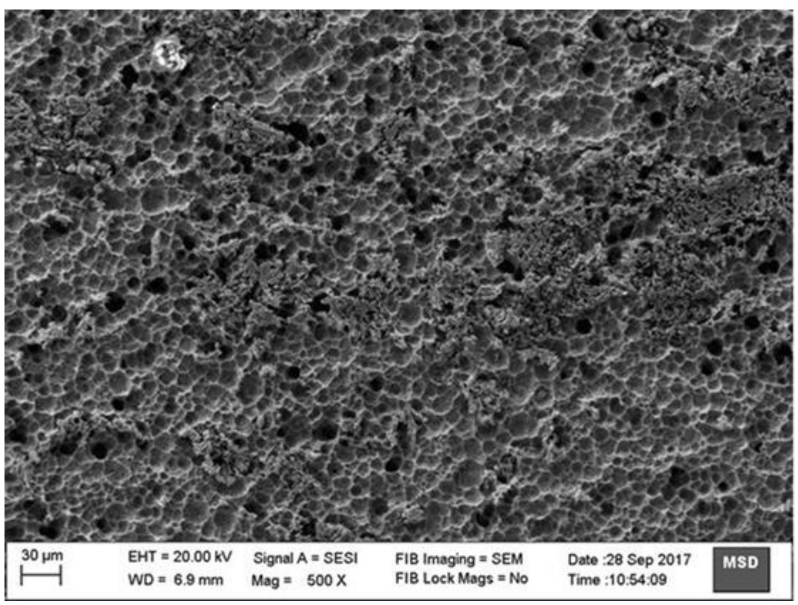

Figure 6.17 SEM pictures show the attack on the P91 WEDM surface after DL-EPR studies at 0.03 M H_2SO_4 solution at room temperature.

From the potentiodynamic experiments on WEDM surfaces and diamond polished surfaces of P91 steel in different pH solutions, the corrosion potential (E_{corr}) and corrosion current density (i_{corr}) observed are specific to electrochemical behaviour of surface layer. The WEDM surface is a recast layer. The general observation made for all surfaces of P91 steel was that in case of high pH solutions corrosion current density, i_{corr} is of the order of 10^{-6} - 10^{-7} mA/cm^2 but as the pH decreases to 0 as in the case of 0.5M H_2SO_4 solution the corrosion current density increases to the order of 10^{-3} mA/cm^2. The increase in the corrosion current density is a result of passive film instability on the surface at rest potential. So, the corrosion product that gets formed on the surfaces at acidic pH gives pseudo passivity.

As the pH of the solution decreases, apart from the increased corrosion current density of the steel in the environment the corrosion potential becomes more cathodic. This makes the surfaces more active in low pH environments and hence increased dissolution. Also, the critical current density (i_A and i_B) increases with decreasing pH. Thus, passive layer formation becomes difficult with increasing concentration of H^+ ions in the environment. The presence of a second anodic critical current density becomes predominant with decreased pH. The presence of second anodic critical potential (E_B)could be a result of oxidation of atomic hydrogen absorbed by the metal, oxidation of Fe^{2+} ions in the acid solution, Ni enrichment on the surface and presence of Cr impoverished regions, and microstructure and compositional effect [34, 35].

In H_2SO_4 solution WEDM surfaces showed lower primary passivation current density (i_{pp}) than diamond polished surface. This could be a result of the dendritic structure of recast layer as compared to wrought structure of the diamond polished surface. The increased dissolution in the dendritic structure will result in availability of free chromium ions which react with the hydroxyl ions to form chromium hydroxide layer to give primary passivity. At higher potentials, the chromium undergoes oxidation resulting in dissolution of passive layer and iron hydroxide formation takes place. Also, since the WEDM operations would result in inherent oxide film formation on the surface which further helps in passive film formation. The electrochemical behaviour of WEDM surfaces in sulphuric acid environment is comparable to the weld metal behaviour of 9Cr-1Mo steel weldment in the same environment. The potentiodynamic plot (Figure 6.9) is shows that WEDM machined surface of P91 has similar electrochemical behaviour which are reported in welded region of P91 by Geogy et.al [19].

In solutions with high pH as in Borate buffer solution and pH-7 solution passive layer forms readily keeping the corrosion rate negligible. When polarised to potentials of 0.4 - 0.7 V_{SCE} the primary transpassive dissolution takes place. It has been reported using an in-situ Raman studies by Gui et al. [36] and Zhang [37] on iron and carbon steel surfaces that the passive film formed at pH 8.4 has an iron hydroxide and magnetite layer but as current increases there is a film breakdown or restructuring which dehydrates to Fe_2O_3 resulting in a temporary loss in passivation. At higher potentials of upto 1.3 V_{SCE} there is secondary transpassive dissolution setting in which results in an increased dissolution of Cr ions.

When 0.25M NaCl is added to H_2SO_4 solution, chloride ions hinder the formation of passive layer. Thus, in solution containing NaCl no passivity was observed. Also, in this solution WEDM surfaces showed more reactivity than diamond polished surface which is due to presence of micro cracks inherent to the recast layer of WEDM surface. This recast layer is the re-solidified metal which has dendritic structure; hence chromium concentration is not uniform in the top recast layer. The micro cracks on the surface acts as the accumulation site for the chloride ions hence causing the pits to initiate and once the pits are formed corrosion takes place at a much faster rate.

The IGC susceptibility studies for P91 alloy in WEDM and diamond polished surfaces revealed the strong effect of microstructure. In case of the smaller grains getting formed on the WEDM surface due to the machining operation resulted in lesser chromium depletion. As the grain size is small chromium diffusion is faster and DOS values are lower than the diamond polished surface.

6.4 Conclusions

- P91 steel wire electrical discharge machined surfaces have better passivation than diamond polished surface in different pH buffer solution and in sulphuric acid environment. (pH-0 to pH-9.2) [38].
- P91 steel wire electrical discharge machined surface show corrosion behaviour similar to that shown by weld metal of P91 steel weldment in sulphuric acid environment [38].
- Pitting resistance of P91 steel wire electrical discharge machined surfaces are poor as prior oxide and pores act as initiation sites compared to diamond polished surface [38].
- IGC resistance of P91 steel wire electrical discharge machined surface is better owing to increased chromium content along the carbides than diamond polished surface due to decreased grain size [38].

6.5 References

[1] A. A. F. Tavassoli, E. Diegele, R. Lindau, N. Luzginova, H. Tanigawa, “Current status and recent research achievements in ferritic/martensitic steels”, J Nucl Mater, 455 (2014): 269-276.

[2] V. K. Shamardin, V. N. Golovanov, T. M. Bulanova, A. V. Povstianko, A. E. Fedoseev, Yu. D. Goncharenko, Z. E. Ostrovsky, “Mechanical properties and microstructure of advanced ferritic- martensitic steels used under high dose neutron irradiation”, J Nucl Materials, 271-272 (1999):155-161.

[3] V. Shankar, M. Valsan, K. Bhanu Sankara Rao, R. Kannan, S. L. Mannan, S. D. Pathak. Low cycle fatigue behavior and microstructural evolution of modified 9Cr-1Mo ferritic steel, Materials Science and Engineering: A, 437 (2006): 413-422

[4] E. E. Bloom, S. J. Zinkle, F. W. Wiffen, “Materials to deliver the promise of fusion power - progress and challenges”, J Nucl Mater, 329 (2004):12-19.

[5] H. Sidhom, “Effect of electro discharge machining (EDM) on the AISI316L SS recast layer microstructure and corrosion resistance”, The Int J Adv Manuf Tech, 65 (2013): 141-153

[6] H.C Tsai, B.H Yan, F.Y Huang, “EDM performance of Cr/Cu-based composite electrodes”, Int J Mach Tools Manuf, 43 (2003):245-252

[7] J. Kruth, L. Stevens, L. Froyen, B. Lauwers, Study of the recast layer of a surface machined by die-sinking electro-discharge machining, CIRP Ann, 44 (1995):169–172.

[8] S. Bhattacharya, A. Mishra, N. Keshkar, S. Kumar, V. Kain and G. K. Dey, “Wire Electric-Discharge Machining (WEDM) of P91 Steel- Microstructure and Thermal Modelling Studies”, Metallurgical and Materials Transactions A, 50 (2019): 5336–5355.

[9] F. Klocke, L. Hensgen, A. Klink, L.Ehle, and A.Schwedt, “Structure and Composition of the White Layer in the Wire-EDM process”, Proc. CIRP, 42 (2016):673-678.

[10] J.C. Rebelo, A.M. Dias, D. Kremer, J.L. Lebrun, “Influence of EDM pulse energy on the surface integrity of martensitic steels”, J. Mater Process Technol, 84 (1998): 90–96.

[11] S.F. Hsieh, S.L. Chen, H.C. Lin, M.H. Lin, S.Y. Chiou, “The machining characteristics and shape recovery ability of Ti–Ni–X (X = Zr, Cr) ternary shape memory alloys using the wire electro-discharge machining”, Int J Mach Tools Manufacturing, 49 (2009): 509–514.

[12] J.F. Liu, Y.B. Guo, T.M. Butler, “Crystallography, compositions, and properties of recast layer by wire electrical discharge machining of nitinol shape memory alloy”, Mat and Design, 109 (2016):1–9

[13] Thomas R. Newton, Shreyes N. Melkotea, Thomas R. Watkins, Rosa M. Trejo, Laura Reister, “Investigation of the effect of process parameters on the formation and characteristics of recast layer in wire-EDM of Inconel 718”, Mat Sci and Engg. A, 513–514 (2009):208–215.

[14] B. H. Yan, Y. C. Lin, F.Y. Huang, "Surface modification of Al–Zn–Mg alloy by combined electrical discharge machining with ball burnish machining", Int J Mach Tools Manufacturing, 42 (2002):925–934.

[15] A. Ntasi, W.D. Mueller, G. Eliades, S. Zinelis, "The effect of electro discharge machining (EDM) on the corrosion resistance of dental alloys", Dent Material, 26 (2010):237–245.

16] Y. Uno, A. Okada, K. Uemura, P. Raharjo, T. Furukawa, K. Karato, "High-efficiency finishing process for metal mould by large-area electron beam irradiation", Precis Engg., 29 (2005):449–455.

[17] H. Obara, H. Satou, M. Hatano, "Fundamental study on corrosion of cemented carbide during wire EDM", J Mater Process Technology, 149 (2004):370–375.

[18] ASTM G102 - 89(2015) e1- Standard Practice for Calculation of Corrosion Rates and Related Information from Electrochemical Measurements

[19] G. George, H. Shaikh, N. Parvathavarthini, R.P. George, and H.S. Khatak, "On the Microstructure-Polarization Behavior Correlation of a 9Cr-1Mo Steel Weld Joint", J. Mat Engg Perfor, 10 (2001):460–467.

[20] R.G. Bates and S. F. Acree, "pH of aqueous mixtures of potassium dihydrogen phosphate and disodium hydrogen phosphate at 0 to 60 ºC", J. Research NBS, 34 (1945):373-394.

[21] R.P. Singh, O.P. Modi, M.N. Mungole, and K.P. Singh, “Corrosion of 2·25Cr–1Mo ferritic steel in subhuric acid and sea water”, British Corrosion Journal, 20 (1985):28-31.

[22] M. Bojinov, G. Fabricius, T. Laitinen, T. Saario, “Transpassivity mechanism of iron-chromium-molybdenum alloys studied by AC impedance, DC resistance and RRDE measurements”, Electrochimica Acta, 44 (1999):4331- 4343.

[23] J.H. Kim, I.S. Hwang, “Development of an in-situ Raman spectroscopic system for surface oxide films on metals and alloys in high temperature water”, Nucl. Engg. Desi, 235 (2005):1029-1040.

[24] M. K. Nieuwoudt, J. D. Comins and I. Cukrowski, “The growth of the passive film on iron in 0.05M NaOH studied in situby Raman micro-spectroscopy and electrochemical polarisation. Part I: near-resonance enhancement of the Raman spectra of iron oxide and oxyhydroxide compounds”, J. Raman Spectrosc., 42 (2011):1335–1339

[25] K. Asami, K. Hashimoto and S. Shimodair, “An XPS study of the passivity of a series of Iron-Chromium alloys in Sulphuric acid”, Corr Sci, 18 (1978):151 -160.

[26] H.P.S. Makkar, P. Siddhuraju and K. Becker, “Methods in Molecular Biology: Plant Secondary Metabolite”, Humana Press, 2007

[27] N. Boucherit, A. Hugot-Le Goff, S. Joiret, “Influence of Ni, Mo and Cr on pitting corrosion of steels studied by Raman Spectroscopy”, Corrosion, 48 (1997): 569-578.

[28] N. Parvathavarthini, R. K. Dayal, J. B. Gnanamoorthy, "Effect of Microstructure on Corrosion Behavior of 9% Chromium-1% Molybdenum Steel", Corrosion; The Journal of Science & Engineering, 52 (1996):540-551.

[29] S.S.M. Tavares, F.J. da Silva, C. Scandian, G.F. da Silva, H.F.G. de Abreu, "Microstructure and intergranular corrosion resistance of UNS S17400 (17-4PH) stainless steel", Corrosion Science, 52 (2010):3835-3839

[30] N. Alonso-Falleiros, M. Magri, I.G.S. Falleiros, "Intergranular Corrosion in a Martensitic Stainless Steel Detected by Electrochemical Tests", Corrosion, 55 (1999):769-78.

[31] I. Taji, M.H. Moayed, M. Mirjalili, "Correlation between sensitisation and pitting corrosion of AISI 403 martensitic stainless steel", 92 (2015):301-308

[32] B. Sunil Kumar, V. Kain, and B. Vishwanadh, "Effect of Tempering Treatments on Microstructure and Intergranular Corrosion of 13 wt% Cr Martensitic Stainless Steel", Corrosion, 73 (2017) :362-378.

[33] B. Poulson, "The sensitization of ferritic steels containing less than 12% Cr", Corr Sci., 18 (1978): 371-395.

[34] L. Felloni, S.S. Traverso, G.L. Zucchini, G.P. Cammarota, "Investigation on the second anodic current maximum on the polarization curves of commercial stainless steels in sulphuric acid", Corros. Sci., 13 (1973):773-789.

[35] F. Ruel, P. Volovitch, L. Peguet, A. Gaugain, and K. Ogle, “On the Origin of the Second Anodic Peak During the Polarization of Stainless Steel in Sulfuric Acid”, Corrosion, 69 (2013):536-542

[36] J. Gui and T.M. Devine, “A SERS Investigation of the Passive Films Formed on Iron in Mildly Alkaline Solutions of Carbonate/Bicarbonate and Nitrate”, Corros. Sci., 37 (1995):1177–1189.

[37] X. Zhang, W. Xu, D.W. Shoesmith, and J.C. Wren, “Kinetics of H_2O_2 Reaction with oxide films on carbon steel”, Corros. Sci., 49, (2007), 4553–4567.

[38] S.Bhattacharya, Geogy J. Abraham, Abhishek Mishra, Vivekanand Kain, and G. K. Dey, “Corrosion behavior of wire electrical discharge machined surfaces of P91 steel”, Journal of Materials Engineering and Performance, 27 (2018): 4561-4570.

Thesis Key words

Name of the Student: **Sujay Bhattacharya**

Name of the CI: **Bhabha Atomic Research Centre** **Enrolment No.:** **ENGG 01201304027**

Thesis Title: **Surface characterization and Optimization of Wire Electric Discharge Machining process of P91 steel**

Discipline: **Engineering Sciences** **Sub-Area of Discipline:** **Un-conventional Machining**

Date of viva voce: **11th August, 2020**

Abrasive Electric Discharge Grinding
Abrasive Jet Machining
Artificial Neural Networking
Analysis of Variance
Computer Aided Manufacturing
Computational Fluid Dynamics
Chemical Machining
Computerised Numerical Control
Central composite design
Current Density
Dipole Ionic Electronic Shift
Degree of Sensitization
Electron Beam Machining
Electric Discharge Machining
Finite Element Method
Focussed Ion Beam
Flushing Efficiency
Flushing Pressure
Full Width Half Maximum
Gap current
Peak current
Grazing Incidence angle X- Ray Diffraction
Heat Affected Zone
High Resolution Transmission Electron Microscopy
Laser Beam Machining
Length of micro-cracks
Local Thermodynamic Equilibrium
Material Removal Rate
Multi Response Signal to Noise
Number density of micro-cracks
Peak Current
Photochemical Machining
Ratio of Two Line Intensity Method
Recast layer
Response Surface Methodology
Rotary Disk Electrode
Rotating Pin Electrode
Saturated Calomel Electrode
Scanning Electron Microscope
Spark off time
Spark on time
Tool Wear Rate
Transmission Electron Microscope
Ultrasonic Machining
Water Jet Machining
Wire Electric Discharge Machining
Wire Feed
Wire Tension
Permittivity of free space

Thesis Highlight

Name of the Student: **Sujay Bhattacharya**

Name of the CI: **Bhabha Atomic Research Centre** **Enrolment No.:** **ENGG 01201304027**

Thesis Title: **Surface characterization and Optimization of Wire Electric Discharge Machining process of P91 steel**

Discipline: **Engineering Sciences** **Sub-Area of Discipline:** **Un-conventional Machining**

Date of viva voce: **11th August, 2020**

Wire Electric Discharge Machining (WEDM) process is one of the most important un-conventional machining processes where intricate geometries can be machined with very fine accuracy. Here Plasma is created due to spark produced between the electrodes separated by a dielectric and which erodes the material and form debris which flushed out by dielectric. Surface characterization and Optimization of WEDM process is the major aim of this research work. The experimental investigations on recast layers produced during WEDM in P91 steel and also in other general industrial metals such as Al 1050, Zircaloy-4, SS304 were carried out. The WEDM process was characterized by experimental temperature measurements of plasma channel, detailed investigations of type of plasma produced and numerical modeling of heat transfer in the work piece during WEDM process. The estimation of temperature experienced by the machined surface due to thermal transient and its effect on the microstructure of the cut surfaces and estimation of WEDM spark plasma temperature were considered to obtain desired surface finish. The effects of variation of WEDM process parameters on the nature of the recast layer formed on the machined surfaces were predicted by numerical modelling substantiated by micro-structural examination.

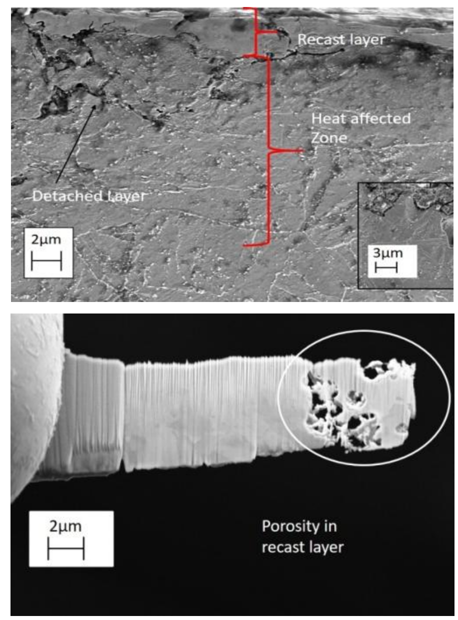

Figure 1. Experimental investigations on recast layer in WEDM process

It is demonstrated that re-solidified layer is formed due to solidification of part of molten metal during cooling phase in WEDM of P91 steel. The thickness of this recast layer depends on the energy of the spark. The peak current, voltage applied and spark on time are the major parameters affecting roughness of the machined surface. The characterization of WEDM machined surface reveals that cooling rate mainly guides the morphology of the recast layer. Investigation using TEM shows presence of nano-crystalline grains and amorphous structure in the recast layer due to high cooling rate. WEDM cut surface contains porosity and cracks which become potential for localized corrosion and failure. Also the HAZ microstructure is found to alter the passivation behavior and resistance to corrosion. Electrochemical polarization study indicates that although WEDM cut surface has better passivation resistance than diamond polished surface, it has poor resistance to IGC and pitting corrosion. The study will be helpful in deciding the process parameters for WEDM process for the materials used in the experiments (specifically P91 steel and other general industrial metals such as Al 1050, Zircaloy-4, SS304).